



Universidade do Minho
Escola de Engenharia

Ana Carina Ferreira Lopes

**Methodology for parameters optimization
and development of new materials for
additive manufacturing of SLS products**



Universidade do Minho

Escola de Engenharia

Ana Carina Ferreira Lopes

**Methodology for parameters optimization
and development of new materials for
additive manufacturing of SLS products**

Tese de Doutoramento

Ciência e Engenharia de Polímeros e Compósitos

Trabalho efetuado sob a orientação de

Professor Doutor António José Vilela Pontes

Professor Doutor Álvaro Miguel do Céu Gramaxo

Oliveira Sampaio

DIREITOS DE AUTOR E CONDIÇÕES DE UTILIZAÇÃO DO TRABALHO POR TERCEIROS

Este é um trabalho académico que pode ser utilizado por terceiros desde que respeitadas as regras e boas práticas internacionalmente aceites, no que concerne aos direitos de autor e direitos conexos. Assim, o presente trabalho pode ser utilizado nos termos previstos na licença abaixo indicada. Caso o utilizador necessite de permissão para poder fazer um uso do trabalho em condições não previstas no licenciamento indicado, deverá contactar o autor, através do RepositóriUM da Universidade do Minho.

Licença concedida aos utilizadores deste trabalho



**Atribuição
CC BY**

<https://creativecommons.org/licenses/by/4.0/>

Acknowledgments

I would like to thank all people and institutions that in some way contributed to the conclusion of this thesis.

First of all, to my supervisors, Professor António J. Pontes and Professor Álvaro M. Sampaio, for their continuous support, scientific guidance and endless motivation.

To CENTIMFE – *Centro Tecnológico da Indústria de Moldes, Ferramentas Especiais e Plásticos*, namely Nuno Fidelis and Gil Pinheiro, for the facilities and SLS equipment needed to process the composite materials in the first stages of development.

To CATIM – *Centro de Apoio Tecnológico à Indústria Metalomecânica*, namely Fernando Ferreira and Hélder Guerra, for the support with the computed tomography analyses presented in this work.

To PIEP – *Pólo de Inovação em Engenharia de Polímeros*, namely Susana Costa and Bruno Sousa, for helped me with the mechanical characterization of the case-study.

To Bosch Car Multimedia S.A., namely the colleagues from the MFE23 department, for the support in all the activities performed with the case-study in industrial environment.

To IPC – *Instituto de Polímeros e Compósitos* and DEP – *Departamento de Engenharia de Polímeros* for the facilities and technical resources provided in the course of the PhD program.

To DONE Lab and all my colleagues for the availability for helping me, for the stimulating discussions, enthusiasm and friendship.

To FCT – *Fundação para a Ciência e a Tecnologia* for the financial support through a PhD grant (2020.04520.BD).

Finally, to my family, friends and Rui for all patience, encouragement and unconditional love to make all this possible.

"Only those who risk going too far can possibly find out how far they can go." T.S. Eliot

DECLARAÇÃO DE INTEGRIDADE

Declaro ter atuado com integridade na elaboração do presente trabalho académico e confirmo que não recorri à prática de plágio nem a qualquer forma de utilização indevida ou falsificação de informações ou resultados em nenhuma das etapas conducente à sua elaboração. Mais declaro que conheço e que respeitei o Código de Conduta Ética da Universidade do Minho.

Universidade do Minho, maio de 2023

Methodology for parameters optimization and development of new materials for additive manufacturing of SLS products

Abstract

The continuous technological progress of Selective Laser Sintering (SLS) is essential for the successful manufacturing of leading-edge products demanded by the industrial society. This includes critical optimization of the SLS process parameters through a comprehensive understanding of the process-structure-property relationship and the development of multi-functional materials for non-conventional applications. In this context, carbon-based composites are raising much interest due to their potential to comply with the requirements of end-use parts that incorporate or are in contact with electronic components. The use of such materials as a preventive measure to protect the sensitive components and preserve their quality demands the establishment of a conductive network capable to ensure a slow electrostatic discharge (ESD) throughout their life cycle.

The influence of the energy density supplied by the laser beam during the SLS process, depending on the laser power, hatch distance, scan speed and layer thickness, was assessed in the initial stage of this work. A series of hatching and contour parameters were defined and applied through single and multiple exposure types in parts produced with Polyamide 12. The characterization included dimensional, geometric, mechanical and morphological tests in order to understand the potential of a combined parameterization to minimize the trade-off between strength and accuracy of SLS parts. After an in-depth understanding of the process, functional composite material integrating Multi-Walled Carbon Nanotubes (MWCNT) and Graphene Nanoplatelets (GNP) in different weight percentages were prepared through mechanical mixing and processed by SLS with adequate energy density. The parts were dimensionally, mechanically, thermally, electrically and morphologically characterized in order to obtain high-value solutions with electrical surface resistance in the ESD range with minimum development costs. Afterwards, the experimental results were used to validate numerical methods needed for the development of models capable to characterize the properties of SLS parts as a function of the input process variables, using ANSYS software. Finally, the feasibility of the research for practical applications was demonstrated with a case-study. A product with protection against ESD interferences was produced by SLS with the composite materials and numerical methodology previously established and validated in real context of application.

KEYWORDS: Additive Manufacturing; Selective Laser Sintering; Process parameters; Energy density; Composite materials; Electrostatic discharge; Numerical analysis.

Metodologia para otimização de parâmetros e desenvolvimento de novos materiais para fabrico aditivo de produtos SSL

Resumo

O continuo progresso tecnológico da Sinterização Seletiva a Laser (SSL) é essencial para o fabrico bem-sucedido de produtos de vanguarda exigidos pela sociedade industrial. Isso inclui uma crítica otimização de parâmetros de processo SSL através de uma abrangente compreensão da relação processo-estrutura-propriedade e do desenvolvimento de materiais multifuncionais para aplicações não convencionais. Neste contexto, materiais compósitos à base de carbono estão a despertar muito interesse devido ao seu potencial para assegurar os requisitos de peças de uso final que incorporam ou estão em contacto com componentes eletrónicos. A utilização desses materiais como uma medida preventiva para proteger os componentes sensíveis e preservar a sua qualidade exige a criação de uma rede condutora capaz de garantir uma descarga eletrostática (ESD) lenta durante o seu ciclo de vida.

A influência da densidade de energia fornecida pelo feixe de laser durante o processo SSL, dependendo da potência do laser, distância entre vetores de laser, velocidade de varredura e espessura da camada, foi avaliada na etapa inicial desta investigação. Uma série de parâmetros de preenchimento e contorno foi definida e aplicada por meio de tipologias de exposição única e múltipla a peças produzidas em Poliamida 12. A caracterização incluiu testes dimensionais, geométricos, mecânicos e morfológicos de modo a compreender o potencial de uma parametrização combinada em assegurar a compatibilidade entre resistência e precisão de peças SSL. Posteriormente, materiais compósitos funcionais incorporando Nanotubos de Carbono de Paredes Múltiplas (MWCNT) e Nanoplaquetas de Grafeno (GNP) em diferentes percentagens em peso foram preparados através de misturas mecânicas e processados por SSL com adequada densidade de energia. As peças produzidas foram caracterizadas dimensionalmente, mecanicamente, termicamente, eletricamente e morfológicamente a fim de se obter soluções com resistência superficial elétrica na gama ESD com o mínimo custo de desenvolvimento. De seguida, os resultados experimentais foram utilizados para a validação de métodos numéricos necessários para o desenvolvimento de modelos capazes de caracterizar as propriedades de peças SSL em função das variáveis de entrada do processo, utilizando o software de simulação ANSYS. Por fim, a viabilidade da investigação para aplicações práticas foi demonstrada com um caso de estudo. Um produto com proteção contra interferências ESD foi produzido por SSL com os materiais compósitos e a metodologia numérica previamente estabelecida e validado em contexto real de aplicação.

PALAVRAS-CHAVE: Fabrico aditivo; Sinterização Seletiva a Laser; Parâmetros de processo; Densidade de energia; Materiais compósitos; Descarga electrostática; Análise numérica.

Contents

Acknowledgments	iii
Abstract	v
Resumo	vi
Contents	vii
List of figures	x
List of tables	xix
List of abbreviations and acronyms	xx
List of scientific publications	xxii
Chapter 1. Introduction	1
1.1. Contextualization and motivation	2
1.2. Objectives and contributions	3
1.3. Thesis organization	5
Chapter 2. A review of Selective Laser Sintering: Parameters, materials and computational modelling	7
2.1. Selective Laser Sintering	8
2.2. Process parameters of Selective Laser Sintering	9
2.3. Materials for Selective Laser Sintering	14
2.3.1. Material requirements for quality processability	15
2.3.2. Conventional polymeric materials	15
2.3.3. Composite materials	17
2.4. Computational modelling of Selective Laser Sintering	28
Final Remarks of Chapter 2	32
Chapter 3. Optimization of SLS process parameters	33
3.1. Introduction	34
3.2. Materials and methods	37
3.3. Characterization tests	37
3.3.1. Mass and general dimensions	38
3.3.2. Dimensional and geometric accuracy	38

3.3.3. Mechanical tests.....	39
3.3.4. Warpage and curling.....	43
3.3.5. Morphological assessment.....	44
3.3.6. Process characterization.....	44
3.4. Results and discussion.....	44
3.4.1. Hatching parameters.....	44
3.4.2. Contour parameters.....	83
3.4.3. Combination of hatching and contour parameters.....	92
Final Remarks of Chapter 3.....	114
Chapter 4. Development and characterization of SLS composite materials.....	115
4.1. Introduction.....	116
4.2. Materials and methods.....	116
4.2.1. Selection of reinforcements.....	117
4.2.2. Preparation of composite materials.....	118
4.2.3. Processing of composite materials.....	119
4.3. Characterization tests.....	120
4.3.1. Mass and general dimensions.....	120
4.3.2. Dimensional and geometric accuracy.....	120
4.3.3. Surface roughness.....	121
4.3.4. Mechanical tests.....	121
4.3.5. Electrical tests.....	122
4.3.6. Thermal tests.....	122
4.3.7. Morphological assessment.....	123
4.3.8. Process characterization.....	123
4.4. Results and discussion.....	124
4.4.1. PA12-MWCNT composites.....	124
4.4.2. PA12-GNP composites.....	147
4.4.3. PA12-MWCNT-GNP composites.....	164
4.4.4. Cost analysis.....	181
Final Remarks of Chapter 4.....	183
Chapter 5. Case-study: Experimental and numerical analysis.....	185
5.1. Introduction.....	186

5.2. Case-study	186
5.3. Production of prototypes	190
5.4. Characterization of prototypes.....	191
5.4.1. Results and discussion.....	193
5.5. Numerical analysis	196
5.5.1. ANSYS simulation	196
5.5.2. Global numerical-experimental agreement	199
5.5.3. Local numerical-experimental agreement.....	200
5.6. Validation of the product for industrial implementation	204
Final Remarks of Chapter 5	210
Chapter 6. Conclusions and future developments	211
6.1. Conclusions.....	212
6.2. Future developments	214
References.....	217
Appendices	229
Appendix A. List of scientific publications focused on SLS computational modelling.....	229
Appendix B. Summary of properties and experimental regressions depending on fundamental SLS process parameters	232
Appendix C. 2D CAD drawing of the robot end-effector.....	235

List of figures

Figure 1.1 Workflow of the thesis.	5
Figure 2.1 SLS process (Adapted from (Schneider, 2011)).	8
Figure 2.2 Chemical structure of PA12 (Wikipedia, 2019).	16
Figure 2.3 Cross-section of PA12 (left) and PA12-MWCNT (right) parts produced by SLS (Adapted from (Salmoria <i>et al.</i> , 2011)).	25
Figure 2.4 Cross-section of PA12 (left) and PA12-MWCNT (right) parts produced by SLS (Adapted from (Bai <i>et al.</i> , 2015)).	25
Figure 2.5 Cross-section of PA12-CF parts produced by SLS at XY (left), YX (middle) and ZX (right) orientations considering the movement of the recoater along the x-axis (Adapted from (Badini <i>et al.</i> , 2020)).	27
Figure 3.1 i) X, ii) Y, iii) XY-S and iv) XY-A strategies of the laser beam path.	35
Figure 3.2 Test artefact for dimensional and geometric evaluation (dimensions in mm).	38
Figure 3.3 Test specimen for tensile tests (dimensions in mm).	39
Figure 3.4 Test specimen for DCB tests (dimensions in mm).	39
Figure 3.5 Mesh and boundary conditions used in the numerical analysis of DCB.	41
Figure 3.6 Trapezoidal bilinear softening cohesive law.	42
Figure 3.7 Test specimen for warpage evaluation (dimensions in mm).	43
Figure 3.8 Position and orientation of the test specimens in the EOS P 396 building platform.	44
Figure 3.9 Fine features of test artefacts produced by SLS with 0.278 J/mm ³ (top), 0.238 J/mm ³ (middle) and 0.198 J/mm ³ (bottom).	46
Figure 3.10 Finishing of surfaces directed to the top (left) and bottom (right) of test specimens produced by SLS with 0.198 J/mm ³	46
Figure 3.11 Fine features of a test artefact produced by SLS with 0.158 J/mm ³ , evidencing the brittleness of pins.	47
Figure 3.12 Fine features of test artefacts produced by SLS with 0.158 J/mm ³ (left) and 0.198 J/mm ³ (right).	47
Figure 3.13 Surface of a test artefact produced by SLS with 0.358 J/mm ³ after cleaning with microbeads blasting.	47
Figure 3.14 Lateral defects in test specimens produced by SLS with 0.358 J/mm ³	48
Figure 3.15 Downward and upward facing surfaces of a test artefact produced by SLS with 0.398 J/mm ³ after cleaning with sand blasting.	48
Figure 3.16 Lateral defects in test specimens produced by SLS with 0.398 J/mm ³	48
Figure 3.17 Surface of a test artefact produced by SLS with 0.318 J/mm ³ in the x-direction after cleaning with sand blasting.	49
Figure 3.18 Lateral defects in test specimens produced by SLS with 0.318 J/mm ³ in the x-direction.	49
Figure 3.19 Surface of a test artefact produced by SLS with 0.318 J/mm ³ in the y-direction after cleaning with sand blasting.	50
Figure 3.20 Lateral characteristics of test specimens produced by SLS with 0.318 J/mm ³ with the x-direction (left) and y- direction (right).	50
Figure 3.21 Test artefact produced by SLS with 0.318 J/mm ³ in the xy-direction-simultaneous after cleaning with sand blasting.	50
Figure 3.22 Test specimens produced by SLS with 0.318 J/mm ³ in the xy-direction-simultaneous.	51
Figure 3.23 Test bars produced by SLS with 0.158 J/mm ³ (top), 0.278 J/mm ³ (middle) and 0.398 J/mm ³ (bottom).	51
Figure 3.24 Warpage and curling phenomena in a test specimen produced by SLS with 0.398 J/mm ³	52
Figure 3.25 Mass of test specimens produced by SLS depending on EDV (XY-A strategy).	53
Figure 3.26 Length of test specimens produced by SLS depending on EDV (XY-A strategy).	54
Figure 3.27 Width of test specimens produced by SLS depending on EDV (XY-A strategy).	54
Figure 3.28 Thickness of test specimens produced by SLS depending on EDV (XY-A strategy).	55
Figure 3.29 Mass (left) and length (right) of test specimens produced by SLS depending on the laser strategy (0.318 J/mm ³).	55

Figure 3.30 Width (left) and thickness (right) of test specimens produced by SLS depending on the laser strategy (0.318 J/mm ³).....	56
Figure 3.31 Geometric characteristics of a test artefact produced by SLS with 0.158 J/mm ³	57
Figure 3.32 Geometric characteristics of a test artefact produced by SLS with 0.318 J/mm ³	57
Figure 3.33 Geometric details of a test artefact produced by SLS with 0.318 J/mm ³	58
Figure 3.34 Flatness of the top surface of test artefacts produced by SLS depending on EDV (XY-A strategy).	58
Figure 3.35 Roundness of central and lateral holes of test artefacts produced by SLS depending on EDV (XY-A strategy). ...	59
Figure 3.36 Perpendicularity of holes with top surface (left) and concentricity of inner cylinders (right) of test artefacts produced by SLS depending on EDV (XY-A strategy).....	59
Figure 3.37 Straightness of the primary surface of test artefacts produced by SLS depending on EDV (XY-A strategy).	60
Figure 3.38 Parallelism of opposite surfaces of test artefacts produced by SLS depending on EDV (XY-A strategy).	60
Figure 3.39 Representation of the positive direction of deviation in positioning (x, y and z axes).....	61
Figure 3.40 Average deviations of negative (left) and positive (right) x-positions of pins in test artefacts produced by SLS depending on EDV (XY-A strategy).	61
Figure 3.41 Average deviations of negative (left) and positive (right) y-positions of pins in test artefacts produced by SLS depending on EDV (XY-A strategy).	62
Figure 3.42 Factor of deviation (in %) for x (left) and y (right) positions of pins in parts produced by SLS depending on EDV (XY-A strategy).	63
Figure 3.43 Average deviations of negative (left) and positive (right) z-positions of staircases in test artefacts produced by SLS depending on EDV (XY-A strategy).	64
Figure 3.44 Diameter of pins of test artefacts produced by SLS depending on EDV (XY-A strategy).	64
Figure 3.45 Diameter of holes of test artefacts produced by SLS depending on EDV (XY-A strategy).....	65
Figure 3.46 Minimum diameter (left) and minimum separation (right) of features of test artefacts produced by SLS depending on EDV (XY-A strategy).	66
Figure 3.47 Surface comparison of test artefacts produced by SLS with 0.158 J/mm ³ (left) and 0.318 J/mm ³ (right) with the CAD model.	66
Figure 3.48 Flatness of the top surface of test artefacts produced by SLS depending on the laser strategy (0.318 J/mm ³)..	67
Figure 3.49 Straightness of the primary surface of test artefacts produced by SLS depending on the laser strategy (0.318 J/mm ³).....	67
Figure 3.50 Parallelism of opposite surfaces of test artefacts produced by SLS depending on the laser strategy (0.318 J/mm ³).	68
Figure 3.51 Test artefacts produced by SLS using the X (left) and Y (right) hatching strategies (0.318 J/mm ³).....	68
Figure 3.52 Diameter of pins of test artefacts produced by SLS depending on the laser strategy (0.318 J/mm ³).....	69
Figure 3.53 Engineering stress-strain curves of test specimens produced by SLS depending on EDV (XY-A strategy).	70
Figure 3.54 Elastic modulus of test specimens produced by SLS depending on EDV (XY-A strategy).	70
Figure 3.55 Tensile stress at yield (left) and tensile strain at yield (right) of test specimens produced by SLS depending on EDV (XY-A strategy).	71
Figure 3.56 Tensile stress at break (left) and tensile strain at break (right) of test specimens produced by SLS depending on EDV (XY-A strategy).....	72
Figure 3.57 Tensile strength of test specimens produced by SLS depending on EDV (XY-A strategy).	72
Figure 3.58 Engineering stress-strain curves of test specimens produced by SLS depending on the laser strategy (0.318 J/mm ³).....	73
Figure 3.59 Elastic modulus of test specimens produced by SLS depending on the laser strategy (0.318 J/mm ³).....	73
Figure 3.60 Tensile stress at yield (left) and tensile strain at yield (right) of test specimens produced by SLS depending on the laser strategy (0.318 J/mm ³).	74
Figure 3.61 Tensile stress at break (left) and tensile strain at break (right) of test specimens produced by SLS depending on the laser strategy (0.318 J/mm ³).	74
Figure 3.62 Tensile strength of test specimens produced by SLS depending on the laser strategy (0.318 J/mm ³).....	74

Figure 3.63 Experimental and numerical P - δ curves (left) and R -curves (right) of test specimens produced by SLS depending on EDV (XY-A strategy) (Dotted-line refers to numerical data).	75
Figure 3.64 Mode I energy release rate of test specimens produced by SLS depending on EDV (XY-A strategy).	76
Figure 3.65 Evolution of CZ as a function of α of SLS test specimens depending on EDV (XY-A strategy) (Dotted-line refers to R -curves).	77
Figure 3.66 Experimental P - δ curves (left) and R -curves (right) of test specimens produced by SLS depending on the laser strategy (0.318 J/mm^3).	78
Figure 3.67 Cross-section of test specimens produced by SLS with medium level of energy (0.278 J/mm^3 , XY-A strategy). ..	79
Figure 3.68 Cross-section of test specimens produced by SLS with low levels of energy (0.158 J/mm^3 (left) and 0.198 J/mm^3 (right), XY-A strategy).	79
Figure 3.69 Cross-section of test specimens produced by SLS with high levels of energy (0.358 J/mm^3 (left) and 0.398 J/mm^3 (right), XY-A strategy).	80
Figure 3.70 Surfaces of test specimens produced by SLS with 0.198 J/mm^3 (left) 0.278 J/mm^3 (middle) 0.358 J/mm^3 (right) after crack propagation under mode I loading (DCB).	81
Figure 3.71 Cross-section of test specimens produced by SLS with 0.318 J/mm^3 using i) XY-A (top-left), ii) X (top-right), iii) Y (bottom-left) and iv) XY-S (bottom-right) strategies.	81
Figure 3.72 Building time of SLS processes depending on the SScan (left) and PLaser (right).	82
Figure 3.73 Building time of SLS processes depending on the laser strategy (0.318 J/mm^3).	83
Figure 3.74 Fine features of a test artefact produced by SLS with 0.007 J/mm (PLaser/SSpeed).	84
Figure 3.75 Surface of a test artefact produced by SLS with 0.015 J/mm (PLaser/SSpeed) after cleaning with microbeads blasting.	84
Figure 3.76 Mass (left) and length (right) of test specimens produced by SLS depending on the contour parameters.	85
Figure 3.77 Width (left) and thickness (right) of test specimens produced by SLS depending on the contour parameters. ...	85
Figure 3.78 Flatness of the top surface of test artefacts produced by SLS depending on the contour parameters.	86
Figure 3.79 Straightness of the primary surface of test artefacts produced by SLS depending on the contour parameters. ...	86
Figure 3.80 Parallelism of opposite surfaces of test artefacts produced by SLS depending on the contour parameters.	86
Figure 3.81 Diameter of pins of test artefacts produced by SLS depending on the contour parameters.	87
Figure 3.82 Engineering stress-strain curves of test specimens produced by SLS depending on the contour parameters.	88
Figure 3.83 Elastic modulus of test specimens produced by SLS depending on the contour parameters.	88
Figure 3.84 Tensile stress at yield (left) and tensile strain at yield (right) of test specimens produced by SLS depending on the contour parameters.	89
Figure 3.85 Tensile stress at break (left) and tensile strain at break (right) of test specimens produced by SLS depending on the contour parameters.	89
Figure 3.86 Tensile strength of test specimens produced by SLS depending on the contour parameters.	90
Figure 3.87 Experimental P - δ curves (left) and R -curves (right) of test specimens produced by SLS depending on the contour parameters.	90
Figure 3.88 Cross-section of test specimens produced by SLS with low levels of contour energy (0.007 J/mm (left) and 0.009 J/mm (right)).	91
Figure 3.89 Cross-section of test specimens produced by SLS with high levels of contour energy (0.013 J/mm (left) and 0.015 J/mm (right)).	91
Figure 3.90 Building time of SLS processes depending on the contour parameters.	92
Figure 3.91 Test artefact produced by SLS with combination of parameters (20% of $t_{\text{Skin}}/t_{\text{Part}}$) after cleaning with sand blasting.	94
Figure 3.92 Fine features of a test artefact produced by SLS with combination of parameters (20% of $t_{\text{Skin}}/t_{\text{Part}}$).	94
Figure 3.93 Details of test specimens produced by SLS with combination of parameters (20% of $t_{\text{Skin}}/t_{\text{Part}}$).	95
Figure 3.94 Fine features of a test artefact produced by SLS with combination of parameters (30% of $t_{\text{Skin}}/t_{\text{Part}}$).	95
Figure 3.95 Details of a test specimen produced by SLS with combination of parameters (30% of $t_{\text{Skin}}/t_{\text{Part}}$).	95
Figure 3.96 Details of a test artefact produced by SLS with combination of parameters (30% of $t_{\text{Skin}}/t_{\text{Part}}$).	96

Figure 3.97 Fine features of a test artefact produced by SLS with combination of parameters (40% of t_{Skin}/t_{Part})	96
Figure 3.98 Details of a test artefact produced by SLS with combination of parameters (40% of t_{Skin}/t_{Part})	97
Figure 3.99 Test bars produced by SLS with single (top) and multiple (bottom) exposure types	97
Figure 3.100 Mass (left) and length (right) of test specimens produced by SLS depending on the combination of parameters	98
Figure 3.101 Width (left) and thickness (right) of test specimens produced by SLS depending on the combination of parameters	98
Figure 3.102 Geometric characteristics of a test artefact produced by SLS with combination of parameters (20% of t_{Skin}/t_{Part})	99
Figure 3.103 Geometric characteristics of test artefacts produced by SLS with 20% (top), 30% (middle) and 40% (bottom) of t_{Skin}/t_{Part}	100
Figure 3.104 Flatness of the top surface of test artefacts produced by SLS depending on the combination of parameters	100
Figure 3.105 Roundness of central and lateral holes of test artefacts produced by SLS depending on the combination of parameters	101
Figure 3.106 Perpendicularity of holes with top surface (left) and concentricity of inner cylinders (right) of test artefacts produced by SLS depending on the combination of parameters	102
Figure 3.107 Straightness of the primary surface of test artefacts produced by SLS depending on the combination of parameters	102
Figure 3.108 Parallelism of opposite surfaces of test artefacts produced by SLS depending on the combination of parameters	103
Figure 3.109 Average deviations of negative (left) and positive (right) x-positions of pins in test artefacts produced by SLS depending on the combination of parameters	103
Figure 3.110 Average deviations of negative (left) and positive (right) y-positions of pins in test artefacts produced by SLS depending on the combination of parameters	104
Figure 3.111 Factor of deviation (in %) for x (left) and y (right) positions of pins in parts produced by SLS depending on the combination of parameters	105
Figure 3.112 Average deviations of negative (left) and positive (right) z-positions of staircases in test artefacts produced by SLS depending on the combination of parameters	105
Figure 3.113 Diameter of pins of test artefacts produced by SLS depending on the combination of parameters	106
Figure 3.114 Diameter of holes of test artefacts produced by SLS depending on the combination of parameters	107
Figure 3.115 Engineering stress-strain curves of test specimens produced by SLS depending on the combination of parameters	107
Figure 3.116 Elastic modulus of test specimens produced by SLS depending on the combination of parameters	108
Figure 3.117 Tensile stress at yield (left) and tensile strain at yield (right) of test specimens produced by SLS depending on the combination of parameters	109
Figure 3.118 Tensile stress at break (left) and tensile strain at break (right) of test specimens produced by SLS depending on the combination of parameters	109
Figure 3.119 Tensile strength of test specimens produced by SLS depending on the combination of parameters	110
Figure 3.120 Experimental $P-\delta$ curves (left) and R -curves (right) of test specimens produced by SLS depending on the combination of parameters	111
Figure 3.121 Mode I energy release rate of test specimens produced by SLS depending on the combination of parameters	111
Figure 3.122 Cross-section of test specimens produced by SLS with 20% (left), 30% (middle) and 40% (right) of t_{Skin}/t_{Part}	112
Figure 3.123 Building time of SLS processes depending on the combination of parameters	113
Figure 4.1 Engineering stress-strain curves of test specimens produced by SLS with composite materials considering a PA12 matrix in a ratio of 100:0% and 50:50%	117

Figure 4.2 Cross-section of test specimens produced by SLS with composite materials considering a PA12 matrix in a ratio of 100:0% (left) and 50:50% (right).....	117
Figure 4.3 TEM images of NANOCYL MWCNT NC7000™ (left) and Graphenest Multi-Layer GNP (right) (NANOCYL, 2016; Graphenest, 2017).	118
Figure 4.4 Test specimens produced by SLS with PA12 with 1.75 wt% of MWCNT with 0.278 J/m ³	119
Figure 4.5 Test specimen for compression tests (dimensions in mm).	121
Figure 4.6. Test specimen for Izod impact tests (dimensions in mm).	122
Figure 4.7 Test specimen for electrical tests (dimensions in mm).	122
Figure 4.8 Position and orientation of the test specimens in the EOS P 396 building platform.	124
Figure 4.9 Test artefacts produced by SLS with PA12 incorporating 0.50 wt%, 1.75 wt% and 3.00 wt% of MWCNT.	125
Figure 4.10 Top surface of test specimens produced by SLS with PA12 incorporating 0.50 wt% (left), 1.75 wt% (middle) and 3.00 wt% (right) of MWCNT.....	126
Figure 4.11 Warpage in test specimens produced by SLS with PA12 incorporating 3.00 wt% of MWCNT.	126
Figure 4.12 Fine features of test artefacts produced by SLS with PA12 incorporating 0.50 wt% (top), 1.75 wt% (middle) and 3.00 wt% (bottom) of MWCNT.	127
Figure 4.13 Mass (left) and length (right) of test specimens produced by SLS depending on the amount of MWCNT (in wt%).	128
Figure 4.14 Width (left) and thickness (right) of test specimens produced by SLS depending on the amount of MWCNT (in wt%).	128
Figure 4.15 Geometric characteristics of test artefacts produced by SLS with PA12 incorporating 0.50 wt% (top), 1.75 wt% (middle) and 3.00 wt% (bottom) of MWCNT.	129
Figure 4.16 Geometric details of a test artefact produced by SLS with PA12 incorporating 3.00 wt% of MWCNT.	129
Figure 4.17 Flatness of the top surface of test artefacts produced by SLS depending on the amount of MWCNT (in wt%). .	130
Figure 4.18 Roundness of central and lateral holes of test artefacts produced by SLS depending on the amount of MWCNT (in wt%).	130
Figure 4.19 Straightness of the primary surface of test artefacts produced by SLS depending on the amount of MWCNT (in wt%).	131
Figure 4.20 Parallelism of opposite surfaces of test artefacts produced by SLS depending on the amount of MWCNT (in wt%).	131
Figure 4.21 Average deviations of negative (left) and positive (right) x-positions of pins in test artefacts produced by SLS depending on the amount of MWCNT (in wt%).	132
Figure 4.22 Average deviations of negative (left) and positive (right) y-positions of pins in test artefacts produced by SLS depending on the amount of MWCNT (in wt%).	133
Figure 4.23 Factor of deviation (in %) for x (left) and y (right) positions of pins in test artefacts produced by SLS depending on the amount of MWCNT (in wt%).	133
Figure 4.24 Average deviations of negative (left) and positive (right) z-positions of staircases in test artefacts produced by SLS depending on the amount of MWCNT (in wt%).	134
Figure 4.25 Diameter of pins (left) and holes (right) of test artefacts produced by SLS depending on the amount of MWCNT (in wt%).	135
Figure 4.26 Surface comparison of test artefacts produced by SLS with PA12 (left) and PA12 incorporating 3.00 wt% of MWCNT (right) with the CAD model.	135
Figure 4.27 Top surface topography of test specimens produced by SLS with PA12 incorporating 0.50 wt% (top), 1.75 wt% (middle) and 3.00 wt% (bottom) of MWCNT.	136
Figure 4.28 Engineering stress-strain curves of test specimens produced by SLS depending on the amount of MWCNT (in wt%).	137
Figure 4.29 Elastic modulus of test specimens produced by SLS depending on the amount of MWCNT (in wt%).	138
Figure 4.30 Tensile stress at yield (left) and tensile strain at yield (right) of test specimens produced by SLS depending on the amount of MWCNT (in wt%).	138

Figure 4.31 Tensile stress at break (left) and tensile strain at break (right) of test specimens produced by SLS depending on the amount of MWCNT (in wt%).	139
Figure 4.32 Tensile strength of test specimens produced by SLS depending on the amount of MWCNT (in wt%).	139
Figure 4.33 Engineering compressive stress-strain curves of test specimens produced by SLS depending on the amount of MWCNT (in wt%).	140
Figure 4.34 Compressive elastic modulus (left) and compressive strength (right) of test specimens produced by SLS depending on the amount of MWCNT (in wt%).	140
Figure 4.35 Notched Izod impact resistance of test specimens produced by SLS depending on the amount of MWCNT (in wt%).	141
Figure 4.36 Surface resistance (left) and electrical conductivity (right) of flat plates produced by SLS depending on the amount of MWCNT (in wt%) (logarithmic scale).	142
Figure 4.37 Melting and crystallization temperatures of SLS composite powders depending on the amount of MWCNT (in wt%).	143
Figure 4.38 Specific heat capacity of test specimens produced by SLS depending on the amount of MWCNT (in wt%) with temperature.	144
Figure 4.39 Onset temperature (left) and percentage of combustible material at 700 °C (right) of test specimens produced by SLS depending on the amount of MWCNT (in wt%).	145
Figure 4.40 Cross-section of test specimens produced by SLS with A) PA12, B) PA12 + 0.50 wt% MWCNT, C) PA12 + 1.75 wt% MWCNT and D) PA12 + 3.00 wt% MWCNT.	146
Figure 4.41 Cross-section of test specimens produced by SLS with PA12 + 0.50 wt% MWCNT (left), PA12 + 1.75 wt% MWCNT (middle) and PA12 + 3.00 wt% MWCNT (right).	146
Figure 4.42 Sintering process of PA12-GNP composites evidencing difficulties in powder spread.	147
Figure 4.43 Surface finishing of test specimens produced by SLS with PA12 incorporating 3.00 wt% of MWCNT (left) and 3.00 wt% of GNP (right).	148
Figure 4.44 Surface finishing of test specimens produced by SLS with PA12 incorporating 0.50 wt% (left), 1.75 wt% (middle) and 3.00 wt% (right) of GNP.	148
Figure 4.45 Fine features of test artefacts produced by SLS with PA12 incorporating 0.10 wt% of GNP.	148
Figure 4.46 Mass (left) and length (right) of test specimens produced by SLS depending on the amount of GNP (in wt%).	149
Figure 4.47 Width (left) and thickness (right) of test specimens produced by SLS depending on the amount of GNP (in wt%).	150
Figure 4.48 Surface comparison of test artefacts produced by SLS with PA12 (left) and PA12 incorporating 1.75 wt% of GNP (right) with the CAD model.	150
Figure 4.49 Flatness of the top surface of test artefacts produced by SLS depending on the amount of GNP (in wt%).	151
Figure 4.50 Roundness of central and lateral holes of test artefacts produced by SLS depending on the amount of GNP (in wt%).	151
Figure 4.51 Parallelism of opposite surfaces of test artefacts produced by SLS depending on the amount of GNP (in wt%).	152
Figure 4.52 Diameter of pins (left) and holes (right) of test artefacts produced by SLS depending on the amount of GNP (in wt%).	152
Figure 4.53 Top surface topography of test specimens produced by SLS with PA12 incorporating 0.10 wt% (top-left), 0.50 wt% (top-right), 1.75 wt% (bottom-left) and 3.00 wt% (bottom-right) of GNP.	153
Figure 4.54 Engineering stress-strain curves of test specimens produced by SLS depending on the amount of GNP (in wt%).	154
Figure 4.55 Elastic modulus of test specimens produced by SLS depending on the amount of GNP (in wt%).	155
Figure 4.56 Tensile stress at yield (left) and tensile strain at yield (right) of test specimens produced by SLS depending on the amount of GNP (in wt%).	155
Figure 4.57 Tensile stress at break (left) and tensile strain at break (right) of test specimens produced by SLS depending on the amount of GNP (in wt%).	156

Figure 4.58 Tensile strength of test specimens produced by SLS depending on the amount of GNP (in wt%).	156
Figure 4.59 Engineering compressive stress-strain curves of test specimens produced by SLS depending on the amount of GNP (in wt%).	157
Figure 4.60 Compressive elastic modulus (left) and compressive strength (right) of test specimens produced by SLS depending on the amount of GNP (in wt%).	158
Figure 4.61 Notched Izod impact resistance of test specimens produced by SLS depending on the amount of GNP (in wt%).	158
Figure 4.62 Surface resistance (left) and electrical conductivity (right) of flat plates produced by SLS depending on the amount of GNP (in wt%) (logarithmic scale).	160
Figure 4.63 Melting and crystallization temperatures of SLS composite powders depending on the amount of GNP (in wt%).	161
Figure 4.64 Specific heat capacity of test specimens produced by SLS depending on the amount of GNP (in wt%) with temperature.	162
Figure 4.65 Onset temperature (left) and percentage of combustible material at 700 °C (right) of test specimens produced by SLS depending on the amount of GNP (in wt%).	162
Figure 4.66 Cross-section of test specimens produced by SLS with A) PA12, B) PA12 + 0.50 wt% GNP, C) PA12 + 1.75 wt% GNP and D) PA12 + 3.00 wt% GNP.	163
Figure 4.67 Cross-section of test specimens produced by SLS with A) PA12 + 0.10 wt% GNP, B) PA12 + 0.50 wt% GNP, C) PA12 + 1.75 wt% GNP and D) PA12 + 3.00 wt% GNP.	164
Figure 4.68 Sintering process of PA12-MWCNT-GNP composites evidencing the powder bed.	165
Figure 4.69 Details of the top surface of test specimens produced by SLS with PA12 incorporating 0.50 wt% of MWCNT (left), 0.50 wt% of MWCNT and 0.10 wt% of GNP (middle) and 0.10 wt% of GNP (right).	165
Figure 4.70 Fine features of test artefacts produced by SLS with PA12 incorporating 0.50 wt% of MWCNT and 0.10 wt% of GNP.	166
Figure 4.71 Flatness of the top surface of test artefacts produced by SLS depending on the carbon-based material.	167
Figure 4.72 Roundness of central and lateral holes of test artefacts produced by SLS depending on the carbon-based material.	167
Figure 4.73 Straightness of the primary surface of test artefacts produced by SLS depending on the carbon-based material.	168
Figure 4.74 Parallelism of opposite surfaces of test artefacts produced by SLS depending on the carbon-based material.	168
Figure 4.75 Average deviations of negative (left) and positive (right) x-positions of pins in test artefacts produced by SLS depending on the carbon-based material.	169
Figure 4.76 Average deviations of negative (left) and positive (right) y-positions of pins in test artefacts produced by SLS depending on the carbon-based material.	169
Figure 4.77 Factor of deviation (in %) for x (left) and y (right) positions of pins in test artefacts produced by SLS depending on the carbon-based material.	170
Figure 4.78 Average deviations of negative (left) and positive (right) z-positions of staircases in test artefacts produced by SLS depending on the carbon-based material.	170
Figure 4.79 Diameter of pins (left) and holes (right) of test artefacts produced by SLS depending on the carbon-based material.	171
Figure 4.80 Surface comparison of test artefacts produced by SLS with PA12 incorporating 0.50 wt% of MWCNT (left), 0.10 wt% of GNP (middle) and 0.50 wt% of MWCNT with 0.10 wt% of GNP (right) with the CAD model.	171
Figure 4.81 Top surface topography of test specimens produced by SLS with PA12 incorporating 0.10 wt% of GNP (top), 0.50 wt% of MWCNT (middle) and 0.50 wt% of MWCNT and 0.10 wt% of GNP (bottom).	172
Figure 4.82 Engineering stress-strain curves of test specimens produced by SLS with combination of MWCNT and GNP.	173
Figure 4.83 Elastic modulus of test specimens produced by SLS with combination of MWCNT and GNP.	173
Figure 4.84 Tensile stress at yield (left) and tensile strain at yield (right) of test specimens produced by SLS with combination of MWCNT and GNP.	174

Figure 4.85 Tensile stress at break (left) and tensile strain at break (right) of test specimens produced by SLS with combination of MWCNT and GNP.	174
Figure 4.86 Tensile strength of test specimens produced by SLS with combination of MWCNT and GNP.	175
Figure 4.87 Engineering compressive stress-strain curves of test specimens produced by SLS with combination of MWCNT and GNP.....	175
Figure 4.88 Compressive elastic modulus (left) and compressive strength (right) of test specimens produced by SLS with combination of MWCNT and GNP.....	176
Figure 4.89 Notched Izod impact resistance of test specimens produced by SLS with combination of MWCNT and GNP...176	
Figure 4.90 Surface resistance (left) and electrical conductivity (right) of flat plates produced by SLS with combination of MWCNT and GNP (logarithmic scale).	178
Figure 4.91 Melting and crystallization temperatures of SLS composite powders with combination of MWCNT and GNP. ...179	
Figure 4.92 Specific heat capacity of test specimens produced by SLS with combination of MWCNT and GNP with temperature.	179
Figure 4.93 Onset temperature (left) and percentage of combustible material at 700 °C (right) of test specimens produced by SLS with combination of MWCNT and GNP.	180
Figure 4.94 Cross-section of test specimens produced by SLS with PA12 (left), PA12 + 0.10 wt% GNP + 0.50 wt% MWCNT at high magnification (middle) and PA12 + 0.10 wt% GNP + 0.50 wt% MWCNT at low magnification (right).	180
Figure 5.1 Representation of the PCB detailing four possible points of contact with the robot end-effector (red marks).	188
Figure 5.2 Types of vacuum suction cups used in the system (dimensions in mm).....	188
Figure 5.3 Proposed robot end-effector.....	188
Figure 5.4 Details of the internal conformal vacuum channel of the robot end-effector (dimensions in mm).	189
Figure 5.5 3D representation of the robot end-effector in mounted condition.....	189
Figure 5.6 Prototype produced by SLS with PA12-GNP.	190
Figure 5.7 Prototype produced by SLS with PA12.	190
Figure 5.8 Production of a PA12-GNP prototype by SLS.	191
Figure 5.9 Prototype produced with PA12-GNP evidencing metallic inserts.	191
Figure 5.10 Installation of the strain gauges in a PA12 prototype.	192
Figure 5.11 Experimental setup used to perform tensile (left) and compression (right) tests.	192
Figure 5.12 Experimental setup of the tensile test on PA12 (left) and PA12-GNP (right) prototypes.	193
Figure 5.13 Experimental setup of the compression test on PA12 (left) and PA12-GNP (right) prototypes.	193
Figure 5.14 Compression load-displacement curve obtained for a prototype produced with PA12-GNP: raw and selected data.	194
Figure 5.15 Load-displacement curves obtained for prototypes produced with PA12 and PA12-GNP in tensile (left) and compression (right) tests.....	195
Figure 5.16 Rupture of prototypes produced with PA12 (left) and PA12-GNP (right) prototypes (tensile test).	196
Figure 5.17 Mesh of components used in the numerical analysis.....	197
Figure 5.18 Modelling of the pretension in the bolts.....	197
Figure 5.19 Boundary conditions imposed for numerical analysis.	198
Figure 5.20 Flowchart of the numerical analysis in ANSYS.	198
Figure 5.21 Load-displacement curves obtained for prototypes produced with PA12 (left) and PA12-GNP (right) in tensile tests. Dotted-lines refers to numerical data.	199
Figure 5.22 Load-displacement curves obtained for prototypes produced with PA12 (left) and PA12-GNP (right) in compression tests. Dotted-lines refers to numerical data.	199
Figure 5.23 Representation of the set of elements selected for numerical local strain monitoring.....	201
Figure 5.24 Numbering of the arms considered for local strain monitoring.	201
Figure 5.25 Local longitudinal strain of prototypes produced with PA12 (left) and PA12-GNP (right) in function of the tensile load. Dotted-lines refers to numerical data.....	202
Figure 5.26 von-Mises stress of a prototype produced with PA12 under tensile loads.	202

Figure 5.27 von-Mises stress of a prototype produced with PA12-GNP under tensile loads.	203
Figure 5.28 Local longitudinal strain of prototypes produced with PA12 (left) and PA12-GNP (right) in function of the compressive load. Dotted-lines refers to numerical data.....	203
Figure 5.29 von-Mises stress of a prototype produced with PA12 under compressive loads.	204
Figure 5.30 von-Mises stress of a prototype produced with PA12-GNP under compressive loads.	204
Figure 5.31 Validation of the robot end-effector produced with PA12 at Bosch Car Multimedia S.A.	205
Figure 5.32 Instrumented PCB for local strain monitoring.	205
Figure 5.33 Experimental setup used in PCB strain measurements.	206
Figure 5.34 PCB strain measured with the robot end-effector produced with PA12 (general-purpose foil strain gauges). ...	206
Figure 5.35 PCB strain measured with the robot end-effector produced with PA12 (rosette strain gauges).....	207
Figure 5.36 PCB strain measured with the robot end-effector produced with PA12-GNP (general-purpose foil strain gauges).	207
Figure 5.37 PCB strain measured with the robot end-effector produced with PA12-GNP (rosette strain gauges).	208
Figure 5.38 Robot end-effector produced with PA12-GNP (final version).	209

List of tables

Table 2.1 EDA and EDV values for pure polyamide materials processed by SLS.	13
Table 2.2 Characteristics of carbon black, graphite, graphene and MWCNT allotropes.	21
Table 2.3 Experiments to develop carbon-based composites for SLS based on a PA12 matrix.	22
Table 3.1 List of experiments to evaluate the hatching parameters.	34
Table 3.2 Process parameters in the EOS Balance standard mode.	35
Table 3.3 List of experiments to evaluate the contour parameters (optimized hatching set).	36
Table 3.4 List of experiments to evaluate the combination of hatching and contour parameters.	36
Table 3.5 Numerical-experimental agreement of the DCB results.	76
Table 3.6 Building time of SLS productions depending on the hatching parameters.	82
Table 3.7 Building time of SLS productions depending on the contour parameters.	92
Table 3.8 Building time of SLS productions depending on the combination of parameters.	112
Table 4.1 Experiments defined to study carbon-based composites.	120
Table 4.2 Surface roughness parameters of PA12-MWCNT composites processed by SLS.	137
Table 4.3 Summary of mechanical properties of PA12-MWCNT composites.	141
Table 4.4 Electrical properties of PA12-MWCNT composites obtained through surface and volume measurements.	142
Table 4.5 Surface roughness parameters of PA12-GNP composites processed by SLS.	154
Table 4.6 Summary of mechanical properties of PA12-GNP composites.	159
Table 4.7 Electrical properties of PA12-GNP composites obtained through surface and volume measurements.	159
Table 4.8 Dimensional properties of PA12-MWCNT-GNP composites.	166
Table 4.9 Surface roughness parameters of PA12-MWCNT-GNP composites processed by SLS.	172
Table 4.10 Summary of mechanical properties of PA12-MWCNT-GNP composites.	177
Table 4.11 Electrical properties of PA12-MWCNT-GNP composites obtained through surface and volume measurements.	177
Table 4.12 Summary of costs of the development of carbon-based composites.	181
Table 5.1 Technical requirements and specifications of the case-study.	187
Table 5.2 Physical, electrical and mechanical characterization of the robot end-effector.	193
Table 5.3 Variation between experimental and numerical load for same displacement.	200
Table 5.4 Maximum absolute values obtained in the PCB strain measurements.	208

List of abbreviations and acronyms

AM	Additive Manufacturing
ANFIS	Adaptive Network-based Fuzzy Inference System
ANN	Artificial Neural Network
BGA	Ball Grid Array
CAD	Computer-Aided Design
CAGR	Compound Annual Growth Rate
CB	Carbon Black
CBBM	Compliance-Based Beam Method
CF	Carbon Fibres
CNN	Convolutional Neural Network
c_p	Specific heat capacity
CT	Computed Tomography
DCB	Double Cantilever Beam
DEM	Discrete Element Model
D_{Hatch}	Hatch distance
DSC	Differential Scanning Calorimetry
EDA	Energy density by unit of area
EDv	Energy density by unit of volume
ED _T	Total energy density
EOS	Electro Optical Systems GmbH
ESD	Electrostatic discharge
ESDS	Electrostatic discharge-sensitive devices
FEA	Finite Element Analysis
GA	Genetic Algorithm
GD&T	Geometric Dimensioning and Tolerancing
G_{lc}	Critical energy release rate
G_{lu}	Energy release rate at maximum load
GNP	Graphene Nanoplatelets
MFI	Melt Flow Index
MWCNT	Multi-Walled Carbon Nanotubes

NIST	National Institute of Standards and Technology
n/a	Not available
PA12	Polyamide 12
PCB	Printed Circuit Boards
P_{Laser}	Laser power
P - δ curves	Load-displacement curves
R -curves	<i>Resistance</i> -curves
RQ _{n}	Research question n
SEM	Scanning Electron Microscopy
SLS	Selective Laser Sintering
S _{Scan}	Scan speed
TEM	Transmission Electron Microscopy
TGA	Thermogravimetric Analysis
t_{Layer}	Layer thickness
t_{Part}	Part thickness
$T_{\text{Preheating}}$	Preheating temperature
t_{Skin}	Skin thickness
vol%	Volume percentage
wt%	Weight percentage
ρ	Density

List of scientific publications

International journal articles

Lopes AC, Sampaio AM and Pontes AJ (2022). The influence of the energy density on dimensional, geometric, mechanical and morphological properties of SLS parts produced with single and multiple exposure types. *Progress in Additive Manufacturing*. <https://doi.org/10.1007/s40964-021-00254-7>

Lopes AC, Silva EC, Dourado N, de Moura MFSF, Sampaio AM and Pontes AJ (2022). The Double Cantilever Beam test applied to mode I fracture characterization of Polyamide 12 processed by Selective Laser Sintering technology. *Engineering Fracture Mechanics*. Vol. 269 (108555) <https://doi.org/10.1016/j.engfracmech.2022.108555>

Lopes AC, Sampaio AM and Pontes AJ (2022). Composite materials with MWCNT processed by Selective Laser Sintering for electrostatic discharge applications. *Polymer Testing*. Vol. 114 (107711) <https://doi.org/10.1016/j.polymertesting.2022.107711>

IN PREPARATION FOR SUBMISSION

Lopes AC, Silva EC, Sampaio AM and Pontes AJ (2023). Understanding dimensional and geometrical tolerances of metal, polymer and composite powder bed fusion additive manufacturing technologies.

Anwar T, Lopes AC, Silva EC, Mould ST, Sampaio AM and Pontes AJ (2023). Cradle-to-gate life cycle assessment and life cycle costing: A comparison of polymer and metal-based additive manufacturing.

SUBMITTED FOR PUBLICATION

Lopes AC, Sampaio AM and Pontes AJ (2023). Development and characterization of composite materials with Multi-Walled Carbon Nanotubes and Graphene Nanoplatelets for Powder Bed Fusion. [Submitted to *Rapid Prototyping Journal*]

Lopes AC, Sampaio AM and Pontes AJ (2023). Design and industrial implementation of a multi-functional part produced by Selective Laser Sintering. [Submitted to *Progress in Additive Manufacturing*]

Oral communications

Lopes AC, Silva EC, Dourado N, Sampaio AM, Pontes AJ. Mode I fracture characterization of polyamide 12 obtained by additive manufacturing with selective laser sintering technology. *1st Virtual ESIS TC4 Conference on Fracture of Polymers, Composites and Adhesives*. Sep 28-29, 2021. Portugal.

Lopes AC, Sampaio AM, Pontes AJ. Carbon-based composite materials processed by Selective Laser Sintering for electrostatic discharge applications. *1st PPI - International Polymer Process Innovation Conference*. Dec 14-15, 2021. Portugal.

Lopes AC, Silva EC, Sampaio AM, Pontes AJ. Understanding dimensional and geometrical tolerances of metal, polymer and composite powder bed fusion additive manufacturing technologies. *Materiais 2022*. Apr 10-13, 2022. Portugal.

Lopes AC, Sampaio AM, Pontes AJ. Development and production of robot end-effectors by Selective Laser Sintering technology. *2nd PPI - International Polymer Process Innovation Conference*. Sep 15-16, 2022. Greece.

Chapter 1. Introduction

Chapter 1 presents a brief introduction to the Selective Laser Sintering (SLS) technology, disclosing the key research topics of this thesis and its relevance in real context of application. The motivation for the research, the research questions, the objectives and proposed contributions are also discussed in this introductory chapter. At the end, the organization of the document is detailed.

1.1. Contextualization and motivation

A few decades ago, Selective Laser Sintering (SLS) emerged on the market as the first Additive Manufacturing (AM) technology operating through powder bed fusion (Gibson *et al.*, 2010). For some years, SLS was considered an efficient and promising AM technology to produce polymeric parts with complex geometries and great properties capable of meeting standard requirements. However, the technological advances and increasing demand to obtain functional and personalised products with high quality, low cost and reduced processing time quickly increased the competitiveness of the market. Therefore, other AM technologies able to manufacture products without tools or moulds through attractive relationships between part properties and process effectiveness were developed in the following years (Wörz *et al.*, 2018). Although in the beginning these AM technologies were mostly considered for primary prototyping purposes, the rising technological progress quickly expanded their use for end-use solutions (SmarTech Markets, 2017; Yuan *et al.*, 2019). Nowadays, SLS guarantees economic and sustainable demands in small and medium series of production, through the manufacturing of parts with properties similar to those produced by conventional processing technologies, such as injection moulding (Kruth *et al.*, 2008; Telenko and Seepersad, 2012). Due to these advantageous capabilities, SLS parts have already been considered in challenging applications exposed to severe and dynamic thermal and mechanical environments, depending on the properties of the base material (Blattmeier *et al.*, 2012; Pilipović *et al.*, 2014). This has propelling the continuous growth of the SLS market, which is projected to reach a CAGR - Compound Annual Growth Rate of 22.8% from 2018 to 2023 (MarketsandMarkets, 2018). However, the extensive implementation of SLS as an AM technology of first choice is still limited by the multitude of factors that influence the performance of the parts produced (Sindinger *et al.*, 2020). One of the most critical impairments concerns the limited knowledge base needed to define appropriate SLS process parameters, since most of them are dependent on a series of internal and external factors in a complex and non-linear interaction (Vasquez *et al.*, 2011; Ma *et al.*, 2018; Beitz *et al.*, 2019). This is a widely researched topic since the definition of optimum process parameters for each building job is essential to avoid common defects developed during the SLS process (*e.g.*, surface roughness, porosity, heterogeneous microstructure, warpage) and to optimize the properties of the parts (Pilipović *et al.*, 2014; Malekipour and El-Mounayri, 2018). Another limitation compared to other AM technologies is the narrow number of polymeric materials available for SLS (Koo *et al.*, 2017). Since its development, the market of SLS materials mostly covers conventional thermoplastics with low to medium performance (Goodridge *et al.*, 2012; Yuan *et al.*, 2019). However, multi-functional composite materials are being constantly required to accomplish complex requirements of advanced applications in automotive, aerospace, biomedical and

other fields (Leon *et al.*, 2016; Asadi and Kalaitzidou, 2018; Yuan *et al.*, 2019). Despite the scientific progress in the development of innovative SLS materials and the on-course research to overcome this drawback, the complex phenomena of powder consolidation, the numerous requirements for a successful sintering and the interdependent process-structure-property relationship makes it difficult to establish a systematic approach capable to optimize the process for a better global performance of functional parts (Yuan *et al.*, 2020). Despite the widespread use of SLS in last years, fundamental understanding to guide process parameters optimization and materials development is continuously necessary (Beitz *et al.*, 2019; Yuan *et al.*, 2020).

In order to strengthen the scientific and technological knowledge in the field, this thesis aims to propose a methodology to optimize the SLS process parameters and to provide fundamental insights guiding the development and processing of composite materials with functional properties. Therefore, the thesis focuses its framework on three main research questions (RQ_n), as follows:

- RQ1. What is the effect of the thermal energy supplied by the laser beam to the powder particles during the SLS process on the overall performance of parts horizontally produced?
- RQ2. How the process parameters should be adjusted to allow the inclusion of functional micro and nanoparticles in SLS? In turn, how composite materials can be successfully processed by SLS?
- RQ3. How the properties of SLS parts can be predicted depending on the geometry, material, and process parameters?

1.2. Objectives and contributions

The current complexity to define the process parameters for each building job, the limited number of conventional materials available and the difficult implementation of new composite materials in SLS demand better knowledge correlating fundamental process parameters, the base-structure of the material and the properties of the laser-sintered parts. In order to provide comprehensive knowledge in this matter, this thesis encompasses three main objectives.

The first objective addresses the study and evaluation of the influence of the thermal energy supplied by the laser beam to the powder particles during the SLS process in the most relevant properties of parts horizontally produced. Therefore, five main steps are mandatory in this activity:

- To review the state of the art about the research topic, understanding the primary influence of the process parameters that define the energy density in the properties of SLS parts and identifying the range of acceptable values for commercial laser-sintering machines;

Chapter 1. Introduction

- To evaluate the influence of different combinations of process parameters in the definition of same values of energy density, using standard processing settings;
- To design a series of experiments defining hatching and contour parameters for different values of energy density, in individual and combined configurations, within the range of acceptable values;
- To characterize the dimensional, geometric, mechanical and morphological properties of SLS parts in order to identify the minimum value of energy density needed to obtain quality outputs;
- To use computational analysis to complement the experimental data.

The second part of the thesis aims the development of multi-functional composite materials integrating conductive reinforcements, in order to enable the applicability of SLS parts in novel fields. The main focus is to obtain a high-value material with potential to protect sensitive electronic components against electrostatic discharge (ESD) during operation. To do so, the specific objectives of this activity are:

- To review the state of the art about the research topic, identifying the main challenges and opportunities in the development of carbon-based composite materials processed by SLS;
- To explore a number of different reinforcements with conductive potential, as well as different weight percentages to be embedded in the polymeric matrix, in individual and combined formulations;
- To define and optimize a single-step method that allows the preparation of composite materials for SLS with minimum development costs;
- To characterize the pure polymeric matrix in respect of the thermal stability for processing and original morphological properties as reference condition;
- To optimize the laser sintering process through the selection of fundamental operating parameters defining the energy density according to the properties of the new materials;
- To characterize the dimensional, geometric, mechanical, electrical, thermal, and morphological properties of the composite materials processed by SLS in order to assess their overall performance depending on the nature and typology of the reinforcement, weight percentage of incorporation and type of composite formulation (*i.e.*, individual or combined approach).

Finally, the third objective embraces the establishment of a numerical method capable to control and predict the mechanical structural behaviour of SLS products, depending on their geometry, material and process parameters. The main goals corresponding to this part are:

- To identify a case-study in the field of automotive electronics;
- To define a quantitative method of mapping the process-structure-property relationship, according to the methodological approach used in the experimental stage;

- To complement the experimental data from the previous activities with numerical results obtained through computational methods;
- To produce the case-study with polymeric composite materials by SLS and to compare with that produced with conventional materials;
- To validate the methodology of optimization through the evaluation of the case-study in real context of application using an action-research strategy of planning, action, observation and reflection with industrials;

Once achieved the objectives of the thesis, its main technological and scientific contributions are i) an in-depth knowledge base on the process-structure-property relationship covering the most relevant SLS process parameters, ii) functional SLS composite materials with potential for ESD shielding applications and iii) a reliable numerical methodology allowing to guide process parameters optimization and materials selection for SLS parts.

1.3. Thesis organization

In order to completely accomplish the objectives described in the previous section, this thesis comprehends several interrelated theoretical and practical activities. Figure 1.1 shows the workflow of the thesis, presenting the conceptual basis that supports the research.

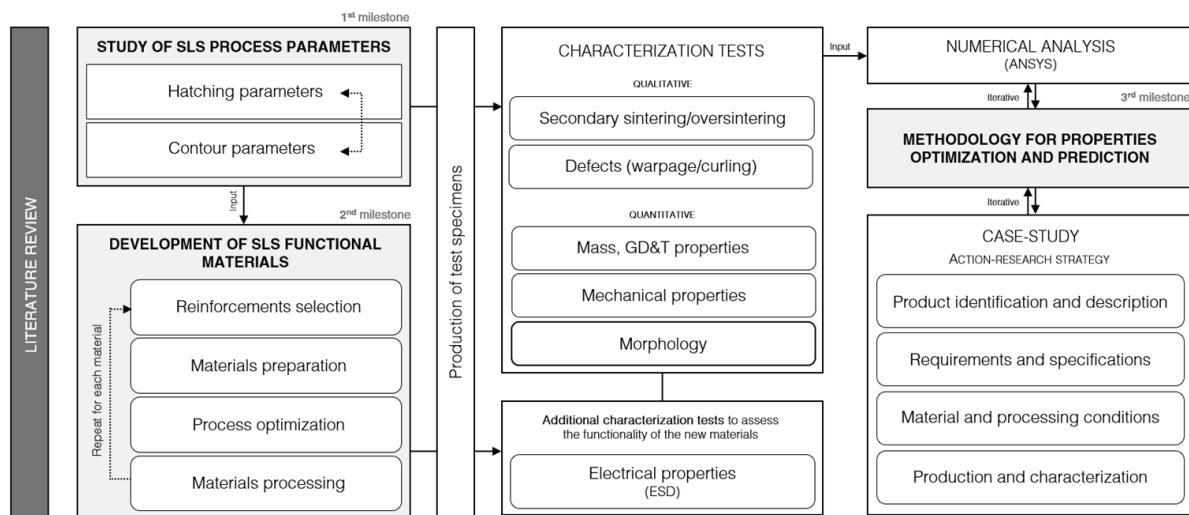


Figure 1.1 Workflow of the thesis.

Based on the objectives and activities of the workflow, this document is organized in six chapters. The current chapter, *Chapter 1*, introduces the motivation and relevance of the research, as well as its main objectives and contributions.

Following a brief introduction, *Chapter 2* in detail describes the SLS technology through the review of the state of the art focused on the process parameters and conventional materials available for the

Chapter 1. Introduction

sintering process. The potential of composite materials processed by SLS is also presented for a variety of industrial applications. In this way, considerations about the typology of the matrix and reinforcements, methods of mixing and preparation and conditions of processing are provided. At the end, quantitative methods of mapping the process-structure-property relationship in order to predict and optimize the SLS process and the properties of parts produced are listed and discussed.

Chapter 3 reports the study of fundamental SLS process parameters, providing a comprehensive description about their effect on the overall performance of parts produced. Results from X-ray computed tomography, mechanical tests and morphological analysis depending on the parameterization mode are included. The influence of the process parameters defining the thermal energy supplied by the laser beam to the powder particles during the sintering process is discussed in this chapter, through the implementation of single and multiple exposure types.

The development and characterization of innovative polymeric materials for SLS is discussed in *Chapter 4*. This chapter describes the systematic methodology used to prepare, process and characterize multi-functional carbon-based composites integrating Multi-Walled Carbon Nanotubes (MWCNT) and Graphene Nanoplatelets (GNP). The evaluation of dimensional, geometric, mechanical, electrical, thermal and morphological properties of parts as well as their potential for ESD shielding applications is investigated in the fourth chapter. In such a way, the overall performance of electrically conductive materials processed by SLS is explored in detail.

Chapter 5 presents the evaluation of a case-study that was selected to implement, validate and improve the results reported in the previous chapters. Initially, it introduces the component defined as case-study and the technical requirements that were focus of analysis. The chapter also covers the development of a numerical methodology capable to predict and optimize the mechanical properties of SLS parts, according to the experimental results obtained in the aforementioned activities. The workflow that empowered this activity is described in detail, as well as the numerical analyses carried out to evaluate the mechanical structural performance of the component. Moreover, this fifth chapter demonstrates the potential and real contribution of the developed methodology and carbon-based materials through the analysis of the product in industrial context at Bosch Car Multimedia S.A.

Finally, the most relevant conclusions of this thesis are summarized in *Chapter 6*. The significance of the achievements related to the SLS process parameters, functional materials and numerical methodology of prediction and optimization is discussed. Future developments to enhance the research are also proposed.

At the end of each chapter, a brief summary highlighting its main activities and results is provided.

Chapter 2. A review of Selective Laser Sintering: Parameters, materials and computational modelling

Chapter 2 reviews the state of the art about the research topic and related scientific areas, including a description of the Selective Laser Sintering (SLS) technology, the main process parameters that define the thermal energy supplied by the laser beam and its influence on the properties of SLS parts. It also focuses on SLS materials, describing the requirements for a successful processing, the most relevant thermoplastics, as well as previous attempts to develop functional composite materials for SLS, considering different carbon-based reinforcements. The potential of computational methods employed to describe, characterize and optimize the SLS process is also explored in this second chapter.

2.1. Selective Laser Sintering

According to the *Standard Terminology for Additive Manufacturing Technologies*, Selective Laser Sintering (SLS) is a powder bed fusion process used to produce polymeric parts in a layer-by-layer processing using powder material (Figure 2.1) (ASTM, 2012). This well-established AM technology operates in a closed chamber with controlled environment to avoid thermo-oxidative reactions and encompasses three main phases (Chatham *et al.*, 2019). In the beginning, after a preheating stage at a temperature between the glass transition and melting, the raw material is spread by a powder dosing device, typically a roller or a blade, over the building platform (Wörz *et al.*, 2018). During this period, heating lamps are continuously active to preheat the surface of the powder bed and to control the temperature of the entire construction (Chatham *et al.*, 2019). Then, the thermal energy of a laser beam locally sinters the regions of cross-section of the parts according to the corresponding Computer-Aided Design (CAD) model, while the surrounding powder that is not directly sintered remains loose as a natural support. The mechanism of consolidation is governed by the polymeric material and mostly occurs by liquid phase sintering or partial melting (Kruth *et al.*, 2007; Goodridge *et al.*, 2012). After a first and quick cooling stage to reach the isothermal temperature of the chamber, a new layer is precisely spread over the previous and the process is repeated until the whole production of the parts (Wörz *et al.*, 2018; Chatham *et al.*, 2019). In the end, the produced parts remain inside the laser-sintering machine for a long cooling period until it is possible to remove them and proceed with post-production operations.

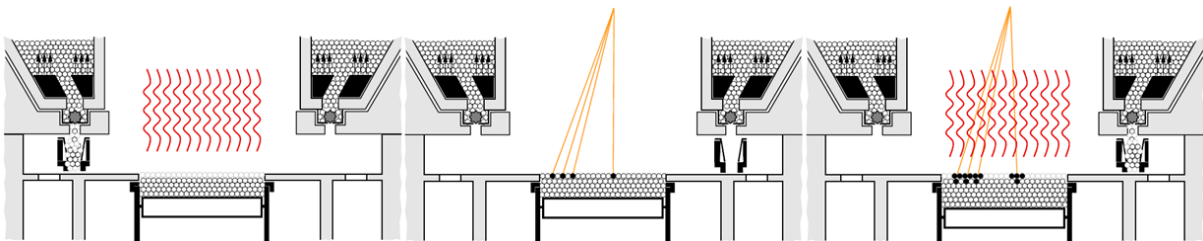


Figure 2.1 SLS process (Adapted from (Schneider, 2011)).

Due to the viscoelasticity of polymeric materials, the complex thermal conditions of processing and characteristic slow cooling rate that occurs after the SLS process are critical factors influencing the relationship between the microstructure of the parts and their macro-scale behaviour (Stichel *et al.*, 2018; Kiani *et al.*, 2020). Therefore, despite their promising capabilities and depending on the polymeric base material, SLS parts often depict warpage and curling effects, surface roughness, some level of porosity and brittleness characteristics, compared to similar parts produced by conventional processing technologies (Majewski *et al.*, 2008; Wörz *et al.*, 2018; Chatham *et al.*, 2019).

2.2. Process parameters of Selective Laser Sintering

Due to the operating principle of powder bed fusion processes, SLS presents a large number of process parameters that can be previously controlled. The most relevant parameters are related to the material itself and the corresponding powder state (*e.g.*, material properties, particles size and shape, mixture ratio, layer thickness), to the temperatures (*e.g.*, preheating temperature, process temperature), to the laser beam (*e.g.*, laser power, beam offset), to the scan (*e.g.*, scan speed, hatch distance, scan pattern) and to the part (*e.g.*, position, orientation) (Kumar, 2003; Gibson *et al.*, 2010; Bourell *et al.*, 2014).

In order to effectively monitor and control the SLS process and to enhance the overall performance of the parts produced, an adjusted and suitable definition of the set of parameters for each building job is essential; however, it is not an easy assignment due to the large number of variables and their mutual dependence and integration (Duan and Wang, 2011). Therefore, several research has been carried out in order to deeper comprehend the influence of the process parameters on the overall performance of SLS parts. To better reproduce the real scenario of the sintering process, most of the works have been considering the interdependent analysis of parameters defining the thermal energy supplied by the laser beam to the powder bed, instead of an individual approach (Beard *et al.*, 2011a; Duan and Wang, 2011; Pilipović *et al.*, 2014; Pavan *et al.*, 2017). Depending on the melting viscosity of the polymeric material and its ability for interparticle coalescence, the evaluation of the SLS process parameters through the energy density allows to assess the degree of particle melt, the effectiveness of powder consolidation and the microstructural and mechanical properties of the parts (Majewski *et al.*, 2008; Pavan *et al.*, 2017; Wörz *et al.*, 2018; Kiani *et al.*, 2020). The energy density supplied by the laser beam to the surface of the powder bed can be defined by unit of area, known as EDA (Beard *et al.*, 2011a; Pilipović *et al.*, 2014; Pavan *et al.*, 2017). EDA is function of the laser power (P_{Laser}), scan speed (S_{Scan}) and hatch distance (D_{Hatch}), respectively related to the intensity, duration and number of times that the laser acts on the surface of the layers of powder, defined by (Amado-Becker *et al.*, 2008; Pavan *et al.*, 2017):

$$ED_A = \frac{P_{Laser}}{S_{Scan} \times D_{Hatch}} \quad (2.1)$$

P_{Laser} displays a significant role in the SLS process. It is reported that with increased values of P_{Laser} , the particles present greater ability to establish strong bonds with each other, improving powder consolidation (Beard *et al.*, 2011b; Setti *et al.*, 2014). In consequence, the resulting parts present smoother surface finishing and improved mechanical performance in terms of strength and hardness (Beard *et al.*, 2011b, 2011a; Setti *et al.*, 2014; Singh *et al.*, 2017). However, when P_{Laser} is critically high, the powder bed becomes extremely compacted, promoting the shrinkage of the parts produced

Chapter 2. A review of Selective Laser Sintering: Parameters, materials and computational modelling

(Singh *et al.*, 2012). In contrast, when P_{Laser} is low, the thermal energy supplied by the laser beam is insufficient to ensure a complete and homogeneous sintering process, leading to weak interparticle bonding and, consequently, final parts with high content of porosity (Wu *et al.*, 2018).

Even with adjusted P_{Laser} values, a high S_{Scan} does not allow sufficient time for efficient interparticle coalescence (Velu and Singamneni, 2015). On the other hand, with low S_{Scan} the interparticle coalescence is enhanced and the surface finishing of the parts produced is smoother, but the building time is longer (Beard *et al.*, 2011a). However, if S_{Scan} reaches very low values and P_{Laser} is too high, the powder may begin to degrade and change its natural colour by the excessive energy supplied by the laser beam (Velu and Singamneni, 2015). These assumptions prove that with very low S_{Scan} values, the requirements of P_{Laser} to ensure a uniform and appropriate interparticle coalescence are reduced (Velu and Singamneni, 2015). Between P_{Laser} and S_{Scan} , Beard *et al.* (2011a) stated that S_{Scan} ensures greater control of the sintering process and repeatability of results.

In turn, D_{Hatch} (*i.e.*, the distance between two consecutive vectors of the laser beam) is considered one of the most relevant parameters influencing the density, hardness and shrinkage of SLS parts (Singh *et al.*, 2012, 2017; Wegner and Witt, 2012; Sharma *et al.*, 2015). If D_{Hatch} is lower than the laser beam diameter, the excessive thermal energy promotes the oversintering of the powder bed (Pilipović *et al.*, 2014). In that situation, the building time is longer and the resulting parts exhibit reduced mechanical properties and poor dimensional accuracy (Pilipović *et al.*, 2014). Otherwise, if D_{Hatch} is higher than the laser beam diameter, some material remains unsintered, leading to final parts with high content of porosity, low density and reduced mechanical performance (Pilipović *et al.*, 2014).

The individual effect of these fundamental SLS process parameters directly influences EDA. In this regard, previous research has proven that when P_{Laser} , S_{Scan} and D_{Hatch} are combined to obtain increased values of EDA, the bonds between the powder particles become stronger, the consolidation is enhanced and the resulting parts present less porosity, high density and improved mechanical performance (Caulfield *et al.*, 2007; Beard *et al.*, 2011a). However, when EDA is increased above a critical value, a substantial amount of surrounding particles is sintered to the surface of the parts by means of heat conduction (*i.e.*, a phenomenon known as 'secondary sintering') (Czelusniak and Amorim, 2020; Tong *et al.*, 2020). In that situation, the mechanical properties remain high, but the overall accuracy is compromised (Tong *et al.*, 2020). This demonstrates that low EDA values are advantageous for some properties (*e.g.*, dimensional accuracy), whereas medium-high values are desired for others (*e.g.*, mechanical properties) (Czelusniak and Amorim, 2020). However, when a limit value is reached, the macromolecular chains of the material are prone to break and degrade, leading to yellowness parts with

high content of porosity, low density and reduced mechanical strength (Ho *et al.*, 1999; Beard *et al.*, 2011a; Dewulf *et al.*, 2016; Ling *et al.*, 2018; Wu *et al.*, 2018).

The effects of EDA on the properties of SLS parts are dependent on the building orientation (Caulfield *et al.*, 2007; Beal *et al.*, 2009; Hofland *et al.*, 2017). Previous studies showed that the properties of parts horizontally and vertically produced reach a stable value at different levels of energy, depending on the area of the corresponding cross-section (Caulfield *et al.*, 2007; Hofland *et al.*, 2017; Pavan *et al.*, 2017). For same EDA values, parts horizontally produced tend to reveal greater performance due to the larger surface exposed to the laser in each layer that allows more time for the interparticle coalescence (Caulfield *et al.*, 2007; Hofland *et al.*, 2017; Pavan *et al.*, 2017). However, the overall performance of SLS parts becomes less dependent on the building orientation when EDA increases (Caulfield *et al.*, 2007; Hofland *et al.*, 2017). Regardless of the EDA value, research conducted by Hofland *et al.* (2017) proved that the contribution of each process parameter for the properties of the parts depends on the building orientation. For instance, in their experiments the elongation at break of parts horizontally produced was most affected by D_{Hatch} , while the elongation at break of parts vertically produced was most affected by S_{Scan} (Hofland *et al.*, 2017). In addition, Bacchewar *et al.* (2007) showed that the effect of the SLS process parameters is not the same for different surfaces of the parts in terms of roughness. They verified that P_{Laser} does not affect the finishing of surfaces directed to the top, but highly influences those directed to the bottom, leading to different surface roughness in upward and downward-facing surfaces (Bacchewar *et al.*, 2007).

Despite these considerations, most research in the field is conducted considering that same values of energy ensure equal final properties regardless of the combination of parameters (*e.g.*, Pilipović *et al.* (2010)). However, some authors have proven the opposite (Velu and Singamneni, 2015; Dewulf *et al.*, 2016). A study conducted by Velu *et al.* (2015) showed that the content of porosity can vary 6% and the elastic modulus 30% for same EDA values defined with different process parameters. In accordance, Dewulf *et al.* (2016) claimed that increased values of EDA lead to different degrees of porosity depending on the selected parameters and stated that the reduction of D_{Hatch} is a good solution to promote great results. To this extent, Pilipović *et al.* (2014) used mathematical modelling to prove the difficulty of selecting the greatest combination of P_{Laser} , S_{Scan} and D_{Hatch} to obtain the suitable EDA value.

Although a large number of investigations are focused on the simplest EDA solution, other approaches consider the input of energy density by unit of volume, known as EDv. EDv includes the layer thickness (t_{Layer}), a critical parameter influencing the building time and surface roughness of the parts, and it is given by (Shi and Gibson, 1997; Hofland *et al.*, 2017; Beitz *et al.*, 2019):

$$ED_V = \frac{P_{Laser}}{S_{Scan} \times D_{Hatch} \times t_{Layer}} \quad (2.2)$$

This method has been extensively used to evaluate the influence of the SLS process parameters on the properties of the parts produced (Starr *et al.*, 2011; Wegner and Witt, 2012; Wegner *et al.*, 2015; Hofland *et al.*, 2017; Czelusniak and Amorim, 2020). As the formulation directly depends on EDA, the effects of ED_V on the properties of the parts are comparable to those previously described. However, Lexow *et al.* (2017) argues that it may be an inaccurate approximation compared to EDA due to the unknown depth of penetration of the laser beam through the layers and its non-negligible interaction with the surrounding powder particles.

$$ED_V = \frac{ED_A}{t_{Layer}} \quad (2.3)$$

In addition to ED_V, some authors claim that the total energy density supplied during the SLS process, known as ED_T, capable to completely describe the process of powder consolidation must include the energy involved in the preheating stage, considering the specific heat capacity (c_p) and density (ρ) of the material, defined by (Hofland *et al.*, 2017):

$$ED_T = ED_V + c_p \times \rho \times T_{Preheating} \quad (2.4)$$

This solution includes the temperature of the preheating stage ($T_{Preheating}$), which is also identified as a crucial variable influencing the mechanisms of consolidation between the powder particles during the sintering (Gusarov *et al.*, 2003). In this regard, previous studies proved that the temperature is one of the most relevant parameters determining the surface roughness, hardness, mechanical strength and, with adjusted values of P_{Laser} and S_{Scan} , the dimensional and geometric accuracy of SLS parts (Wang *et al.*, 2007; Kumar *et al.*, 2016; Karthick Raja *et al.*, 2019; Mavoori *et al.*, 2019). The effects of this parameter are similar to those reported for the energy density, since high temperatures, within a range of 175 - 178 °C, are advantageous for the quality flowability of the polymeric material, reducing the content of porosity and improving the mechanical performance of SLS parts (Jain *et al.*, 2008; Ling *et al.*, 2018).

Regardless of the solution (*i.e.*, EDA, ED_V or ED_T), most of the previously mentioned research is focused on a single set of process parameters. However, the sintering process and the final properties of parts are differently affected by parameters that define their internal layers (*i.e.*, the hatching parameters) and external layers (*i.e.*, the contour parameters) (Pilipović *et al.*, 2014). In this regard, Pilipović *et al.* (2014) proved that parts are more affected by the hatching parameters due to the larger volume involved. Because of that, the requirements of the contour parameters are often smaller (*e.g.*, a difference of 5 W in P_{Laser}) (Pilipović *et al.*, 2014). Kummert *et al.* (2018) also studied these two classes of parameters,

changing the contour settings for a fixed combination of hatching parameters. As result, they verified similar relationships between the contour parameters and the final properties of the parts, as reported for the hatching (Kummert and Schmid, 2018).

Due to the multiplicity of factors that affect the energy density and its dependence on the polymeric material, the establishment of the optimum value for each SLS building job is not trivial. Because of that, the evaluation of fundamental SLS process parameters using the concept of energy density is commonly accomplished through empirical research for specific laser-sintering machines and materials (Goodridge *et al.*, 2012). However, not all authors who focus the research on this specific subject identify the most suitable values of energy to achieve optimal overall outputs. Table 2.1 summarizes some recommended EDA and ED_v values for neat polyamide powders processed by SLS.

Table 2.1 EDA and ED_v values for pure polyamide materials processed by SLS.

SLS MACHINE	POLYMERIC MATERIAL COMMERCIAL NAME	EDA (J/mm ²)	ED _v (J/mm ³)	REFERENCE
Sinterstation 2500 Plus	PA12 DuraForm PA12	> 0.012	n/a	(Caulfield <i>et al.</i> , 2007)
EOS P 380	PA12 EOS PA 2200	> 0.010 < 0.048	n/a	(Bacchewar <i>et al.</i> , 2007)
EOS P 380	PA12 EOS PA 2200	0.027	n/a	(Jain <i>et al.</i> , 2009)
n/a	PA12 DuraForm PA12	0.020 - 0.080	n/a	(Franco <i>et al.</i> , 2010)
Formiga P 100	PA12 EOS PA 2200	0.050	n/a	(Pilipović <i>et al.</i> , 2010)
Sinterstation 2500 Plus	PA12 DuraForm PA12	n/a	> 0.091	(Starr <i>et al.</i> , 2011)
Sinterstation 2500 HS	PA12 EOS PA 2200	n/a	0.350 - 0.400	(Wegner and Witt, 2012)
n/a	PA12 DuraForm PA12	0.020 – 0.100	n/a	(Franco and Romoli, 2012)
Sinterstation 2500 Plus	PA12 DuraForm PA12	0.025	n/a	(Castoro, 2013)
Sinterstation 2500 HS	PA11 EOS PA 1101	n/a	0.400 – 0.580	(Wegner <i>et al.</i> , 2015)
EOS P 395	PA12 EOS PA 2200	n/a	0.370 (0° parts) 0.460 (90° parts)	(Hofland <i>et al.</i> , 2017)
Formiga P 100	PA12 EOS PA 2200	0.057	n/a	(Pilipović <i>et al.</i> , 2018)

The most common purpose of the research conducted to understand the complex process-structure-property relationship is to improve the global performance of SLS parts. However, some of them are carried out as an attempt to minimize some defects intrinsically related with the SLS process reducing the quality of the parts, such as the warpage and curling. Examples of these experiments were performed

Chapter 2. A review of Selective Laser Sintering: Parameters, materials and computational modelling

by Wang *et al.* (2010), Soe (2012), Mousa (2016), Dastjerdi *et al.* (2017) and Yeganeh *et al.* (2019). Furthermore, this type of investigation is also considered to allow the implementation of new composite materials in SLS, identifying the optimal set of process parameters for efficient processing. Some of these works were conducted by Song *et al.* (2017), Wang *et al.* (2017), Aldahash (2018) and Kummert *et al.* (2018).

In addition to the parameters that directly define conditions of sintering, the orientation and position of SLS parts on the building platform also have a significant influence on the resulting properties. The orientation, defined by the alignment of the part along its longest dimension in relation to the plane of construction, affects the building height and, consequently, the time and costs of production (Caulfield *et al.*, 2007; Delfs *et al.*, 2016). As it is related to the stair-stepping effect of the layer-by-layer processes, it also influences the surface quality and accuracy of the details of the parts (Delfs *et al.*, 2016). Regarding the orientation, it is proven that the vertical alignment is the weakest for failure due to the reduced interlayer bonding (Shaw and Dirven, 2016). The position of the parts also exhibits a direct relationship with the building time and costs, depending on the height of the plane of construction considered. Shrinkage characteristics are also influenced by the position of the parts, due to the thermal gradients experienced in different locations of the building chamber (Soe *et al.*, 2013).

Despite the large number of studies in the field and the increasing scientific progress that has been reported, it is still challenging to establish and control the real effect of the processing parameters on the final properties of SLS parts (Beitz *et al.*, 2019; Marrey *et al.*, 2019; Yuan *et al.*, 2020).

2.3. Materials for Selective Laser Sintering

As discussed in *Chapter 1*, composite materials that combine two or more materials to obtain final properties not presented in the individual constituents are particularly interesting for SLS due to their valuable potential to overcome some limitations of this sintering process and to extend the applicability of SLS parts to novel fields (X. Wang *et al.*, 2017; Yuan *et al.*, 2019; Wu *et al.*, 2020). However, the operating principle of SLS does not allow the implementation of all materials, since they must have to exhibit some specific characteristics to be quality processed (Kruth *et al.*, 2008; Goodridge *et al.*, 2012). Therefore, in order to efficiently develop new functional materials for SLS and to be able to properly adjust the corresponding process parameters, it is essential to completely understand the requirements for a quality processability, as well as the sintering behaviour and most important properties of the well-established materials, such as polyamide-based thermoplastics (Goodridge *et al.*, 2012). This section presents the most significant fundamentals of these research topics.

2.3.1. Material requirements for quality processability

In order to ensure a successful processability by SLS, the polymeric material must have to fulfil a series of requirements regarding its properties and typology of the resulting powder particles. First of all, the polymeric material must be available in powder form with an appropriate particle size to efficiently absorb the energy density provided by the laser beam, to be easily spread on the building platform and to present a suitable thermal diffusivity and rheological properties (Goodridge *et al.*, 2012; Vasquez *et al.*, 2014; Chatham *et al.*, 2019). In this regard, powder particles with spherical shape and diameter between 45 μm and 90 μm are recommended to ensure smooth flowability and efficient packaging (Bourell *et al.*, 2014; Verbelen *et al.*, 2016). A distribution of particle size can also be advantageous to attain a good compromise between the content of porosity and density of the parts produced (Goodridge *et al.*, 2012).

With respect to the base structure, thermoplastics are predominantly used in SLS due to their advantageous capability to be processed and reprocessed in consecutive cycles of heating and cooling (Yuan *et al.*, 2019). Compared with amorphous, it is reported that semi-crystalline materials can be sintered with superior performance in terms of density and mechanical strength (Zarringhalam *et al.*, 2006; C. Yan *et al.*, 2011). In preference, the semi-crystalline material should present a large range between the melting and crystallization temperatures defining the SLS processing window, and high melting enthalpy to prevent the heat conduction to the surrounding particles; however, the melting temperature should not be excessively high to secure minimum thermal requirements of the sintering process (Dupin *et al.*, 2012; Goodridge *et al.*, 2012; Dadbakhsh *et al.*, 2017).

In addition, due to the high temperatures of processing and because of this AM technology is based on laser-sintering, the material should present good heat resistance to avoid material degradation in areas where no sintering is programmed (Drummer *et al.*, 2010). The material also should present a suitable capability to absorb the thermal energy at the wavelength of the corresponding laser beam (Schmid *et al.*, 2014). Finally, to ensure homogeneous deposition of the powder on the building platform and quality interparticle coalescence, the material must have to present low melting viscosity and low surface tension to enable the compaction of the material during the sintering process, as there is no additional compacting source in SLS (Schmid *et al.*, 2014).

2.3.2. Conventional polymeric materials

Nowadays, the flexibility of SLS allows the inclusion of a variety of materials when the requirements for a quality processability are guaranteed. However, Polyamide 12 (PA12) has still a predominant position in the market of conventional polymeric materials due to its well-established sintering behaviour, good thermal and mechanical properties, easy processability and reduced costs (Goodridge *et al.*, 2012;

Yuan *et al.*, 2019). Because of that, an in-depth understanding of the chemical structure of PA12 and its micro and macro-scale properties becomes particularly relevant for the development of new materials for SLS.

According to the polymers science, PA12 is a semi-crystalline thermoplastic material with a chemical structure composed by an amorphous region defining toughness characteristics and a crystalline region responsible for mechanical properties such as stiffness and brittleness (Figure 2.2) (Pham *et al.*, 2008).

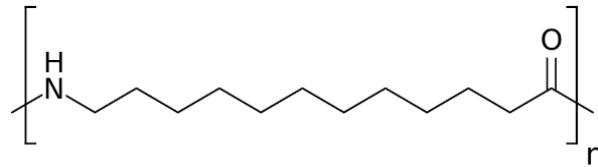


Figure 2.2 Chemical structure of PA12 (Wikipedia, 2019).

Most polyamide-based materials commercially available for conventional processing technologies are synthesized by anionic ring-opening polymerization of cyclic amides, called lactams (Wakeman and Manson, 2005). Depending on the activator, initiator and temperature, this process is capable to ensure suitable kinetics of polymerization in order to obtain materials with desired molecular weight (O'dian, 2004; Wakeman and Manson, 2005). In addition to the conventional methods, the production of polyamide-based materials for powder bed fusion processes demands complementary procedures. To obtain the powder particles, some researchers suggest an additional process of solution-precipitation in ethanol at high temperatures and pressures facilitating the crystal modification, with a subsequent inclusion of nucleating agents (*e.g.*, silica) to improve the whiteness and flowability of the base material (Dadbakhsh *et al.*, 2017; Chen *et al.*, 2018). This process allows the creation of powder particles with controlled size, spherical shape and low porosity in a wide range of molecular weights for most commercial laser-sintering machines (Becker, 2016). Complementary treatments to ensure a large processing window for SLS are also often considered (Schmid *et al.*, 2014). As a result of these methods of production and preparation, typical PA12 material presents excellent intrinsic properties (*i.e.*, temperature of glass transition: 50 °C, melting temperature: 180 °C, crystallization temperature: 150 °C), combining the greatest characteristics of polyamides and polyolefins, including high density, chemical resistance, good strength, high toughness, fatigue resistance, low moisture absorption compared to other polyamide groups and easy capability to be modified with reinforcements and/or additives (Mark, 1999; Dencheva *et al.*, 2008; Kallio and Hedenqvist, 2008; Salazar *et al.*, 2014; O'Connor *et al.*, 2018; Chatham *et al.*, 2019).

2.3.3. Composite materials

Although PA12 is a common choice for most SLS applications due to its efficient ability to satisfy the standard requirements, this conventional material is sensible to thermal environments during consecutive building cycles, which empowers the development of residual stresses and microstructural modifications, influencing the properties of the parts produced (Yuan *et al.*, 2019). In addition to the undesirable characteristics of polyamide-based thermoplastics, the market of SLS materials is continually demanding novel solutions with mechanical, thermal and electrical improvements to be applied in advanced purposes (Picard *et al.*, 2020). Therefore, innovative composite materials suitable for powder bed fusion processes are already being explored in order to improve capabilities, enable new functionalities and ensure the repeatability of the process and the properties of the parts produced (Yuan *et al.*, 2019). Compared to conventional manufacturing technologies, SLS is particularly advantageous to include these solutions because it does not involve compacting sources or shear forces, which allows the preservation of the aspect ratio of the reinforcement embedded in the matrix through a conductive network at lower percolation thresholds (Eshraghi *et al.*, 2013). Thus, the reinforcement of SLS polymeric matrices with micro and/or nanosized particles is extensively reported in literature, including metallic (*e.g.*, aluminium (*e.g.*, (Yan *et al.*, 2009)), copper (*e.g.*, (Balzereit *et al.*, 2018))), ceramic (*e.g.*, silica (*e.g.*, (Chunze *et al.*, 2009)), clays (*e.g.*, (Tiwari *et al.*, 2018))), glass (*e.g.*, glass fibres or glass bends (*e.g.*, (Mousa, 2014))), carbon (*e.g.*, carbon fibres (*e.g.*, (Liu *et al.*, 2019)), carbon nanotubes (*e.g.*, (Yuan *et al.*, 2018)), graphite (*e.g.*, (Lahtinen *et al.*, 2019)), graphene (*e.g.*, (Makuch *et al.*, 2015))) and organic (*e.g.*, PA6 (*e.g.*, (Salmoria *et al.*, 2009)), wood (*e.g.*, (Yu *et al.*, 2018)), sand (*e.g.*, (Xu *et al.*, 2014))) reinforcements with a variety of valuable and sustainable properties for promising applications within automotive, packaging, defence or aerospace industries (Goodridge *et al.*, 2012; Yuan *et al.*, 2019).

Although some of these solutions are already available in the market of AM materials, the real implementation of tailored composites is still difficult due to the complex consolidation behaviour and numerous combinations of properties required for successful sintering, including intrinsic and extrinsic properties, respectively determined by the structure of the polymeric material and method used to produce the powders (Schmid and Wegener, 2016; Türk *et al.*, 2017). Therefore, some limitations regarding the efficient processing of these functional materials are frequently reported. Of all of them, the most common are the lack of a homogeneous distribution and dispersion of the reinforcement, its difficult orientation and alignment within the matrix, the development of a weak interparticle adhesion, the complexity of processing, the increased content of porosity, agglomeration and migration problems, lower

resolution and higher processing time and costs (Parandoush and Lin, 2017; Asadi and Kalaitzidou, 2018).

In fact, the establishment of a quality interaction between the reinforcement and the polymeric matrix with uniform dispersion, homogenous distribution and reduced structural defects is crucial for the successful development of composite materials (Goodridge *et al.*, 2012; Asadi and Kalaitzidou, 2018). When these desirable conditions are not fully reached and the previously mentioned problems are verified, the maximum efficiency of the reinforcement is compromised due to the heterogeneous transference of stress to the matrix, resulting in a weak interparticle adhesion and, therefore, in a worse and anisotropic performance of the composite (Asadi and Kalaitzidou, 2018).

The most important topics related to the production, processing and properties of composite materials to ensure successful applicability in SLS are discussed in the following sections.

2.3.3.1. Preparation of composite materials

The final properties of composite materials not only depend on the intrinsic characteristics of all constituents but also on the method and corresponding experimental conditions used in its formulation and preparation, which highly influence its resulting morphological structure and relevant characteristics of flowability and surface energy (Goodridge *et al.*, 2012; Asadi and Kalaitzidou, 2018; Chatham *et al.*, 2019). There is a variety of methods to prepare powders for SLS considering chemical and/or mechanical approaches. Based on different principles of operation, the most reported are spray drying, precipitation of solutions, milling-based methods at cryogenic temperatures, melt-compounding combined with milling procedures and mechanical mixing (Chatham *et al.*, 2019; Yuan *et al.*, 2019). The general principle of these processes is well described by Yuan *et al.* (2019) in *Polymeric composites for powder-based additive manufacturing: Materials and applications*. Spray drying consists in apply pressure to spray polymeric droplets at low temperatures to obtain the particles (Yuan *et al.*, 2019). Despite its advantages, the final powders obtained by spray drying are often irregular, porous and exhibit inferior performance (Yuan *et al.*, 2019). On the other hand, processes of precipitation of solutions are based on the dispersion of reinforcements in soluble solutions of polymers at high temperatures, using surfactants and coupling agents (Yuan *et al.*, 2019). Although this class of processes is recommended to obtain composite materials with good characteristics of flowability, they cannot be applied to all types of materials because of the undesirable interactions that can be established with the solvents (Chatham *et al.*, 2019; Yuan *et al.*, 2019). The milling-based methods use metallic balls for the fragmentation of matrices and reinforcements at cryogenic temperatures to be further mixed to obtain the composite (Yuan *et al.*, 2019). Typically, a good dispersion is easily achieved, but the flowability can be comprised due to the difficult

control of the size, shape and morphology of the particles (Yuan *et al.*, 2019). The melt-compounding combined with milling procedures uses a twin-screw extruder to disperse the reinforcement in a melted polymer and requires an additional process to obtain the powder particles (Yuan *et al.*, 2019). It is advantageous due to the solvent-free condition, but it can be difficult to conduct in polymeric materials with high melting viscosity (Yuan *et al.*, 2019). Finally, mechanical mixing is the most reported method in literature to prepare reinforced polymers for SLS (Goodridge *et al.*, 2012; Yuan *et al.*, 2019). In fact, it ensures a simple and quick preparation with economic advantages, however, when powder materials with distinct particle sizes (*e.g.*, micro and nanosized) and/or densities (*e.g.*, polymeric and metallic particles) are considered, an efficient and uniform mixture is challenging to obtain (Goodridge *et al.*, 2012). As a consequence, the coagulation phenomenon and migration of the reinforcement to the outer edges of the parts during the process are frequently observed (Koo *et al.*, 2017). Because of that, some authors claim that the preparation of a single composite powder using advanced methods is advantageous to ensure uniform final parts, compared to the combination of both using mechanical mixing (Kumar and Kruth, 2010). Regardless of the method of preparation, it is essential to ensure the development of powder particles with desired size, shape and morphology, otherwise the resulting mechanical properties of the composite are lower than those of the polymeric matrix (Goodridge *et al.*, 2012). These assumptions prove that the method of preparation determines important characteristics of the final composite and, consequently, its performance during the SLS process (Yuan *et al.*, 2019).

In addition to the method of powder preparation, it is also often recommended a pre-treatment or pre-modification of the reinforcement to ensure a stronger interaction between the particles. These treatments depend on the selected reinforcement and mostly require the inclusion of functional groups and/or a program of temperature (Francis and Jain, 2015; Jing *et al.*, 2017; Parandoush and Lin, 2017). After production, some post-treatments are also frequently considered to promote an improved consolidation between the reinforcement and the polymeric matrix, despite the increase in costs and time of production (X. Wang *et al.*, 2017). Regardless of the preparation method, the definition of the critical weight or volume percentage of reinforcement (respectively denoted by wt% and vol%) to obtain a composite with enhanced properties is also important. The ideal mixture ratio that allows the establishment of the percolation threshold depends on the properties of the polymeric base material, the interaction established between the reinforcement and matrix, the preparation methods, the sintering parameters and the characteristics desired for the final composite (Eshraghi *et al.*, 2013; Asadi and Kalaitzidou, 2018).

2.3.3.2. Processing of composite materials

After the preparation of the composite material through single or multiple-step methods, the sintering process can be conducted. In that stage, the suitable definition of the process parameters depending on the composite material is decisive to ensure its quality processability. Several researches have proven that the input of thermal energy supplied by the laser beam has a significant influence on the interparticle adhesion, packaging characteristics and physical integrity of the parts produced (Greiner *et al.*, 2017; Koo *et al.*, 2017). However, the processing conditions and the interaction of the laser beam with the powder particles are determined by a number of variables focused on specific combinations of materials and methods. Some opportunities and challenges related to the sintering process of SLS composite materials are discussed in the next section for different typologies of reinforcement.

2.3.3.3. Typology and properties of reinforcements

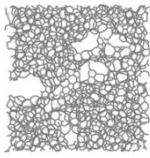
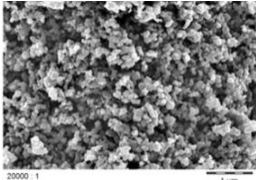
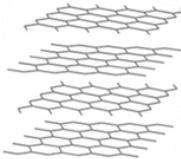
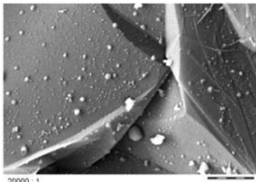

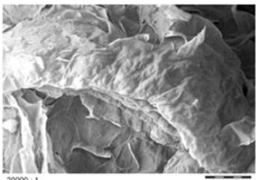
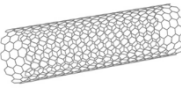
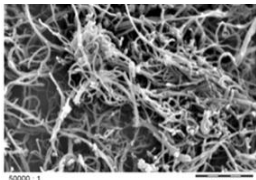
In addition to the chemical nature of the reinforcement embedded into the polymeric matrix, the sintering process also depends on its typology (*e.g.*, short or long fibres, micro or nanoparticles, etc). In this regard, it is reported that the use of short fibres instead of long fibres simplifies the SLS process, ensuring greater powder flowability, easier processability and more attractive costs (Kumar and Kruth, 2010; Zhu *et al.*, 2016). Nanoparticles with at least one nanosized dimension have also attracted great interest for SLS due to their considerable effect on the properties of polymer materials by using small amounts of incorporation (Goodridge *et al.*, 2012; Wu *et al.*, 2020). Compared to conventional short or long fibres, the inclusion of nanoparticles ensures greater isotropic response and requires fewer modifications in the standard operating principle of SLS; however, these class of particles often inhibit the movement of the macromolecules of the polymeric material decreasing the SLS processability (Kumar and Kruth, 2010; Asadi and Kalaitzidou, 2018; Wu *et al.*, 2020).

Fundamentals of carbon-based composites

Since polymers are insulating materials, carbon-based composites are one of the most explored to be used in SLS applications (Francis and Jain, 2015; Salmoria *et al.*, 2017; Wu *et al.*, 2020). In fact, conductive polymeric materials are being considered modern alternative solutions to conventional metals in diverse fields from automotive to medical, mainly as lightweight and corrosion resistant shielding structures to protect electronic equipment (Nazir *et al.*, 2019). Focusing on their potential for such variety of applications, various solutions using Carbon Nanotubes (in particular, Multi-Walled Carbon Nanotubes (MWCNT)), Carbon Fibres (CF), Carbon Black (CB), Graphite Nanoplatelets and Graphene have been extensively reported in literature due to their natural ability to establish strong interactions with the polymeric matrix and to ensure a homogenous dispersion, resulting in final composites with outstanding

mechanical, thermal and electrical properties (Francis and Jain, 2015). All mentioned carbon allotropes are similar in terms of chemical composition but exhibit some modifications in relation to their structural rearrangement and size depending on the type of hybridization (Ma-Hock *et al.*, 2013; Kharisov and Kharissova, 2019). These modifications determine the resulting microstructure that is responsible to induce slight differences in properties that are function of the type and structure of the constituents, including the mechanical and electrical (Ma-Hock *et al.*, 2013; Asadi and Kalaitzidou, 2018; Kharisov and Kharissova, 2019; Razeghi, 2019). Table 2.2 describes the main characteristics of the carbon allotropes mostly used in composite structures.

Table 2.2 Characteristics of carbon black, graphite, graphene and MWCNT allotropes.

	ATOMIC STRUCTURE (Adapted from (Razeghi, 2019))	MICROSTRUCTURE (Adapted from (Ma-Hock <i>et al.</i> , 2013))	GENERAL DESCRIPTION
Carbon black			CB is a specific amorphous carbon form comprising elemental carbon-based spherical particles that aggregate to a final size between 30 nm and 100 nm (Ferreira, 2013; Ma-Hock <i>et al.</i> , 2013; Asadi and Kalaitzidou, 2018).
Graphite			Graphite is the most stable allotrope composed by carbon atoms arranged in an hexagonal lattice disposed in ordered layers with 0.335 nm of spacing (Ferreira, 2013; Ma-Hock <i>et al.</i> , 2013; Asadi and Kalaitzidou, 2018; Kharisov and Kharissova, 2019).
Graphene			Graphene is a two-dimensional monolayer of carbon atoms disposed in a similar hexagonal network, <i>i.e.</i> , a single sheet of graphite obtained through exfoliation (Ferreira, 2013; Ma-Hock <i>et al.</i> , 2013; Asadi and Kalaitzidou, 2018; Kharisov and Kharissova, 2019).
MWCNT			MWCNT belong to a subclass of carbon nanotubes consisting in more than two concentric cylinders of graphene sheets with final diameters ranging from 1.4 nm to 100 nm (Ferreira, 2013; Ma-Hock <i>et al.</i> , 2013; Asadi and Kalaitzidou, 2018). A chemical functionalization is recommended to improve the dispersion and interfacial interactions of MWCNT in polymeric matrices (Ferreira, 2013).

The development of composite materials for SLS including carbon-based reinforcements has expanded in the last few years. Several research articles have already been published considering the inclusion of

this variety of reinforcements in different matrices processed by SLS, such as polyamide 11 (*e.g.*, (Gaikwad *et al.*, 2013; Bai *et al.*, 2017)), polystyrene (*e.g.*, (Lahtinen *et al.*, 2019)), polyurethane (*e.g.*, (Yuan, Chua, *et al.*, 2016; Lahtinen *et al.*, 2019)), polycarbonate (*e.g.*, (Ho *et al.*, 2002)), polylactic acid (*e.g.*, (Wang *et al.*, 2019; Jiang *et al.*, 2020)), polyvinylidene fluoride (*e.g.*, (Shuai *et al.*, 2020)), polyether ether ketone (*e.g.*, (Yan *et al.*, 2018)), polyimide (*e.g.*, (Chuang *et al.*, 2019)), bioactive glass (*e.g.*, (Liu *et al.*, 2015)), diopside (*e.g.*, (Shuai *et al.*, 2016)), wood (*e.g.*, (Zhang *et al.*, 2017)), paraffin wax (*e.g.*, (Nofal *et al.*, 2019)), etc. Focusing on the scope of this research, Table 2.3 summarizes a series of experiments conducted to develop carbon-based composites based on the most widely studied PA12 matrix. A brief description of the functional properties influenced by the type of reinforcement, pre- and post-treatments and preparation methods that were reached in each experiment is provided.

Table 2.3 Experiments to develop carbon-based composites for SLS based on a PA12 matrix.

CARBON-BASED COMPOSITE	PRE AND POST TREATMENTS	PREPARATION METHOD	FUNCTIONAL PROPERTIES OBTAINED	REFERENCE
PA12 & MWCNT 0.5 wt%	n/a	Mechanical mixing for 1:10 hours.	Composite parts with flexural tensile strength 10% higher and flexural elongation 11-9% lower than neat-PA12 parts.	(Salmoria <i>et al.</i> , 2011)
PA12 & MWCNT 0.1 wt%	n/a	Specific coating method.	Composite parts with elastic modulus and density respectively 54% and 4.1% higher than neat-PA12 parts.	(Bai <i>et al.</i> , 2013)
PA12 & MWCNT 0.5, 1.0, 3.0 wt%	n/a	Magnetic stirring of solutions and mechanical mixing.	1.7 wt% of MWCNT combined with medium P_{Laser} and high S_{Speed} values is suitable to produce quality composite parts by SLS (ANOVA analysis).	(Paggi <i>et al.</i> , 2013)
PA12 & MWCNT 0.1, 0.2 wt%	n/a	Specific coating method.	Composite parts with melting viscosity between 300 and 900 Pa.s (depending on the temperature) and dynamic elastic modulus 20% higher for 0.2 wt% ($T < T_g$).	(Bai <i>et al.</i> , 2014)
PA12 & MWCNT 0.1 wt%	n/a	Specific coating method.	Composite parts with thermal conductivity 14.2% higher than neat-PA12 parts, until 0.13 $WK^{-1}m^{-1}$ (depending on the temperature).	(Bai <i>et al.</i> , 2015)
PA12 & MWCNT 0.5 wt%	Pre-modification of MWCNT with sodium cholate.	Precipitation of solutions.	Composite parts with tensile strength, elastic modulus and toughness respectively 31.8%, 0.8% and 84.9% higher than neat-PA12 parts.	(Yuan, Bai, <i>et al.</i> , 2016)
PA12 & MWCNT 0.5, 1.0, 3.0 wt%	n/a	Mechanical mixing for 1:10 hours.	Composite parts with 1.0 wt% of MWCNT with flexural strength 25.8% higher than neat-PA12 parts. Electrical percolation threshold for 3.0 wt% (reduced mechanical properties).	(Salmoria <i>et al.</i> , 2017)
PA12 & MWCNT 0.1, 0.5, 1.0 wt%	Pre-modification of MWCNT with sodium cholate.	Precipitation of solutions.	Composite parts with 0.5 wt% of MWCNT with electrical conductivity of 10^5 S/cm and thermal conductivity of 0.40 $WK^{-1}m^{-1}$.	(Yuan <i>et al.</i> , 2018)
PA12 & CF	Pre-purification and modification of	Melt-compounding	Composite parts with storage modulus 22% higher than neat-PA12 parts.	(Goodridge <i>et al.</i> , 2011)

Chapter 2. A review of Selective Laser Sintering: Parameters, materials and computational modelling

3.0 wt%	CF with methylene chloride.	and cryogenic milling.		
PA12 & CF 30.0, 40.0, 50.0 wt%	Pre-modification of CF with nitric acid.	Precipitation of solutions.	Composite parts with 30.0 wt% of CF with flexural strength and flexural modulus respectively 44.5% and 93.4% higher than neat-PA12 parts. Best mechanical results for 50.0 wt%.	(Chunze Yan <i>et al.</i> , 2011)
PA12 & CF 30.0 wt%	Pre-modification of CF with nitric acid and heating at 400°C for 2 hours.	Mechanical mixing for 1 hour.	Composite parts with tensile strength and elastic modulus respectively 77% and 346% higher than neat-PA12 parts.	(Jing <i>et al.</i> , 2017)
PA12 & CF n/a wt%	n/a	n/a	Composite parts at 0° and 90° with tensile strength respectively 298% and 117% higher and elastic modulus 110% and 50% higher than the corresponding neat-PA12 parts. 85.5% lower content of porosity.	(Flodberg <i>et al.</i> , 2018)
PA12 & CF 40.0 wt% Commercial composite	n/a	n/a	Composite parts with flexural strength and flexural modulus respectively 100% and 380% higher than neat-PA12 parts. Thermal conductivity 104% higher, until 0.19 WK ⁻¹ m ⁻¹ .	(Tian <i>et al.</i> , 2018)
PA12 & CF 35.0 vol%	n/a	n/a	Composite parts with tensile strength 53% higher and elongation 92% lower than neat-PA12 parts.	(Liu <i>et al.</i> , 2019)
PA12 & Chopped CF Commercial composite	n/a	n/a	Depending on the movement of the recoater, the orientation of CF is different according to the building orientation, which affects the resulting properties.	(Badini <i>et al.</i> , 2020)
PA12 & CB 4.0 wt%	n/a	Mechanical mixing for 24 hours.	Composite parts with electrical conductivity of 10 ⁻¹ S/cm. Electrical percolation threshold below 4.0 wt%.	(Athreya <i>et al.</i> , 2010)
PA12 & CB 4.0 wt%	n/a	Mechanical mixing for 24 hours.	Composite parts with electrical conductivity of 10 ⁻¹ S/cm and HDT 30-40% lower than neat-PA12 parts. Storage modulus between 10 ³ and 10 ⁶ Pa.	(Athreya <i>et al.</i> , 2012)
PA12 & CB 1.5, 3.0, 5.0, 10.0 wt%	n/a	Mechanical mixing for 5 hours.	Composite parts with 1.5 wt% of CB with tensile strength 260% higher than neat-PA12 parts. Electrical percolation threshold between 1.5-3.0 wt%.	(Espera <i>et al.</i> , 2019)
PA12 & CB 0.5, 1.0, 2.0, 4.0, 8.0 wt%	n/a	Specific suspension-based method.	Electrical percolation threshold for 0.87 wt%, achieving a maximum of 0.1 S/m for 8.0 wt%. Elastic modulus increases with wt%.	(Hong <i>et al.</i> , 2019)
PA12 & CB 0.5, 1.0, 2.0 wt%	n/a	Mechanical mixing for 2 hours.	From 0.5 wt% to 2.0 wt% the surface coverage increases from 20% to 95%. Diffuse reflectance decreases from 20.5% in PA12 to 7% with 2.0 wt% of CB. Highest mechanical properties for 0.5 wt% of CB. Electrical conductivity of 10 ⁻³ S/cm for 2.0 wt% of CB.	(Xi <i>et al.</i> , 2020)

Chapter 2. A review of Selective Laser Sintering: Parameters, materials and computational modelling

PA12 & Graphite nanoplatelets 3.0, 5.0 wt%	n/a	Precipitation of solutions.	Composite parts with 5.0 wt% of graphite nanoplatelets with electrical conductivity of 10^8 S/cm. Highest elastic modulus and density for 3.0 wt% of graphite nanoplatelets. Required higher P_{Laser} for the sintering.	(Eshraghi <i>et al.</i> , 2013)
PA12 & Graphite nanoplatelets 3.0, 5.0 wt%	n/a	Specific coating method.	Composite parts with 3.0 wt% of graphite nanoplatelets with highest tensile modulus (> 2.2 GPa). Composite parts with 5.0 wt% of graphite nanoplatelets with highest electrical conductivity (10^7 S/cm).	(Karevan <i>et al.</i> , 2013)
PA12 & Graphite nanoplatelets 0.1, 0.25 wt%	Pre-modification of graphite nanoplatelets with nitric acid.	Solution intercalation in autoclave.	Composite parts with 0.25 wt% of graphite nanoplatelets with ultimate strength and elastic modulus respectively 11.3% and 30% higher than neat-PA12 parts.	(Kim <i>et al.</i> , 2013)
PA12 & Graphite 5.0-40.0 wt%	n/a	Mechanical mixing.	Electrical percolation threshold between 10.0-15.0 wt% with a maximum value of 0.9 S/m for 40.0 wt%.	(Lahtinen <i>et al.</i> , 2019)
PA12 & Graphene flakes 1.0 wt%	n/a	Mechanical mixing for 1, 2, 4 and 8 hours.	The mixing time influences the dispersion of the reinforcement and its interfacial adhesion with the matrix. The longest mixing time (8 hours) was advantageous for the sintering.	(Makuch <i>et al.</i> , 2015)
PA12 & Graphene oxide 0.12, 0.18, 0.36, 0.72 vol%	Pre-exfoliation of graphene oxide nanosheets.	Precipitation of solutions.	Composite parts with 0.36 vol% with elastic modulus 48% higher than neat-PA12 parts (similar tensile strength). Electrical percolation threshold for 0.05 vol% (MATLAB analysis).	(De Leon <i>et al.</i> , 2018)

Table 2.3 evidences a number of different scientific publications that, in general, have successfully developed carbon-based composites with enhanced mechanical, thermal and/or electrical properties, compared to the pure polymeric matrix. Most of the positive results of the experiments were justified by the great interaction established between the laser beam and the carbon-based reinforcements that showed to be responsible to intensity the heat conduction of the energy through the layers of powder (Tian *et al.*, 2018). This phenomenon was observed in composites produced with MWCNT by Salmoria *et al.* (2011), Bai *et al.* (2014), Bai *et al.* (2013) and Bai *et al.* (2015), in composites produced with CB by Athreya *et al.* (2010) and Xi *et al.* (2020) and in composites produced with CF by Flodberg *et al.* (2018) and Tian *et al.* (2018). In fact, it was proved that the inclusion of MWCNT has a critical effect on the rheological and viscoelastic properties of the final material, influencing the melting viscosity, flowability, sintering window and efficiency to absorb the energy of the laser beam (Salmoria *et al.*, 2011; Bai *et al.*, 2014; Yuan, Bai, *et al.*, 2016). As a result, the conduction of the thermal energy into the powder bed during the sintering process becomes “wider and deeper”, allowing to reduce the porosity and increase the density of the parts produced (Figure 2.3 and Figure 2.4) (Salmoria *et al.*, 2011; Bai *et al.*, 2013, 2015).

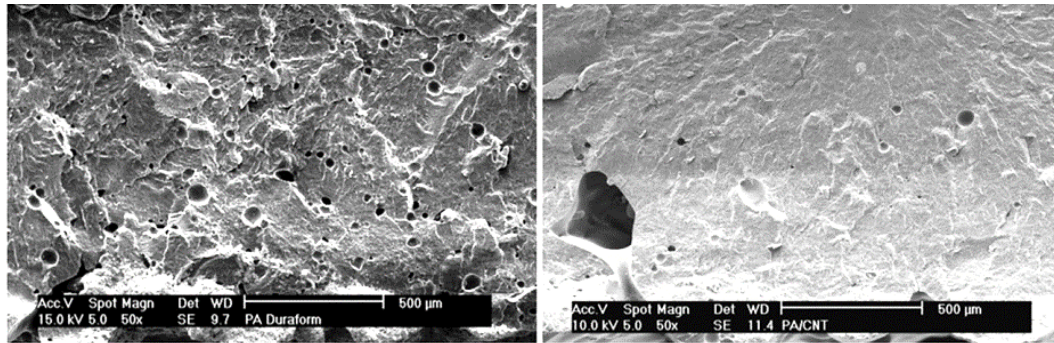


Figure 2.3 Cross-section of PA12 (left) and PA12-MWCNT (right) parts produced by SLS (Adapted from (Salmoria *et al.*, 2011)).

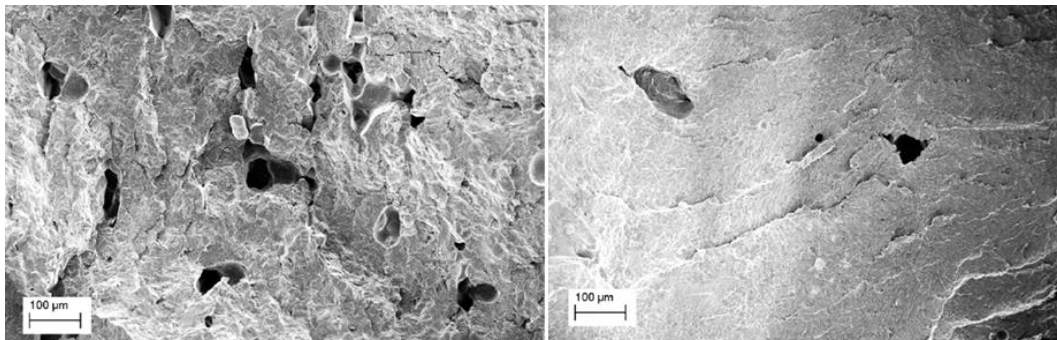


Figure 2.4 Cross-section of PA12 (left) and PA12-MWCNT (right) parts produced by SLS (Adapted from (Bai *et al.*, 2015)).

Similar results were obtained in composites produced with CB (Athreya *et al.*, 2010; Xi *et al.*, 2020). Xi *et al.* (2020) proved the benefits of CB in the flowability, mechanical properties and in the reduction of structural defects of SLS parts due to its higher thermal conductivity and greater capability to absorb the energy of the laser beam. The enhanced ability to absorb the energy of the laser beam was also verified for CF. Tian *et al.* (2018) developed PA12 parts with 40.0 wt% of CF exhibiting 15.5% higher melting depth than neat-PA12 parts. In turn, Flodberg *et al.* (2018) obtained 85.5% lower content of porosity in parts produced with CF, compared to neat-PA12 parts. Due to these capabilities, the inclusion of CF in general reduces the thermal requirements of the sintering process (Chunze Yan *et al.*, 2011)

All thermal interactions established between the laser source and the carbon-based composites, as well as the dependence of the SLS process parameters on the properties of the material (*i.e.*, melting and crystallization temperatures) prove the importance to proceed with a prior optimization of the operating settings for each building job to guarantee a successful sintering process (Yuan, Bai, *et al.*, 2016; Tian *et al.*, 2018; Lahtinen *et al.*, 2019). A prior optimization of the energy density supplied to the powder bed during the process was efficiently conducted by Athreya *et al.* (2010), Eshraghi *et al.* (2013), Karevan *et al.* (2013), Paggi *et al.* (2013), Tian *et al.* (2018), Yuan *et al.* (2018) and Hong *et al.* (2019). In fact, this initial procedure is considered vital to control the successive cycles of heating and cooling, to avoid warpage and curling characteristics and to maximize the mechanical strength of the parts, depending on

the reinforcement (Eshraghi *et al.*, 2013; Paggi *et al.*, 2013; Tian *et al.*, 2018; Hong *et al.*, 2019). However, it is reported that the amount of reinforcement is more influential in the properties of the final composite than the operating parameters defined for the sintering process (Yuan *et al.*, 2018). In this regard, Hong *et al.* (2019) showed that the amount of CB is the most significant variable influencing the elastic modulus and Paggi *et al.* (2013) proved that the amount of MWCNT has a predominant effect on the apparent density and flexural properties of SLS parts. Nevertheless, the definition of the optimum amount of reinforcement is not trivial. In studies conducted by Salmoria *et al.* (2017) and Espera *et al.* (2019), the percolation threshold for mechanical and electrical properties was attained for different weight percentages of MWCNT and CB, respectively. In their experiments, a high incorporation of reinforcement promoted a conductive network suitable for electrical conductivity, but inadequate for mechanical performance due to agglomeration problems and weak interfacial adhesion. Reduced mechanical properties with higher amounts of carbon-based reinforcements were also reported by Athreya *et al.* (2010), Karevan *et al.* (2013) and Xi *et al.* (2020). This can be explained by the different mechanisms governing the thermal, electrical and mechanical properties of SLS parts (Yuan *et al.*, 2018). In this context, Yuan *et al.* (2018) stated that the SLS operating principle has a promising capability to produce parts with electrical conductivity, instead of thermal conductivity due to the intrinsic content of porosity of the parts produced. Besides that, carbon-based composites can exhibit great functional properties at low percolation thresholds when an efficient method of preparation capable to create a strong interfacial adhesion and a quality conductive network is adopted (Hong *et al.*, 2019). The simplest method of mechanical mixing is one of the most used due to its cost-benefit. In this respect, Makuch *et al.* (2015) underlines the influence of the mixing time in the dispersion of the reinforcements. In their research, graphene flakes were well dispersed and exhibited great interfacial adhesion with an increased surface coverage after longer periods of mixing (Makuch *et al.*, 2015). In accordance, and besides some level of agglomeration and different melting viscosity and molecular weight, Athreya *et al.* (2012) obtained composite parts produced by SLS through mechanical mixing with better properties than similar composite parts produced by injection moulding through melt-mixing, in terms of electrical conductivity and storage modulus. These potentialities allowed lower percolation thresholds in the SLS parts than in the injection moulding ones (Athreya *et al.*, 2012).

Although a large number of the scientific publications described in Table 2.2 does not mention pre-treatments, it is reported that common carbon-based composites require a chemical modification of the reinforcement to improve the compatibility between the components (Francis and Jain, 2015). For instance, Jing *et al.* (2017) proved the importance of this procedure by obtaining a pre-treated CF/PA12

composite with a tensile strength 11% higher than the corresponding non-treated composite. Similar pre-treatments were conducted by Kim *et al.* (2013) who claimed that a pre-modification is vital to improve the interfacial adhesion of the composite, allowing the incorporation of smaller amounts of reinforcement for quality outputs. In accordance, Chunze Yan *et al.* (2011) showed the potential of a surface treatment of CF to increase its reactivity with the matrix and surface roughness to promote the mechanical interlocking, combined with an efficient preparation method to obtain composites with quality morphological structure, suitable sintering behaviour and desired final properties.

Regardless of the pre-treatments, the orientation of the parts on the building platform also influences its final performance, especially when CF are considered (Figure 2.5) (Flodberg *et al.*, 2018; Badini *et al.*, 2020). In that situation, the orientation of the parts is crucial to align the fibres in the direction where higher overall performance is required (Badini *et al.*, 2020). Due to the different alignment of the fibres, Flodberg *et al.* (2018) obtained PA12-CF composites with 117% and 50% higher tensile strength in parts horizontally and vertically produced, respectively, compared to neat-PA12 parts.

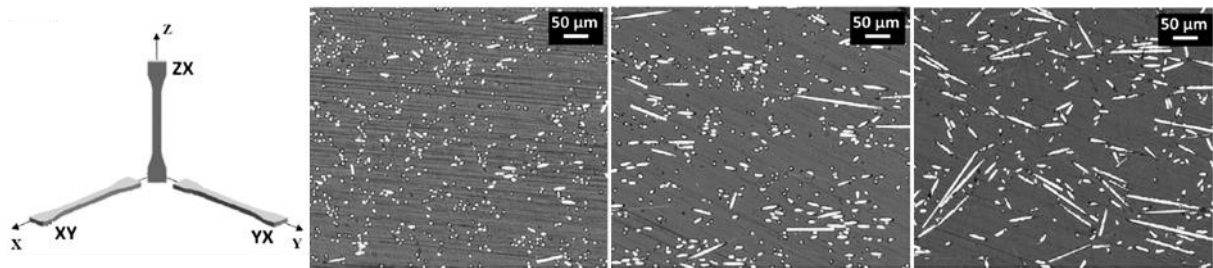


Figure 2.5 Cross-section of PA12-CF parts produced by SLS at XY (left), YX (middle) and ZX (right) orientations considering the movement of the recoater along the x-axis (Adapted from (Badini *et al.*, 2020)).

Despite these assumptions, it was already proved that when the set of process parameters is properly defined and the preparation methods fully optimized, the properties of SLS parts can effectively be improved through the inclusion of carbon-based reinforcements. Based on comparative studies, Kalaitzidou *et al.* (2009), Athreya *et al.* (2012) and Karevan *et al.* (2013) showed that SLS parts respectively developed with Graphite Nanoplatelets, CB and Carbon Nanoparticles exhibit higher elastic modulus, flexural modulus and electrical conductivity than similar composites produced by conventional injection moulding. This evidences that the operating principle of SLS (*e.g.*, slow cooling rate that promotes specific crystalline characteristics) is promising to produce carbon-based composites with quality outputs (Kalaitzidou *et al.*, 2009).

In sum, this section proved that there is a variety of opportunities related to the development and implementation of composite materials in SLS applications. However, some challenges and limitations focused on their difficult processing, building time, costs and end-of-life recycling still persist (Wu *et al.*,

2020). Based on such concern, in *Recent developments in polymers/polymer nanocomposites for additive manufacturing*, Wu *et al.* (2020) highlighted the potential of using “reliable modelling prediction and optimization of AM part performance” to consistently predict the properties of SLS parts, depending on the multitude of process parameters involved and their final application.

2.4. Computational modelling of Selective Laser Sintering

As SLS is governed by multi-physics phenomena with complex and non-linear interaction between parameters, the implementation of computational methods for modelling and simulation is essential to achieve a better understanding for a global process optimization with reduced time and cost consumption, in complement to experimental data (Ganeriwala and Zohdi, 2016; Papazoglou *et al.*, 2021). Since there are no established modelling frameworks for SLS, various modelling strategies have been developed over the years within the scientific and academic community considering different assumptions and computational simplifications (Papazoglou *et al.*, 2021). Therefore, several numerical strategies focused on diverse fields (*e.g.*, process, part or process-part modelling) are being employed with the intention to provide useful insights in three main extents, namely i) in-depth understanding of the process-structure-property relationships, ii) process prediction and monitoring and iii) establishment of design rules for SLS parts (Qi *et al.*, 2019; Papazoglou *et al.*, 2021). Because SLS modelling is material-specific, depending on its rheological, thermal and mechanical properties, only numerical studies focused on polymers were considered for discussion in this section¹, especially with regard to process prediction (Li *et al.*, 2020).

Despite the exponential usage of computer simulation in recent years, first studies using computational tools to characterize the SLS process of polymeric materials date back to 90's (*e.g.*, (Bugada *et al.*, 1999)). Most of the publications are focused on the thermal modelling of SLS to simulate temperature fields, melting pools and density distribution during heating and/or cooling. This is based on the hypothesis that the comprehension of these phenomena is essential to understand the dependence of the main properties of SLS parts on fundamental sintering variables (*e.g.*, energy density) (Chatham *et al.*, 2021). Therefore, a common numerical methodology is to use Finite Element Analysis (FEA) to account and correlate the interaction between the laser beam and powder particles, the coalescence mechanisms and change of phase form during the sintering through governing equations which are considered appropriate to mimic these laser-sintering phenomena (Dong *et al.*, 2009). These methodologies are mostly based on 2D or 3D approaches diverging in the main scope, type of powder bed modelling (*i.e.*, multiple or single layers, continuous or discrete fields), initial and boundary conditions,

¹ See *Appendix A* for detailed access to the list of publications considered for discussion in this section.

thermal-physical parameters and validation methods. Besides the computational methods, experiments are also commonly performed to determine the thermal-physical properties of the specific-material as input for the numerical model. This procedure was conducted by Tian *et al.* (2018) and Li *et al.* (2021). Although most numerical models are narrowly focused, in recent years scientific research in the area has been extended to assess the influence of a larger set of process parameters. As example, Li *et al.* (2021) and Chatham *et al.* (2021) respectively evaluated molten pool sizes and temperature profiles at various process parameters defining different values of energy density. In order to validate the accuracy and applicability of the models, numerical and/or experimental validations are also frequently performed through results obtained from literature (*e.g.*, (Dong *et al.*, 2008), (Singh and Prakash, 2010), (Mokrane *et al.*, 2018)) or own experiments (*e.g.*, (Li *et al.*, 2018), (Li *et al.*, 2020), (Soldner *et al.*, 2021)). Besides the predominant use of PA12 (*e.g.*, (Josupeit *et al.*, 2016), (Balemans *et al.*, 2018), (Mokrane *et al.*, 2018)), other materials are also being focus of analysis, such as polycarbonate (*e.g.*, (Dong *et al.*, 2009)), polypropylene (*e.g.*, (Ganci *et al.*, 2017)), polyurethane (*e.g.*, (Yuan *et al.*, 2020)) and other polymer-based composites (*e.g.*, (Li *et al.*, 2021)). Such numerical models are mostly implemented through Python scripts in ABAQUS software (*e.g.*, (Li *et al.*, 2021)).

Numerical studies accounting for the relationship between processing variables and properties of sintered parts with respect to sustainability concerns are also frequently considered. Mathematical models, Genetic Algorithms (GA) and Artificial Neural Networks (ANN) emerge as possibility for process characterization and prediction within this class of publications, mainly for estimating the building time (*e.g.*, (Munguía *et al.*, 2009)) and the energy consumption and material costs (*e.g.*, (Verma and Rai, 2017), (Ma *et al.*, 2018)) in computed platforms such as MATLAB.

FEA, GA, ANN and related methodologies are also widely employed to evaluate properties of SLS parts, such as density (*e.g.*, (Vijayaraghavan *et al.*, 2016)), shrinkage (*e.g.*, (Negi and Sharma, 2016)), warpage (*e.g.*, (Dastjerdi *et al.*, 2017)), position and orientation (*e.g.*, (Hur *et al.*, 2001)), mechanical properties (*e.g.*, (Lindberg *et al.*, 2018)), etc. With regard to mechanical properties, most scientific publications make use of FEA in ABAQUS or ANSYS software for different purposes. In this way, Cahill *et al.* (2009) and Doyle *et al.* (2015) used computational modelling to characterize tensile and compression properties of scaffolds with different designs for application in bone tissue engineering. Bai *et al.* (2020) established numerical models to evaluate the loading capacity and energy absorption of lattice structures under compression loads. Similarly, the mechanical properties of lattice structures depending on the cell type, cell size and other elemental parameters were also estimated by Jin *et al.* (2018) and Savio *et al.* (2019) through FEA. Different cellular elements and percentages of porosity were also evaluated by Cerardi *et*

al. (2013) with the aim to propose a predictive model for lattice structures. Schneider *et al.* (2020) simulated tensile and compression tests based on experimental results in order to ultimately create a three network material model for use in lattice structures of thermoplastic materials. Taking advantage of the design flexibility of SLS, Crookston *et al.* (2008) evaluated the mechanical response of base repeating units of deformable textiles through progressive damage models within ABAQUS environment. Lindberg *et al.* (2018) used FEA complemented with experimental material models expecting to predict the location and intensity of a mechanical failure for prosthesis development and testing. Through Representative Volume Element models and FEA, Tang *et al.* (2021) studied the effects of the volume fraction and orientation of carbon fibres on the mechanical behaviour of composites by means of theoretical constitutive models. Maeshima *et al.* (2021) used governing equations describing mechanical and thermal fields coupled with surface tension and viscoelastic-plastic models for thermo-mechanical characterization. In addition to FEA, methods based on the principles of artificial intelligence are also being employed. Baturynska (2019) compared linear regression models with machine learning methods (*i.e.*, Gradient Boosting Regressor, Decision Tree Regressor and AdaBoost Regressor) and demonstrated that linear regression models are accurate to predict tensile modulus and elongation at break. Adaptive Network-based Fuzzy Inference System (ANFIS) was used by Sohrabpoor *et al.* (2018) and Aldahash *et al.* (2020) to mechanically characterize PA12-based composites. Sohrabpoor *et al.* (2018) compared ANFIS with Grey Relational Analysis in the evaluation of the effect of the part bed temperature, laser powder, scan speed, scan spacing and scan length on the elongation and ultimate tensile strength of SLS parts. In turn, Aldahash *et al.* (2020) used experimental data obtained from tensile, compressive and flexural tests divided into two sets to train and validate the ANFIS model, using a total of 320 test specimens. The model was developed to predict the greatest combination of energy density and weight percentage of reinforcement able to produce parts with tailored mechanical performance. Finally, Fountas *et al.* (2021) used a multi-objective genetic algorithm to estimate the density, hardness and tensile strength of SLS parts based on quadratic equations derived from statistical analysis. A virus-evolutionary genetic algorithm was proposed and validated considering other population-based methods.

In sum, research in the field demonstrated that to enhance the accuracy of computational models, experiments may be performed to provide input parameters and to allow an ultimate validation, ensuring the establishment of theoretical functions capable of reliably describing the mechanical properties of SLS parts (Bai *et al.*, 2020; Yuan *et al.*, 2020). Regarding FEA, the analyses showed that the models need to account for the intrinsic porosity of SLS parts, otherwise the mechanical properties may be overestimated in numerical predictions (Crookston *et al.*, 2008). This highlights the importance of an in-depth SLS

Chapter 2. A review of Selective Laser Sintering: Parameters, materials and computational modelling

understanding in order to control the process and, consequently, the reliability between FEA predictions and actual properties of sintered-parts (Lindberg *et al.*, 2018). In turn, ANN is a powerful tool to establish complex correlations between input and output parameters; however, this computed method requires large experimental datasets to formulate and validate models for accurate predictions (Sohrabpoor *et al.*, 2018; Baturynska, 2019).

Final Remarks of Chapter 2

Chapter 2 comprises a critical review of relevant scientific publications focused on key SLS domains, namely: i) evaluation of fundamental process parameters, ii) development of functional composite materials and iii) process modelling and simulation. Regarding the first domain, the experiments reviewed in this chapter proved that the definition of operating parameters suited to each SLS process is vital to improve the overall properties of parts and to allow the successful processing of functional materials through this AM technology. These operating parameters can be selected according to the value of energy that is supplied by the laser beam to the powder particles, which significantly influences the properties of the parts produced. However, even with critical control of the process, SLS remains limited to conventional thermoplastic materials due to the numerous requirements needed for a successful sintering process. In fact, the real implementation of functional composite materials is still a complex assignment owing to its dependence on the nature and properties of the matrix, typology and amount of the reinforcements, preparation methods, additional treatments, process parameters, etc. In addition to costs and time of production, the biggest challenge is to establish a strong integration between the matrix and the reinforcement in order to produce quality composite materials. Despite the difficulties of development, carbon-based composites are one of the most explored. When properly optimized, these functional materials processed by SLS can present enhanced mechanical, thermal and/or electrical properties, being able to replace conventional materials processed by AM or traditional processing technologies. For optimization, computational modelling and simulation based on FEA or ANN methods are attractive tools to monitor and predict the process, to understand the process-structure-property relationships and, in a last instance, to establish design rules for SLS parts.

Chapter 3. Optimization of SLS process parameters

Chapter 3 addresses the methodology employed in this research to evaluate SLS process parameters, providing an overall description of the main activities, materials, methods and laser-sintering processes. The influence of fundamental process parameters on dimensional, geometric, mechanical and morphological properties of SLS parts is assessed through different hatching and contour settings defining the energy density supplied by the laser beam during the manufacturing. Results from X-Ray computed tomography, tensile tests, fracture mechanics tests and morphological characterization are presented and discussed in detail in this chapter for each experimental condition.

3.1. Introduction

SLS is a process based on selective sintering that requires a laser source and a thermally controlled chamber to produce the parts. Thus, the methodological approach defined to study the process parameters included the individual and combined effect of hatching and contour parameters in terms of energy density. It was carried out according to Eq. (2.2) (see *Chapter 2*) which allows the simultaneous evaluation of EDA and EDv. The series of experiments were planned to completely understand the influence of the most relevant variables, their mutual interaction and relative contribution, in order to further identify the range of SLS operating parameters capable to ensure the production of acceptable quality parts in a sintering process with minimum energy requirements.

In this regard, the first activity of the research encompassed the study of the individual effect of hatching parameters, considering various combinations of the laser power (P_{Laser}), scan speed (S_{Scan}), hatch distance (D_{Hatch}) and layer thickness (t_{Layer}), according to the list of experiments described in Table 3.1.

Table 3.1 List of experiments to evaluate the hatching parameters.

	Hatching Strategy	t_{Layer} (mm)	P_{Laser} (W)	D_{Hatch} (mm)	S_{Scan} (mm/s)	EDA (J/mm ²)	EDv (J/mm ³)
P1	XY-A	0.12	40.00	0.30	4000	0.033	0.278
P2			38.00		3800		
P3			36.00		3600		
P4		0.15	43.80		3500	0.042	
P5			40.00		3200		
P6	XY-A	0.12	17.10	0.30	3000	0.019	0.158
P7			32.00		4500	0.024	0.198
P8			32.00		3730	0.029	0.238
P9			32.00		2800	0.038	0.318
P10			38.70		3000	0.043	0.358
P11			43.00		3000	0.048	0.398
P12	X	0.12	32.00	0.30	2800	0.038	0.318
P13	Y						
P14	XY-S						

The initial productions, from P1 to P5, were conducted to understand the effect of the same value of energy defined with different combinations of parameters, in order to previously validate the selected approach. Thus, P1, P2 and P3 evaluate the random combination of parameters for same values of EDA and EDv, while P4 and P5 assess same values of EDv for different values of EDA. Based on the results,

the following experiments, from P6 to P11, were conducted to evaluate the influence of EDv at constant intervals of 0.04 J/mm³, from 0.158 J/mm³ to 0.398 J/mm³. In the end, for a specific value of EDv, different strategies of the laser beam path were also studied through experiments P12 to P14. Thus, the x-direction (X)², the y-direction (Y)³ and the xy-direction-simultaneous (XY-S) were considered and further compared with the conventional xy-direction-alternating (XY-A) strategy used in experiments P1 to P11 (Figure 3.1).

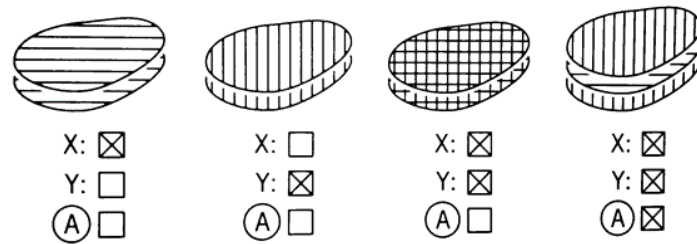


Figure 3.1 i) X, ii) Y, iii) XY-S and iv) XY-A strategies of the laser beam path.

In this activity, contour and post-contour, edges and post-edges and parameters from the preheating phase, as well as the material dependent scaling (after the periodic EOS technical service), were fixed according to the standard mode, ensuring a balanced compromise between the stability of the process and the overall properties of the parts (Table 3.2).

Table 3.2 Process parameters in the EOS Balance standard mode.

CONTOUR AND POST CONTOUR	Scan Speed (mm/s)	3000	Material Dependent Scaling (%)	X	3.22
	Laser Power (W)	34		Y	3.13
	Extra Beam Offset (mm)	0		Z (0)	2.55
EDGES AND POST EDGES	Edge Factor	1.80		Z (600)	1.40
	Threshold	3			
	Min. Radius Factor	0			
	Extra Beam Offset (mm)	0			
	Scan Speed (mm/s)	1500			
	Laser Power (W)	20			
HATCHING	Extra Beam Offset (mm)	0.12			
	Process Chamber Temperature (°C)	173			
	Removal Chamber Temperature (°C)	130			
	Beam Offset (mm)	0.32			

² In EOS P 396, the laser beam using the x-strategy operates in the normal direction of the recoater movement.

³ In EOS P 396, the laser beam using the y-strategy operates in the parallel direction of the recoater movement.

Chapter 3. Optimization of SLS process parameters

Considering optimized hatching settings, the following stage of the research was focused on the evaluation of contour parameters. To this aim, the individual effects of P_{Laser} (experiments P15 and P16) and S_{Scan} (experiments P17 and P18) in the definition of EDV were evaluated in a same extent to upward and downward-facing surfaces (Table 3.3). In this activity, edges and post-edges, parameters from the preheating phase and the material dependent scaling were also fixed according to the values reported in Table 3.2.

Table 3.3 List of experiments to evaluate the contour parameters (optimized hatching set).

	P_{Laser} (W)	S_{Scan} (mm/s)	P_{Laser}/S_{Scan} (J/mm)	HATCHING PARAMETERS	Laser Strategy	Y
P15	30	3000	0.007		t_{Layer} (mm)	0.12
P16	38	3000	0.009		P_{Laser} (W)	32.00
P13	34	3000	0.011		DHatch (mm)	0.30
P17	34	2000	0.013		S_{Scan} (mm/s)	2800
P18	34	4000	0.015		EDV (J/mm ³)	0.318

After the individual analysis, the last activity of the research was designed to evaluate balanced correlations between hatching and contour parameters. To do so, an advanced parameterization mode was selected to apply two different parameterization sets in the same part, depending on the thickness defined for the skin (*i.e.*, the external layers) (experiments P19 to P21) (Table 3.4). The main purpose of this activity was to maximize the mechanical strength of parts through the core (*i.e.*, internal layers), ensuring the dimensional and geometric accuracy of features in smooth surfaces through the skin. Based on results obtained from previous activities, a promising combination of hatching and contour parameters was defined considering the thickness of skin (t_{Skin}) ranging from 20% to 40% of the thickness of part (t_{Part}). In this way, it was intended to optimize the compromise between the requirements of the sintering process and the overall properties of SLS parts at all levels.

Table 3.4 List of experiments to evaluate the combination of hatching and contour parameters.

CORE PARAMETERS	Hatching	EDV (J/mm ³)	0.318	t_{Skin}/t_{Part} (%)	
		Strategy	Y		
SKIN PARAMETERS	Contour	P_{Laser}/S_{Scan} (J/mm)	0.007	P19	20
	Hatching	Strategy	X	P20	30
SKIN PARAMETERS		Contour	P_{Laser}/S_{Scan} (J/mm)	0.007	P21
	SKIN PARAMETERS	Hatching	EDV (J/mm ³)	0.198	
SKIN PARAMETERS		Contour	P_{Laser}/S_{Scan} (J/mm)	0.007	

The process parameters not listed in Table 3.4 were fixed in the standard mode (Table 3.2).

In all experiments, several different test specimens were produced and characterized in order to in-depth understand the effect of SLS process parameters on a complete range of macro and micro-scale properties of laser-sintered parts. Hence, *section 3.2* describes the materials, methods and characterization tests selected for the analysis.

3.2. Materials and methods

The study of SLS process parameters was accomplished in an EOS P 396 laser-sintering machine. This is an equipment for AM of polymer-based materials supplied by Electro Optical Systems (EOS) GmbH, with an effective building volume of 340 x 340 x 600 mm, operating with a CO₂ laser and precision optics of F-theta-lens. A neat PA12 powder with an average diameter of 56 µm (*i.e.*, PA 2200 from EOS GmbH) was used for the building jobs. In order to reproduce real conditions of sintering, the productions were conducted with a fixed ratio of 50% of virgin with 50% of processed material. According to the technical datasheet, SLS parts produced with these material conditions and the EOS standard parameterization mode present a laser-sintered density of 930 kg/m³, an elastic modulus of 1650 MPa, a tensile strength of 48 MPa, a strain at break of 18% and a flexural modulus of 1500 MPa (EOS GmbH, 2018).

The test specimens required for the characterization tests were horizontally produced in the central region of the building platform in order to minimize the influence of the thermal gradients generated during the sintering. The corresponding data files were prepared for the sintering process using Magics Materialize, EOS RP Tools and EOS PSW 3.8 software. Depending on the process parameters, specific exposure types were created for each building job using the EOS PSW 3.8 software. In the exposure editor, it was selected the path *No_Exposure* → *_Default_EOS* for the individual analysis, modifying the default parameters used to produce parts for standard requirements and the path *No_Exposure* → *SkinCore* for the combined analysis, applying multiple exposure types.

After the production and cooling inside the laser-sintering machine, the test specimens were cleaned with compressed air in a Normfinish Leering Hengelo system and with plastic microbeads blasting in a Norblast equipment. No additional post-production treatments were considered for this study. Before testing, the test specimens were stored in a room with a controlled environment of 22 °C and 40 rH%.

3.3. Characterization tests

A series of characterization tests were planned to completely understand the influence of the thermal energy supplied by the laser beam on the properties of parts produced by SLS. Therefore, the analysis of hatching and contour parameters was extended to dimensional, geometric, mechanical and morphological properties, as following described in *sections 3.3.1* to *3.3.5*.

3.3.1. Mass and general dimensions

After production and cooling, the mass of the test specimens was evaluated with a KERN Precision balance. The thickness, width and length were also assessed using a GARANT DC2 calliper, considering the average of three points of each dimension in all test specimens. The measurements of mass and general dimensions were performed in a minimum of three test specimens per condition.

3.3.2. Dimensional and geometric accuracy

A standard test artefact developed by the *National Institute of Standards and Technology* (NIST) to investigate the performance of AM systems was considered in this research to evaluate the limitations and capabilities of SLS to produce parts with dimensional and geometric accuracy (Figure 3.2) (Moylan *et al.*, 2014).

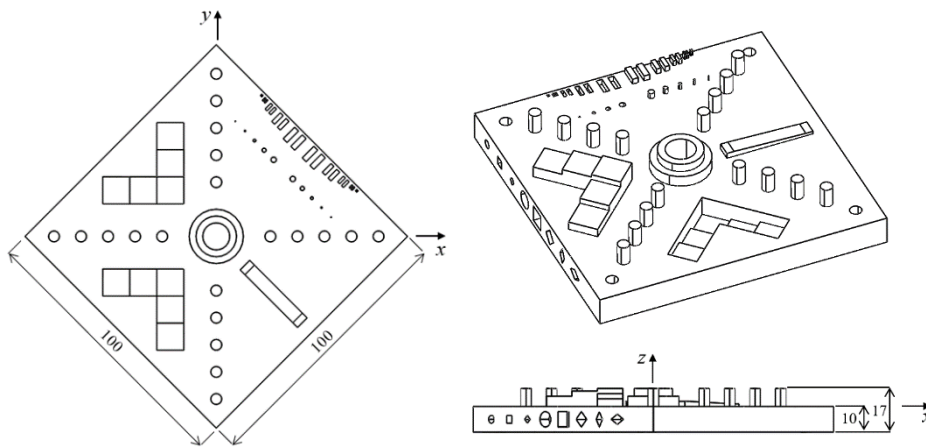


Figure 3.2 Test artefact for dimensional and geometric evaluation (dimensions in mm).

The part covers a number of different features (*e.g.*, holes, cylinders, staircases, fine features) that allow evaluating the capability of SLS to produce flat surfaces, round and concentric holes, parallel and perpendicular edges, features in different planes, etc; and to identify the minimum size achievable for each feature and the minimum distance required between them, depending on the parameterization set.

This part was produced in the centre of the building platform and measured by X-Ray Computed Tomography (CT) in a ZEISS METROTOM 800 225 kV equipment ($\pm (0.0035+L/100) \mu\text{m}$) using the METROTOM OS software. The CT images were taken with a voltage of 120 kV and a current of 1000 μA , considering 500 ms of integration time and 2500 projections. The analysis was based on the Feldkamp reconstruction algorithm and VAST scanning method (full scan).

The dimensional and geometric characteristics were assessed according to the corresponding criteria and measurement rules proposed by NIST (*i.e.*, recommended measuring devices, number of points and surface coverage (Moylan *et al.*, 2014)) using the INSPECTplus software. A minimum of five

measurements per feature was taken in each test artefact to identify the corresponding standard deviation. The results were compared between parameterization sets and the CAD model.

3.3.3. Mechanical tests

The mechanical properties of test specimens produced with different processing parameters were evaluated through uniaxial tensile tests and mode I fracture analysis (*i.e.*, opening mode).

3.3.3.1. Tensile tests

The tensile tests were performed in an Instron 5969 Universal Testing System with video extensometer to determine mechanical properties such as the elastic modulus, tensile strength, tensile stress at yield (0.2% offset), tensile stress at break, tensile strain at yield and tensile strain at break (ISO 527-1). Five test specimens, type 1BA (ISO 527-2) (Figure 3.3), were produced and tested at 10 mm/min with a load-cell of 50 kN at room temperature (ISO, 1996).

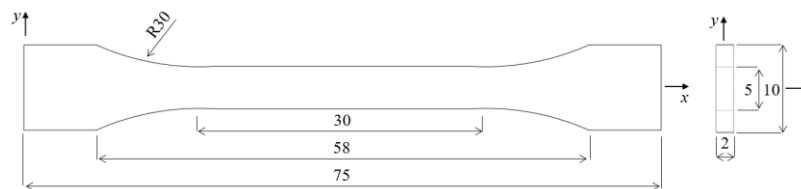


Figure 3.3 Test specimen for tensile tests (dimensions in mm).

3.3.3.2. Fracture tests

The mode I fracture analysis was performed through Double Cantilever Beam (DCB) tests. A minimum of three test specimens were directly produced with holes to easily apply the load and then prepared for DCB in a Bridgeport milling machine. A ceramic cutting blade (thickness: 0.8 mm) and a thin cutter (thickness: 0.4 mm) were used to prepare an initial crack with a length of 28.3 mm. A lateral notch in a half-height on both sides of the test specimens with a depth of 0.5 mm was also machined with a metal cutting blade (thickness: 1.2 mm; cut angle: 70°) (Figure 3.4).

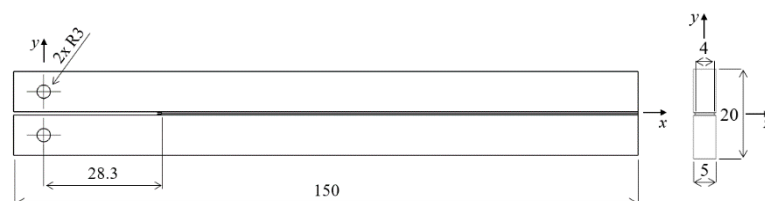


Figure 3.4 Test specimen for DCB tests (dimensions in mm).

The DCB tests were conducted in an Instron 5969 Universal Testing System at 3.6 mm/min with a load-cell of 50 kN at room temperature. The applied load (P) and attained displacement (δ) were recorded with an acquisition rate of 10 Hz allowing to obtain the $P\delta$ curves. Then, the Compliance-Based Beam

Chapter 3. Optimization of SLS process parameters

Method (CBBM) was employed to obtain the corresponding *Resistance-curves* (*R-curves*), in order to determine the critical energy release rate (G_{Ic}) of the material, quantifying its resistance against crack propagation (*i.e.*, fracture toughness). In order to identify the remaining cohesive parameters, the experimental data was complemented with numerical analysis, employing a trapezoidal cohesive bilinear damage law, through a user subroutine of the ABAQUS software.

COMPLIANCE-BASED BEAM METHOD (CBBM)

Since the crack growth was not directly monitored during the DCB tests, a data reduction scheme proposed by de Moura *et al.* (2008) was used in this research to evaluate the fracture toughness of SLS parts depending on the process parameters. This approach, known as Compliance-Based Beam Method (CBBM), considers the Timoshenko beam theory and the concept of an equivalent crack length (a_e), depending on the compliance of the test specimen (C) (de Moura *et al.*, 2008; Pereira *et al.*, 2017). Based on this method and considering the beam theory, the elastic strain energy of the test specimen, U , including the flexural and shear components, is given by:

$$U = 2 \left[\int_0^a \frac{M_f^2}{2EI} dx + \int_0^a \int_{-h/2}^{h/2} \frac{\tau^2}{2G} B dy dx \right] \quad (3.1)$$

where M_f is the bending moment, I the second moment of area, τ the shear stress, B the width of the test specimen in the cracked region, a the current crack length, h the half-height of the test specimen, E the elastic modulus and G the shear modulus (de Moura *et al.*, 2008). Considering the Castigliano theorem and Eq. (3.1), the resulting displacement is obtained as follows:

$$\delta = \frac{dU}{dP} = \frac{8Pa^3}{EBh^3} + \frac{12Pa}{5BhG} \quad (3.2)$$

with P standing for the load applied in the test specimen. Taking into account Eq. (3.2), the compliance of the test specimen, $C = \delta/P$, can be obtained by (Pereira *et al.*, 2017):

$$C = \frac{8a^3}{EBh^3} + \frac{12a}{5BhG} \quad (3.3)$$

This method supposes the determination of a_e which considers the effect of the fracture process zone at the crack tip, influencing the P - δ curve profile. The analytical solution of Eq. (3.3) for the equivalent crack length, a_e , is obtained by:

$$a_e = \frac{1}{6\alpha} A - \frac{2\beta}{A} \quad (3.4)$$

with, α , β and A defined according to:

The energy release rate, G_I , is computed using the Irwin-Kies equation:

$$\alpha = \frac{8}{Bh^3E} ; \beta = \frac{12}{5BhG} ; A = ((108C + 12 \sqrt{3(\frac{4\beta^3 + 27C^2\alpha}{\alpha})})\alpha^2)^{\frac{1}{3}} \quad (3.5)$$

$$G_I = \frac{P^2 dC}{2b da} \quad (3.6)$$

Finally, the combination of Eqs. (3.3) and (3.6) yields:

$$G_I = \frac{6P^2}{Bbh} \left(\frac{2a_e^2}{Eh^2} + \frac{1}{5G} \right) \quad (3.7)$$

which was adapted to account for the reduction of width (*i.e.*, parameter b) following the production of the lateral notches (de Moura *et al.*, 2008; Pereira *et al.*, 2017). In this research, E was determined via numerical analysis based on the initial compliance by fitting the elastic region of the numerical P - δ curve to the experimental one and G was defined according to the corresponding E and ν (*i.e.*, Poisson's ratio).

NUMERICAL ANALYSIS

The numerical model implemented in the finite element analysis used linear 8-nodes hexahedral elements. In order to simplify the analysis and to reduce the computational effort, only a half-width of the test specimen was considered with a mesh particularly refined in the region of crack propagation, improving the accuracy of the analysis in that section. Therefore, the total mesh comprised 83 elements along the x-axis, 28 elements along the y-axis and 3 elements along the z-axis (Figure 3.5). The boundary conditions were imposed according to the experimental tests, concerning conditions of symmetry and degrees of freedom of each set of nodes. In accordance, the displacement of the symmetry plan was constrained along the z-axis, the displacement of the set of nodes of the inferior beam of the test specimen was constrained along the x and y axes, while the set of nodes of the superior beam was only constrained along the x-axis. A small load displacement was applied to this set of nodes along y-direction to allow smooth and stable crack propagation in the course of the loading process.

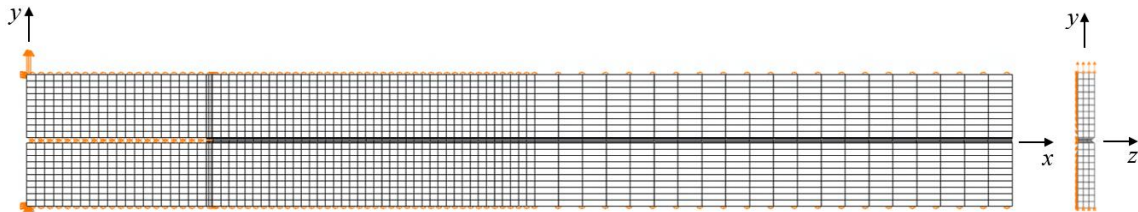


Figure 3.5 Mesh and boundary conditions used in the numerical analysis of DCB.

COHESIVE MODELLING

Due to the attainment of a non-negligible plateau in the experimental $P\text{-}\delta$ curves, the inverse method was employed using a trapezoidal bilinear softening cohesive law (Figure 3.6). This cohesive law is able to replicate linear and bilinear configurations, by proper selection of the characteristic parameters (*i.e.*, position of points 2 and 3 aligned with corresponding positions of point 1 and δ_u).

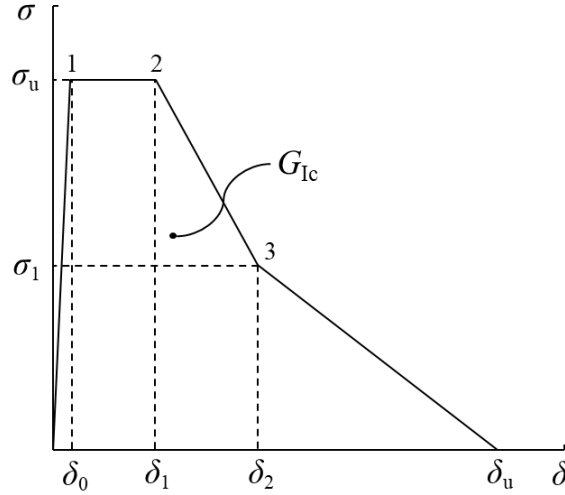


Figure 3.6 Trapezoidal bilinear softening cohesive law.

The fundamental equations of this cohesive law were developed by Silva *et. al* (2016). According to the formulation and considering k as the stiffness of the interface assumed equal to 10^6 N/mm³, the first ascending region of the curve, when $\delta < \delta_0$, is described by:

$$\sigma(\delta) = k\delta \tag{3.8}$$

After that, when the local strength is achieved, σ_u , damage mechanisms occur, and the reduction of stiffness is given by:

$$\sigma(\delta) = (1 - d)k\delta \tag{3.9}$$

where d is a parameter that quantifies the damage that develops ahead of the crack tip, ranging from 0 at δ_0 to 1 at δ_u . In the plateau of the model, the stiffness slightly decreases according to:

$$d = 1 - \frac{\delta_0}{\delta} \tag{3.10}$$

Finally, considering the bi-linearity of the cohesive law defined by two branches after the post-peak, Eq. (3.11) and (3.12) are respectively applied to the first (*i.e.*, $\delta_1 < \delta < \delta_2$) and second (*i.e.*, $\delta_2 < \delta < \delta_u$) descending sections:

$$d = 1 - \frac{\frac{\sigma_2}{k}(\delta - \delta_1) + \delta_0(\delta_2 - \delta)}{\delta(\delta_2 - \delta_1)} \tag{3.11}$$

$$d = 1 - \frac{\sigma_2(\delta_u - \delta)}{k\delta(\delta_u - \delta_2)} \quad (3.12)$$

The parameters of the trapezoidal bilinear cohesive law representing the behaviour of PA12 parts produced by SLS were identified through the numerical-experimental agreement of the P - δ and R curves.

3.3.4. Warpage and curling

Warpage and curling are considered critical defects of SLS parts with known dependence on the process parameters (Dastjerdi *et al.*, 2017). They are a result of a shape deformation caused by the stages of thermal expansion and contraction experienced during the successive deposition of layers and heating-cooling cycles (Ha *et al.*, 2020). Besides the thermal gradients developed inside the building chamber, the difference in density between the powder particles and sintered part also directly influences these effects (Ha *et al.*, 2020). In this way, the test cross illustrated in Figure 3.7 (*i.e.*, EOS GmbH benchmark sample used for curling control) was used in this work to qualitatively evaluate these characteristics in both x and y directions after a controlled cooling period.

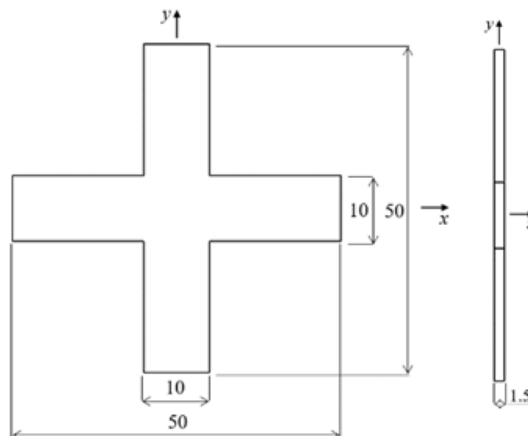


Figure 3.7 Test specimen for warpage evaluation (dimensions in mm).

Because this test cross did not reveal notorious warpage characteristics after the SLS process, long and thin test bars (200 x 2.5 x 1.5 mm) were also produced with the longest dimension parallel to the x-axis (*i.e.*, XYZ orientation) and y-axis (*i.e.*, YXZ orientation) of the building platform, using the most promising parameterization modes identified in the research to in-depth understand these phenomena. The test bars were positioned 15 mm apart in order to minimize the influence of the other parameterization modes and produced with the process parameters of experiments i) P3, P6 and P11 to evaluate the effect of the energy density (EDV), ii) P9, P12 and P13 to evaluate the effect of the laser strategy, iii) P9 and P15 to evaluate the effect of the contour parameters and iv) P9 and P21 to evaluate the effect of the combined parameterization mode (see *section 3.1*). After 18h of cooling inside the laser-sintering machine, the test bars were qualitatively evaluated.

3.3.5. Morphological assessment

A NanoSEM FEI Nova 200 equipment was used to carry out Scanning Electron Microscopy (SEM) analyses in order to observe the microstructure of test specimens. Therefore, the cross-section of tensile specimens obtained by cryogenic fracture was evaluated in relation to the content of porosity and consolidation of powder particles. The fracture surfaces in the tip of the crack of the most relevant parameterization sets were also observed (after the DCB tests). For the measurements, the samples were prepared with 15 nm of gold coating and the electron secondary imaging was recorded with an acceleration voltage of 10 kV.

3.3.6. Process characterization

Figure 3.8 reveals the position of test specimens oriented at 0° in relation to the powder bed in the central region of the EOS P 396 building platform, in reference to the x, y and z axes. In addition to the assessment of the properties of test specimens, qualitative and quantitative properties of the SLS process were recorded by monitoring the sintering chamber and the building time, respectively.

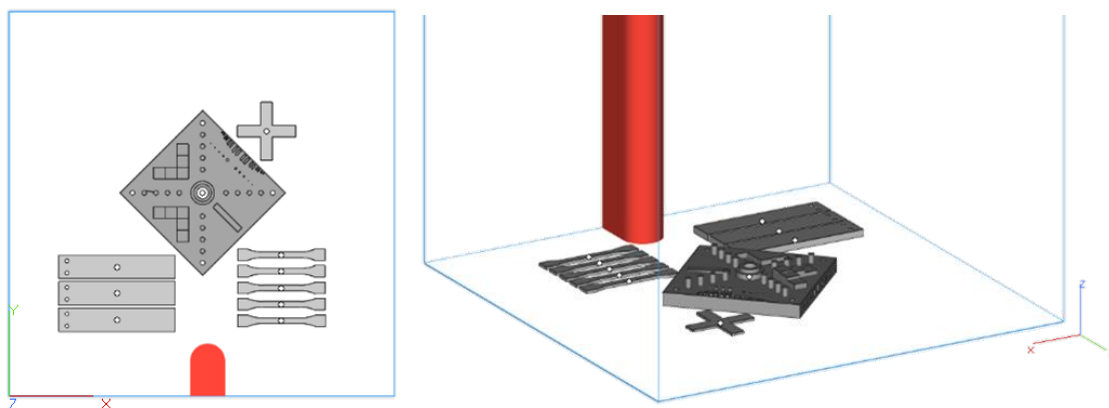


Figure 3.8 Position and orientation of the test specimens in the EOS P 396 building platform.

3.4. Results and discussion

This section presents the main results obtained from the characterization tests concerning the effect of hatching and contour parameters in the most relevant properties of SLS parts. All quantitative results collected for discussion were prior validated with a statistical treatment to ensure a normal distribution of the data. To this aim, a Normality Test (Anderson-Darling test type) combined with an Outlier Test with a significance level of 0.05 were applied using the Basic Statistics Tools of the MINITAB software.

3.4.1. Hatching parameters

As opposed to contour, hatching refers to the internal layers of the part, defining the largest portion of its bulk volume. Because of that, the assessment of hatching settings is decisive to deeper comprehend

the effect of fundamental SLS process parameters on the process and properties of parts. Therefore, the hatching parameters were evaluated in this section with regard to different ED_v values (*i.e.*, from 0.158 J/mm³ to 0.398 J/mm³ at constant intervals of 0.04 J/mm³) and key-strategies of the laser beam path (*i.e.*, X, Y, XY-S and XY-A) (see Table 3.1 in *section 3.1*).

3.4.1.1. Description of observations

From the experiments described in *section 3.1*, it was observed that the combination of ED_A and ED_v is critical and requires a mutual and interdependent analysis. For same values of ED_v, a t_{Layer} of 0.15 mm instead of 0.12 mm is exposed to increased ED_A values. In that situation, smoke is released from the sintering process during the action of the laser beam. For that reason, the study was mostly planned for a t_{Layer} of 0.12 mm.

Regardless of t_{Layer}, the initial experiments showed that the overall appearance of parts produced with 0.278 J/mm³ was not critically sensitive to different combinations of parameters. On the other hand, it was observed that the variation of ED_v had direct influence on the quality of features. The most evident characteristic was the advantage of low values of energy to reproduce fine holes and the disadvantage to reproduce fine pins in surfaces at 0° directed to the top. In this regard, Figure 3.9 in detail reveals fine features of test artefacts produced with ED_v values of 0.278 J/mm³ (top), 0.238 J/mm³ (middle) and 0.198 J/mm³ (bottom). Based on a qualitative evaluation, it was possible to verify that the standard value of 0.278 J/mm³ did not reproduce any quality hole with a nominal diameter of less than 2.00 mm, while in the test artefact produced with 0.198 J/mm³ holes until 1.00 mm were detectable.

Chapter 3. Optimization of SLS process parameters

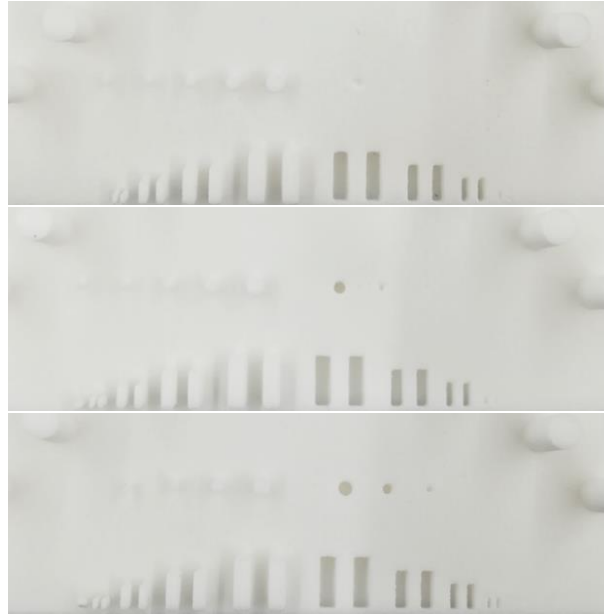


Figure 3.9 Fine features of test artefacts produced by SLS with 0.278 J/mm³ (top), 0.238 J/mm³ (middle) and 0.198 J/mm³ (bottom).

Despite the greater capability of low values of energy for the manufacturing of holes, the test artefact produced with 0.198 J/mm³ exhibited some defects in terms of surface finishing and planar deformation. Qualitative differences between the average roughness of surfaces directed to the top and to the bottom were also observed (Figure 3.10).



Figure 3.10 Finishing of surfaces directed to the top (left) and bottom (right) of test specimens produced by SLS with 0.198 J/mm³.

The results of the test artefact produced with the lowest value of energy defined for the analysis, *i.e.*, 0.158 J/mm³, were similar to those obtained in the test artefact produced with 0.198 J/mm³ in relation to fine holes. However, the manufacturing of fine pins was not as efficient. In the test artefact produced with 0.158 J/mm³, positive features with nominal dimension of less than 1.00 mm showed brittle behaviour with high tendency to break (Figure 3.11).

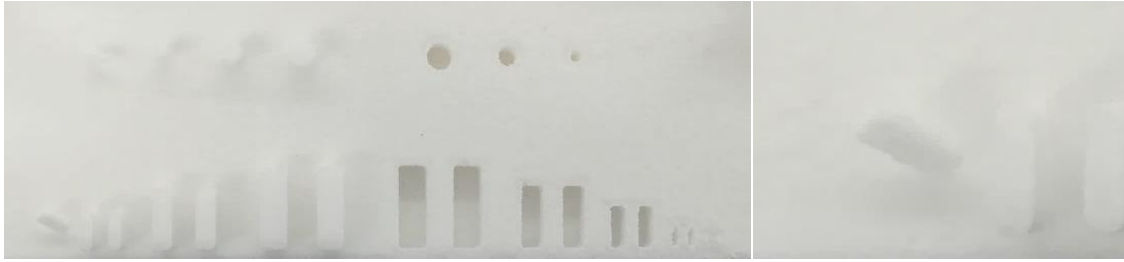


Figure 3.11 Fine features of a test artefact produced by SLS with 0.158 J/mm^3 , evidencing the brittleness of pins.

In addition, the test artefact produced with 0.158 J/mm^3 presented increased surface roughness in surfaces directed to the top compared to the test artefact produced with 0.198 J/mm^3 (Figure 3.12).

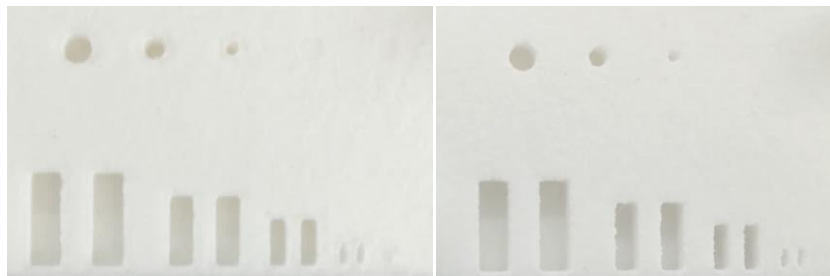


Figure 3.12 Fine features of test artefacts produced by SLS with 0.158 J/mm^3 (left) and 0.198 J/mm^3 (right).

On the other hand, EDv values above the reference level of 0.278 J/mm^3 empowered the heat conduction to surrounding powder particles, creating heat concentrations in those regions. As a result of the high compaction of powder close to the test specimens, their surfaces became harder to clean with compressed air influencing the accurate reproducibility of holes, fine features and edges. These effects were observed to a slight extent in the test artefact produced with 0.318 J/mm^3 . In the test artefact produced with the energy increased to 0.358 J/mm^3 , the powder from those critical locations was completely sintered and impossible to clean even with microbeads blasting. As consequence, the resulting surfaces exhibited poor quality, rougher finishing and inaccuracy of details (Figure 3.13).



Figure 3.13 Surface of a test artefact produced by SLS with 0.358 J/mm^3 after cleaning with microbeads blasting.

This primary qualitative evaluation also showed that for increased values of energy, there is a minimum distance required between the positioning of parts on the building platform. When that distance reaches

Chapter 3. Optimization of SLS process parameters

a minimum critical value (in this case < 3.0 mm), some defects are prone to be developed in the lateral surfaces of the parts. For instance, Figure 3.14 reveals excessive compaction of surrounding powder particles influencing the dimensional accuracy of test specimens produced with 0.358 J/mm^3 .



Figure 3.14 Lateral defects in test specimens produced by SLS with 0.358 J/mm^3 .

As expected, the test specimens produced with the highest EDv value considered in the experiments, *i.e.*, 0.398 J/mm^3 , presented reduced overall quality with more pronounced problems of cleaning, surface quality and dimensional accuracy (Figure 3.15 and Figure 3.16). These findings allowed to identifying the upper limit of EDv beyond which the process becomes unfeasible for the laser-sintering system and material considered in this research.

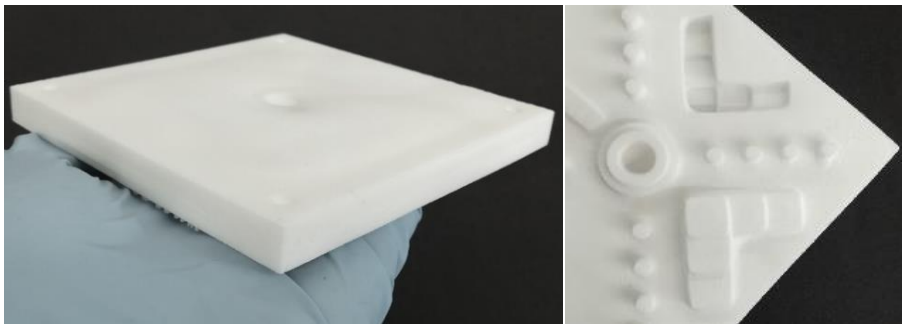


Figure 3.15 Downward and upward facing surfaces of a test artefact produced by SLS with 0.398 J/mm^3 after cleaning with sand blasting.



Figure 3.16 Lateral defects in test specimens produced by SLS with 0.398 J/mm^3 .

Moreover, the results obtained from experiments P12, P13 and P14 showed that the strategy of the laser beam also influences the SLS process, as well as the properties of the parts produced. Regardless

of the experiment, all test specimens exhibited high compaction of the powder particles compromising the attainment of smooth surfaces, quality holes and straight edges, as exemplarily illustrated in Figure 3.17 for the x-direction. These characteristics are a result of the laser beam strategy combined with the medium-high EDv value selected for the experiment.



Figure 3.17 Surface of a test artefact produced by SLS with 0.318 J/mm^3 in the x-direction after cleaning with sand blasting.

It was also observed that the x-direction strategy enhanced the heat conduction in the direction of the smallest distance between the parts. As consequence, the test specimens with low-spaced positioning exhibited highly compacted powder in their lateral surfaces, as observed before in experiments P₁₀ and P₁₁ (Figure 3.18). Regardless of the EDv value, this proves that the strategy of the laser beam also influences the minimum distance required between the positioning of parts. In this experiment, the lateral effects were reduced after cleaning with microbeads blasting.

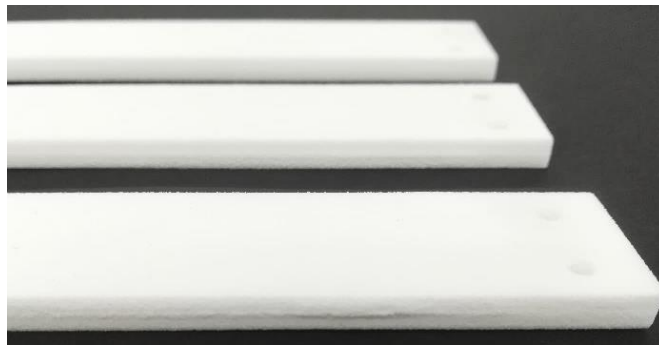


Figure 3.18 Lateral defects in test specimens produced by SLS with 0.318 J/mm^3 in the x-direction.

The permanent compaction of powder particles in critical regions of features was also observed in the test artefacts produced with the y-direction strategy. For instance, Figure 3.19 shows a non-quality surface of a test artefact produced with this laser beam path after cleaning with microbeads blasting.

Chapter 3. Optimization of SLS process parameters

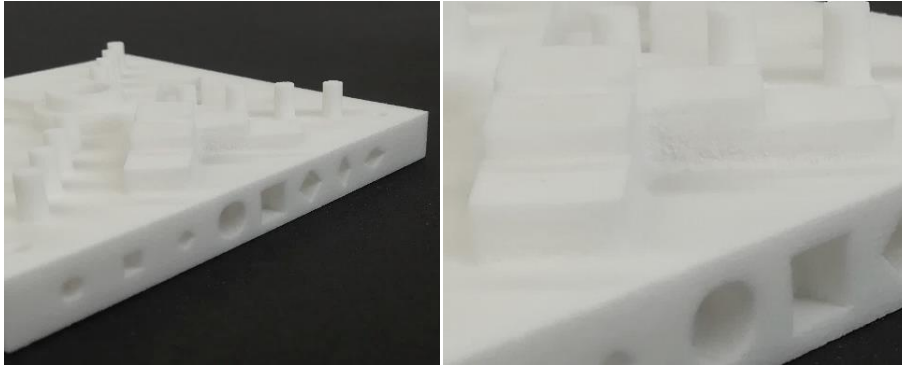


Figure 3.19 Surface of a test artefact produced by SLS with 0.318 J/mm^3 in the y-direction after cleaning with sand blasting.

However, as in this experiment the movement of the laser beam was transversal to the direction of the smallest distance between the parts, the resulting test specimens did not exhibit lateral defects. In addition, even with the same EDv value, the test specimens produced with the y-direction exhibited greater geometric similarity to those produced with the standard xy-direction-alternating than those obtained with the x-direction (Figure 3.20).

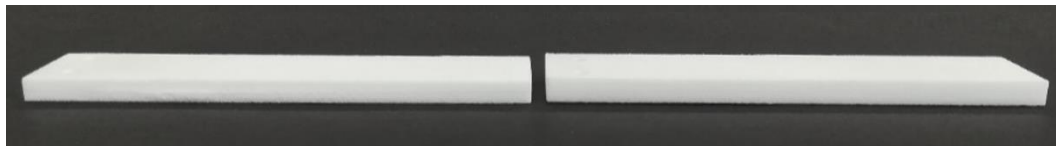


Figure 3.20 Lateral characteristics of test specimens produced by SLS with 0.318 J/mm^3 with the x-direction (left) and y-direction (right).

The experiment P14 conducted with the xy-direction-simultaneous strategy resulted in non-conforming parts with the full-sintering of holes, loss of precision, poor edges, oversizing and surface roughness (Figure 3.21). These defects were more pronounced in test specimens produced with these operating parameters (*i.e.*, 0.318 J/mm^3 (XY-S) (P14)) than in test specimens produced with the highest value of energy considered in the research (*i.e.*, 0.398 J/mm^3 (XY-A) (P11)).

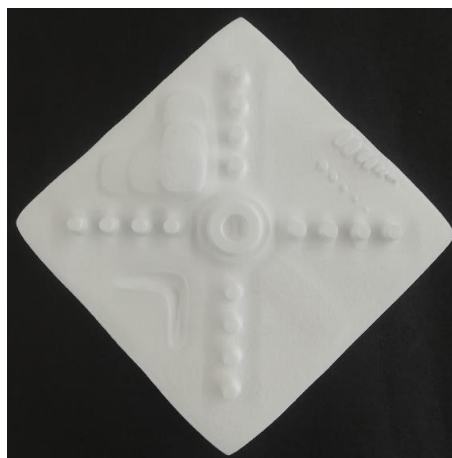


Figure 3.21 Test artefact produced by SLS with 0.318 J/mm^3 in the xy-direction-simultaneous after cleaning with sand blasting.

Although in P12, P13 and P14 the EDv value was the same (*i.e.*, 0.318 J/mm³), the amount of energy supplied to the powder particles in P14 was intensified by the simultaneous action of the laser beam in both x and y directions. For that reason, some test specimens were solidified to each other during the sintering, becoming invalid for the characterization tests (Figure 3.22).



Figure 3.22 Test specimens produced by SLS with 0.318 J/mm³ in the xy-direction-simultaneous.

Furthermore, the continuous monitoring of the building chamber revealed that the sintering process took place without significant evidence of shape deformation in all conditions, suggesting the preponderant influence of the cooling time on warpage. In this regard, it was verified that the most notorious effects were caused by the EDv value for both XYZ and YXZ orientations (Figure 3.23).



Figure 3.23 Test bars produced by SLS with 0.158 J/mm³ (top), 0.278 J/mm³ (middle) and 0.398 J/mm³ (bottom).

The test bars produced with extremely low and high EDv values revealed significant warpage, in contrast to the test bar produced with a medium EDv value which showed less warpage. The profile of the shape deformation was different for each condition, depending on the thermal differences established between the powder bed and each sintered layer. The test bar produced with 0.158 J/mm³ exhibited downward warpage with convex profile, while the test bar produced with 0.398 J/mm³ exhibited upward warpage with concave profile. Regarding the test crosses with smaller length/thickness ratio, only the one produced with the severe thermal conditions of experiment P11 exhibited warpage and curling

Chapter 3. Optimization of SLS process parameters

characteristics (Figure 3.24). The high level of energy of that experiment combined with the thermal environment developed within the building chamber were responsible to generate a complex gradient of temperatures and, therefore, a non-uniform cooling of the parts produced causing warpage and curling effects in critical surfaces (Dastjerdi *et al.*, 2017).

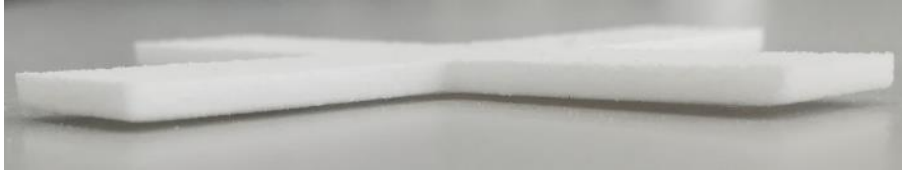


Figure 3.24 Warpage and curling phenomena in a test specimen produced by SLS with 0.398 J/mm³.

Regardless of the parameterization mode, this primary qualitative analysis suggested that the test bars produced with the XYZ orientation are most prone to warpage. This can be explained by the alignment of the longest dimension of the test bar in relation to the movement of the recoater. When the longest dimension is transversal to the direction of the movement of the recoater (*i.e.*, YXZ orientation), a large portion of the test bar is covered with a new layer of powder at the same time, allowing for a smaller gradient of temperatures compared with a parallel alignment (*i.e.*, XYZ orientation). Despite these assumptions, with the increase of the cooling time outside the laser-sintering machine, the test bars have undergone some stress relaxation, reverting the high shape deformation that was verified immediately after the unpacking. The experiments conducted to evaluate the influence of the strategy of the laser beam did not reveal notorious differences between the test bars.

In summary, this first qualitative evaluation suggested that SLS parts must preferably be produced with EDv values between 0.198 J/mm³ and 0.318 J/mm³ to obtain acceptable overall outputs. In this regard, the results showed that with lower values of energy, the surface roughness of parts increases and the upward and downward-facing surfaces present different quality. On the other hand, higher values of energy cause the full sintering of critical holes, compromising the functionality of the parts. In addition, it was proved that the strategy of the laser beam path also influences the heat distribution of the supplied EDv through the powder bed and, therefore, the properties of the parts produced. In this way, both xy-direction-alternating and y-direction strategies enable the production of parts with acceptable overall quality. Because of the aforementioned non-conformity occurrences, the test specimens from experiments P10, P11 and P14 were not considered for geometric evaluation; the test specimens from experiments P11 and P14 were not considered for DCB tests and the test specimens from experiments P14 were not considered for dimensional evaluation.

3.4.1.2. Mass and general dimensions

The initial experiments, from P1 to P5, showed that the test specimens produced by SLS with same ED_v values obtained with different combinations of parameters exhibit similar values of mass, length, width and thickness, without significant variation between experiments. On the other hand, different trends were obtained for experiments P6 to P11. Figure 3.25 shows the variation of mass of test specimens as a function of ED_v, for the XY-A strategy of the laser beam. As a matter of reference, the mass obtained from the nominal volume and the laser-sintered density reported in the technical datasheet of the material is also specified (*i.e.*, 9.230 g).

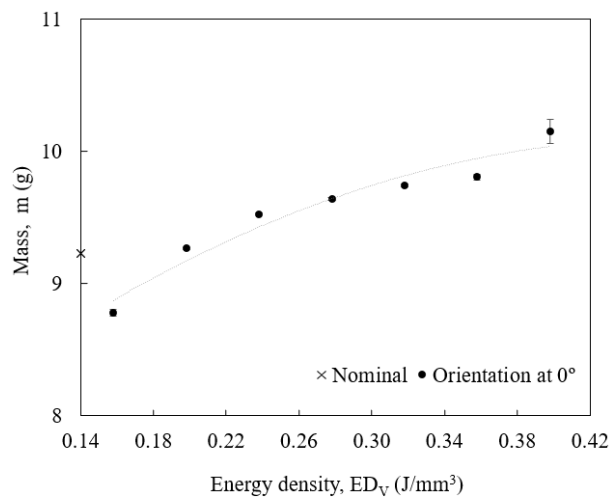


Figure 3.25 Mass of test specimens produced by SLS depending on ED_v (XY-A strategy).

As can be seen in Figure 3.25, the mass of SLS parts tends to increase with ED_v. The test specimens produced with 0.158 J/mm³ recorded the lowest value of 8.777 ± 0.025 g (*i.e.*, below the nominal), while the test specimens produced with 0.398 J/mm³ reached the highest value of 10.153 ± 0.089 g (*i.e.*, above the nominal). This represents a variation of 15% in 0.24 J/mm³, evidencing the greater heat conduction and enhanced consolidation of powder particles induced by high values of ED_v. However, it was verified that when a critical level of energy is attained, the value of mass is affected by the sintering of surrounding particles to the surfaces of the parts (*i.e.*, known in literature as 'secondary sintering'). This phenomenon was responsible for the high standard deviation obtained in test specimens produced with 0.398 J/mm³.

In turn, the length of the test specimens was not influenced by the ED_v value (Figure 3.26). All results were close to the nominal value of 100 mm, proving that this dimension is not sensitive to the thermal conditions selected for the SLS process.

Chapter 3. Optimization of SLS process parameters

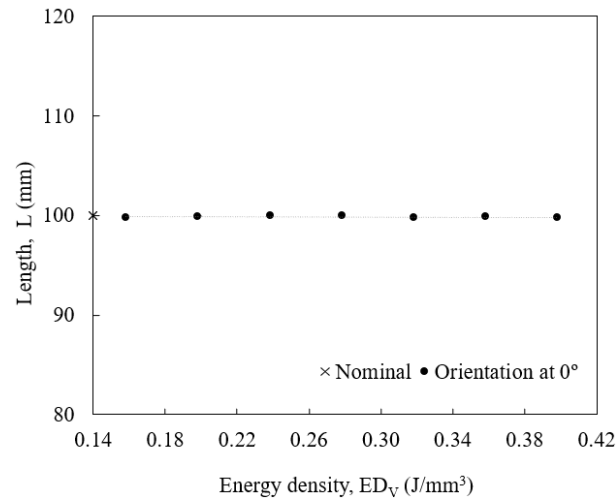


Figure 3.26 Length of test specimens produced by SLS depending on ED_v (XY-A strategy).

The width of the test specimens also did not show a significant variation between experiments from low to medium ED_v values (Figure 3.27). Until $0.318 J/mm^3$, the results were close to the nominal value of 20 mm. However, for the critical high ED_v values of $0.358 J/mm^3$ and $0.398 J/mm^3$, the width of the test specimens increased 2.1% and 5.4% of the nominal, respectively. The high standard deviation of these values is a consequence of the defects present in the lateral surfaces of the corresponding test specimens, as illustrated in Figure 3.14.

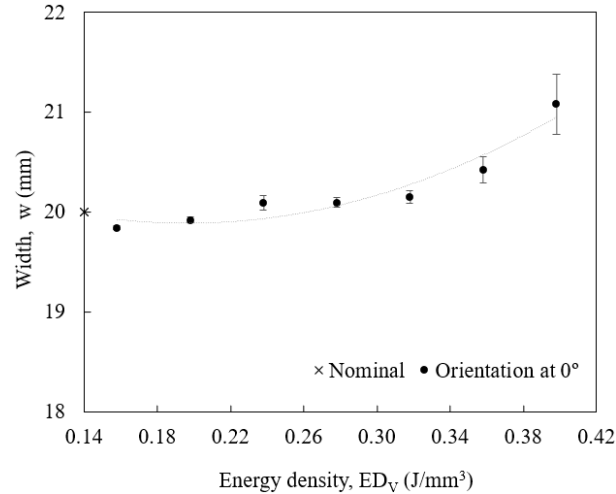


Figure 3.27 Width of test specimens produced by SLS depending on ED_v (XY-A strategy).

The dimensional analysis also proved that the thickness of SLS parts tends to increase with ED_v (Figure 3.28). In this regard, the thickness reached a maximum of 10% of variation in $0.24 J/mm^3$, from 4.79 ± 0.03 mm (*i.e.*, below the nominal) in test specimens produced with $0.158 J/mm^3$ to 5.26 ± 0.09 mm (*i.e.*, above the nominal) in test specimens produced with $0.398 J/mm^3$.

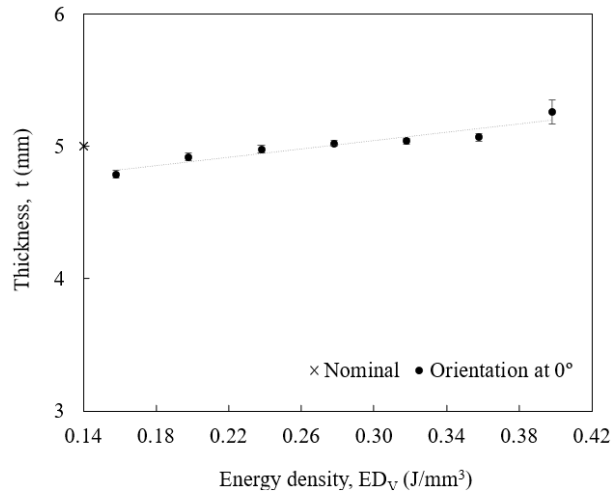


Figure 3.28 Thickness of test specimens produced by SLS depending on ED_v (XY-A strategy).

Moreover, Figure 3.29 and Figure 3.30 respectively demonstrate the influence of the laser beam strategy in the mass, length, width, and thickness of test specimens produced with 0.318 J/mm^3 (*i.e.*, experiments P12 to P14). In accordance with the assumptions described in *section 3.4.1.1.*, the results suggested that the xy-direction-alternating and the y-direction ensure similar dimensional outputs. Both strategies presented great dimensional stability with reduced standard deviation. In contrast, the test specimens produced with the x-direction exhibited lower mass, higher width and reduced thickness (see Figure 3.20). This proves that the xy-direction-simultaneous and x-direction strategies combined with the medium-high ED_v selected for the sintering are not able to fulfil dimensional specifications with accuracy.

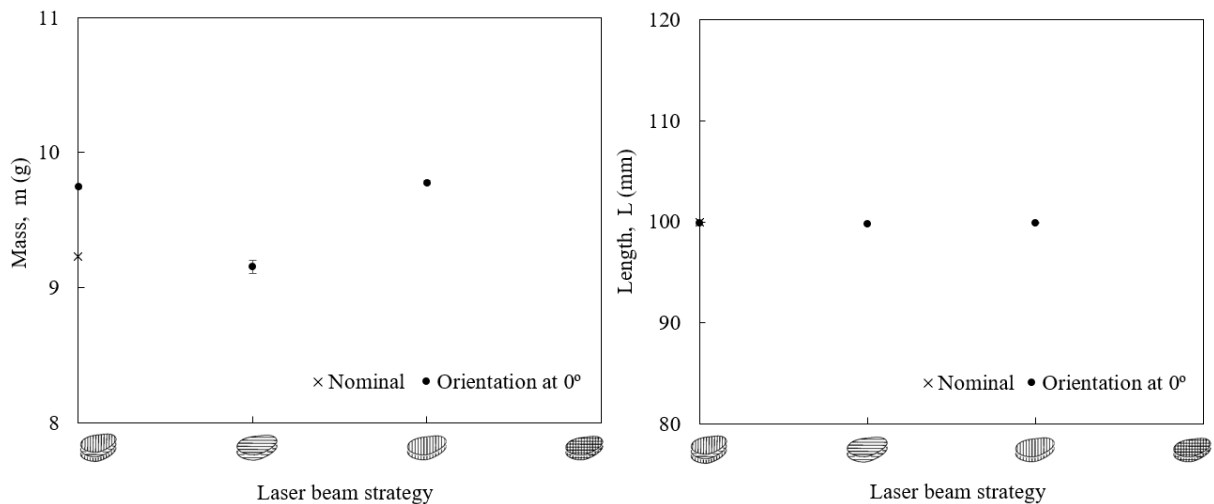


Figure 3.29 Mass (left) and length (right) of test specimens produced by SLS depending on the laser strategy (0.318 J/mm^3).

Chapter 3. Optimization of SLS process parameters

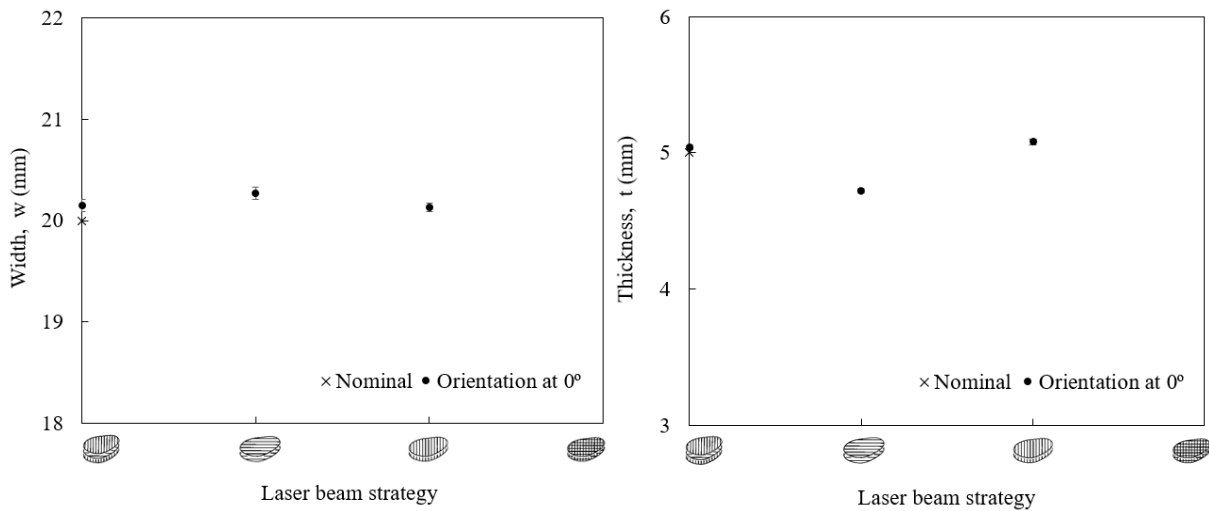


Figure 3.30 Width (left) and thickness (right) of test specimens produced by SLS depending on the laser strategy (0.318 J/mm³).

3.4.1.3. Dimensional and geometric accuracy

The evaluation of the dimensional and geometric accuracy of test artefacts produced by SLS encompassed the qualitative analysis of the CT images combined with the basic principles of Geometric Dimensioning and Tolerancing (GD&T) measurements. Three types of tolerancing were considered for analysis, including i) form of single features (*e.g.*, flatness, straightness, roundness, cylindricity), ii) orientation of features in relation to others using datum reference frames (*e.g.*, perpendicularity, parallelism), and iii) location of features in relation to axes or centre lines (*e.g.*, position, concentricity) (Puncochar, 1997).

Focusing on the primary qualitative analysis, Figure 3.31 and Figure 3.32 in detail evidences CT images of the surface of the test artefacts produced with the lowest (*i.e.*, 0.158 J/mm³) and highest (*i.e.*, 0.318 J/mm³) values of energy considered for dimensional and geometric evaluation.

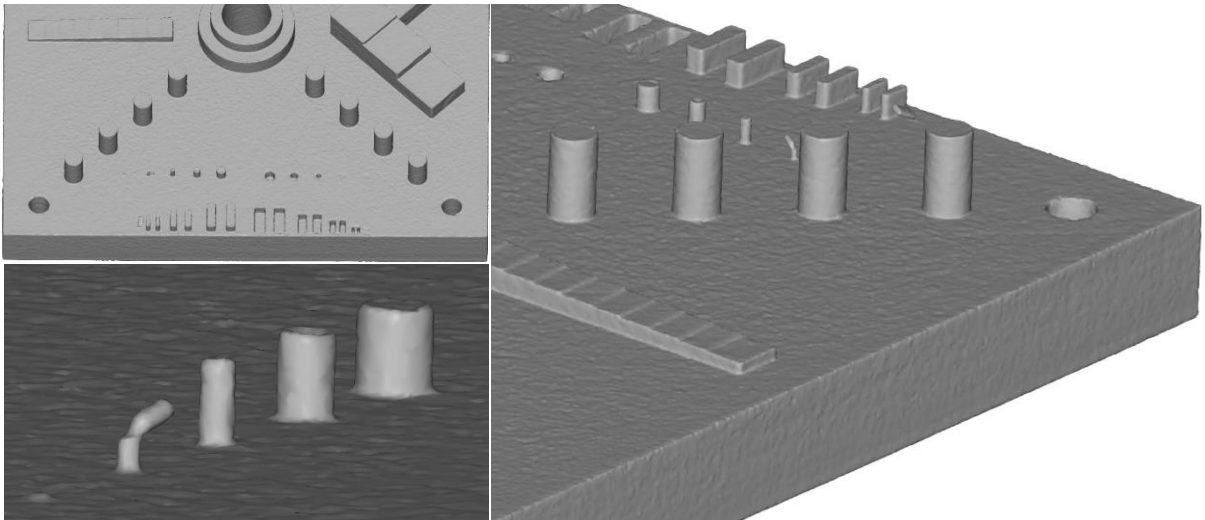


Figure 3.31 Geometric characteristics of a test artefact produced by SLS with 0.158 J/mm^3 .

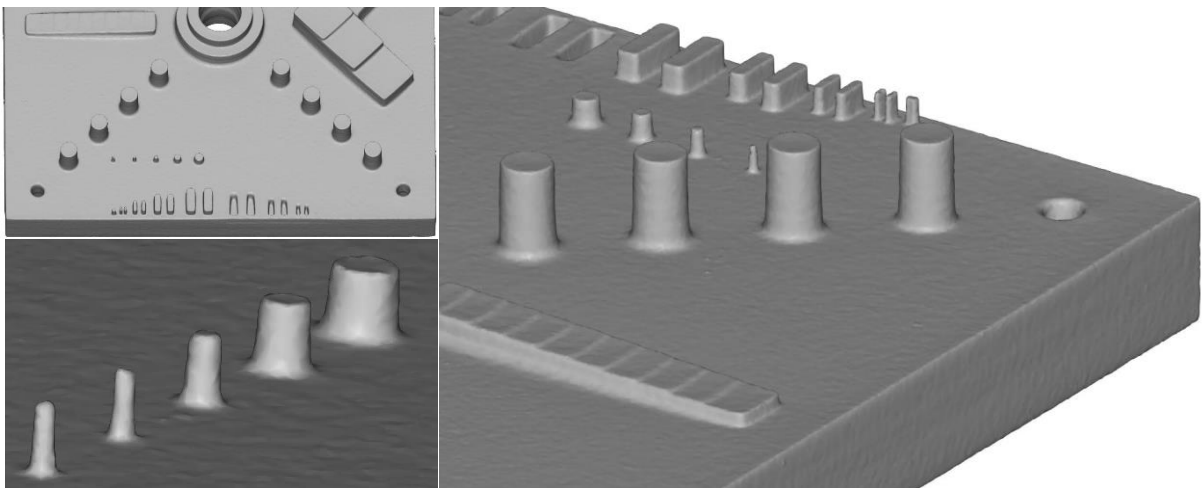


Figure 3.32 Geometric characteristics of a test artefact produced by SLS with 0.318 J/mm^3 .

In accordance with the observations reported in *section 3.4.1.1*, the results proved that the EDv value of 0.158 J/mm^3 ensures the production of SLS parts with quality holes, high surface roughness and brittle pins (Figure 3.31). However, the CT images of the test artefacts produced with medium EDv values showed that this trend is reversed when the energy provided during the sintering process increases. Therefore, in contrast, the test artefact produced with 0.318 J/mm^3 exhibited smooth surfaces and high-quality pins (Figure 3.32). Nevertheless, Figure 3.33 proves that high EDv values are not desired to produce SLS parts with small holes and straight edges.

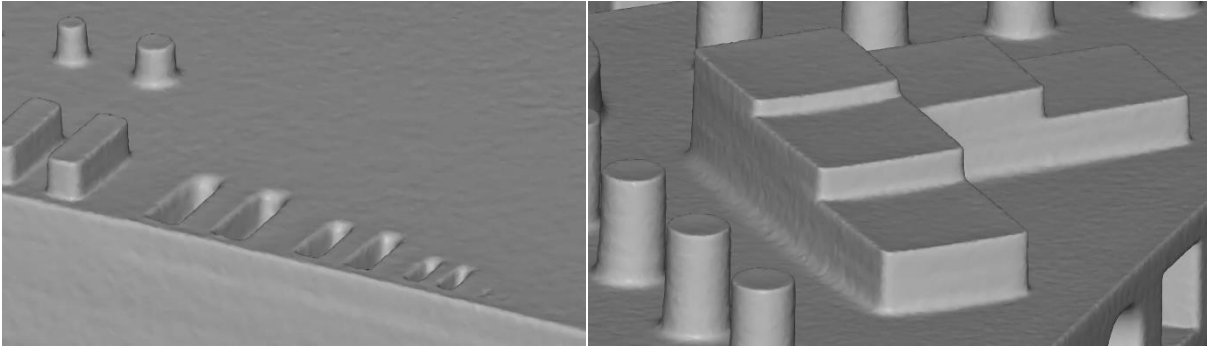


Figure 3.33 Geometric details of a test artefact produced by SLS with 0.318 J/mm^3 .

These characteristics had a direct influence on the GD&T results collected in each experiment, as well as on the standard deviation of the measurements, depending on the quality of surfaces and features. As it plays a crucial role in the repeatability of successive measurements, the following dimensional and geometric analysis provides useful insights to assess the ability of the laser-sintering system to accomplish design requirements in terms of tolerancing⁴.

Figure 3.34 shows the flatness of the horizontal top plane of test artefacts produced by SLS depending on ED_v.

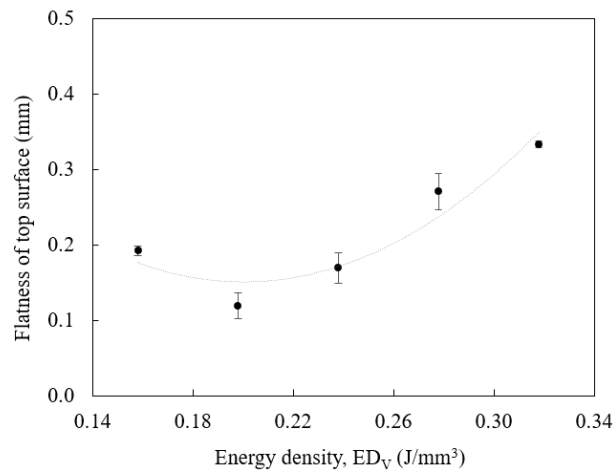


Figure 3.34 Flatness of the top surface of test artefacts produced by SLS depending on ED_v (XY-A strategy).

The results of the primary datum feature indicated that low ED_v values are advantageous to produce flat surfaces. Until 0.238 J/mm^3 , the test artefacts presented a flatness between 0.10 mm and 0.20 mm on average. In contrast, and as a consequence of the increase of these values with ED_v, the test artefact produced with the highest level of energy, *i.e.*, 0.318 J/mm^3 , exhibited a flatness above 0.30 mm. In addition to the high heat conduction that empowers the sintering of the surrounding powder particles to the top surface of the test artefact, this result is evidence of the warpage characteristics coming from the residual stress of the sintering process conducted under high ED_v values (see Figure 3.24).

⁴ The NIST test artefact itself does not include a tolerance (Moylan *et al.*, 2014).

The roundness of central and lateral holes of test artefacts produced by SLS as a function of ED_v is illustrated in Figure 3.35.

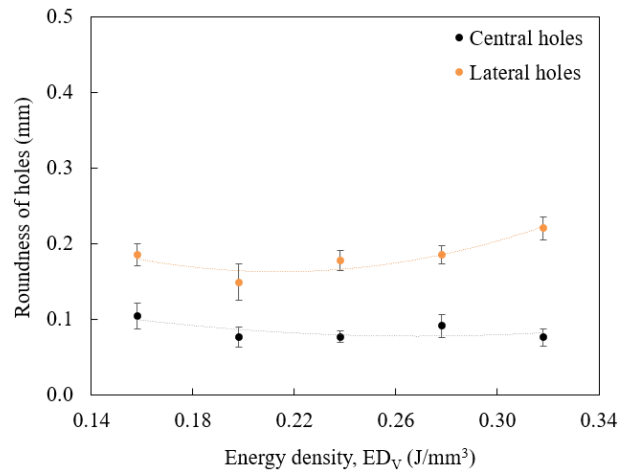


Figure 3.35 Roundness of central and lateral holes of test artefacts produced by SLS depending on ED_v (XY-A strategy).

Regardless of the experiment, the results proved that the tested laser-sintering system has greater ability to produce round holes in top surfaces than in the lateral ones. In this regard, it was verified a difference of 0.10 mm, considering an average roundness of 0.10 mm in central holes and 0.20 mm in lateral holes. Although the slight tendency of the roundness of the lateral holes to increase with the level of energy, this specific deviation of form did not exhibit a significant variation with ED_v.

The perpendicularity of holes with the top surface and the concentricity of inner cylinders of the test artefacts were also not critical sensitive to the variation of ED_v, displaying values below 0.10 mm in all experiments (Figure 3.36 (left and right, respectively)).

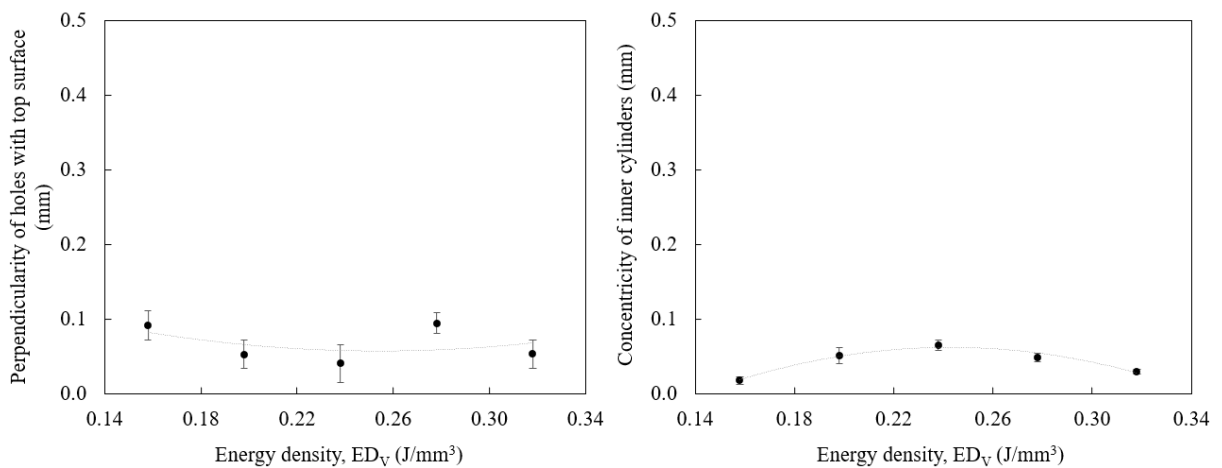


Figure 3.36 Perpendicularity of holes with top surface (left) and concentricity of inner cylinders (right) of test artefacts produced by SLS depending on ED_v (XY-A strategy).

In turn, the straightness of the primary surface showed to be highly affected by the ED_v value (Figure 3.37). In fact, the straightness of the test artefacts produced with low to medium levels of energy reached

Chapter 3. Optimization of SLS process parameters

similar values (*i.e.*, 0.18 mm on average). However, a rising trend was verified in test artefacts produced with high levels of energy. In this regard, a maximum straightness value of 0.30 mm was recorded in the test artefact produced with 0.318 J/mm³. This result is in accordance with the geometric observations reported in Figure 3.33, as a consequence of the enhanced heat conduction provided by high EDv values.

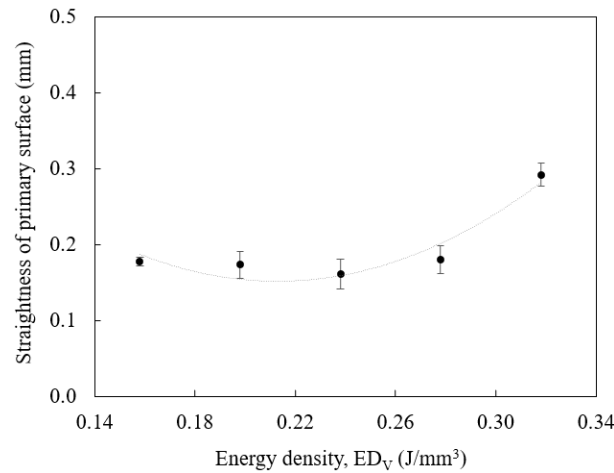


Figure 3.37 Straightness of the primary surface of test artefacts produced by SLS depending on EDv (XY-A strategy).

In fact, the sintering of surrounding powder particles due to the heat concentrations allowed by high levels of energy has proven to be a critical factor influencing the dimensional and geometric accuracy of SLS parts. In this way, the parallelism of opposite surfaces was the GD&T function most influenced by the EDv value (Figure 3.38).

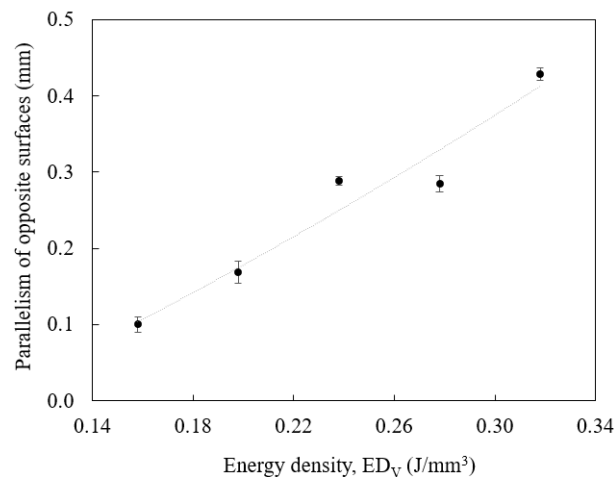


Figure 3.38 Parallelism of opposite surfaces of test artefacts produced by SLS depending on EDv (XY-A strategy).

The results indicated that low EDv values are advantageous to produce parallel surfaces. In 0.16 J/mm³, the parallelism of opposite surfaces increased more than 4 times, from 0.10 mm in the test artefact produced with 0.158 J/mm³ to above 0.40 mm in the test artefact produced with 0.318 J/mm³. It is coherent with the variation of straightness as a function of EDv (Figure 3.37).

The tolerancing of location is evaluated in the following figures. Pins with 4.00 mm of nominal diameter positioned from -50.00 mm to 50.00 mm along the x and y axes and staircases positioned from -7.00 mm to 7.00 mm along the z-axis in relation to the centre of the test artefact were considered for this analysis. In general, the measurements revealed that the linear displacement deviation tends to be higher when the distance between the centre of the feature increases in relation to the centre of the part, in particular for the x and y positions. In addition, it was verified that the deviations of features are mostly directed towards the centre of the part due to the shrinkage effects induced by the SLS process. Because of that, the positive direction of deviation in positioning in x, y and z axes as illustrated in Figure 3.39 was adopted to represent the data.

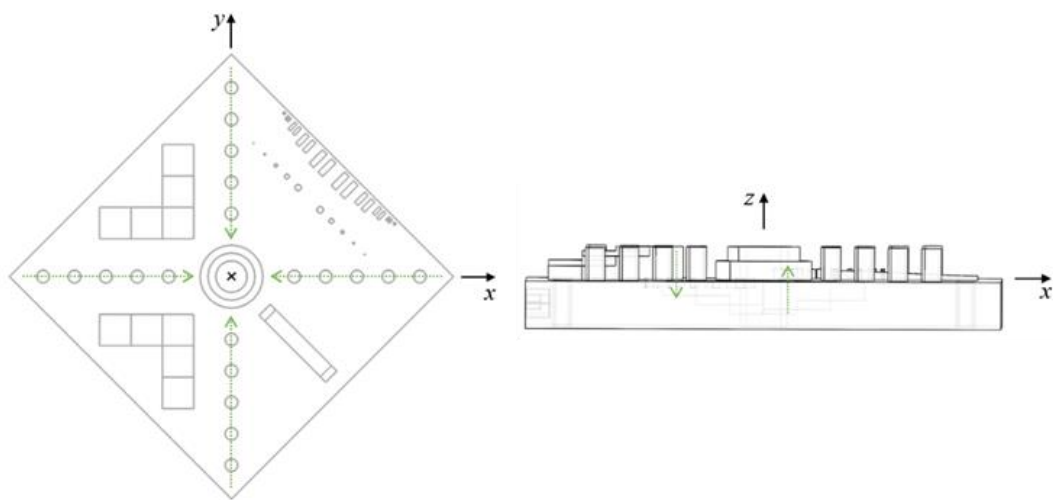


Figure 3.39 Representation of the positive direction of deviation in positioning (x, y and z axes).

The average deviations of negative and positive x and y positions of test artefacts produced by SLS depending on ED_v are respectively plotted in Figure 3.40 and Figure 3.41.

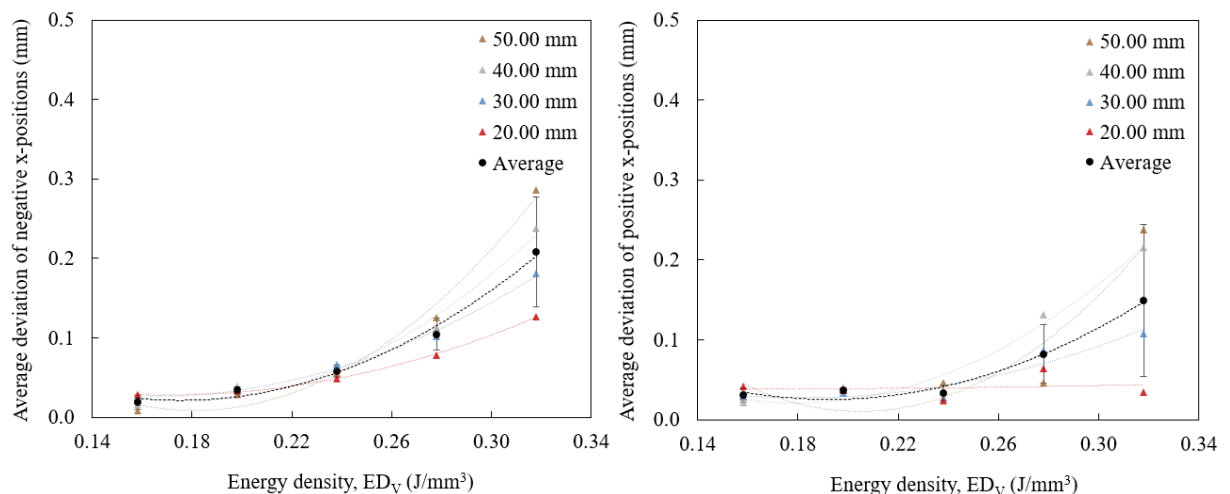


Figure 3.40 Average deviations of negative (left) and positive (right) x-positions of pins in test artefacts produced by SLS depending on ED_v (XY-A strategy).

Chapter 3. Optimization of SLS process parameters

As aforementioned, the linear displacement deviation of negative and positive x-positions was higher in features positioned at -50.00 mm and 50.00 mm and lower in features positioned at -20.00 mm and 20.00 mm, respectively (Figure 3.40). Although the linear displacement deviation of pins spaced 30.00 mm apart was not significant in test artefacts produced with low ED_v values, in test artefacts produced with medium-high ED_v values (*e.g.*, 0.318 J/mm³) the linear displacement deviation reached a difference of 0.16 mm and 0.20 mm between those negative and positive x-positions, respectively. Despite that, the average values revealed that the linear displacement deviation of negative x-positions increased from 0.01 mm in the test artefact produced with 0.158 J/mm³ to an average of 0.19 mm in the test artefact produced with 0.318 J/mm³, while the linear displacement deviation of the positive x-positions increased from 0.01 mm in the test artefact produced with 0.158 J/mm³ to an average of 0.13 mm in the test artefact produced with 0.318 J/mm³. This suggests that SLS parts should preferably be produced with ED_v values equal to or less than 0.238 J/mm³ to ensure a maximum deviation of ± 0.10 mm in x-positions.

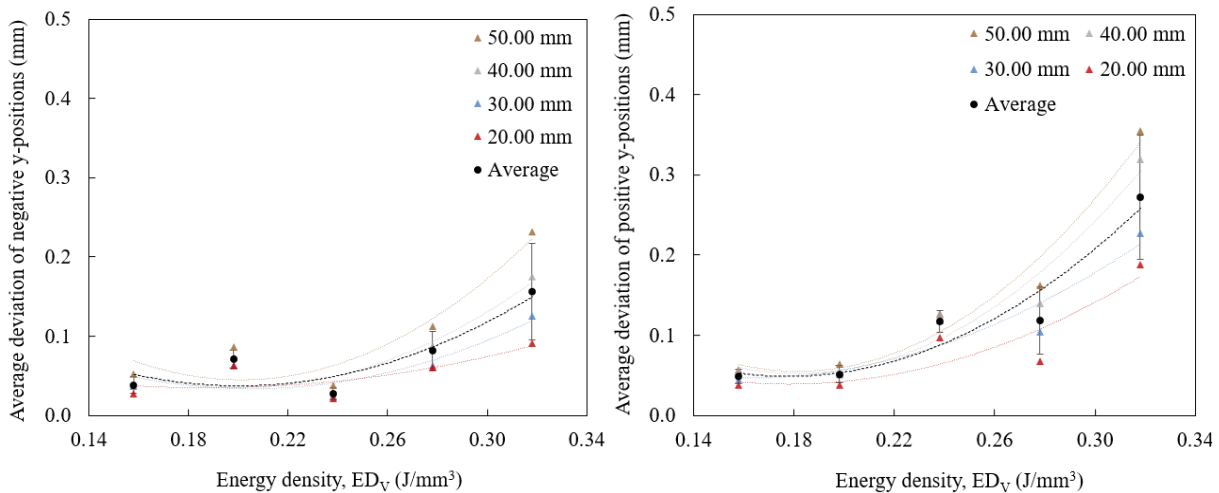


Figure 3.41 Average deviations of negative (left) and positive (right) y-positions of pins in test artefacts produced by SLS depending on ED_v (XY-A strategy).

As observed for the x-axis, the analysis of the y-positions also revealed that the linear displacement deviation depends on the position of the pins, especially in test artefacts produced with medium-high levels of energy (Figure 3.41). For instance, the test artefact produced with 0.318 J/mm³ recorded a difference of deviations of 0.14 mm between pins positioned at -50.00 mm and -20.00 mm and 0.17 mm between pins positioned at 50.00 mm and 20.00 mm. In turn, the average trendline showed that the linear displacement deviation of the negative y-positions increased from 0.02 mm in the test artefact produced with 0.158 J/mm³ to an average of 0.14 mm in the test artefact produced with 0.318 J/mm³, while the linear displacement deviation of the positive y-positions increased from 0.05 mm in the test

artefact produced with 0.158 J/mm^3 to an average of 0.27 mm in the test artefact produced with 0.318 J/mm^3 . This means that a maximum ED_v value of 0.198 J/mm^3 is suitable to produce SLS parts with a deviation in y-positions below $\pm 0.10 \text{ mm}$.

The unbalanced values of deviation obtained between negative and positive positions in both x and y axes may be explained by the asymmetric disposition of features in the top surface of the test artefact that causes a slight thermal gradient in the region of the pins depending on the time that the laser beam acts on each quadrant of the test artefact.

This analysis allowed defining a factor of deviation (in %) for negative and positive x and y pins, regardless of their nominal coordinates, that can be applied in parts produced by SLS depending on ED_v (Figure 3.42).

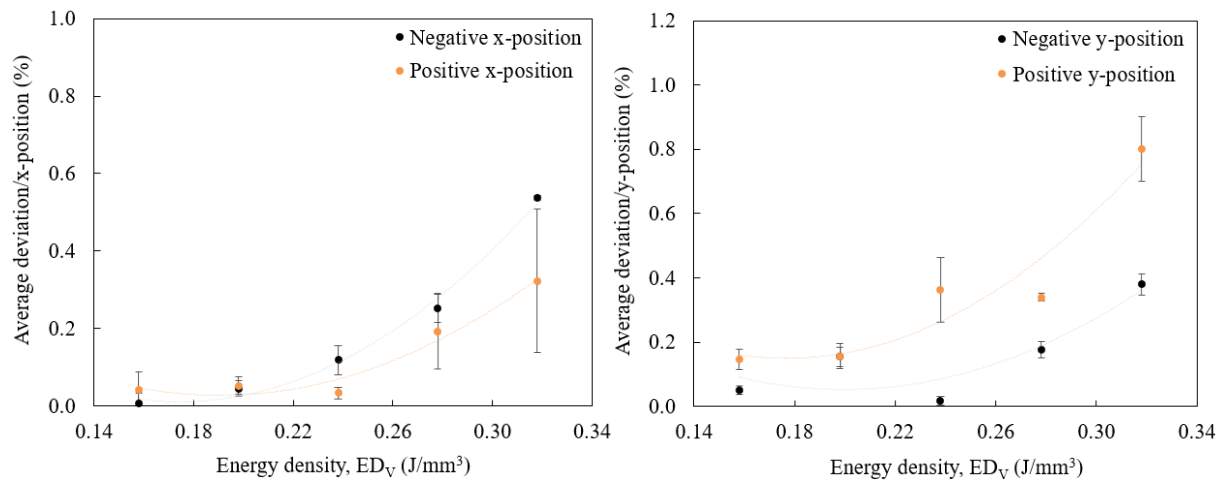


Figure 3.42 Factor of deviation (in %) for x (left) and y (right) positions of pins in parts produced by SLS depending on ED_v (XY-A strategy).

The average deviations of negative and positive z-positions of test artefacts produced by SLS depending on ED_v are plotted in Figure 3.43.

Chapter 3. Optimization of SLS process parameters

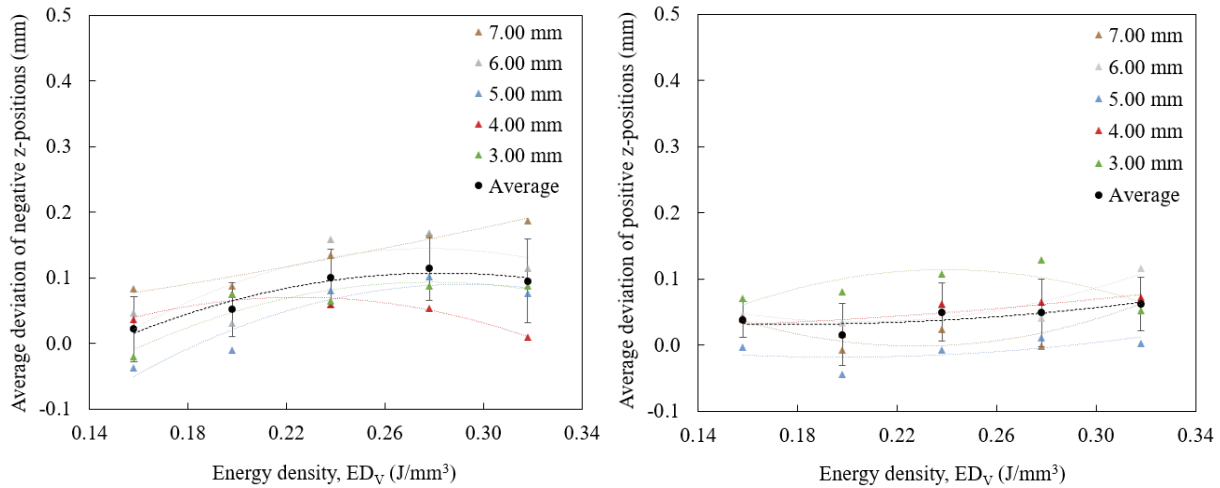


Figure 3.43 Average deviations of negative (left) and positive (right) z-positions of staircases in test artefacts produced by SLS depending on EDv (XY-A strategy).

As opposed to the x and y axes, the analysis of the z-axis did not demonstrate a direct dependence on the linear displacement deviation with the positions of the negative and positive staircases. The average linear displacement deviation of the negative z-positions increased with EDv from 0.02 mm in the test artefact produced with 0.158 J/mm³ to a maximum average of 0.12 mm in the test artefact produced with 0.278 J/mm³. This means that negative staircases of parts produced by SLS with medium-high values of energy are prone to present 0.10 mm lower depth (on average). In turn, the linear displacement deviation of the positive z-positions was lower, achieving a maximum of 0.06 mm in the test artefact produced with 0.318 J/mm³. In other words, the positive staircases of parts produced by SLS with medium-high values of energy are prone to present 0.05 mm lower height (on average).

Figure 3.44 reports the average diameter of pins of test artefacts produced by SLS depending on EDv for the nominal values of 2.00 mm, 1.50 mm, 1.00 mm, 0.50 mm and 0.25 mm.

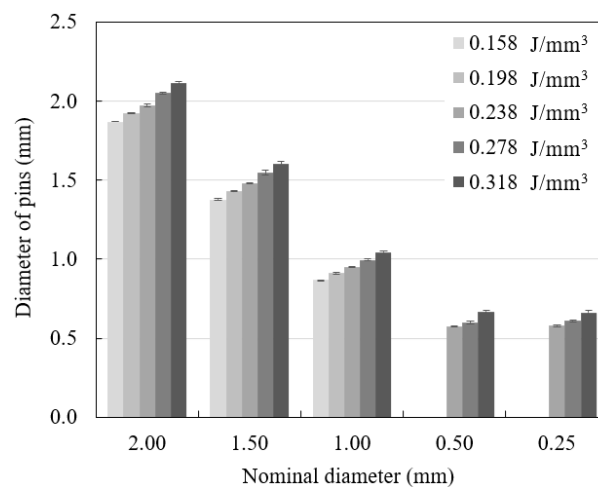


Figure 3.44 Diameter of pins of test artefacts produced by SLS depending on EDv (XY-A strategy).

The results proved that all EDv values considered for dimensional and geometric evaluation, ranging from 0.158 J/mm³ to 0.318 J/mm³, can produce pins until a minimum of 1.00 mm of nominal diameter. Pins with 0.50 mm and 0.25 mm of nominal diameter were not produced with low EDv values (*i.e.*, 0.158 J/mm³ and 0.198 J/mm³). Despite the capability of the laser-sintering system to produce fine pins, it is important to evaluate the dimensional accuracy attained in each condition. In this regard, the results showed that the average diameter of pins gradually increases with EDv. Therefore, the test artefact produced with 0.158 J/mm³ exhibited the highest deviation to a minimum value until 0.13 mm below the nominal, while the test artefact produced with 0.318 J/mm³ exhibited the highest deviation to a maximum value until 0.17 mm above the nominal. A medium EDv of 0.238 J/mm³ showed to be the most suitable value to produce pins meeting nominal specifications. Regardless of the experiment, it was proved that the minimum pin size achievable is 0.50 mm since pins with a nominal diameter of 0.25 mm were produced with an average diameter close to 0.50 mm in all conditions.

Opposite trends were verified for holes with nominal diameters of 2.00 mm, 1.50 mm, 1.00 mm, 0.50 mm and 0.25 mm of test specimens produced by SLS depending on EDv (Figure 3.45).

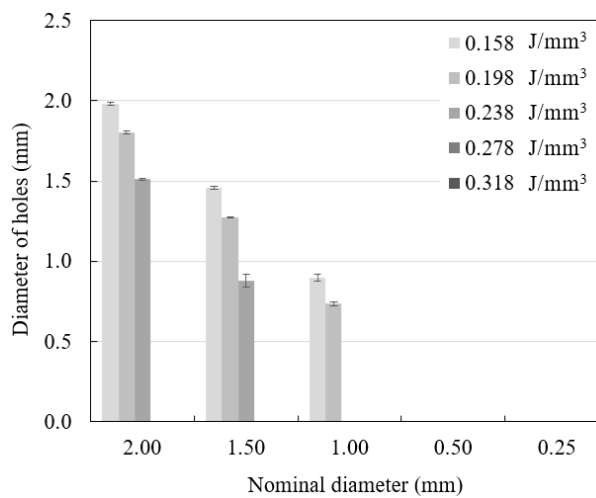


Figure 3.45 Diameter of holes of test artefacts produced by SLS depending on EDv (XY-A strategy).

As discussed before, low values of energy are advantageous to produce fine holes. In accordance, only test artefacts produced with EDv values below 0.238 J/mm³ exhibited fine holes on their top surfaces. In this way, EDv values above 0.238 J/mm³ were not able to produce fine holes with a nominal diameter equal to or less than 2.00 mm. Despite that, the results proved that the average diameter of holes gradually decreases with EDv. For instance, the EDv of 0.238 J/mm³ was only able to produce holes until a nominal diameter of 1.50 mm, with a maximum deviation of 0.62 mm below the nominal. In turn, EDv values of 0.198 J/mm³ and 0.158 J/mm³ were able to produce holes until a nominal diameter of 1.00 mm. However, the test artefact produced with 0.198 J/mm³ exhibited a deviation until 0.26 mm below

Chapter 3. Optimization of SLS process parameters

the nominal. The test artefact produced with 0.158 J/mm^3 ensured the greatest accuracy of holes until 1.50 mm , achieving a maximum deviation of 0.10 mm in holes with a nominal diameter of 1.00 mm .

Based on previous results, Figure 3.46 identifies the minimum diameter of features that ensures a maximum deviation of $\pm 0.10 \text{ mm}$ from the nominal value (left), as well as the minimum required separation between them (right) as a function of ED_v .

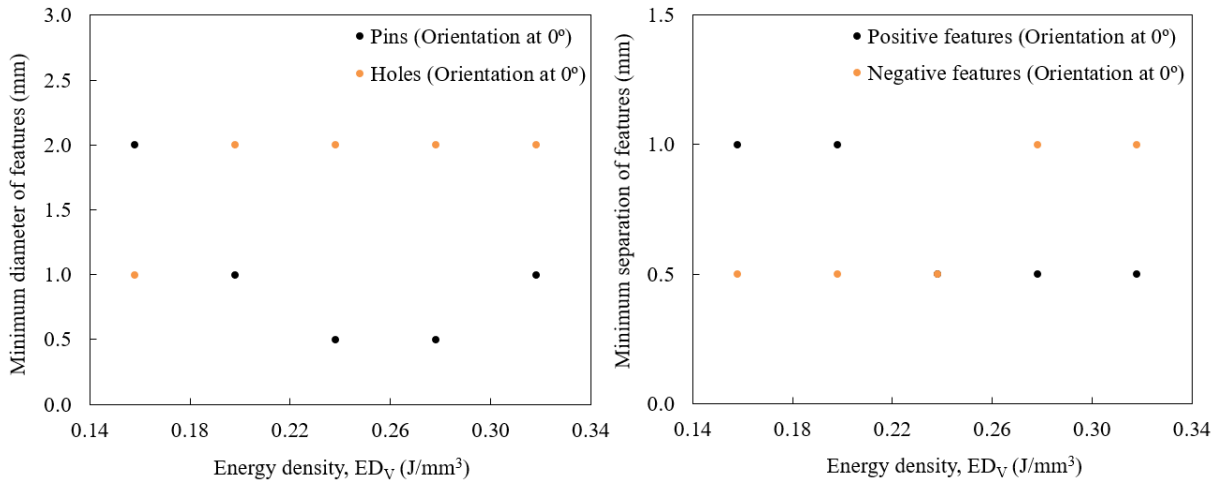


Figure 3.46 Minimum diameter (left) and minimum separation (right) of features of test artefacts produced by SLS depending on ED_v (XY-A strategy).

All aforementioned findings were corroborated with a surface comparison of the test artefacts produced with 0.158 J/mm^3 and 0.318 J/mm^3 (*i.e.*, extreme ED_v values considered for the GD&T analysis) with the corresponding CAD model (Figure 3.47). This comparative analysis revealed an overall decrease in the dimensional and geometric accuracy with ED_v since the test artefact produced with the highest level of energy exhibited greater colouring gradient with reddish marks in regions where secondary sintering occurred, and, consequently, where the deviations in relation to the nominal reached maximum values (*e.g.*, edges, holes, etc).

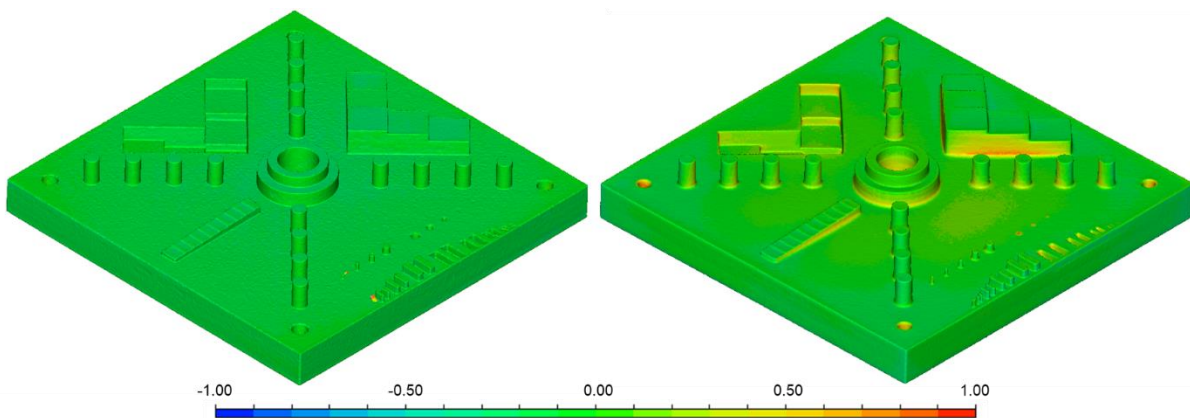


Figure 3.47 Surface comparison of test artefacts produced by SLS with 0.158 J/mm^3 (left) and 0.318 J/mm^3 (right) with the CAD model.

In turn, the dimensional and geometric evaluation of the test artefacts produced with 0.318 J/mm^3 using different laser beam strategies showed some differences in the quality of surfaces and edges, with particular effects on flatness (Figure 3.48), straightness (Figure 3.49) and parallelism (Figure 3.50).

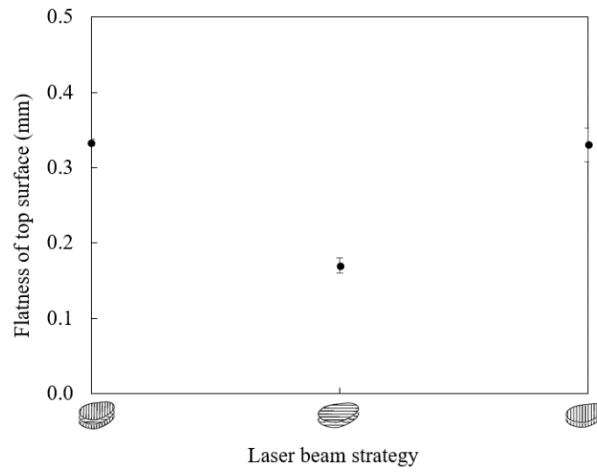


Figure 3.48 Flatness of the top surface of test artefacts produced by SLS depending on the laser strategy (0.318 J/mm^3).

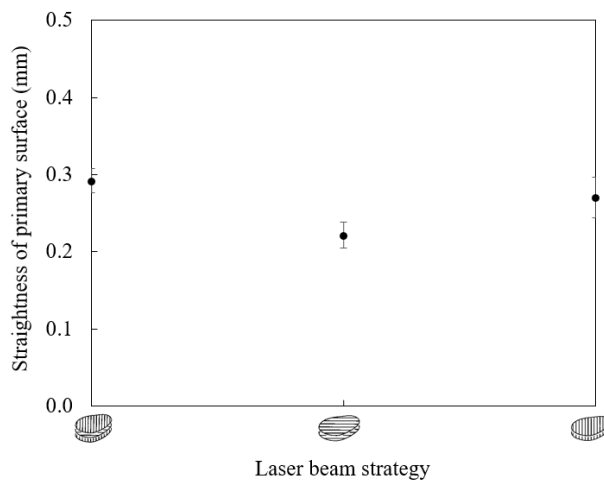


Figure 3.49 Straightness of the primary surface of test artefacts produced by SLS depending on the laser strategy (0.318 J/mm^3).

Chapter 3. Optimization of SLS process parameters

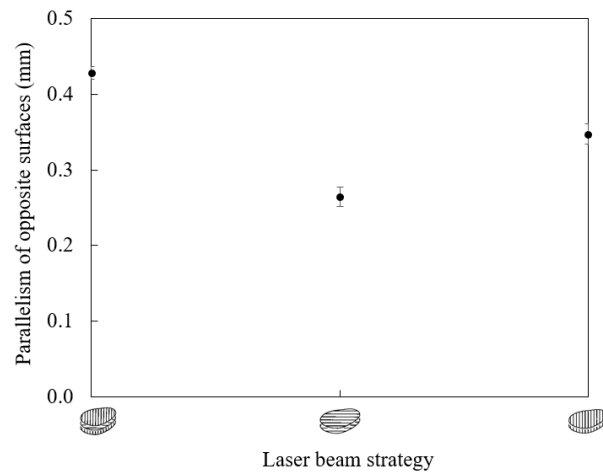


Figure 3.50 Parallelism of opposite surfaces of test artefacts produced by SLS depending on the laser strategy (0.318 J/mm^3).

In general, the results evidenced that the XY-A and Y strategies allow the production of SLS parts with similar dimensional and geometric characteristics. However, compared to these conditions of production, the analysis showed that the X strategy is more advantageous to produce SLS parts with greater quality by obtaining flat, straight and parallel surfaces. The qualitative evaluation of the CT images obtained in each condition did not evidence significant differences between test artefacts beyond these characteristics (Figure 3.51).

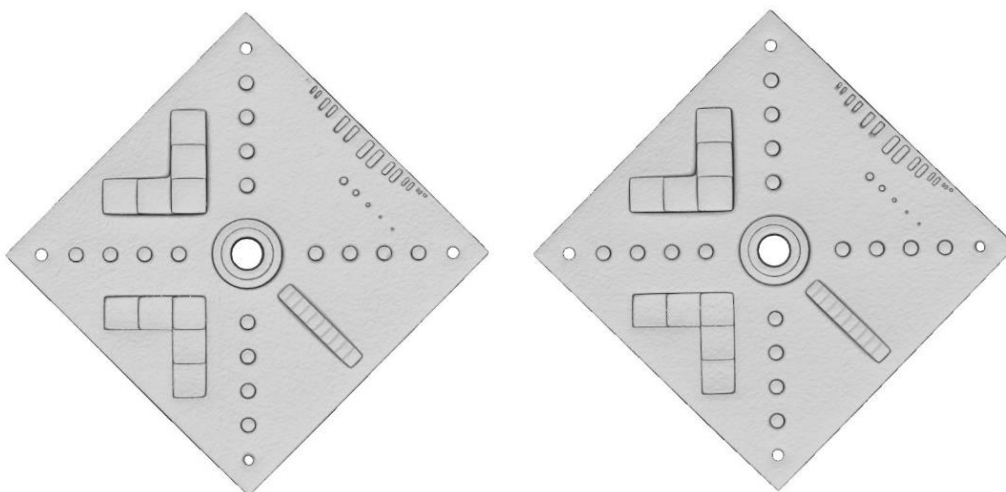


Figure 3.51 Test artefacts produced by SLS using the X (left) and Y (right) hatching strategies (0.318 J/mm^3).

Moreover, the strategy of the laser beam did not have influence on the manufacturing of fine holes. Regardless of the laser beam path, holes with nominal diameter equal to or less than 2.00 mm were not sintered in test artefacts produced with 0.318 J/mm^3 . On the other hand, all fine pins up to the nominal diameter of 0.25 mm were produced. Of all conditions, pins produced with the laser beam operating in the x-direction exhibited the smallest diameter with values closer to the nominal (Figure 3.52).

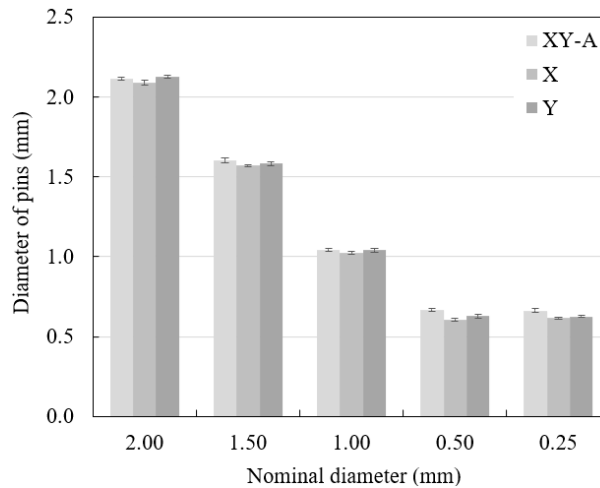


Figure 3.52 Diameter of pins of test artefacts produced by SLS depending on the laser strategy (0.318 J/mm³).

In summary, this analysis proved that medium-low values of energy are desired to ensure dimensional and geometric accuracy. In contrast, the heat concentrations created along the powder bed through high ED_v values promote the sintering of surrounding powder particles, reducing the global accuracy of the parts produced (Minetola *et al.*, 2020). According to these assumptions, the best outputs of concentricity of cylinders, straightness and parallelism of surfaces, average deviations in positioning and reproducibility and accuracy of fine holes were attained in the test artefact produced with 0.158 J/mm³; the best outputs of flatness of surfaces, roundness of holes and perpendicularity of holes with top surface were attained in the test artefact produced with 0.198 J/mm³; and the best outputs of reproducibility and accuracy of fine pins were attained in the test artefact produced with 0.238 J/mm³. For a fixed ED_v value, the strategy of the laser beam in the x-direction was preferable to improve the dimensional and geometric accuracy of features according to the basic principles of the GD&T measurements, despite the lower mass and thickness of the parts produced with this laser beam path.

3.4.1.4. Mechanical properties

Tensile properties

The tensile results of the test specimens produced in the initial experiments, from P1 to P5, showed a slight variation of the elastic modulus and tensile strength to a maximum of 14% and 10%, respectively. It can be a result of the real conditions of sintering replicated in this research (*e.g.*, variable processing level of the 50% of material and different thermal and atmospheric environments of the productions days) and instrumental and/or operator errors. In addition, this variation was not significant when compared with the mechanical results obtained for test specimens produced with different ED_v values (*i.e.*, P6 to P11). Thus, in the scope of this research, it was considered that test specimens produced by SLS with

Chapter 3. Optimization of SLS process parameters

same ED_v values obtained with different combinations of parameters present similar mechanical performance.

Figure 3.53 shows representative engineering stress-strain curves of test specimens produced by SLS as a function of ED_v, with the laser beam operating with the XY-A strategy.

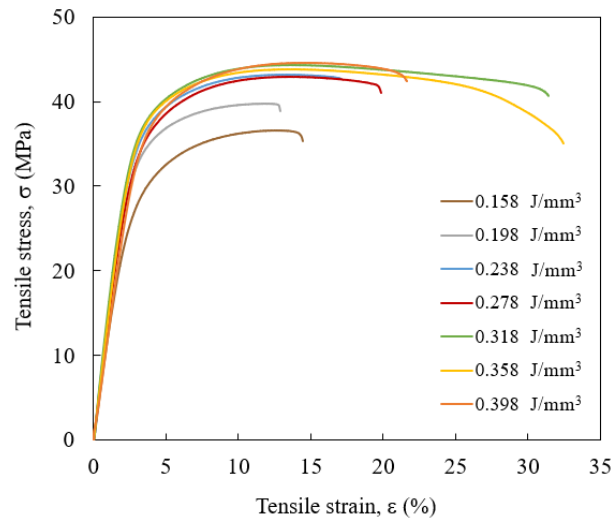


Figure 3.53 Engineering stress-strain curves of test specimens produced by SLS depending on ED_v (XY-A strategy).

This initial evaluation proved the significant influence of the hatching process parameters quantified by ED_v on the mechanical performance of SLS parts. Based on the corresponding engineering stress-strain curves, Figure 3.54 presents the variation of the elastic modulus of test specimens produced by SLS with ED_v.

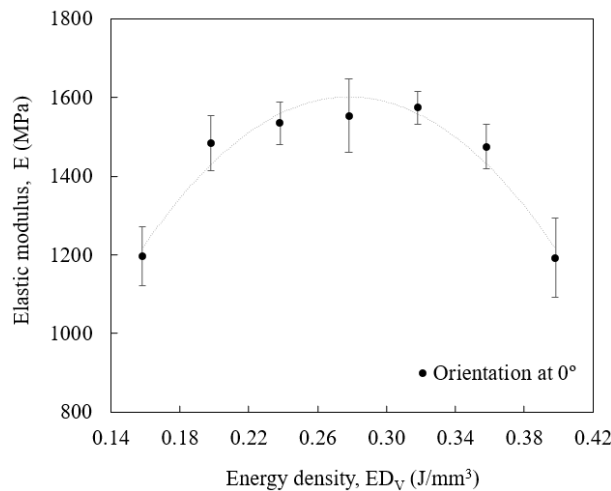


Figure 3.54 Elastic modulus of test specimens produced by SLS depending on ED_v (XY-A strategy).

As shown in Figure 3.54, the elastic modulus increased approximately 30% from an average of 1197.0 ± 74.2 MPa in test specimens produced with 0.158 J/mm³ to 1553.6 ± 93.3 MPa in test specimens produced with 0.278 J/mm³. After that inflection point, the elastic modulus evidenced a downward trend until 1192.7 ± 100.8 MPa in test specimens produced with 0.398 J/mm³. This means that a range of

EDv values between 0.258 J/mm³ and 0.318 J/mm³ is desired to obtain the greatest performance of SLS parts in respect of elastic modulus.

The tensile stress at yield exhibited an increasing trend with EDv, ranging from 22.1 ± 1.2 MPa in test specimens produced with 0.158 J/mm³ to 30.5 ± 1.3 MPa in test specimens produced with 0.398 J/mm³, recording a difference of 38% (Figure 3.55 (left)). The corresponding tensile strain at yield had a non-sensitive effect in test specimens produced with medium-low values of energy but exhibited a tendency to increase with high EDv values (Figure 3.55 (right)).

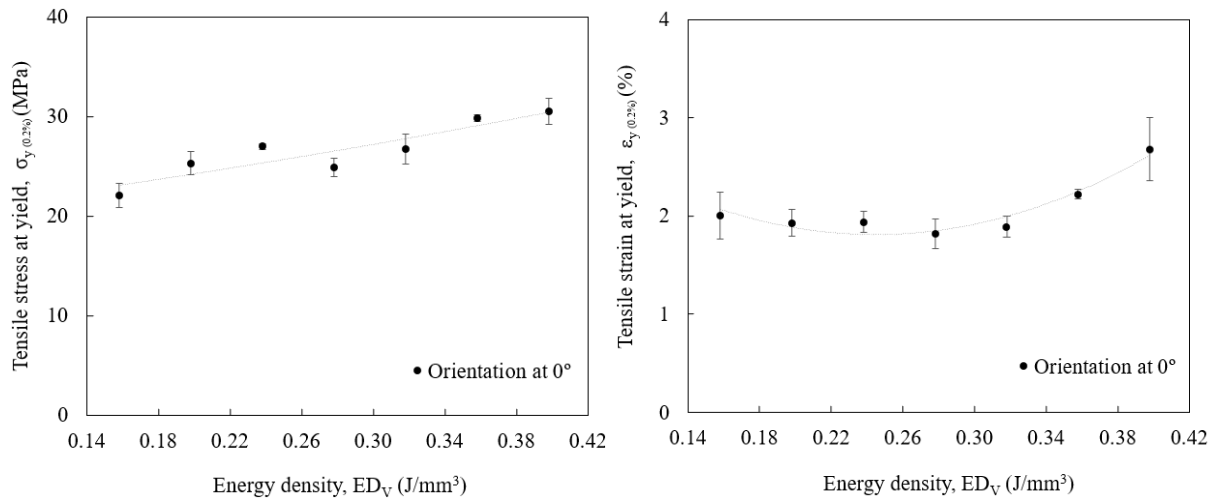


Figure 3.55 Tensile stress at yield (left) and tensile strain at yield (right) of test specimens produced by SLS depending on EDv (XY-A strategy).

The tensile stress at break did not exhibit a relevant trend with EDv (Figure 3.56 (left)). On the other hand, the tensile strain at break showed an increasing trend with the level of energy (Figure 3.56 (right)). The high tensile strain at break obtained in test specimens produced with high EDv values combined with the large plastic region evidenced in the corresponding stress-strain curves demonstrated that SLS parts become less brittle when EDv increases (Caulfield *et al.*, 2007).

Chapter 3. Optimization of SLS process parameters

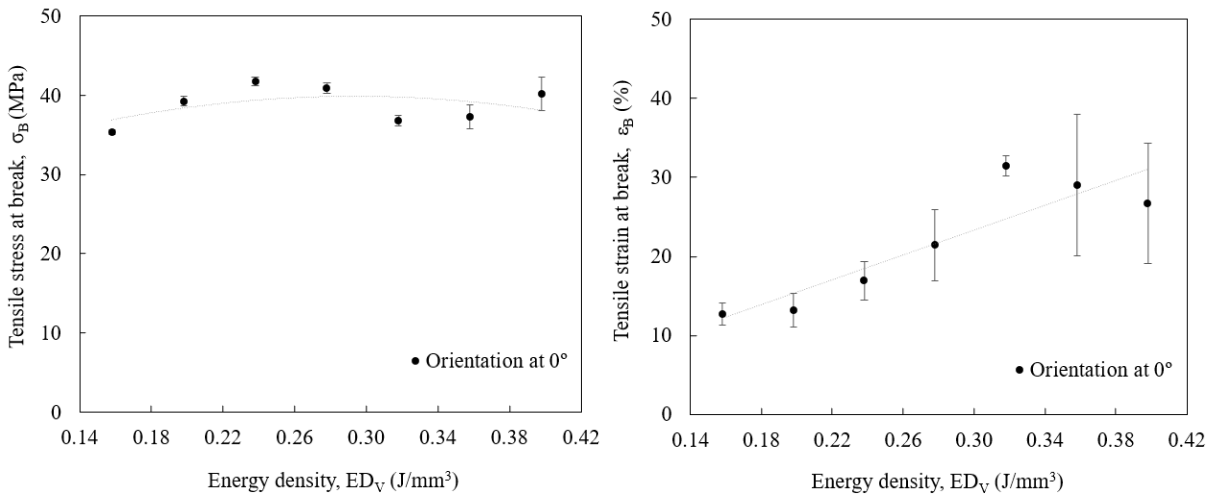


Figure 3.56 Tensile stress at break (left) and tensile strain at break (right) of test specimens produced by SLS depending on ED_V (XY-A strategy).

Furthermore, Figure 3.57 shows that the tensile strength (*i.e.*, the maximum tensile stress attained by the test specimens during the uniaxial mechanical load), increased with ED_V to a great extent from 0.158 J/mm^3 to 0.318 J/mm^3 , achieving a maximum variation of 22%. After that, an asymptotic value close to 44.0 MPa was reached with a variation of less than 1.0% between experiments. This output, as well as the results of tensile stress at yield, evidenced that medium-high levels of energy are desired to improve the mechanical strength of SLS parts above 20%.

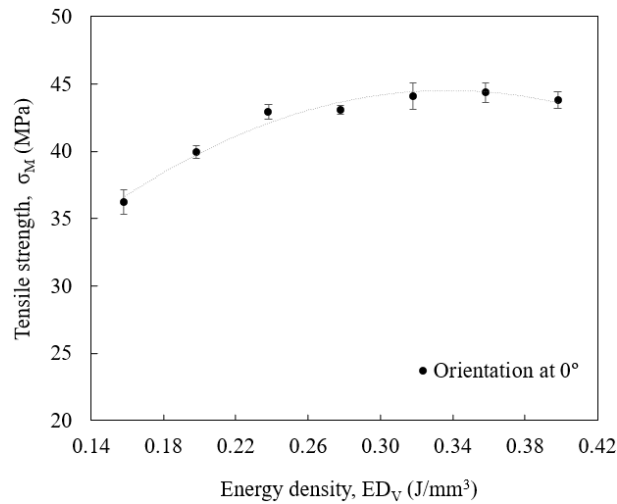


Figure 3.57 Tensile strength of test specimens produced by SLS depending on ED_V (XY-A strategy).

Figure 3.58 presents representative engineering stress-strain curves of test specimens produced with 0.318 J/mm^3 , using the XY-A, X, Y and XY-S strategies of the laser beam (*i.e.*, experiments P12 to P14).

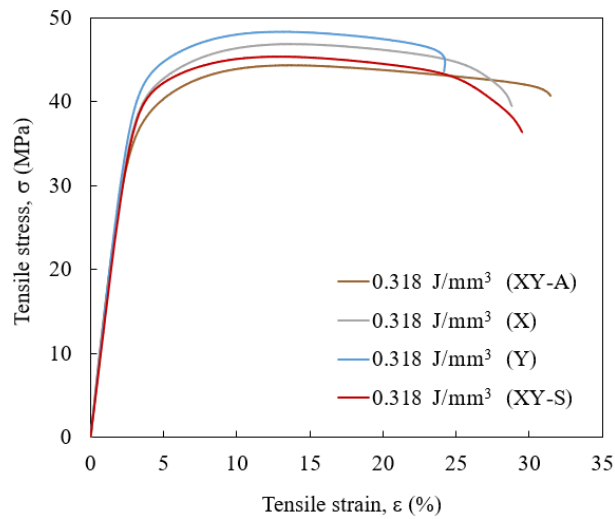


Figure 3.58 Engineering stress-strain curves of test specimens produced by SLS depending on the laser strategy (0.318 J/mm³).

In a first analysis and compared with Figure 3.53, the effect of the laser beam strategy seems to be less significant on the mechanical behaviour of SLS parts than the EDV value. The resulting elastic modulus, tensile stress at yield, tensile strain at yield, tensile stress at break, tensile strain at break and tensile strength of test specimens produced by SLS depending on the laser beam strategy are illustrated in Figure 3.59, Figure 3.60, Figure 3.61 and Figure 3.62, respectively.

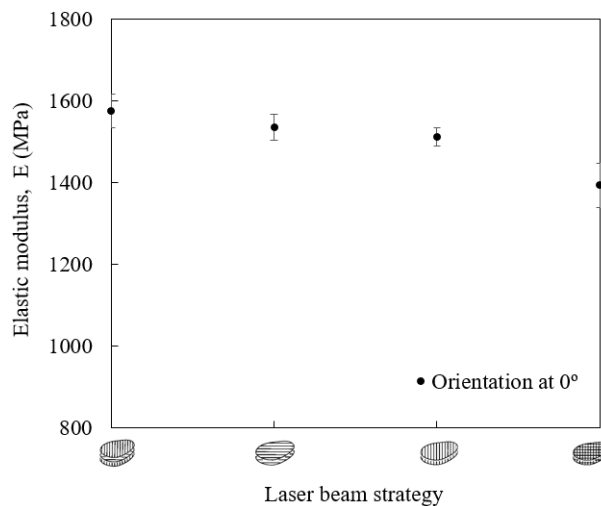


Figure 3.59 Elastic modulus of test specimens produced by SLS depending on the laser strategy (0.318 J/mm³).

Chapter 3. Optimization of SLS process parameters

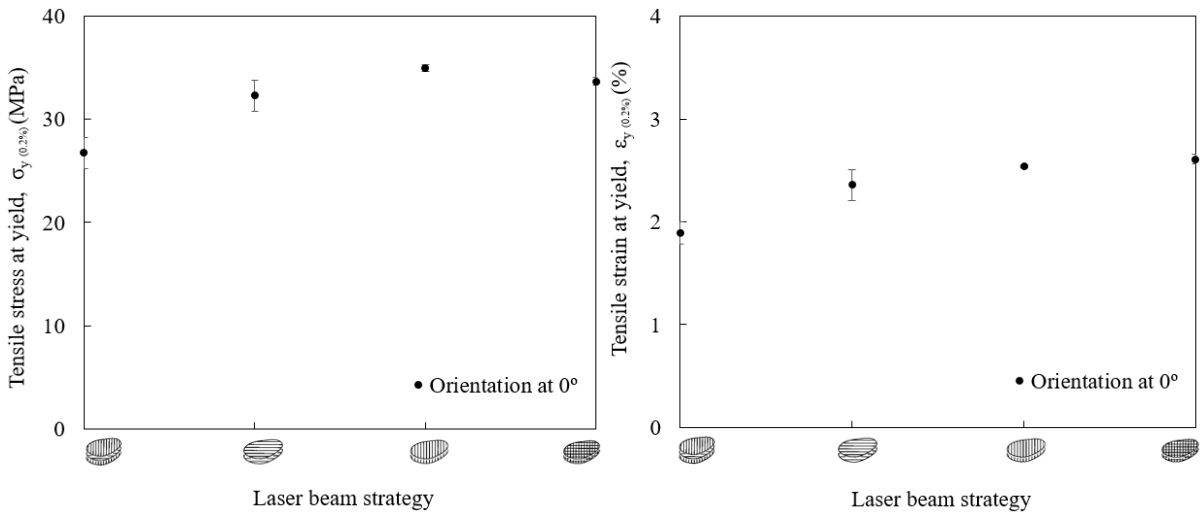


Figure 3.60 Tensile stress at yield (left) and tensile strain at yield (right) of test specimens produced by SLS depending on the laser strategy (0.318 J/mm³).

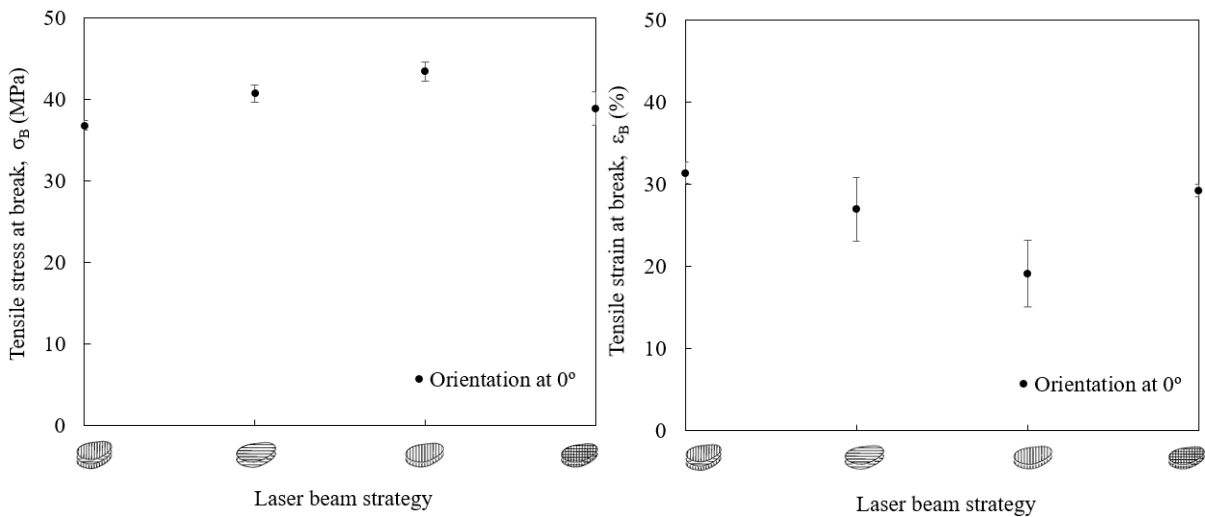


Figure 3.61 Tensile stress at break (left) and tensile strain at break (right) of test specimens produced by SLS depending on the laser strategy (0.318 J/mm³).

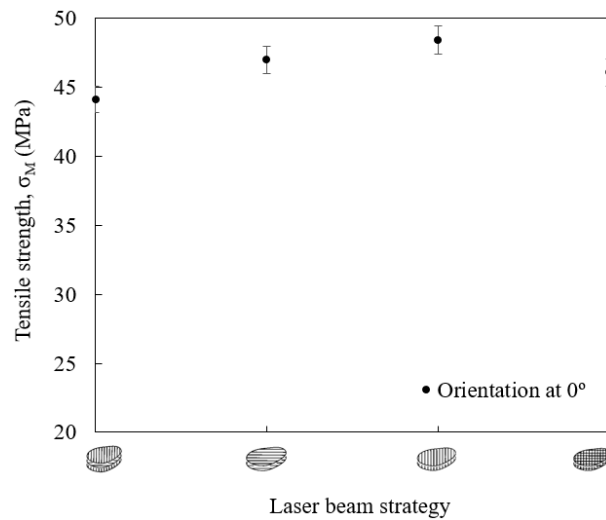


Figure 3.62 Tensile strength of test specimens produced by SLS depending on the laser strategy (0.318 J/mm³).

The results proved that the highest values of tensile stress at yield, tensile stress at break and tensile strength were obtained in test specimens produced with the laser beam operating in the y-direction. For instance, the tensile strength of test specimens produced with this strategy was 9.8% higher compared with the conventional XY-A (*i.e.*, from 44.1 ± 1.0 MPa to 48.4 ± 1.0 MPa). The difference in elastic modulus was lower, achieving 4.1% from 1511.6 ± 22.6 MPa in test specimens produced in the y-direction to 1573.9 ± 41.5 MPa in test specimens produced with the XY-A strategy. The test specimens produced in the x-direction also exhibited great mechanical performance; however, as discussed in *section 3.4.1.2*, parts produced by SLS with this laser beam path are not able to fulfil dimensional specifications with accuracy. The XY-S strategy also presented suitable mechanical behaviour; however, the sintering process proved to be unfeasible under these conditions (see *section 3.4.1.1*). Based on these criteria, the X and XY-S strategies of the laser beam were not considered for selection in terms of mechanical performance.

Fracture properties

The DCB tests conducted in experiments P1 to P5 showed that the test specimens produced with the same EDv value (*i.e.*, 0.278 J/mm^3) obtained with different combinations of parameters exhibit similar fracture toughness, with G_{Ic} values ranging from 25 N/mm to 30 N/mm. In turn, significant differences were observed in experiments P6 to P10 considering different levels of energy. Figure 3.63 shows experimental P - δ curves and corresponding R -curves by applying the CBBM of test specimens produced by SLS depending on EDv.

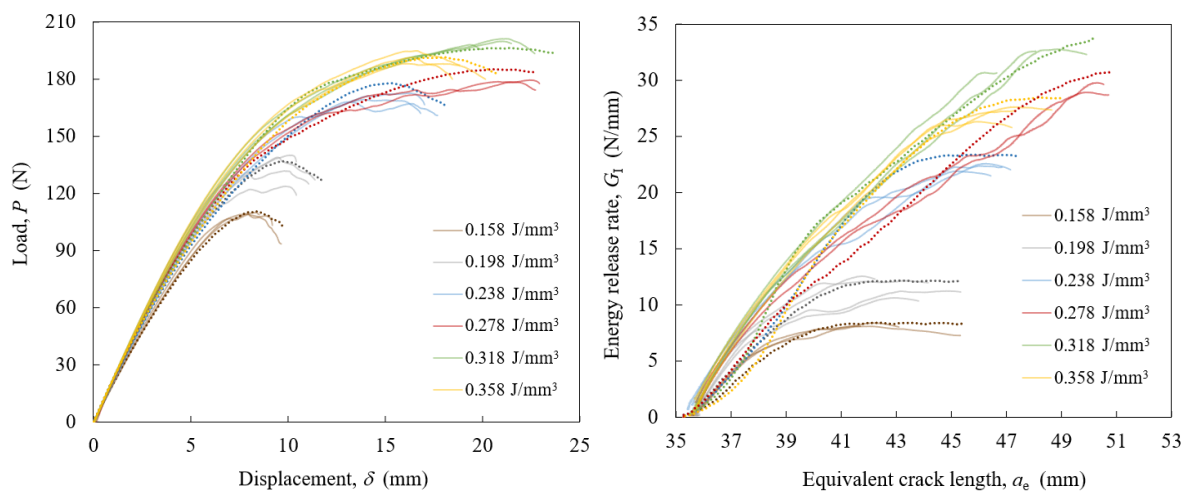


Figure 3.63 Experimental and numerical P - δ curves (left) and R -curves (right) of test specimens produced by SLS depending on EDv (XY-A strategy) (Dotted-line refers to numerical data).

The P - δ curves revealed that the initial elastic compliance of the test specimens gradually increased with EDv. This behaviour became more evident after the peak-point, where the load for same values of

Chapter 3. Optimization of SLS process parameters

displacement experienced a notorious rising trend with the level of energy, influencing the local cohesive strength under mode I loading. In the corresponding R -curves, it was possible to detect an initial growing trend of the energy release rate, which is due to the development of the fracture process zone that occurs before crack initiation. That growing trend typically occurred at higher rates in test specimens produced with high EDv values. After that, a pronounced plateau is presented, which is intrinsically related to the post-peak region of the P - δ curves, corresponding to the crack propagation.

The variation of G_{Ic} and G_{Iu} at the maximum load (G_{Iu}) depending on EDv is presented in Figure 3.64.

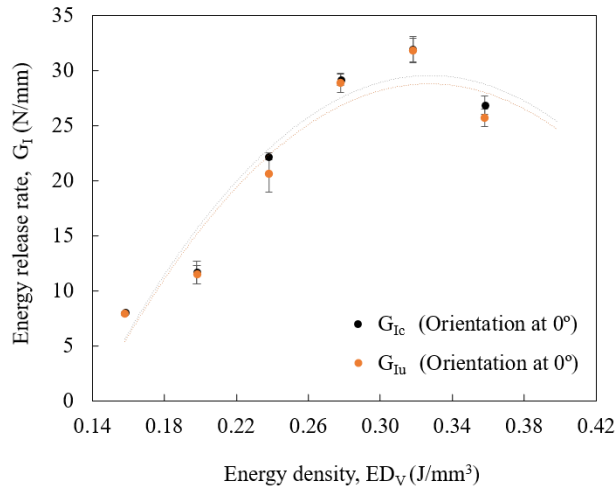


Figure 3.64 Mode I energy release rate of test specimens produced by SLS depending on EDv (XY-A strategy).

The fracture toughness of test specimens, quantified by G_{Ic} and G_{Iu} , was significantly affected by the EDv value. G_{Ic} increased from 8.1 ± 0.1 N/mm in test specimens produced with 0.158 J/mm³ to 32.0 ± 1.1 N/mm in test specimens produced with 0.318 J/mm³, recording a difference of 295% in 0.16 J/mm³. After the rising trend, an inflection point at 0.318 J/mm³ was verified with a downward trend until 26.9 ± 0.8 N/mm in test specimens produced with 0.358 J/mm³. Similar behaviour was observed for G_{Iu} . As both variables were significantly influenced by the hatching settings, a numerical analysis was performed in order to identify the corresponding cohesive parameters in pure mode I loading, considering a trapezoidal cohesive bilinear damage law (Figure 3.6). The numerical-experimental agreement of each condition is plotted in Figure 3.63 and the corresponding results are listed in Table 3.5.

Table 3.5 Numerical-experimental agreement of the DCB results.

EDv (J/mm ³)	E (MPa)	G _{Ic} (N/mm)	$\sigma_{2,I}$ (MPa)	$\delta_{2,I}$ (mm)	$\sigma_{3,I}$ (MPa)	$\delta_{3,I}$ (mm)
0.158	1516.70	8.10	12.00	0.25	9.00	0.35
0.198	1650.00	11.70	16.00	0.10	10.00	0.40
0.238	1616.70	22.20	15.00	0.05	11.00	0.40
0.278	1687.50	29.10	16.00	0.05	5.50	1.00

0.318	1700.00	32.00	14.00	0.60	4.50	1.60
0.358	1716.70	26.90	12.00	0.60	6.00	1.60

In addition, Figure 3.65 shows the evolution of the cohesive zone length (l_{CZ}), as a function of the equivalent crack length (a_e) for each level of energy, EDv, together with two numerical R -curves for extreme G_{Ic} values. This complementary analysis demonstrated that l_{CZ} increases in the initial stage of the loading process, revealing a critical size (l_{CZc}) in the final phase before total rupture. This behaviour is characteristic of the DCB test, and it is an essential condition to obtain accurate G_{Ic} values by ensuring self-similar crack propagation. Figure 3.65 also reveals that the variation of l_{CZc} with EDv is coherent with the trend obtained for G_{Ic} (Figure 3.64).

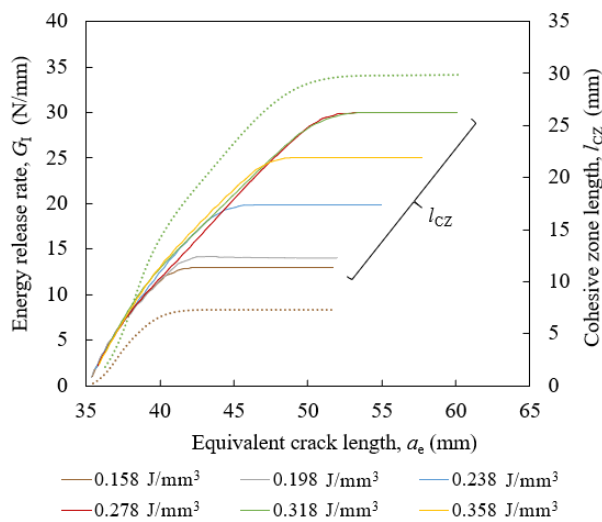


Figure 3.65 Evolution of l_{CZ} as a function of a_e of SLS test specimens depending on EDv (XY-A strategy) (Dotted-line refers to R -curves).

The experimental $P-\delta$ curves and corresponding R -curves of test specimens produced by SLS depending on the laser strategy are given in Figure 3.66.

Chapter 3. Optimization of SLS process parameters

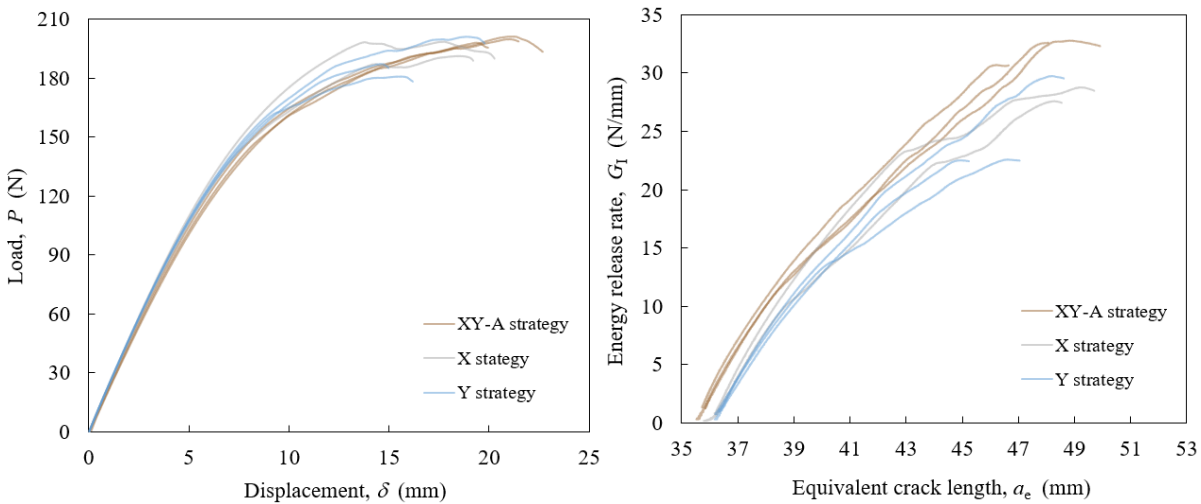


Figure 3.66 Experimental $P\delta$ curves (left) and R curves (right) of test specimens produced by SLS depending on the laser strategy (0.318 J/mm^3).

The $P\delta$ curves obtained from the test specimens produced in experiments P9, P12 to P13 revealed low variation in relation to the data shown in Figure 3.63. On the other hand, the corresponding R curves presented some dispersion of results. Despite that, the resulting G_{Ic} values are included within a narrow range of 25 N/mm to 32 N/mm , on average. Although the results were not conclusive, they suggested that the strategy of the laser beam does not have a significant influence on the fracture toughness as the EDv value. Because of that, these results were not complemented with numerical analysis.

In summary, the experimental results discussed in this section combined with the analytical solutions of the polynomial trend functions (by means of the first order derivative to identify the maximum values) revealed that the EDv value of 0.318 J/mm^3 allows the production of SLS parts with valuable mechanical properties, particularly if the laser operates in the y-direction. These findings were considered to establish the optimized hatching settings fixed in the following activities of the research (*e.g.*, evaluation of contour parameters).

3.4.1.5. Morphological properties

The evaluation of the microstructure of test specimens was crucial in this research to more clearly understand the macroscopic results presented and discussed in the previous sections. Therefore, the cross-section of test specimens was analysed at a microscopical level using an ultra-high-resolution microscope to be able to explain why their dimensional, geometric and mechanical properties are highly affected by the EDv value supplied for the hatching layers during the sintering process. In this regard, Figure 3.67 shows SEM micrographs of the cross-section of test specimens produced by SLS with a medium level of energy, *i.e.*, 0.278 J/mm^3 , using the XY-A strategy.

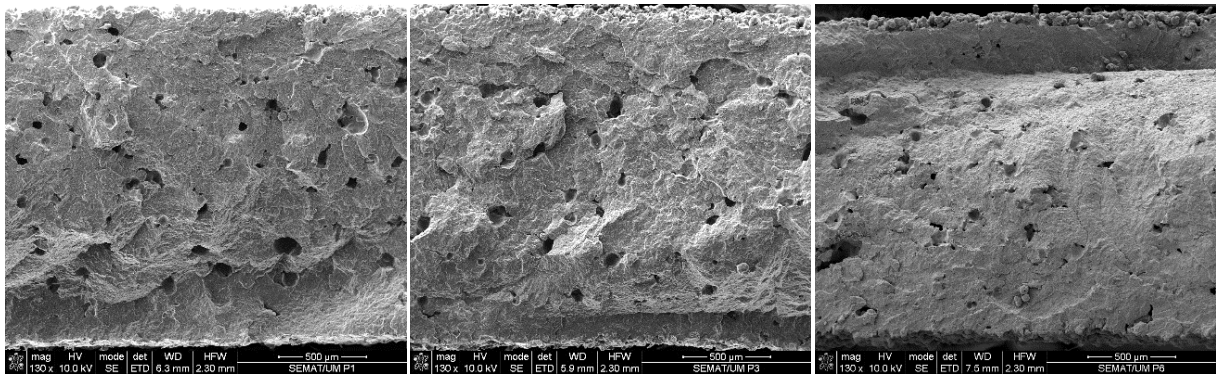


Figure 3.67 Cross-section of test specimens produced by SLS with medium level of energy (0.278 J/mm^3 , XY-A strategy).

The results did not reveal significant morphological differences in the cross-section of test specimens produced with same EDv values obtained with different combinations of parameters. All of them evidenced high content of porosity and fine crystalline structures (observed at high magnification levels), which is intrinsically related to the operating principle of powder bed fusion processes (Yao *et al.*, 2020). On the other hand, relevant morphological characteristics were observed in test specimens produced with different EDv values. Figure 3.68 illustrates the cross-section of test specimens produced with 0.158 J/mm^3 and 0.198 J/mm^3 .

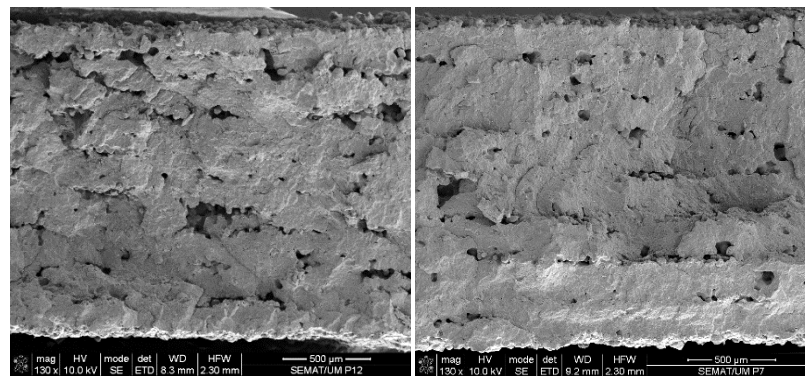


Figure 3.68 Cross-section of test specimens produced by SLS with low levels of energy (0.158 J/mm^3 (left) and 0.198 J/mm^3 (right), XY-A strategy).

The test specimens produced with low EDv values exhibited a cross-section with weakened connection between the layers of powder. This is a physical evidence that the energy supplied by the laser beam to the powder particles in these SLS processes was not sufficient for efficient coalescence and material consolidation (Caulfield *et al.*, 2007). The SEM micrographs revealed that under these processing conditions, the test specimens exhibit voids and gaps in the regions of interface between layers, evidencing the presence of unsintered powder particles. These defects combined with the distribution of pores along the cross-section of test specimens may be responsible for their macro-scale performance. In fact, this explains the lowest values of mass (*i.e.*, $8.777 \pm 0.025 \text{ g}$ and $9.266 \pm 0.010 \text{ g}$), tensile

Chapter 3. Optimization of SLS process parameters

strength (*i.e.*, 36.2 ± 0.9 MPa and 40.0 ± 0.5 MPa) and fracture toughness (*i.e.*, 8.1 ± 0.1 N/mm and 11.7 ± 1.1 N/mm) obtained in this research in test specimens produced with these low levels of energy. Despite the slight improvement of the morphological structure and overall properties from 0.158 J/mm³ to 0.198 J/mm³, the cross-section of the corresponding test specimens still presents poor microstructure with high content of porosity. In turn, Figure 3.69 presents the cross-section of test specimens produced under high levels of energy (*i.e.*, 0.358 J/mm³ and 0.398 J/mm³).

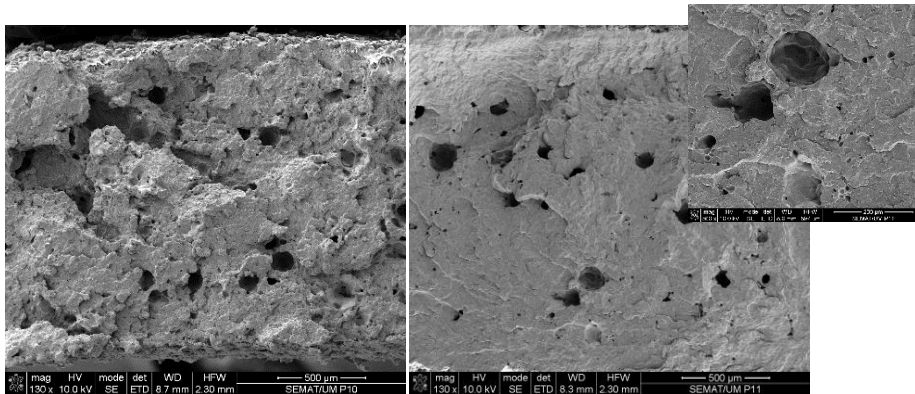


Figure 3.69 Cross-section of test specimens produced by SLS with high levels of energy (0.358 J/mm³ (left) and 0.398 J/mm³ (right), XY-A strategy).

The morphological analysis of these test specimens proved that an intensive exposure of the powder particles to the laser beam operating with excessive levels of energy results in a damaged cross-section, with spherical shaped voids reaching 160 µm of diameter (on average). These inhomogeneities allowed to justify the worst overall performance of test specimens produced with high levels of energy (*e.g.*, 16% lower fracture toughness in test specimens produced with 0.358 J/mm³, compared to test specimens produced with the medium-high level of 0.318 J/mm³). These results proved that the test specimens of experiments P10 and P11 were produced with values of energy beyond the upper limit allowed for quality sintering.

Moreover, the analysis of the surface of crack propagation of test specimens after mode I testing allowed to confirm that the content of porosity is a discontinuity source that more easily allow crack propagation under mechanical loading, influencing the overall performance of the resulting parts (Figure 3.70) (Brugo *et al.*, 2016). These findings are supported by the high values of fracture toughness obtained in test specimens presenting fewer pores in the pre-crack region.

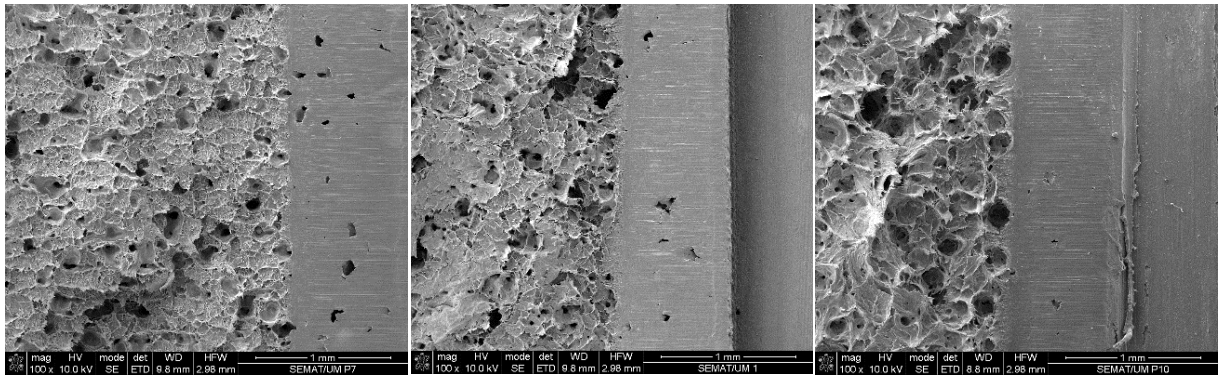


Figure 3.70 Surfaces of test specimens produced by SLS with 0.198 J/mm³ (left) 0.278 J/mm³ (middle) 0.358 J/mm³ (right) after crack propagation under mode I loading (DCB).

Figure 3.71 presents the cross-section of test specimens produced with different laser beam strategies. For the same microscope magnification, the SEM micrographs allowed to verify the reduced thickness of the test specimens produced with the laser beam operating in the x-direction (see Figure 3.30). Despite that, the test specimens produced with this hatching setting exhibited the lowest content of porosity compared to the other laser beam strategies.

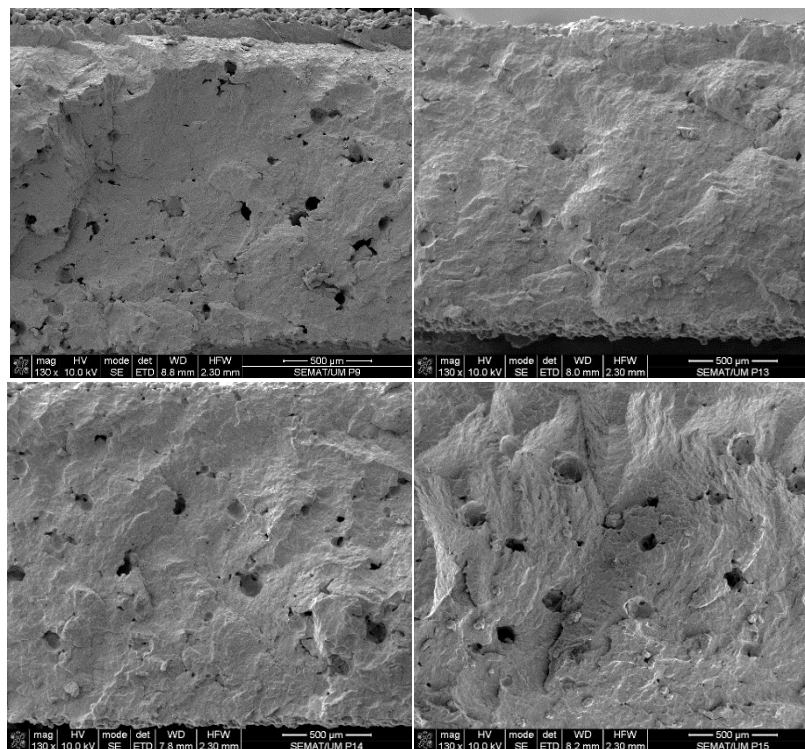


Figure 3.71 Cross-section of test specimens produced by SLS with 0.318 J/mm³ using i) XY-A (top-left), ii) X (top-right), iii) Y (bottom-left) and iv) XY-S (bottom-right) strategies.

In fact, this microscopical analysis provided useful insights to comprehend why the properties of test specimens produced by SLS with the X strategy presented some unexpected results. The corresponding morphological characteristics may indicate that the X strategy is less intensive (which is beneficial for

Chapter 3. Optimization of SLS process parameters

dimensional and geometric tolerancing, but worse for the mass and thickness of parts), but equally efficient (which can explain the reduced content of porosity and high tensile stress at yield, tensile stress at break and tensile strength). Despite that, the strategy of the laser beam did not induce significant morphological differences in the cross-section of test specimens, compared with the effect of EDv.

3.4.1.6. Process characterization

Table 3.6 lists the building time of all productions considered to study the hatching parameters.

Table 3.6 Building time of SLS productions depending on the hatching parameters.

Building time, t (s)			
P1	3703	P8	4072
P2	3926	P9	4473
P3	4127	P10	4364
P4	3207	P11	4423
P5	3487	P12	4461
P6	4398	P13	4545
P7	3905	P14	6186

The results indicated that the building time of the sintering process is mostly affected by the t_{Layer} , regardless of the other parameters considered. In this regard, it was found that the building time was higher in the experiments conducted with lower t_{Layer} values (*i.e.*, 0.12 mm instead of 0.15 mm). The S_{Scan} also showed a significant effect on this processing variable (Figure 3.72 (left)). The experiments conducted with high values of S_{Scan} recorded reduced building time. In opposition, P_{Laser} did not exhibit a substantial impact on the building time (Figure 3.72 (right)).

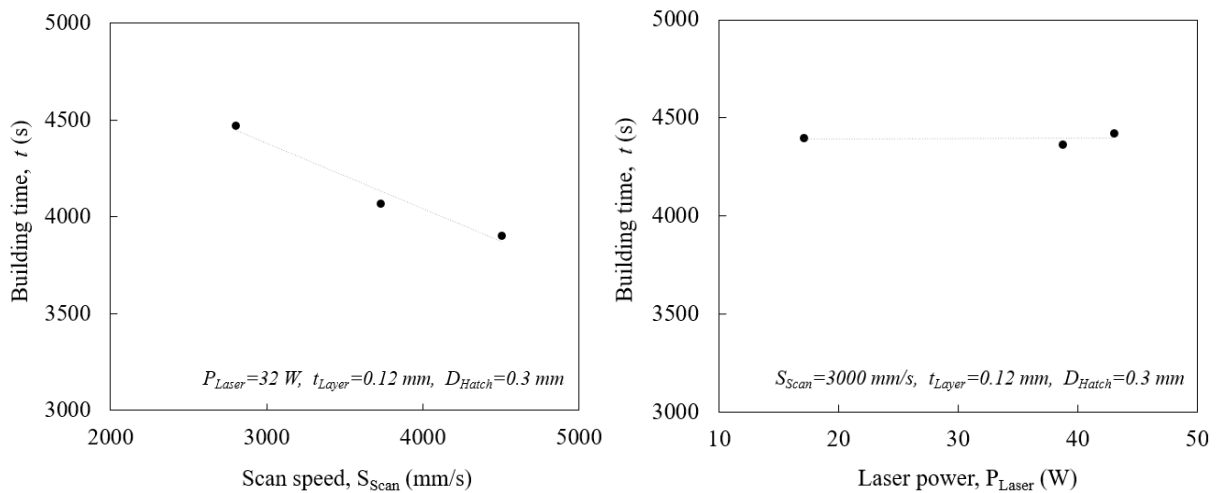


Figure 3.72 Building time of SLS processes depending on the S_{Scan} (left) and P_{Laser} (right).

Moreover, the results from experiments P12, P13 and P14, proved that the building time was similar for the XY-A, X and Y strategies of the laser beam; however, it was significantly higher for the XY-S strategy (Figure 3.73). Considering same parameterization settings, the simultaneous action of the laser source in both x and y directions increased the building time by 38%.

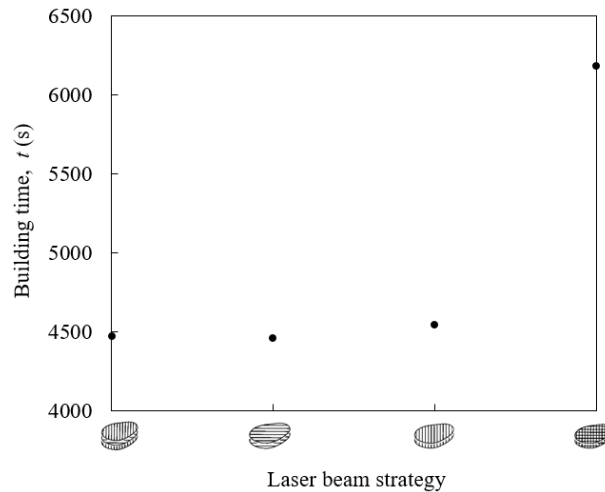


Figure 3.73 Building time of SLS processes depending on the laser strategy (0.318 J/mm³).

3.4.2. Contour parameters

In accordance with Table 3.3 (*section 3.1*) and based on the results reported in the previous section, the contour parameters were evaluated considering an optimized ED_v of 0.318 J/mm³ supplied to the hatching layers, with the laser beam operating in the y-direction (*i.e.*, Y strategy). The purpose of the activities conducted in this section was to evaluate the influence of the contour parameters in the overall performance of SLS parts, with particular focus on the dimensional and geometric accuracy of the features presented on the surface. Therefore, the main goal was to overcome the limitations that were not fully optimized through the modification of the hatching settings. The direct relationship of P_{Laser}/S_{Scan}, within the interval 0.007 J/mm to 0.015 J/mm, was considered in the analysis of contour parameters.

3.4.2.1. Description of observations

The experiments defined to study the contour parameters did not reveal significant differences in the general appearance of the parts. Even the test artefact produced with the lowest level of energy, *i.e.*, 0.007 J/mm, presented high compaction of the powder particles in its surfaces. In consequence, no fine holes with a nominal diameter below 2.00 mm were detectable in its horizontal top plane (Figure 3.74). This proves that the observations reported in experiment P13 (see Figure 3.19 in *section 3.4.1.1*) were

Chapter 3. Optimization of SLS process parameters

not overcome by changing the contour parameters to low energy values, considering the standard and unchanged thickness established for the contour in the default menu.



Figure 3.74 Fine features of a test artefact produced by SLS with 0.007 J/mm ($P_{\text{Laser}}/S_{\text{Speed}}$).

In turn, the test artefacts produced with high levels of energy required more rigorous and intensive cleaning steps, making them more susceptible to burn marks from the compressed air and microbeads blasting systems. For instance, Figure 3.75 shows the coarse surface finishing obtained in the test artefact produced with these contour settings, after the post-processing operations.

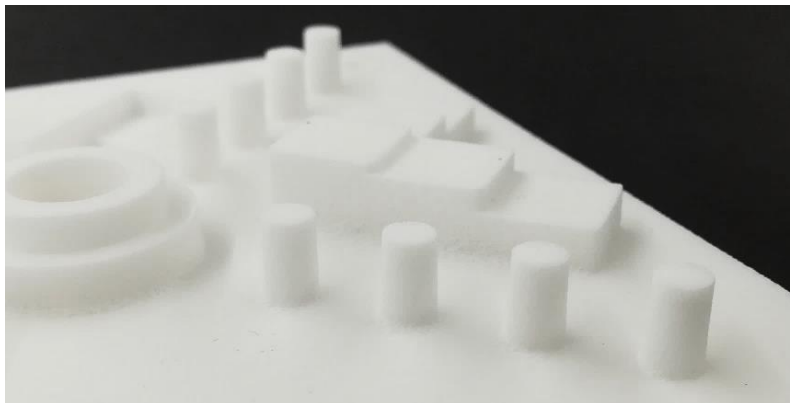


Figure 3.75 Surface of a test artefact produced by SLS with 0.015 J/mm ($P_{\text{Laser}}/S_{\text{Speed}}$) after cleaning with microbeads blasting.

No significant qualitative effects of warpage and curling were observed in the test crosses produced with the contour parameters defined in experiments P15 to P18, not even in the test bars with higher length/thickness ratio.

3.4.2.2. Mass and general dimensions

Figure 3.76 and Figure 3.77 respectively show the influence of the contour parameter on the mass, length, width and thickness of test specimens produced by SLS.

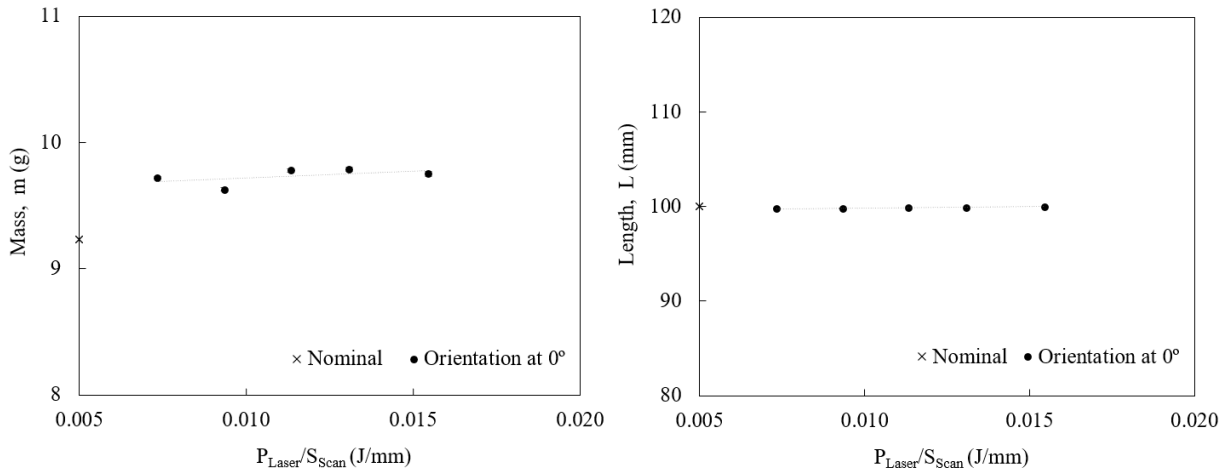


Figure 3.76 Mass (left) and length (right) of test specimens produced by SLS depending on the contour parameters.

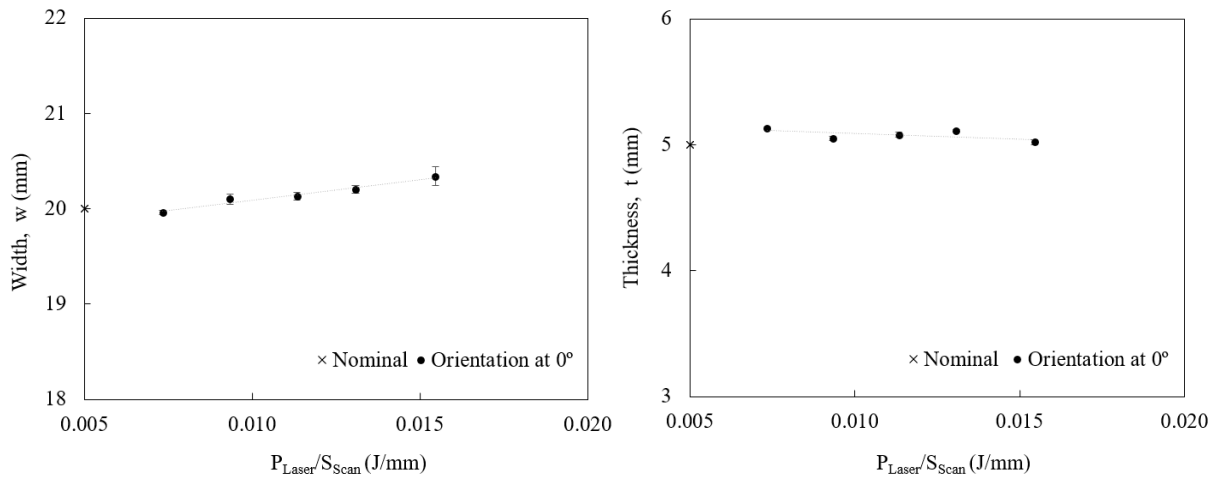


Figure 3.77 Width (left) and thickness (right) of test specimens produced by SLS depending on the contour parameters.

The results showed that the mass and general dimensions of test specimens were not sensitive to the contour parameters defined within the range of values considered in the experiments. A slight effect was only observed in the width, which increased 1.9% from test specimens produced with 0.007 J/mm to test specimens produced with 0.015 J/mm in a rising trend. An average mass of 9.733 g, an average length of 99.9 mm and an average thickness of 5.1 mm were measured in the test specimens, without significant variation between experiments.

3.4.2.3. Dimensional and geometric accuracy

The primary qualitative analysis of the CT images of the surface of test artefacts produced with different contour parameters did not reveal substantial differences. In accordance, the quantitative influence of the P_{Laser}/S_{Scan} relationship on the dimensional and geometric accuracy was not as significant as previously verified for the hatching settings. The most notorious effects were observed on flatness (Figure 3.78), straightness (Figure 3.79) and parallelism (Figure 3.80) of the resulting surfaces.

Chapter 3. Optimization of SLS process parameters

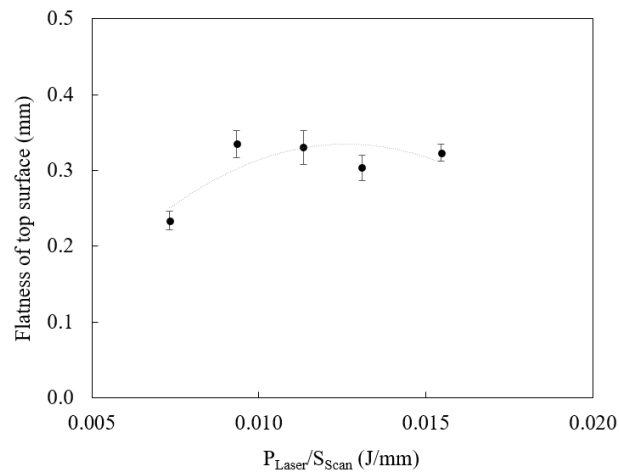


Figure 3.78 Flatness of the top surface of test artefacts produced by SLS depending on the contour parameters.

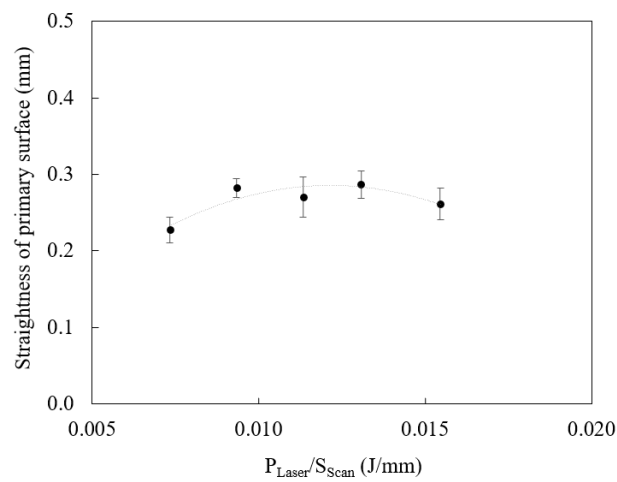


Figure 3.79 Straightness of the primary surface of test artefacts produced by SLS depending on the contour parameters.

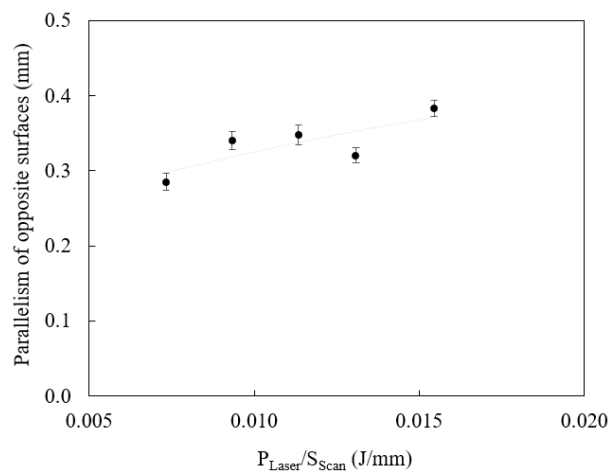


Figure 3.80 Parallelism of opposite surfaces of test artefacts produced by SLS depending on the contour parameters.

In fact, the GD&T measurements did not exhibit a clear relationship with the $P_{\text{Laser}}/S_{\text{Scan}}$, in particular for medium-high levels of energy. However, the test artefact produced with 0.007 J/mm stood out from the others, revealing the lowest values of flatness (*i.e.*, 0.23 ± 0.01 mm), straightness (*i.e.*, 0.23 ± 0.02

mm) and parallelism (*i.e.*, 0.29 ± 0.01 mm). As explained in *section 3.4.1.3*, these results are related to the high heat conduction enhanced by high levels of energy that impairs the overall quality of the surfaces.

The variation of the contour parameters did not influence the reproducibility of holes. Holes with nominal diameter equal to or less than 2.00 mm are not sintered in test artefacts produced with 0.318 J/mm³, regardless of the contour parameters and the laser beam path. On the other hand, all P_{Laser}/S_{Scan} values considered for dimensional and geometric evaluation were able to produce fine pins until 0.25 mm of nominal diameter (Figure 3.81).

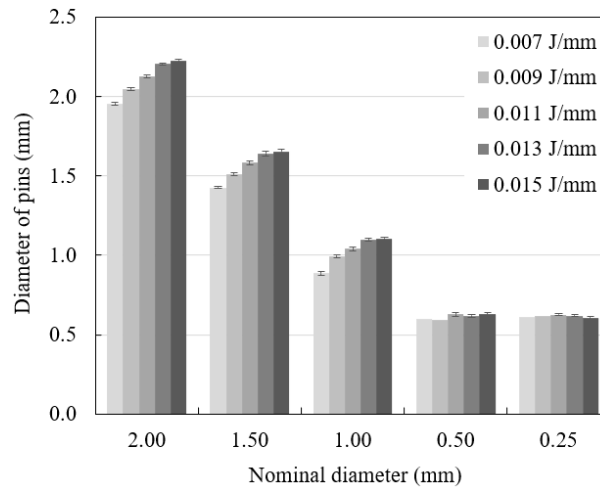


Figure 3.81 Diameter of pins of test artefacts produced by SLS depending on the contour parameters.

The results showed that the average diameter of pins gradually increases with the P_{Laser}/S_{Scan} relationship, which is intrinsically related with the energy supplied to the contour layers. Therefore, the test artefact produced with 0.007 J/mm exhibited the highest deviation to a minimum value until 0.11 mm below the nominal, while the test artefact produced with 0.015 J/mm exhibited the highest deviation to a maximum value until 0.23 mm above the nominal. A medium-low value of 0.009 J/mm showed to be the most suitable option to produce pins meeting nominal specifications. Regardless of the experiment, it was proved that the minimum pin size achievable is 0.50 mm since pins with the nominal diameter of 0.25 mm were produced with an average diameter close to 0.50 mm in all conditions.

3.4.2.4. Mechanical properties

Tensile properties

Figure 3.82 shows representative engineering stress-strain curves of test specimens produced by SLS depending on the contour parameters.

Chapter 3. Optimization of SLS process parameters

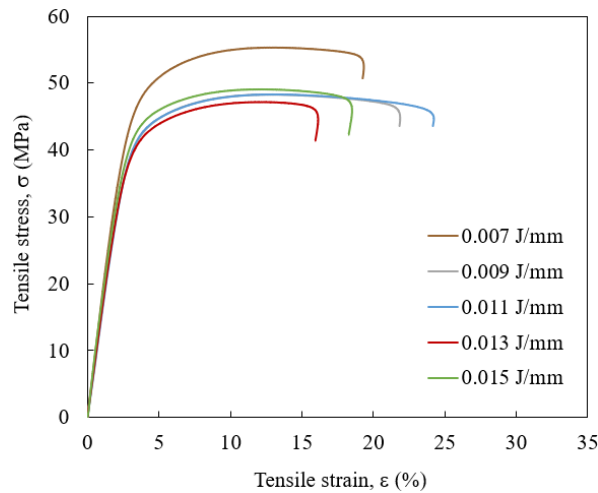


Figure 3.82 Engineering stress-strain curves of test specimens produced by SLS depending on the contour parameters.

The plots suggested better mechanical performance for test specimens produced with the lowest value of energy supplied to the contour. This was not an expected outcome, since in the previous section it was verified the opposite with the hatching parameters (*i.e.*, better mechanical performance in test specimens produced with high EDv values). Despite that, all other test specimens exhibited a similar behaviour compared to the reference value of 0.011 J/mm (*i.e.*, experiment P13). Based on the corresponding stress-strain curves, Figure 3.83 presents the variation of the elastic modulus of test specimens produced by SLS as a function of different contour parameters.

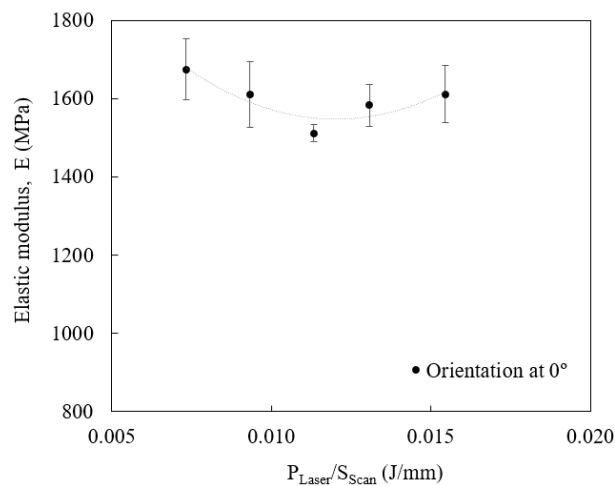


Figure 3.83 Elastic modulus of test specimens produced by SLS depending on the contour parameters.

The elastic modulus reached the highest value in test specimens produced with 0.007 J/mm, recording 1674.5 ± 77.7 MPa. Until the medium value of 0.011 J/mm, the elastic modulus decreased 9.7% to a minimum of 1511.6 ± 22.6 MPa and after that, an increasing trend was again reached to 1611.5 ± 72.5 MPa in test specimens produced with 0.015 J/mm.

The results of tensile stress at yield, tensile strain at yield, tensile stress at break, tensile strain at break and tensile strength of test specimens produced by SLS depending on the contour parameters are following reported in Figure 3.84, Figure 3.85 and Figure 3.86, respectively.

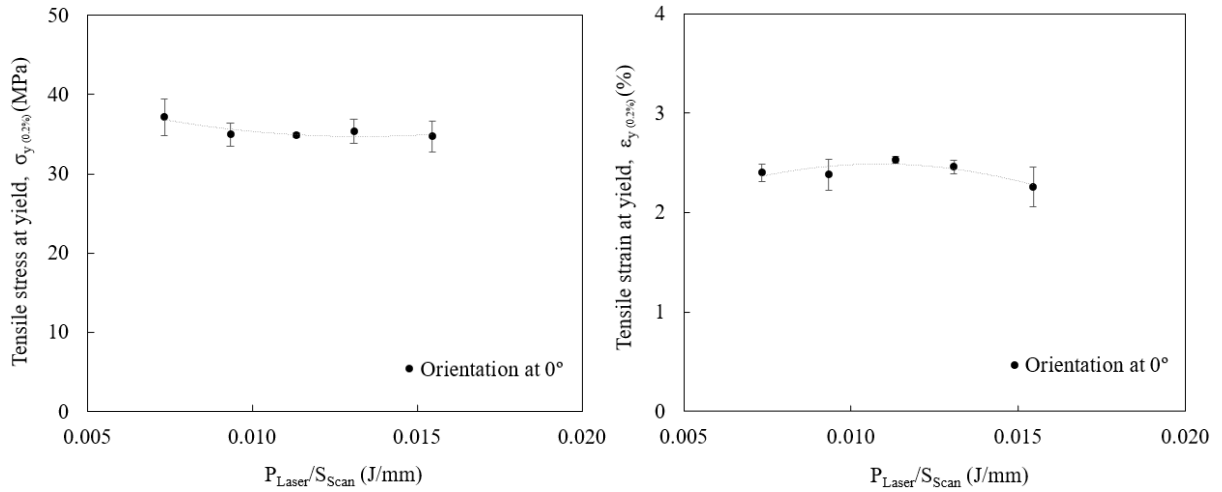


Figure 3.84 Tensile stress at yield (left) and tensile strain at yield (right) of test specimens produced by SLS depending on the contour parameters.

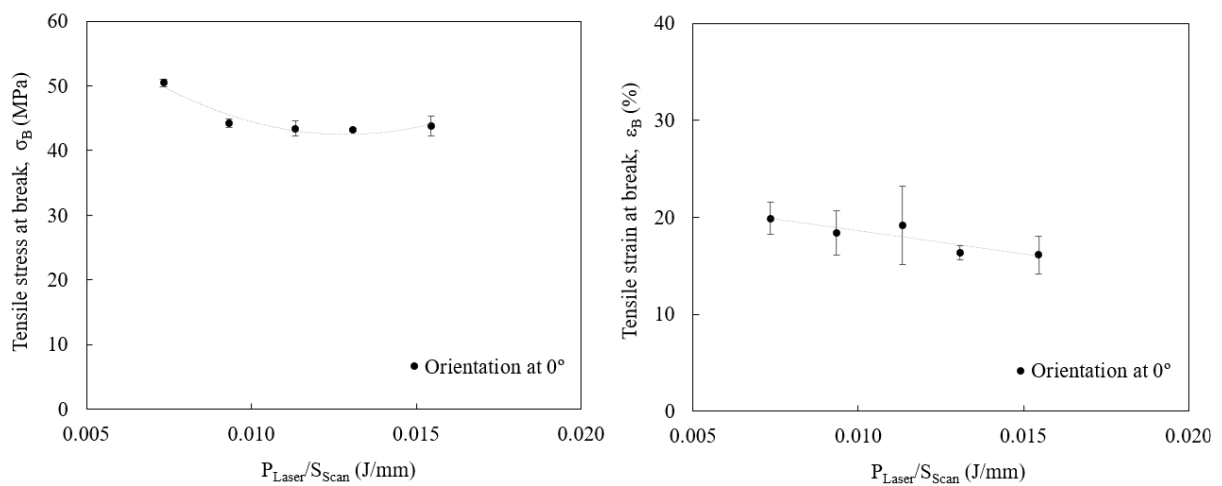


Figure 3.85 Tensile stress at break (left) and tensile strain at break (right) of test specimens produced by SLS depending on the contour parameters.

Chapter 3. Optimization of SLS process parameters

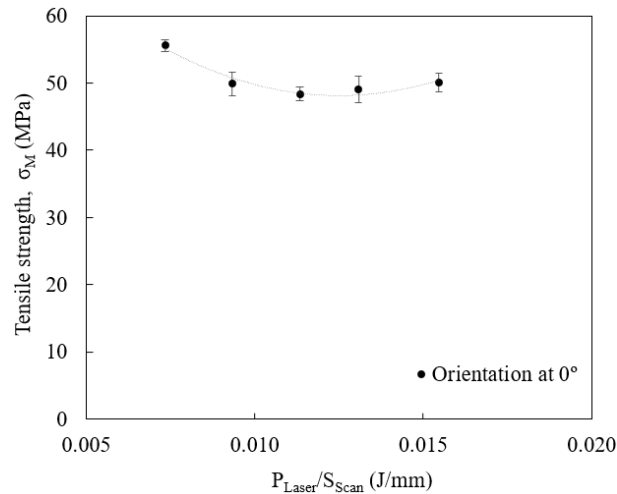


Figure 3.86 Tensile strength of test specimens produced by SLS depending on the contour parameters.

The tensile stress at yield, tensile stress at break and tensile strength exhibited the maximum values in the test specimens produced with 0.007 J/mm, recording 37.2 ± 2.3 MPa, 50.5 ± 0.5 MPa and 55.6 ± 0.8 MPa, respectively. All of these mechanical properties decreased in the test specimens produced with 0.009 J/mm. The test specimens produced with this level of energy presented 35.0 ± 1.5 MPa of tensile stress at yield, 44.2 ± 0.7 MPa of tensile stress at break and 50.0 ± 1.8 MPa of tensile strength. Above 0.009 J/mm, all test specimens revealed similar mechanical outputs. These results suggested that a medium-high level of energy defined for the hatching, combined with a medium-high level of energy defined for the contour results in SLS parts with inferior mechanical properties. For the EDv of 0.318 J/mm³, the P_{Laser}/S_{Scan} of 0.007 J/mm ensure acceptable outputs, within the considered range of values.

Fracture properties

Figure 3.87 shows experimental P - δ curves obtained from the DCB tests and corresponding R -curves by applying the CBBM of test specimens produced by SLS depending on the contour parameters.

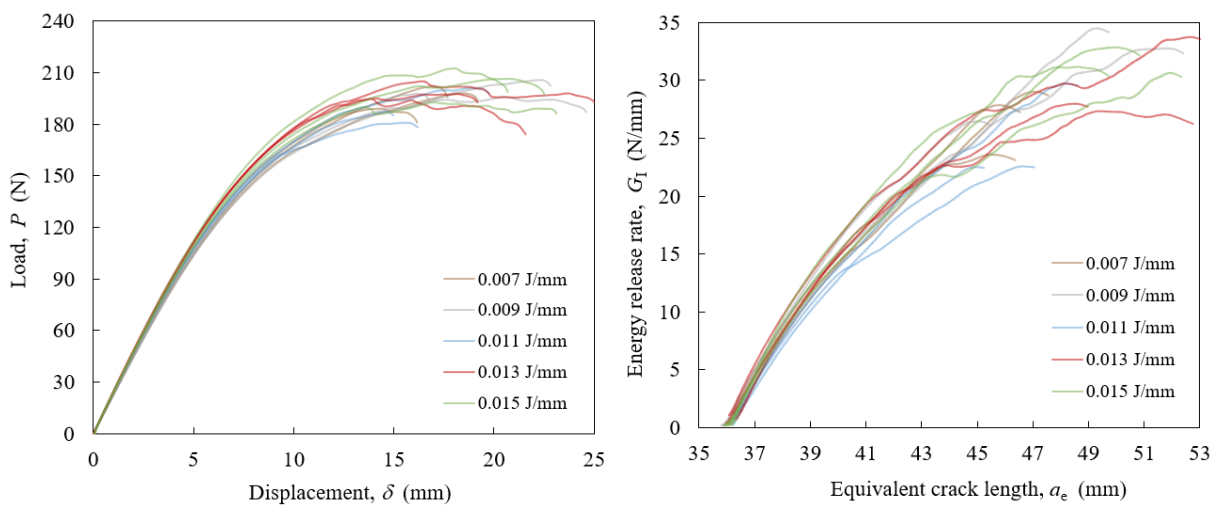


Figure 3.87 Experimental P - δ curves (left) and R -curves (right) of test specimens produced by SLS depending on the contour parameters.

In general, the results did not demonstrate a clear trend of the fracture toughness with the P_{Laser}/S_{Scan} relationship. The resulting R curves presented a large dispersion with G_{Ic} values ranging from 25 N/mm to 32 N/mm, on average. Although the results were not conclusive, they suggested that the contour parameters do not have a significant influence on the fracture toughness as the hatching parameters (*i.e.*, G_{Ic} showed a significant dependence on the hatching settings (see Figure 3.63)). Due to this reason, the experimental results of test specimens produced with different contour parameters were not complemented with numerical analysis.

3.4.2.5. Morphological properties

Figure 3.88 and Figure 3.89 respectively show SEM micrographs of the cross-section of test specimens produced by SLS with low (*i.e.*, 0.007 J/mm and 0.009 J/mm) and high (*i.e.*, 0.013 J/mm and 0.015 J/mm) levels of energy supplied to the contour during the sintering process, by means of the P_{Laser}/S_{Scan} relationship.

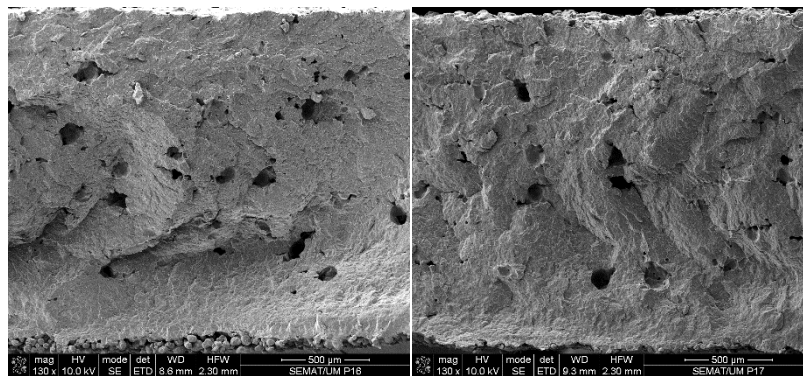


Figure 3.88 Cross-section of test specimens produced by SLS with low levels of contour energy (0.007 J/mm (left) and 0.009 J/mm (right)).

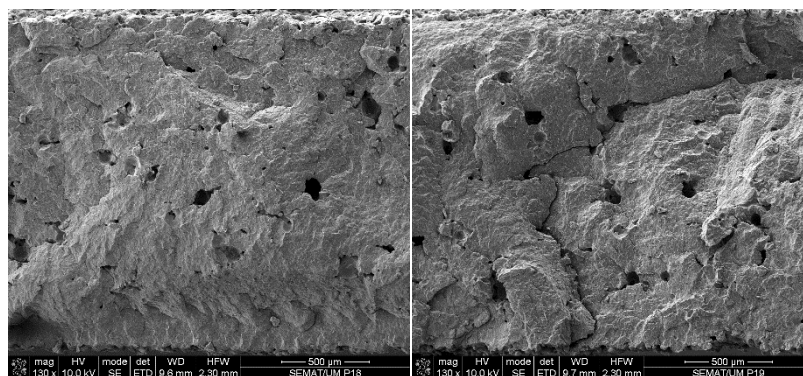


Figure 3.89 Cross-section of test specimens produced by SLS with high levels of contour energy (0.013 J/mm (left) and 0.015 J/mm (right)).

The morphological results presented in this section did not provide relevant conclusions for the study since the cross-section of the test specimens produced in experiments P15 to P18 did not reveal clear differences between the hatching and contour layers. This fact evidenced that the definition of the contour

Chapter 3. Optimization of SLS process parameters

settings through the standard parameterization mode of the EOS PSW 3.8 software does not allow significant modifications in the properties of SLS parts. This justifies the low-sensitive dimensional, geometric, and mechanical variations obtained between these experiments. Therefore, this proves that the most relevant properties of SLS parts are more affected by the hatching parameters than the contour settings defined for a standard number of layers.

3.4.2.6. Process characterization

Table 3.7 lists the building time of all productions considered to study the contour parameters.

Table 3.7 Building time of SLS productions depending on the contour parameters.

Building time, t (s)	
P15	4593
P16	4533
P13	4545
P17	4547
P18	4548

The results proved that the relationship between P_{Laser} and S_{Scan} to define the energy supplied to the contour layers do not have a significant influence on the building time (Figure 3.90). As verified before for the micro and macro-scale properties of parts, the SLS process itself is also mostly influenced by the hatching parameters due to the larger volume of the part defined by them.

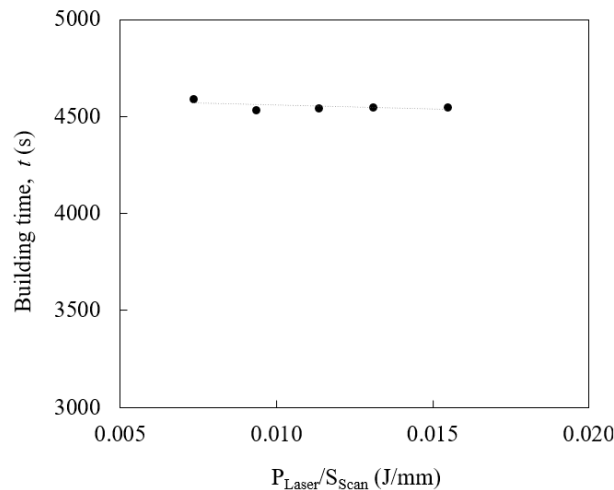


Figure 3.90 Building time of SLS processes depending on the contour parameters.

3.4.3. Combination of hatching and contour parameters

The individual analysis of hatching and contour parameters demonstrated that when the energy provided during the SLS process is high, the heat conduction empowers the secondary sintering of

surrounding powder particles, improving the mechanical properties but reducing the dimensional and geometric accuracy of parts. In general terms, this means that medium-high EDv values are beneficial for mechanical strength, while medium-low EDv values are preferable for surface finishing and dimensional and geometric accuracy of features. This explains the relevance of combining two different sets of parameters in the same part in order to optimize its overall performance.

In this section, the combination of parameters was evaluated considering a balanced compromise between mechanical performance (*i.e.*, in respect of tensile modulus and strength) with dimensional and geometric accuracy (*i.e.*, in respect of tolerancing of form, orientation and location). In accordance with Table 3.4 (*section 3.1*) and based on the results reported in the previous sections, enhanced mechanical properties were reached in parts produced with $EDv = 0.318 \text{ J/mm}^3$, laser strategy = Y, $P_{\text{Laser}}/S_{\text{Scan}} = 0.007 \text{ J/mm}$. Hence, this set of parameters was considered for the core, defining the largest volume of the part. As great dimensional and geometric outputs were attained in a range between 0.158 J/mm^3 and 0.238 J/mm^3 , the set of parameters $EDv = 0.198 \text{ J/mm}^3$, laser strategy = X, $P_{\text{Laser}}/S_{\text{Scan}} = 0.007 \text{ J/mm}$ was selected for the skin, defining 20%, 30% and 40% of the thickness of the part. It is important to note that each percentage corresponds to the final value, combining the thickness of the contour of the top and bottom surfaces. To account for that, in the EOS PSW 3.8 software, the corresponding exposure type was defined with the ratio $t_{\text{Skin}}/t_{\text{Part}}$ divided by two. For comparison, attention was given to the results obtained in experiment P15 corresponding to parts entirely produced with the core parameters selected for this combined analysis (*i.e.*, experiment hereafter referred to as 0% of $t_{\text{Skin}}/t_{\text{Part}}$).

3.4.3.1. Description of observations

The qualitative evaluation of test specimens produced with different process parameters defining specific skin/core combinations evidenced significant effects on the surface finishing and quality of features. No additional cleaning steps were required in these experiments because the powder particles did not reveal excessive compaction as reported in the previous sections for test specimens produced with 0.318 J/mm^3 using a non-combined parameterization.

Figure 3.91 shows the test artefact produced with the lowest value of t_{Skin} considered for the analysis (*i.e.*, experiment P19) after cleaning with microbeads blasting.

Chapter 3. Optimization of SLS process parameters

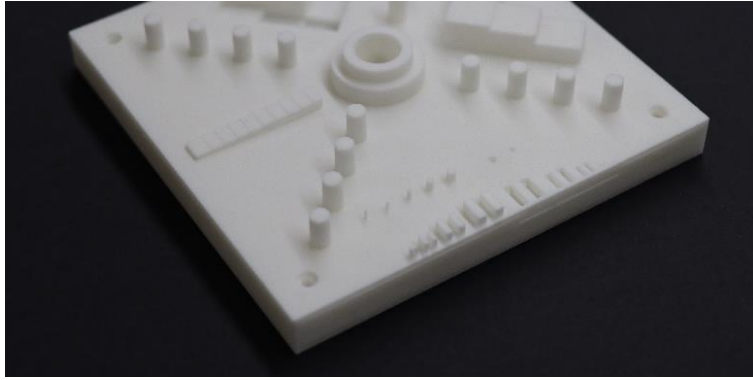


Figure 3.91 Test artefact produced by SLS with combination of parameters (20% of $t_{\text{Skin}}/t_{\text{Part}}$) after cleaning with sand blasting.

As demonstrated in *section 3.4.1.3* (see Figure 3.33), when the SLS process is conducted with the medium-high level of 0.318 J/mm^3 , the test artefact considered for dimensional and geometric analysis do not reveal fine holes equal to or less than 2.00 mm of nominal diameter. In turn, experiment P19 showed that when that ED_v value is combined with 1.00 mm of skin (*i.e.*, $t_{\text{Skin}}/t_{\text{Part}}$ of 20%) defined with a medium-low level of energy, fine holes above 1.50 mm of nominal diameter are detectable in the top surface of the test artefact (Figure 3.92). Despite the advantages of this combination of parameters in the manufacturing of fine holes, this value of t_{Skin} was not able to ensure the quality of the larger holes that remained negatively affected by the medium-high level of energy defined for the core.



Figure 3.92 Fine features of a test artefact produced by SLS with combination of parameters (20% of $t_{\text{Skin}}/t_{\text{Part}}$).

In addition to these characteristics, all test specimens produced in this experiment exhibited a clear interface between the layers defining the skin and core (Figure 3.93). This effect was observed through an additional edge produced as a consequence of the substantial difference in energy density that was supplied by the laser beam to each specific area.

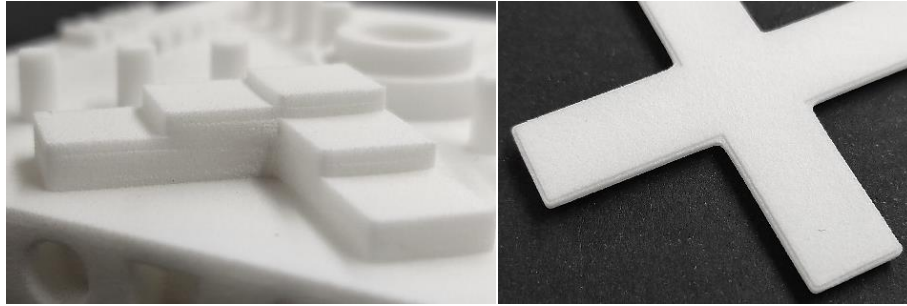


Figure 3.93 Details of test specimens produced by SLS with combination of parameters (20% of t_{Skin}/t_{Part}).

As expected, the test specimens produced with higher values of t_{skin} (*i.e.*, experiment P20) revealed smoother surfaces and higher quality features. In accordance, the corresponding test artefact showed greater reproducibility of fine holes and negative features (Figure 3.94). Under these conditions of production, fine holes above 1.00 mm were visible and the quality of the larger holes was improved.

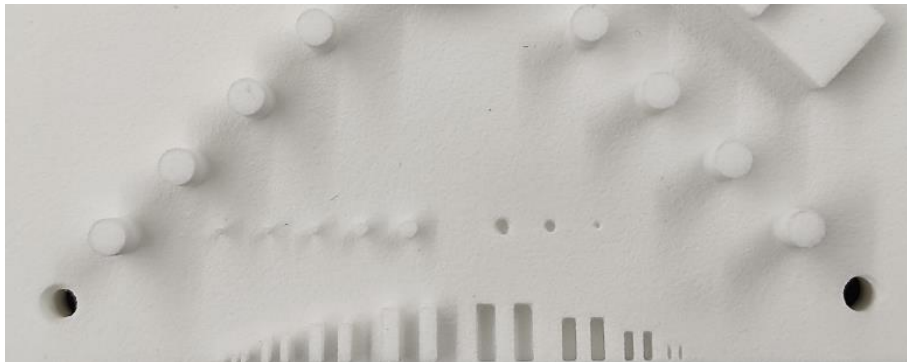


Figure 3.94 Fine features of a test artefact produced by SLS with combination of parameters (30% of t_{Skin}/t_{Part}).

In this experiment, the test specimens with low thickness (*e.g.*, the test cross for warpage evaluation) also exhibited the skin/core division through an extra edge observed in the surfaces (Figure 3.95).



Figure 3.95 Details of a test specimen produced by SLS with combination of parameters (30% of t_{Skin}/t_{Part}).

Chapter 3. Optimization of SLS process parameters

However, in the test artefact (*i.e.*, the test specimen with highest thickness), the skin/core interface was not detected by an edge, but by a slight difference in colour (Figure 3.96). Due to the different levels of energy involved, the layers of powder defining the skin exhibited a white appearance in contrast to the yellowish appearance of the core.

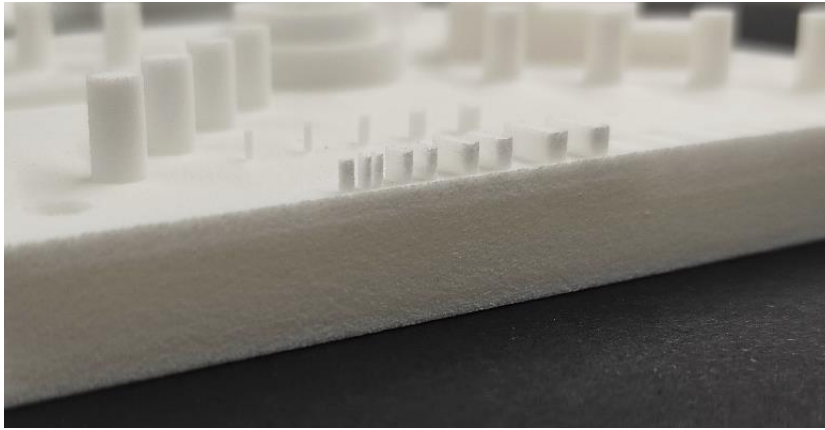


Figure 3.96 Details of a test artefact produced by SLS with combination of parameters (30% of $t_{\text{skin}}/t_{\text{Part}}$).

Figure 3.96 also demonstrates that these operating conditions allowed to improve the quality of holes without compromising the manufacturing of fine pins, including the smallest one with 0.25 mm of nominal diameter.

Moreover, this first qualitative analysis revealed more significant differences between experiments P19 and P20 than between experiments P20 and P21. However, some improvements were verified in the experiment conducted with the highest value of t_{skin} in relation to holes (Figure 3.97).

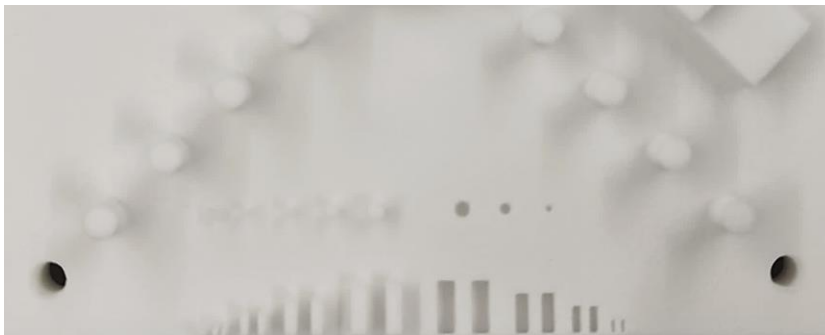


Figure 3.97 Fine features of a test artefact produced by SLS with combination of parameters (40% of $t_{\text{skin}}/t_{\text{Part}}$).

Despite the advantages in the manufacturing of holes, in this experiment the fine pin with nominal diameter of 0.25 mm was not produced with quality (Figure 3.98). These observations may suggest that the $t_{\text{skin}}/t_{\text{Part}}$ ratio of 30% (*i.e.*, experiment P20) establishes the limit value to ensure balanced dimensional and geometric outputs of fine pins, for the combination of parameters considered in this analysis.

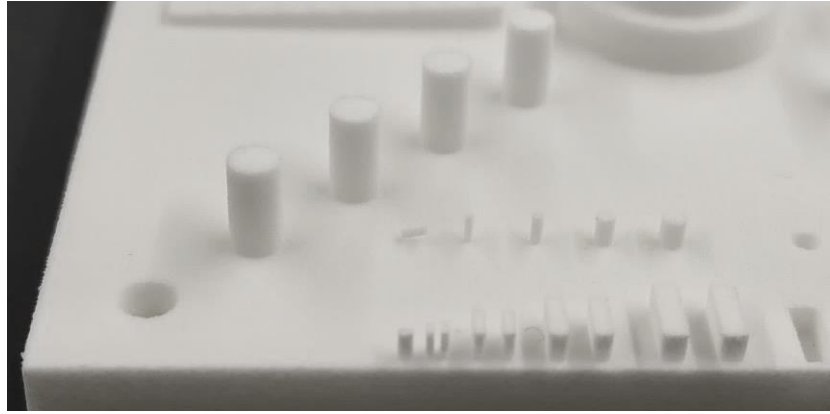


Figure 3.98 Details of a test artefact produced by SLS with combination of parameters (40% of $t_{\text{skin}}/t_{\text{Part}}$).

No significant qualitative effects of warpage and curling were observed in the test crosses produced with the combination of parameters defined in experiments P19 to P21. In turn, substantial effects of warpage were observed in the long and thin test bar produced with the combined parameterization mode of experiment P21, compared with the test bar produced with a single exposure type of experiment P9 (Figure 3.99).



Figure 3.99 Test bars produced by SLS with single (top) and multiple (bottom) exposure types.

3.4.3.2. Mass and general dimensions

The results of mass and general dimensions of test specimens produced by SLS with different combinations of skin/core parameters are reported in the following figures. The experiments revealed that the mass of test specimens decreases when the number of layers of powder sintered with a medium-low level of energy increases as a function of t_{Skin} (Figure 3.100 (left)). Compared with the reference value of 0% recording 9.723 ± 0.008 g, the mass decreased 2.9% in test specimens produced with 20% and 4.2% in test specimens produced with 40% to 9.440 ± 0.017 g and 9.318 ± 0.013 g, respectively. On the other hand, the length of the test specimens was not affected by the combination of parameters considered for the analysis, reproducing with accuracy the nominal value of 100 mm (Figure 3.100 (right)).

Chapter 3. Optimization of SLS process parameters

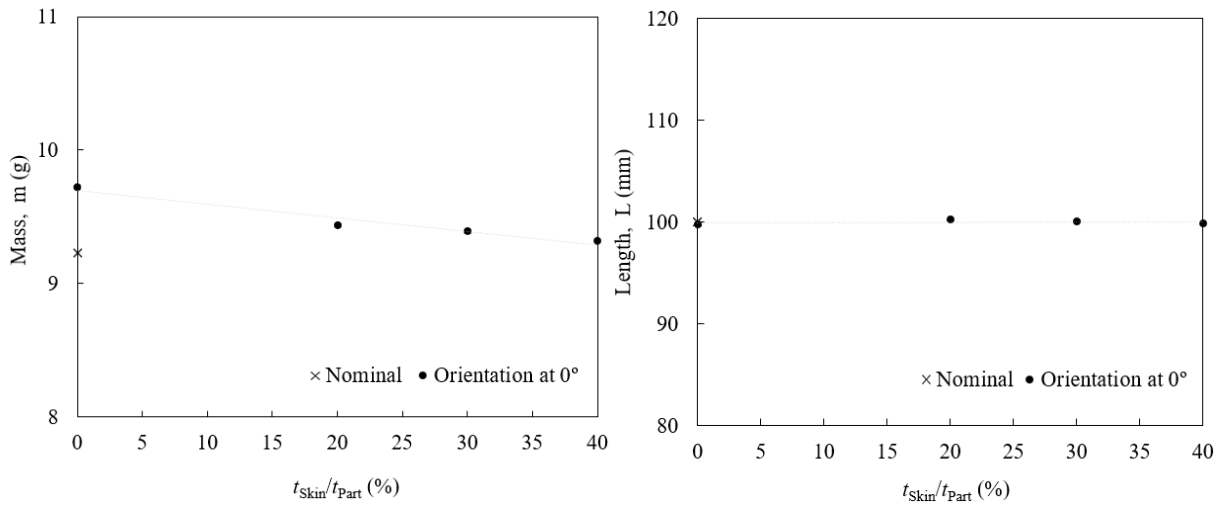


Figure 3.100 Mass (left) and length (right) of test specimens produced by SLS depending on the combination of parameters.

The width of test specimens also decreased with the t_{Skin}/t_{Part} relationship (Figure 3.101 (left)). The test specimens produced with a medium-high level of energy defining the largest portion of its bulk volume exhibited a width of 20.35 ± 0.05 g (*i.e.*, slightly above the nominal). In contrast, the test specimens produced with the highest number of skin layers sintered with a medium-low level of energy recorded a width of 19.93 ± 0.02 g (*i.e.*, slightly below the nominal). This demonstrates that a variation of 20% in t_{Skin} resulted in a difference of 2.1% (on average) in the width of test specimens. The reference value of 0% of t_{Skin} exhibited a width similar to that obtained in experiment P21.

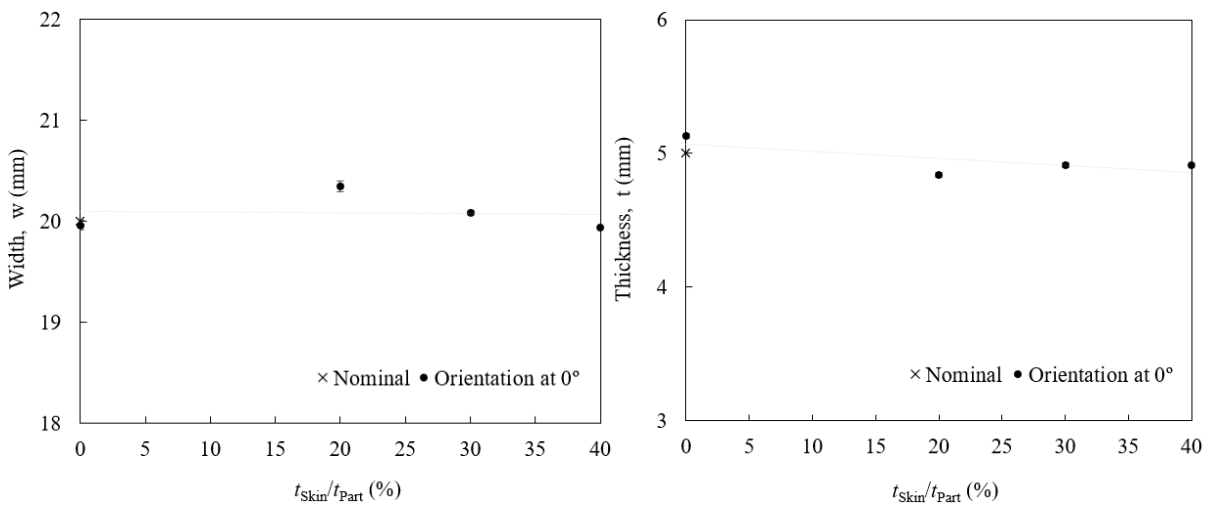


Figure 3.101 Width (left) and thickness (right) of test specimens produced by SLS depending on the combination of parameters.

The thickness of test specimens did not show a significant variation with the combination of skin/core parameters (Figure 3.101 (right)). Despite the slight increase from 4.84 ± 0.02 g in test specimens produced in experiment P19 to 4.92 ± 0.02 g in test specimens produced in experiment P21, all values

remained below the nominal (*i.e.*, 5.00 mm) as opposed to the reference condition of P15 that recorded an average value above the nominal.

3.4.3.3. Dimensional and geometric accuracy

The CT images of test artefacts produced with different skin/core combinations revealed the direct influence of these parameterization settings on the general appearance of parts. In this regard, Figure 3.102 evidences the geometric characteristics of the test artefact produced by SLS with the lowest value of t_{Skin} .

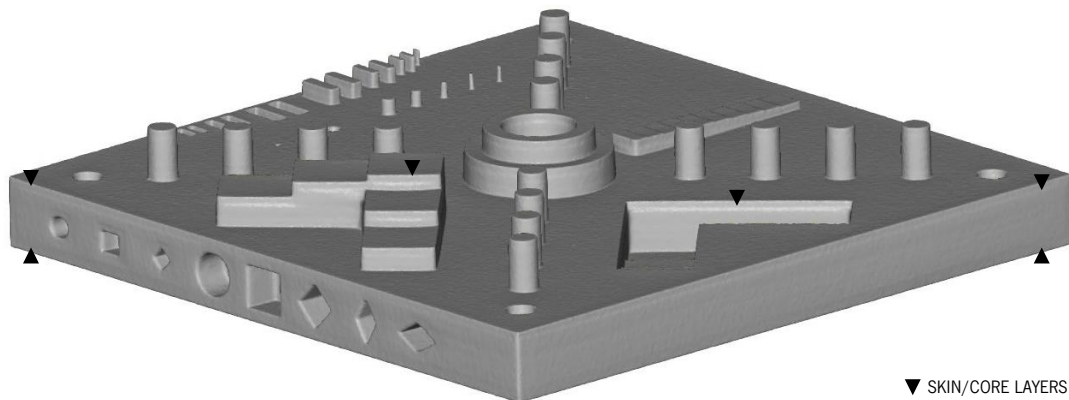


Figure 3.102 Geometric characteristics of a test artefact produced by SLS with combination of parameters (20% of t_{Skin}/t_{Part}).

As reported in *section 3.4.3.1* (see Figure 3.93), the test specimens produced under these operating conditions exhibited a clear separation between the skin and core layers. The corresponding CT image showed that this phenomenon is especially evidenced in lateral surfaces and positive and negative staircases closer to the outer edge of the test artefact, depending on the t_{Skin} . This effect had a direct influence on the quantitative results, with more notorious consequences on flatness of the corresponding surfaces and their parallelism and perpendicularity with the others.

In addition, the comparative analysis of all CT images revealed in detail the influence of the medium-low level of energy supplied to the skin layers to improve the quality of holes presented in the top surface of the test artefacts, including the fine features and larger holes of the corners (Figure 3.103). It was also shown that fine pins exhibited a reversed trend, revealing greater quality in SLS processes conducted under medium-high levels of energy, as in experiment P19.

Chapter 3. Optimization of SLS process parameters

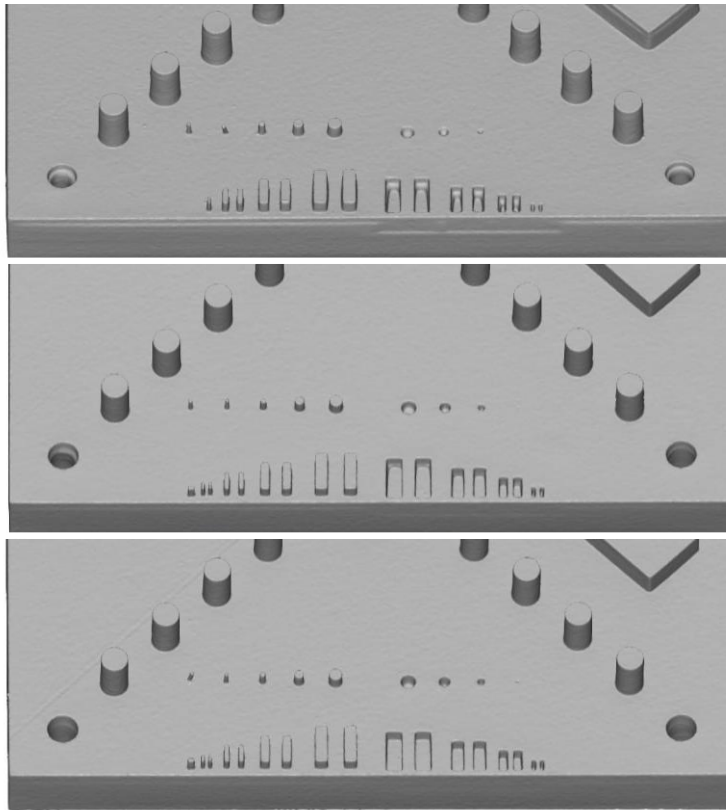


Figure 3.103 Geometric characteristics of test artefacts produced by SLS with 20% (top), 30% (middle) and 40% (bottom) of $t_{\text{Skin}}/t_{\text{Part}}$.

Figure 3.104 shows the flatness of the top surface of test artefacts produced by SLS depending on the combination of skin/core parameters.

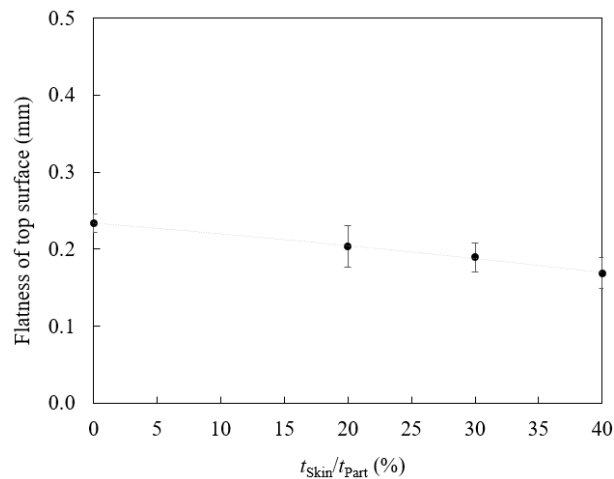


Figure 3.104 Flatness of the top surface of test artefacts produced by SLS depending on the combination of parameters.

The results demonstrated that the flatness of parts produced by SLS with 0.318 J/mm^3 can be reduced until 26.1% (*i.e.*, decreasing from 0.23 mm to 0.17 mm (on average)), when a $t_{\text{Skin}}/t_{\text{Part}}$ of 40% produced with 0.198 J/mm^3 is considered. In fact, the individual and combined analysis of the dimensional and

geometric accuracy proved that the flatness of upward-facing surfaces of polymeric parts produced by SLS is highly dependent on the process parameters selected for the sintering.

The roundness of central and lateral holes of test artefacts produced by SLS depending on the combination of skin/core parameters is illustrated in Figure 3.105.

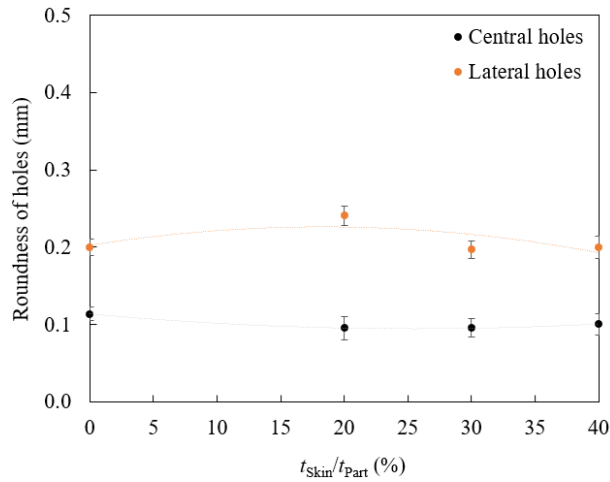


Figure 3.105 Roundness of central and lateral holes of test artefacts produced by SLS depending on the combination of parameters.

As evidenced before (see Figure 3.35), the roundness of lateral holes is tendency 0.10 mm higher (on average) than the roundness of central holes, regardless of the process parameters considered for the manufacturing. Besides that, this type of tolerancing of form did not show significant variation with the combination of parameters considered in this analysis.

The perpendicularity of holes with the top surface and the concentricity of inner cylinders also revealed few differences with the $t_{\text{skin}}/t_{\text{part}}$ relationship (Figure 3.106). The results showed that the perpendicularity of holes was reduced from 0.14 mm in the test artefact produced with a single exposure type to 0.10 mm or less in the test artefacts produced with a multiple exposure type (Figure 3.106 (left)). It was also observed a decrease in the concentricity of inner cylinders with the combined parameterization (Figure 3.106 (right)). Nevertheless, all measurements of this GD&T parameter recorded values below 0.10 mm.

Chapter 3. Optimization of SLS process parameters

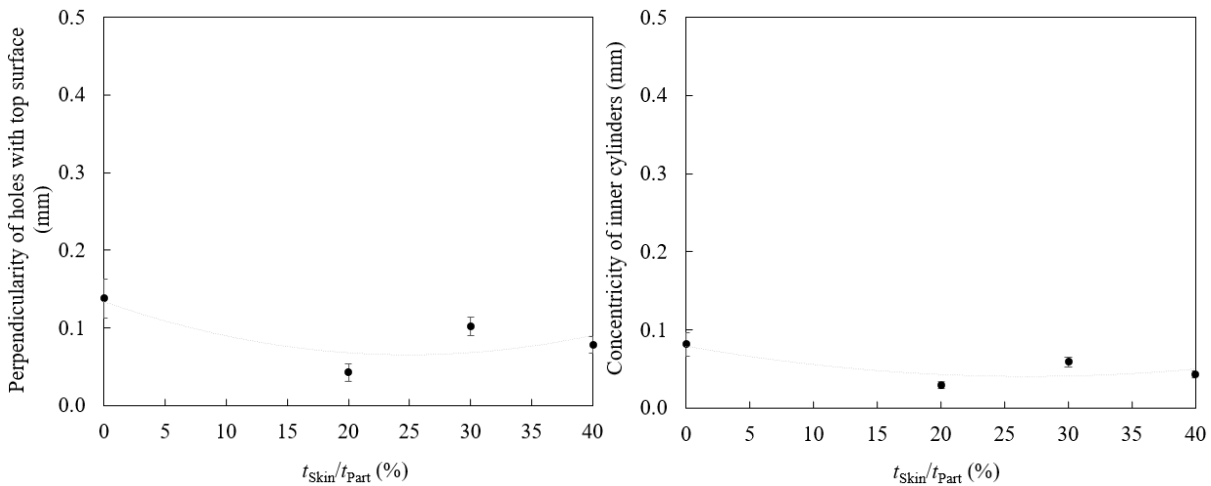


Figure 3.106 Perpendicularity of holes with top surface (left) and concentricity of inner cylinders (right) of test artefacts produced by SLS depending on the combination of parameters.

In turn, the straightness of the primary surface showed a strong dependence on the skin/core ratio (Figure 3.107). While the test artefacts entirely produced with 0.318 J/mm^3 presented a straightness above 0.20 mm , the inclusion of skin layers sintered with 0.198 J/mm^3 allowed a reduction to a range of $0.14 - 0.18 \text{ mm}$, regardless of the t_{Skin} .

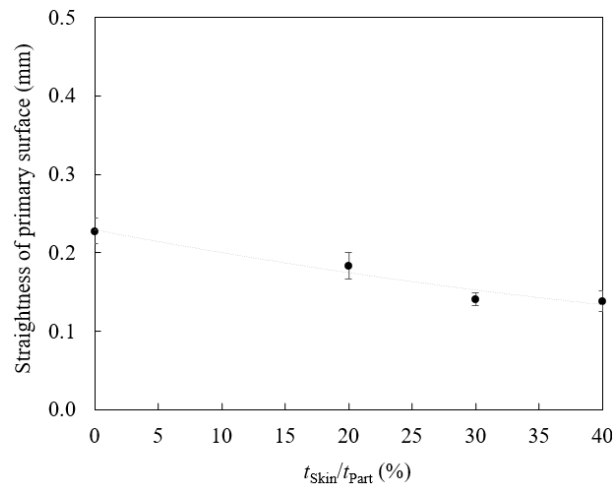


Figure 3.107 Straightness of the primary surface of test artefacts produced by SLS depending on the combination of parameters.

Figure 3.108 shows the results of the parallelism of opposite surfaces obtained from experiments P15, P19, P20 and P21. It was verified that the parallelism decreased from 0.44 mm to 0.29 mm in test artefacts produced with t_{Skin} increasing from 20% to 40% of t_{Part} , respectively. However, the test artefact produced with 0% of t_{Skin} recorded the lowest value of 0.29 mm . This unexpected result can be explained by the physical interface observed between the skin and core layers that prevented the production of flat lateral surfaces and, consequently, their parallelism with opposite surfaces. This phenomenon is illustrated in Figure 3.93 and Figure 3.102 and shown in more detail in the following figure.

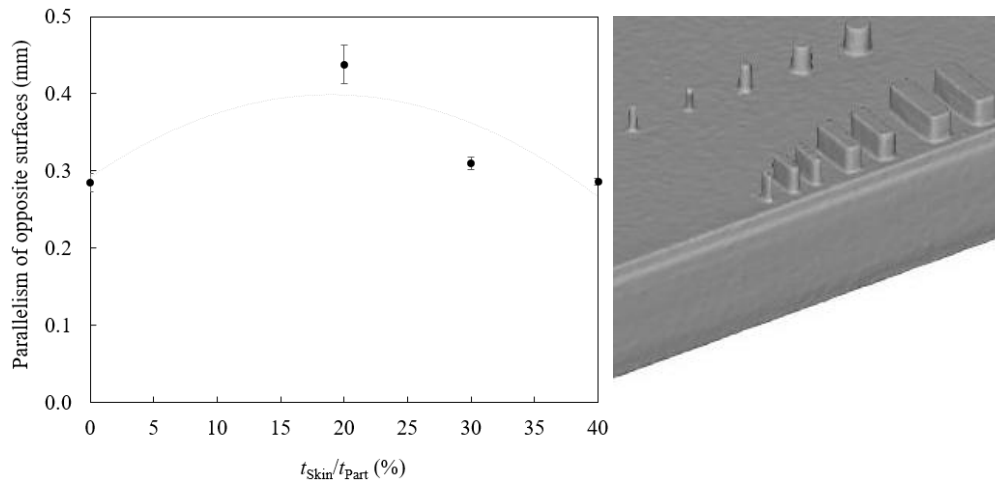


Figure 3.108 Parallelism of opposite surfaces of test artefacts produced by SLS depending on the combination of parameters.

The tolerancing of location of negative and positive x, y and z positions of test artefacts produced by SLS depending on the combination of skin/core parameters is plotted in Figure 3.109, Figure 3.110 and Figure 3.111, according to the methodology adopted before for the hatching parameters. In general, the measurements proved that the linear displacement deviation is tendency higher when the distance between the centre of the feature and the centre of the part increases, as previously verified in *section 3.4.1.3*. Therefore, the pins positioned at -50.00 mm and 50.00 mm and the staircases positioned at -7.00 mm and 7.00 mm exhibited the highest deviations of location. In contrast, the pins and staircases closest to the centre of the test artefacts showed the smallest deviations. Despite that, the results demonstrated a clear dependence on the average values with the combination of parameters.

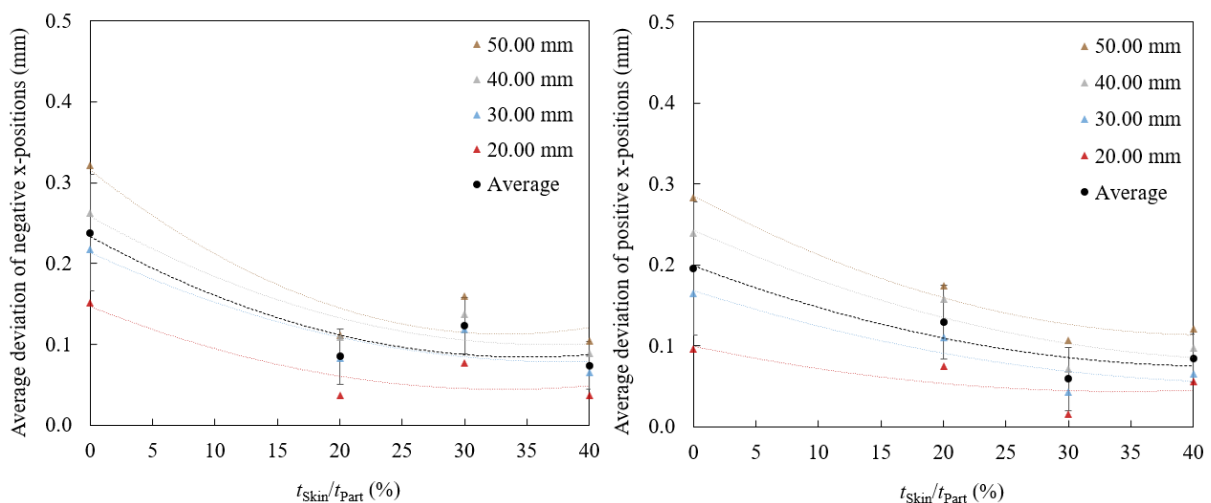


Figure 3.109 Average deviations of negative (left) and positive (right) x-positions of pins in test artefacts produced by SLS depending on the combination of parameters.

Regarding the x-axis, the results showed that the linear displacement deviation of positions gradually decreased from values above 0.20 mm in test specimens produced with a single exposure type to values

Chapter 3. Optimization of SLS process parameters

below 0.10 mm in test specimens produced with 40% of $t_{\text{Skin}}/t_{\text{Part}}$, for both positive and negative features (Figure 3.109). The linear displacement deviation between pins produced in the same test artefact with different location also decreased with the combination of parameters.

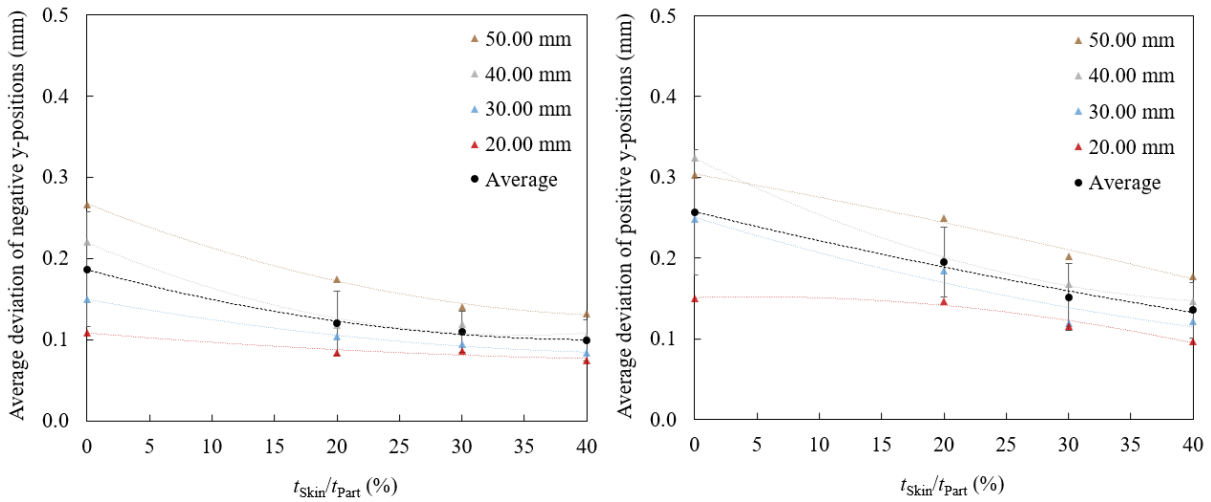


Figure 3.110 Average deviations of negative (left) and positive (right) y-positions of pins in test artefacts produced by SLS depending on the combination of parameters.

The multiple exposure type also allowed the reduction of the linear displacement deviation of positions along the y-axis (Figure 3.110). In this respect, it was found that the average deviations of y-positions are tendency higher for positive than for negative features, as previously verified in Figure 3.41. In fact, the negative y-positions presented average deviations decreasing from a maximum of 0.19 mm to a minimum of 0.10 mm, while the positive y-positions presented average deviations ranging from 0.26 mm to 0.14 mm.

This analysis allowed to define a factor of deviation (in %) for negative and positive x and y pins, regardless of their specific coordinates, that can be applied in parts produced by SLS depending on the combination of parameters (Figure 3.111).

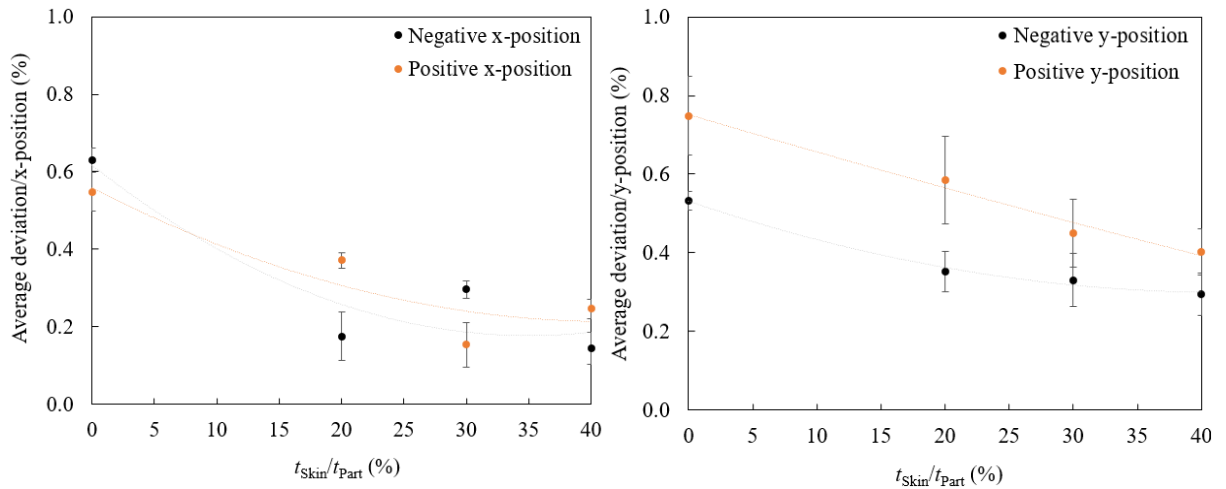


Figure 3.111 Factor of deviation (in %) for x (left) and y (right) positions of pins in parts produced by SLS depending on the combination of parameters.

The tolerancing of location of negative and positive z-positions is illustrated in Figure 3.112.

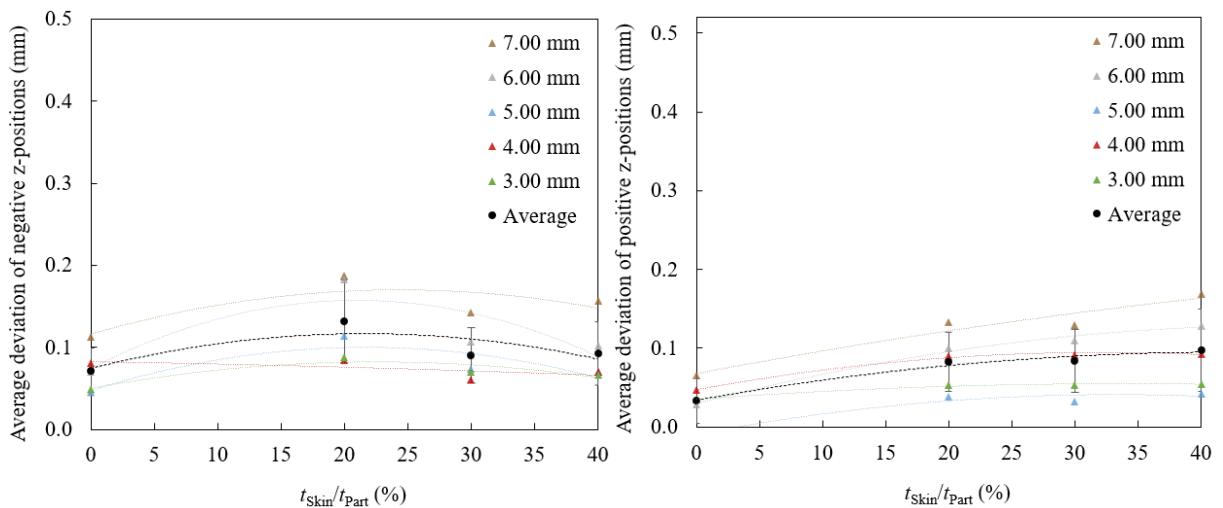


Figure 3.112 Average deviations of negative (left) and positive (right) z-positions of staircases in test artefacts produced by SLS depending on the combination of parameters.

Based on the plots, it was verified that the linear displacement deviation of z-positions did not reveal significant variations with the combination of parameters adopted in P19, P20 and P21. Regardless of the experiment, all deviations remained below 0.10 mm (on average).

The dimensional and geometric analysis of pins and holes of test artefacts produced by SLS depending on the combination of skin/core parameters is shown in Figure 3.113 and Figure 3.114, respectively.

Chapter 3. Optimization of SLS process parameters

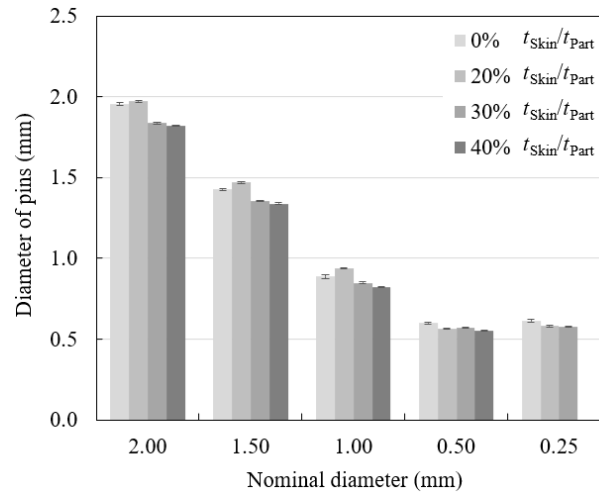


Figure 3.113 Diameter of pins of test artefacts produced by SLS depending on the combination of parameters.

In these experiments, all fine pins until 0.25 mm of nominal diameter were produced, except the condition of 40% of t_{Skin}/t_{Part} that was not able to produce the smallest one (see Figure 3.98). The dimensional accuracy of each fine pin was influenced by the combination of parameters. In this way, it was demonstrated that experiments P15 and P19 revealed similar outputs, although experiment P19 has ensured greater dimensional accuracy. Despite that, both experimental conditions were able to produce fine pins until 0.50 mm of nominal diameter with deviations less than 0.10 mm, on average. In contrast, experiments P20 and P21 exceeded deviations of 0.10 mm in all fine pins and, therefore, did not reach a satisfactory dimensional tolerance. Regardless of the experiment, it was also proved that fine pins with nominal diameter of 0.25 mm exhibit an average diameter above 0.50 mm, which establishes the minimum pin size achievable by the laser-sintering system.

Moreover, the results related to the holes showed that the combination of skin/core parameters allows the sintering of the fine holes that were not observed in test artefacts produced with 0% of t_{Skin} (Figure 3.114). As medium-low values of energy are advantageous to produce fine holes, higher values of t_{Skin} sintered with 0.198 J/mm³ are desired. In this regard, 20% of t_{Skin}/t_{Part} allowed the production of fine pins until 1.50 mm, while 30% and 40% of t_{Skin}/t_{Part} allowed the production of fine pins until 1.00 mm of nominal diameter. Despite that, a satisfactory dimensional tolerance below 0.10 mm was not attained by any condition.

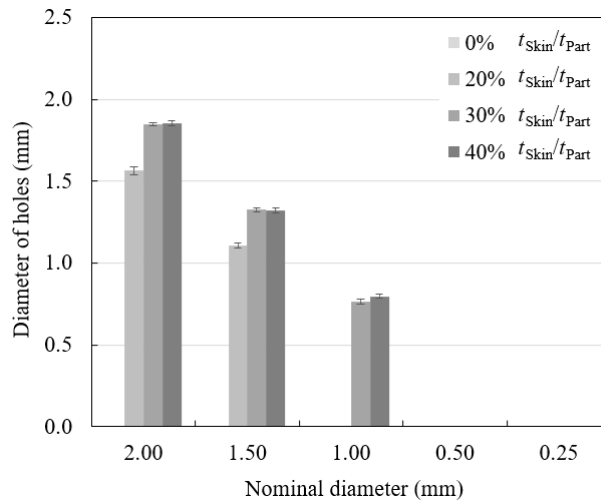


Figure 3.114 Diameter of holes of test artefacts produced by SLS depending on the combination of parameters.

In summary, this analysis demonstrated the valuable potential of the combination of parameters to improve the dimensional and geometric accuracy of parts produced by SLS with a medium-high level of energy defined for the core. This approach that combines different values of energy had particular influence on the flatness of the horizontal top plane, straightness of the primary surface, average deviations of x and y positions and manufacturing of fine holes. A great compromise between the GD&T functions is allowed depending on the combination of parameters that are defined.

3.4.3.4. Mechanical properties

Tensile properties

Representative engineering stress-strain curves of test specimens produced by SLS depending on the combination of parameters are presented in Figure 3.115.

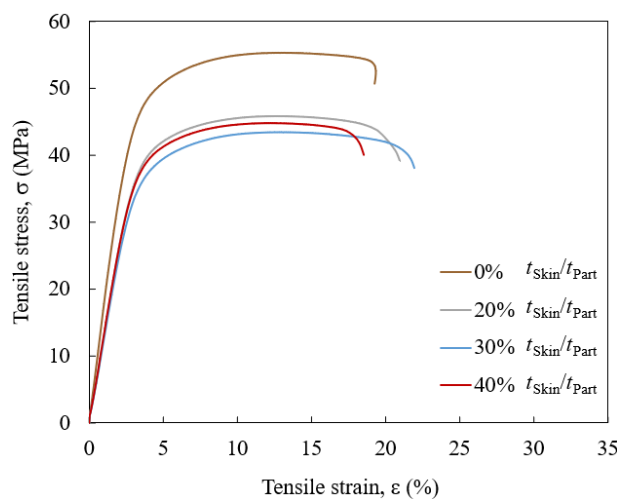


Figure 3.115 Engineering stress-strain curves of test specimens produced by SLS depending on the combination of parameters.

Chapter 3. Optimization of SLS process parameters

This first analysis revealed that the overall mechanical properties decreased in test specimens produced with 20%, 30% and 40% of $t_{\text{Skin}}/t_{\text{Part}}$ sintered with 0.198 J/mm^3 , compared to test specimens entirely produced with 0.318 J/mm^3 . In fact, this was an expected outcome since it was previously proved that medium-high EDv values are advantageous to increase the elastic modulus and tensile strength of SLS parts (see *section 3.4.1.4*). This behaviour was clearly observed through the representation of the variation of the elastic modulus of test specimens produced by SLS as a function of the combination of parameters (Figure 3.116).

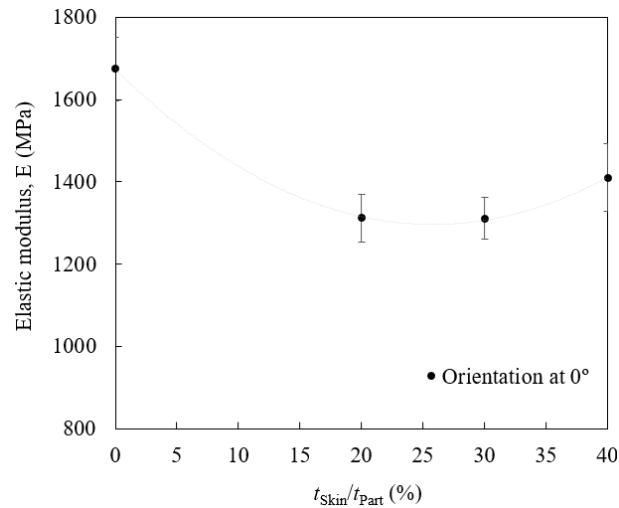


Figure 3.116 Elastic modulus of test specimens produced by SLS depending on the combination of parameters.

The elastic modulus decreased from $1674.5 \pm 77.7 \text{ MPa}$ in test specimens produced with a single exposure type to values ranging from $1311.6 - 1409.7 \text{ MPa}$ in test specimens produced with a combination of parameters. These values are slightly below to those recorded by test specimens produced with 0.198 J/mm^3 under similar conditions. Furthermore, the results did not demonstrate a direct dependence on the variation of the elastic modulus with the $t_{\text{Skin}}/t_{\text{Part}}$ relationship.

The tensile stress at yield and corresponding tensile strain revealed a coherent behaviour (Figure 3.117 (left and right, respectively)).

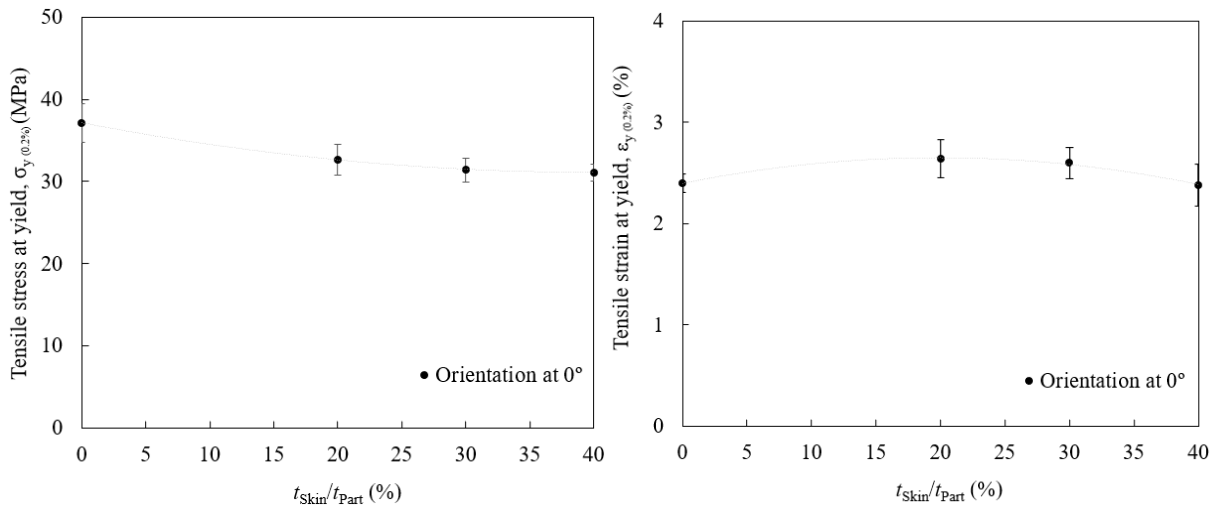


Figure 3.117 Tensile stress at yield (left) and tensile strain at yield (right) of test specimens produced by SLS depending on the combination of parameters.

The tensile stress at yield gradually decreased from 37.2 ± 2.3 MPa in test specimens produced without combination of parameters to a minimum of 31.1 ± 1.0 MPa in test specimens produced with 40% of t_{Skin}/t_{Part} , recording a reduction of 16.4 % (Figure 3.117 (left)). Compared with test specimens entirely produced with 0.198 J/mm^3 (*i.e.*, 25.3 ± 1.1 MPa), test specimens produced with combination of parameters exhibited intermediate values of tensile stress at yield, achieving an appropriate balance between the properties of skin and core layers. The results of tensile strain at yield showed a slight increase in test specimens produced in P19, P20 and P21, recording values closer to those obtained for the conditions used in the core than for the conditions used in the skin (Figure 3.117 (right)). Similar outputs were verified for the tensile stress at break (Figure 3.118 (left)).

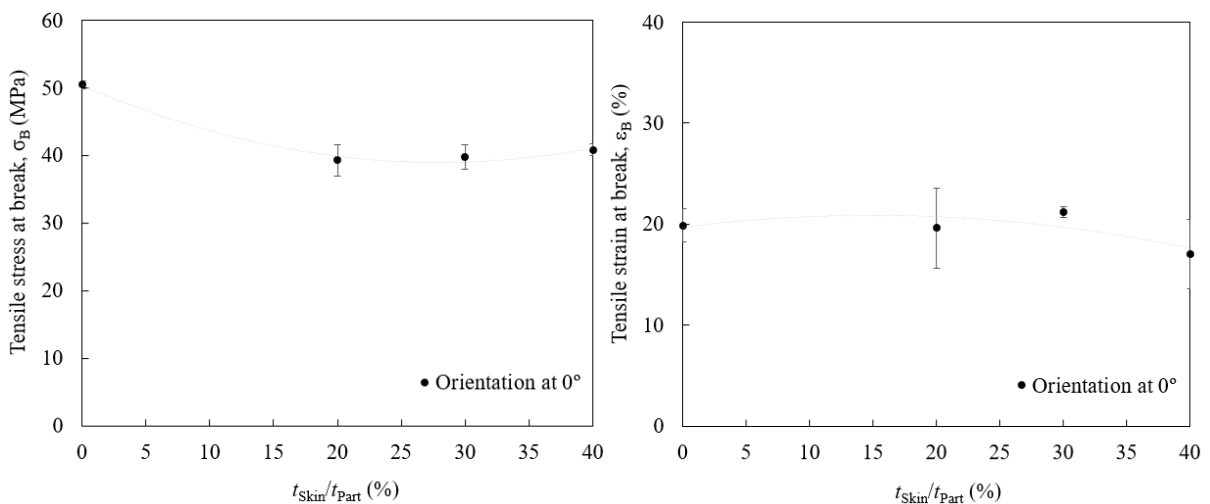


Figure 3.118 Tensile stress at break (left) and tensile strain at break (right) of test specimens produced by SLS depending on the combination of parameters.

The tensile stress at break reduced 19.2% from 50.5 ± 1.1 MPa in test specimens produced without combination of parameters to 40.8 ± 0.9 MPa in test specimens produced with 40% of t_{Skin}/t_{Part} . These

Chapter 3. Optimization of SLS process parameters

values were closer to those obtained for the conditions used in the skin than for the conditions used in the core. In contrast, the tensile strain at break did not reveal a significant variation with the $t_{\text{Skin}}/t_{\text{Part}}$ relationship, recording values similar to those obtained in test specimens entirely produced with 0.318 J/mm^3 (Figure 3.118 (right)).

The tensile strength reached a maximum reduction of 20.3% from $55.6 \pm 0.8 \text{ MPa}$ to values ranging between $44.3 - 46.0 \text{ MPa}$ (Figure 3.119). In fact, these values are more similar to those obtained in test specimens entirely produced with 0.198 J/mm^3 (*i.e.*, EDv value defined for the skin) than to those obtained in test specimens entirely produced with 0.318 J/mm^3 (*i.e.*, EDv value defined for the core).

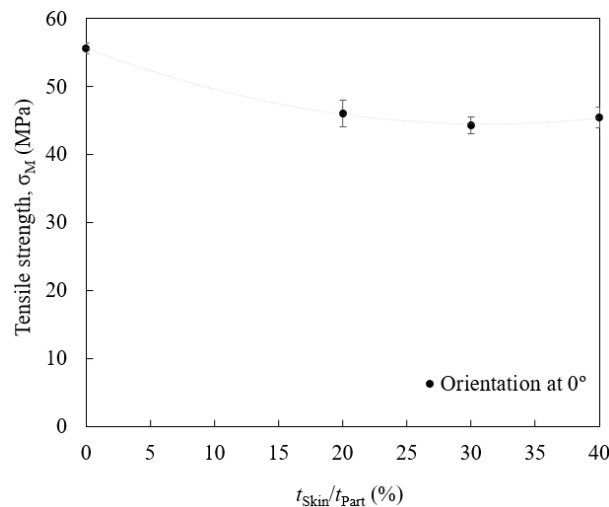


Figure 3.119 Tensile strength of test specimens produced by SLS depending on the combination of parameters.

The results obtained from uniaxial tensile testing revealed that the mechanical properties of SLS parts produced with the combination of parameters selected for this analysis are reduced 20% (on average), concerning the elastic modulus and characteristic tensile stresses. This is a consequence of the increasing number of layers sintered with low EDv values instead of the medium-high level of energy defined for the core. The effect between combined and non-combined configurations had greater influence on the overall properties of the test specimens than the specific $t_{\text{Skin}}/t_{\text{Part}}$ relationship adopted in experiments P19, P20 and P21. In general, the tensile stress at yield presented the most satisfactory output, the tensile stress at break and tensile strength presented intermediate-low values, the elastic modulus presented the highest reduction and the tensile strain at yield and tensile strain at yield break did not exhibit a significant variation. In addition to the low EDv value defined for the skin, these outputs can be explained by the combination of such different values that may not be favourable for the overall performance of parts produced by SLS.

Fracture properties

Figure 3.120 shows experimental P - δ curves obtained from DCB tests and corresponding R -curves by applying the CBBM of test specimens produced by SLS depending on the combination of parameters.

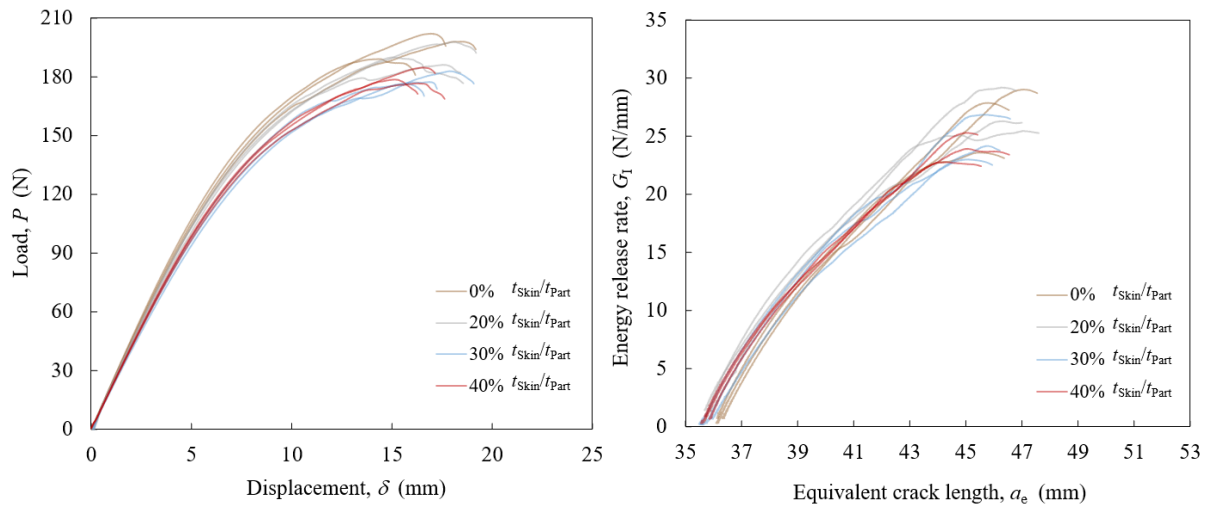


Figure 3.120 Experimental P - δ curves (left) and R -curves (right) of test specimens produced by SLS depending on the combination of parameters.

In these experiments, the test specimens revealed less initial elastic compliance and reduced values of G_{Ic} and G_{Iu} with the increase of the t_{Skin}/t_{Part} relationship (Figure 3.121). The results demonstrated that G_{Ic} gradually decreased from 26.8 ± 2.9 N/mm in test specimens produced with a single exposure type to a minimum of 23.9 ± 1.3 N/mm in test specimens produced with 40% of t_{Skin}/t_{Part} , recording a difference of 11%. This is a consequence of the enhanced fracture toughness attained in test specimens produced under high levels of energy. Despite that, these outputs evidence that the combination of parameters did not have as much influence on this mechanical property as the hatching parameters defined by the EDv value that induced differences of G_{Ic} above 300% (see Figure 3.63).

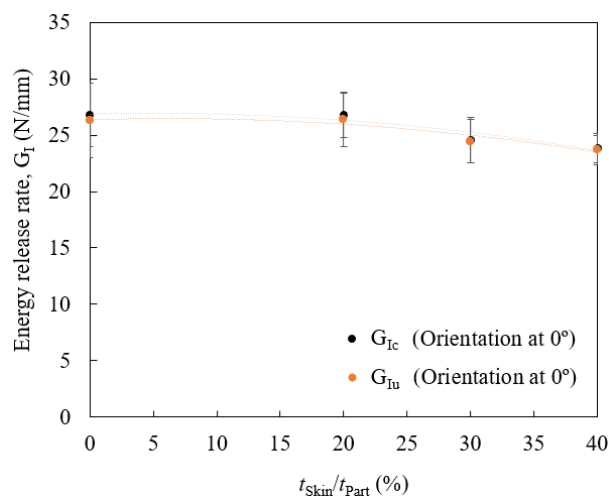


Figure 3.121 Mode I energy release rate of test specimens produced by SLS depending on the combination of parameters.

3.4.3.5. Morphological properties

Figure 3.122 illustrates SEM micrographs of the cross-section of test specimens produced by SLS with combination of parameters, including 20% (left), 30% (middle) and 40% (right) of t_{Skin}/t_{Part} sintered with low EDv values.

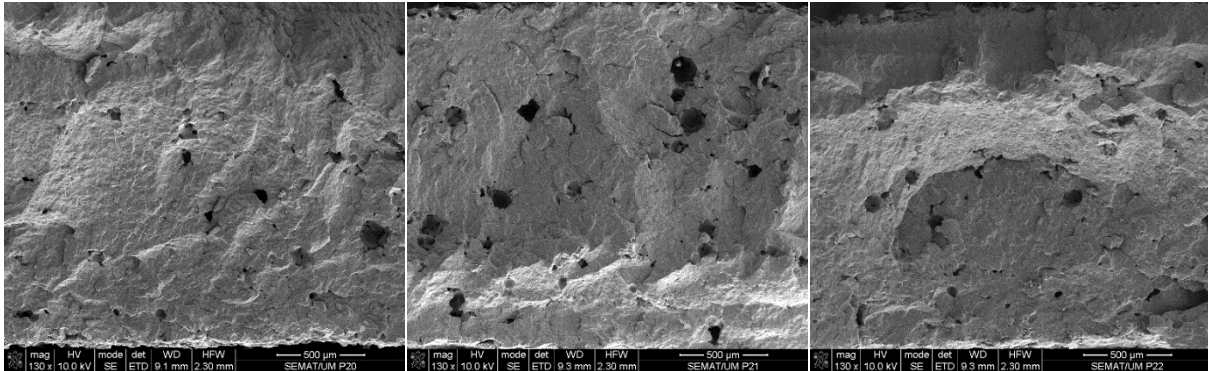


Figure 3.122 Cross-section of test specimens produced by SLS with 20% (left), 30% (middle) and 40% (right) of t_{Skin}/t_{Part} .

This morphological characterization showed that the cross-section of test specimens produced with the combination of parameters considered for this section still presented high content of porosity with microcracks reaching an average of 150 μm of diameter. However, the micrographs did not reveal clear differences between the layers defining the skin and core configurations and no significant modifications in the cross-section of test specimens produced in experiments P19, P20 and P21. In accordance with the assumptions provided in *section 3.4.2.5* for the contour parameters, this suggests that the morphological structure of SLS parts is mostly governed by the EDv value supplied for the hatching layers.

3.4.3.6. Process characterization

Table 3.8 lists the building time of all productions considered to study the combination of parameters.

Table 3.8 Building time of SLS productions depending on the combination of parameters.

Building time, t (s)	
P15	4593
P19	4502
P20	4568
P21	4440

The results proved that the adoption of a multiple exposure type instead of a single configuration does not have a significant influence on the building time, considering the combination of parameters selected for the analysis (Figure 3.123).

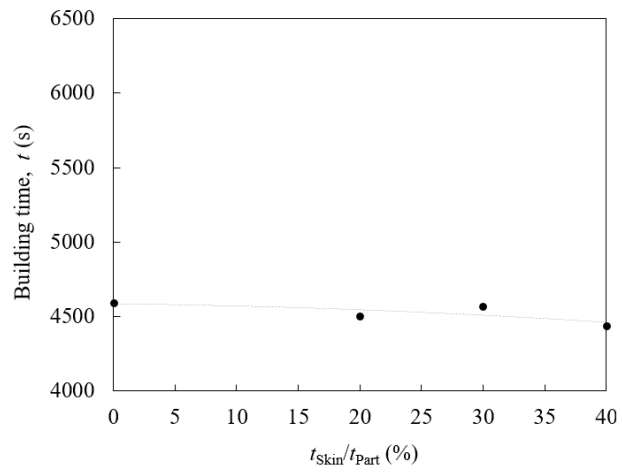


Figure 3.123 Building time of SLS processes depending on the combination of parameters.

Final Remarks of Chapter 3

Chapter 3 provides critical knowledge about the effect of the thermal energy supplied by the laser beam to the powder particles during the SLS process on the global performance of parts horizontally produced, answering the RQ₁ (see *Chapter 1*). The experiments analysed in this chapter demonstrated that the energy density by unit of volume, ED_v, has a significant influence on the dimensional, geometric, mechanical and morphological properties of SLS parts. In this regard, it was proved that medium-low ED_v values defining the hatching set, namely from 0.158 J/mm³ to 0.238 J/mm³, are advantageous to ensure great dimensional and geometric outputs. In contrast, medium-high ED_v values, namely from 0.278 J/mm³ to 0.318 J/mm³, are beneficial to maximize the mass and mechanical properties of parts. The macro and micro-scale characterization revealed that the process becomes unfeasible above 0.318 J/mm³ due to the excessive level of energy and negative effects induced by the secondary sintering. For an elected ED_v value (*i.e.*, 0.318 J/mm³), the results showed that the laser beam should preferably be operating in the xy-direction-alternating and y-direction, rather than the xy-direction-simultaneous and x-direction strategies, in order to maximize some relevant outputs. For an optimum hatching set, it was verified that the modification of the contour parameters in the conventional parameterization mode, from low to high values of energy, does not have a significant impact on the overall performance of parts. In turn, a promising balance between non-compatible properties that require different process parameters to be optimized can be assured by applying a multiple exposure type. This advanced parameterization mode makes it possible to combine medium-low values of energy supplied to the external layers promoting dimensional and geometric accuracy and medium-high values of energy supplied to the internal layers ensuring mechanical strength. In this respect, the experiments indicated that the implementation of a skin/core configuration allows the production of SLS parts with a valuable set of properties, minimizing the trade-off between mechanical strength and overall accuracy. Although in this chapter the combined analysis was focused on a balanced compromise of properties, the methodology can be extended to different combinations of parameters depending on the technical specifications demanded by industrials. The estimation of the properties of SLS parts as a function of the process parameters is allowed by the comprehension of the process-structure-property relationship⁵ investigated in this chapter which is essential for the process control and monitoring.

⁵ *Appendix B* summarizes the main properties and experimental regressions obtained in this work for different SLS process parameters.

Chapter 4. Development and characterization of SLS composite materials

Chapter 4 provides the methodological approach implemented in this research to develop multi-functional composite materials for SLS, including a description of the reinforcements, methods of preparation, conditions of processing and macro and micro-scale characterization. Obtaining a carbon-based material with electrical surface resistance in the electrostatic dissipative range, maintaining reasonable mechanical and morphological properties, was the main focus of this activity. Throughout the chapter, useful insights to incorporate micro and nanoparticles into conventional thermoplastic materials for successful SLS processing are provided.

4.1. Introduction

Electrostatic discharge (ESD) problems generated between electronic components presenting different electrical potential are responsible for about 25% of a complete failure, leading to critical economic declines (Joseph *et al.*, 2014; de Souza Vieira *et al.*, 2021). Because of that, functional materials capable to protect sensitive electronic devices against premature and irreversible damages caused by ESD interferences during handling, storage, transportation and operation are continuously required (Narkis *et al.*, 1999; Silva *et al.*, 2020). With the purpose to replace conventional metals, highly conductive carbon-based reinforcements embedded in polymeric matrices are frequently considered due to their potential to ensure lightweight, great properties and easy processability, while ensuring a slow electrostatic discharge when a specific range of electrical surface resistance is attained (Nazir *et al.*, 2018; de Souza Vieira *et al.*, 2021). Despite the on-course developments, conductive polymeric composites for powder bed fusion processes with the aim of being used as ESD protective materials are still scarce. Based on that application purpose, this chapter focuses on the development of SLS composite materials with dimensional accuracy, mechanical strength and ESD properties allowing their use in components with direct contact with electrostatic discharge-sensitive devices (ESDS) for the electronics industry. To this aim, a series of experiments was conducted to evaluate the individual and combined effect of different carbon-based reinforcements, various weight percentages of incorporation and different conditions of preparation in the final properties of composite parts produced by SLS. The following sections describe the four main sequential activities of this work, namely i) selection of reinforcements, ii) composite preparation, iii) composite processing and iv) composite characterization.

4.2. Materials and methods

Initially, the experiments established to develop multi-functional composite materials for SLS were carried out in a sPro 60 SLS Center laser-sintering machine. This is an equipment for AM supplied by 3D SYSTEMS Inc., with an effective building volume of 381 x 350 x 457 mm, operating with a CO₂ laser. This open-system machine was used to execute first production attempts and to define primary conditions of development with regard to the matrix and mixing methods. After these preliminary experiments, the study was conducted in an EOS P 396 laser-sintering machine. Due to its operating principle, powder vibrating devices were coupled to the feed containers aiming to avoid eventual compaction effects caused by the inclusion of carbon-based reinforcements.

In all experiments, a non-conductive PA12 powder, namely the PA 2200 from EOS GmbH, was used as polymeric matrix. In the beginning, the performance of composite materials produced with highly reprocessed PA12 (*i.e.*, without mixtures) and with a mixture of 50% of processed with 50% of virgin PA12

was assessed, maintaining the same conditions of preparation and processing. According to the results, the influence of different carbon-based reinforcements was evaluated assuming a mixture ratio of 50:50%, as this allows the production of parts with greater mechanical performance and reduced content of porosity (Figure 4.1 and Figure 4.2).

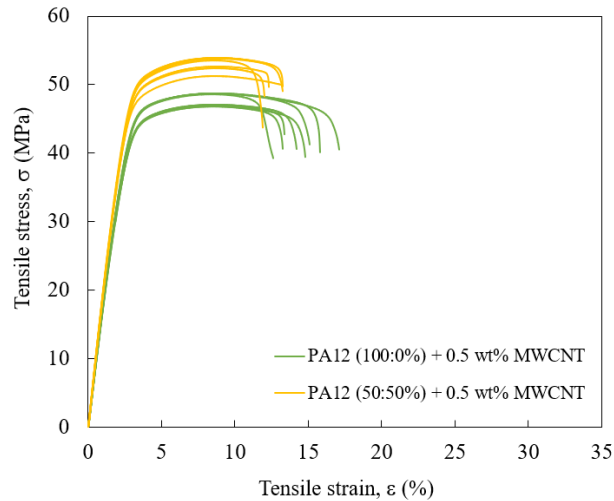


Figure 4.1 Engineering stress-strain curves of test specimens produced by SLS with composite materials considering a PA12 matrix in a ratio of 100:0% and 50:50%.

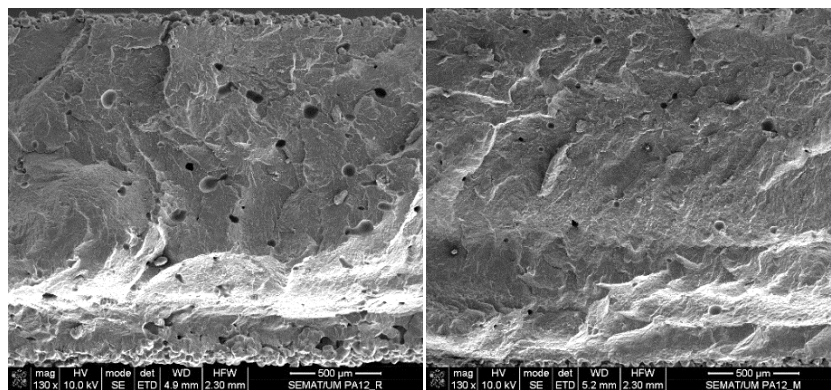


Figure 4.2 Cross-section of test specimens produced by SLS with composite materials considering a PA12 matrix in a ratio of 100:0% (left) and 50:50% (right).

4.2.1. Selection of reinforcements

Focusing on the purpose of obtaining SLS composite materials with electrical surface resistance in the ESD range, this research embraced the evaluation of carbon-based composites produced with MWCNT and Graphene Nanoplatelets (GNP) in individual and combined configurations. To do so, the MWCNT NC7000™ supplied by NANOCYL and the Multi-Layer GNP supplied by Graphenest, S.A were used. The MWCNT are produced by catalytic chemical vapor deposition presenting 90% of carbon purity and nominal average dimensions of 9.5 nm of diameter and 1.5 μm of length (NANOCYL, 2016). In turn, the GNP are produced by liquid-phase exfoliation with lateral dimensions ranging from 1 μm to 20 μm (Graphenest,

2017). Figure 4.3 shows the original morphological structure of each as-received carbon-based reinforcement obtained by Transmission Electron Microscopy (TEM).

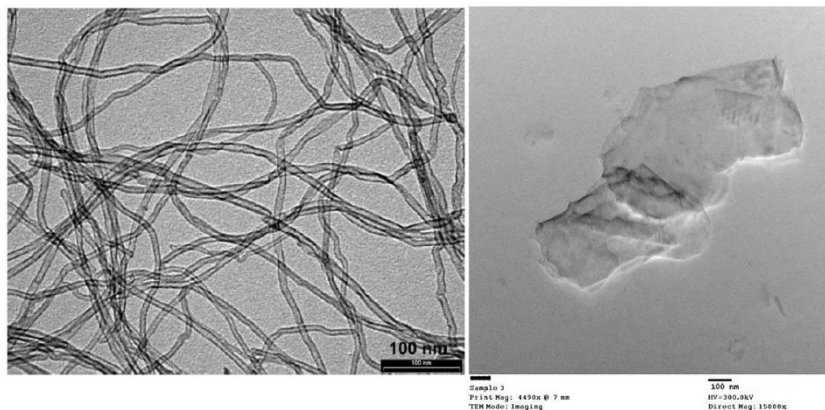


Figure 4.3 TEM images of NANOCYL MWCNT NC7000™ (left) and Graphenest Multi-Layer GNP (right) (NANOCYL, 2016; Graphenest, 2017).

In the first approach, the weight percentages of 0.50 wt%, 1.75 wt% and 3.00 wt% of MWCNT and GNP were considered in independent productions (experiments P1 to P6 (Table 4.1)), seeking for the critical amount of reinforcement that guarantees the physical contact between the conductive particles reducing the electrical resistivity, without compromising the mechanical and rheological properties of the matrix (de Souza Vieira *et al.*, 2021). In the second approach, a combined formulation of both carbon-based reinforcements was prepared in order to foster a synergistic effect. Based on the results collected in the initial experiments, the analysis was extended to composites produced with 0.50 wt% MWCNT + 0.10 wt% GNP (experiment P7 (Table 4.1)).

4.2.2. Preparation of composite materials

To avoid high development costs, the composite materials were prepared through mechanical mixing. The main challenge of using this method was to establish a simple and systematic approach capable to guarantee uniform dispersion and distribution of the reinforcements ensuring the repeatability of results between experiments. Therefore, the mechanical mixing was carried out in a 3devo AIRID Polymer Dryer that operates with a self-sufficient mixing system through a stirring rotator. The mixture was prepared in a continuous process at 15 rpm for 12, 18 and 24 hours at 23 °C. Since initial experiments demonstrated that the main properties of the composites are almost insensitive to the mixing time above 12 hours (for the considered setup), it was set at 12 hours for all experiments. It is important to note that in addition to the preparation method, the movement of the recoater to spread the powder particles across the building platform during the processing also plays a critical role in the dispersion and distribution of the carbon-based reinforcements within the matrix.

4.2.3. Processing of composite materials

As literature suggests that the inclusion of carbon-based reinforcements intensifies the conduction of energy through the layers of powder, a value below the optimal EDv proposed in *Chapter 3* was selected for the experiments. Hence, the composite materials were processed with the medium-low value of 0.238 J/mm³, defined with the process parameters of experiment P8 (see Table 3.1). This value was selected after a prior optimization that took into account the number of test specimens positioned in the x-y plane determining the time between the deposition of two consecutive layers. Above 0.238 J/mm³, the high thermal gradient generated inside the building chamber between sintered and unsintered powder particles of PA12-MWCNT and PA12-GNP caused the warpage of the test specimens between the successive deposition of layers, restricting the smooth movement of the recoater (Figure 4.4). In consequence of the drag effects, the sintering process conducted with higher EDv values proved to be unfeasible to produce parts with the composite materials developed within the scope of this research.

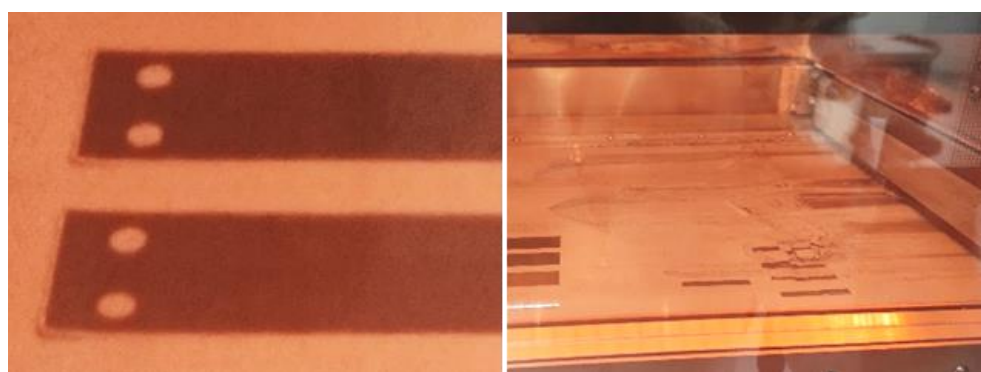


Figure 4.4 Test specimens produced by SLS with PA12 with 1.75 wt% of MWCNT with 0.278 J/m³.

After the process optimization, the test specimens planned for characterization were produced. The test specimens were horizontally positioned in the central region of the building platform in order to reduce the influence of the thermal gradients. The corresponding data files were prepared for the sintering process using Magics Materialize, EOS RP Tools and EOS PSW 3.8 software, considering the process parameters previously selected. After production and cooling inside the laser-sintering machine, the test specimens were cleaned in a Sintratec Blasting Station with compressed air and in a Sintratec Polishing Station with stainless-steel magnetic polishing pins to ensure smooth surface finishing. No additional post-production treatments were considered in this study. Before testing, the test specimens were stored in a room with controlled environment of 22 °C and 40 rH%.

Table 4.1 summarizes the experiments conducted to study the carbon-based composites, according to the methodological approach previously described.

Table 4.1 Experiments defined to study carbon-based composites.

	POLYMERIC MATRIX (MIXTURE RATIO)	CARBON-BASED REINFORCEMENT	PREPARATION METHOD	RATIO (wt%)	
				MWCNT	GNP
P ₁	PA12 (50:50%)	MWCNT	Mechanical mixing (12h at 15 rpm)	0.50	Not included
P ₂				1.75	
P ₃				3.00	
P ₄	PA12 (50:50%)	GNP	Mechanical mixing (12h at 15 rpm)	Not included	0.50
P ₅					1.75
P ₆					3.00
P ₇	PA12 (50:50%)	MWCNT + GNP	Mechanical mixing (12h at 15 rpm)	0.50	0.10

4.3. Characterization tests

Several characterization tests were carried out at different stages of the materials development, in the condition of powder and full-sintered part. The composite powders prepared through mechanical mixing were thermally characterized aiming to identify the SLS processing window and suitable conditions of sintering. In turn, the analysis of test specimens comprised the assessment of dimensional, geometric, mechanical, electrical, thermal and morphological properties. Test specimens produced with neat-PA12 material using the same conditions of processing were also produced and characterized for reference. The testing conditions used in this analysis are following described in *section 4.3.1* to *section 4.3.7*.

4.3.1. Mass and general dimensions

After production and cooling, five test specimens per condition were evaluated in terms of thickness, width and length in three different points using a GARANT DC2 calliper. The mass of test specimens was also recorded using a KERN Precision balance.

4.3.2. Dimensional and geometric accuracy

The dimensional and geometric accuracy of the composite solutions was evaluated with the test artefact illustrated in Figure 3.2 using X-Ray CT and the measurement rules adopted in *section 3.3.2* (see *Chapter 3*). The GD&T parameters were determined with an average of five measurements per feature and condition. The quantitative results and corresponding CT images were compared with the CAD model and with test artefacts produced with other carbon-based formulations.

4.3.3. Surface roughness

The surface roughness of test specimens produced with the developed composite materials was determined through optical 3D measurements based on the Focus-Variation technology. For the analysis, an InfiniteFocusSL Alicona microscope operating with a 10x objective magnification with lateral topographic resolution of 2.0 μm was used. The surface roughness of the polymeric matrix was not experimentally assessed as white samples cannot be measured by this optical system. The experimental parameters (*e.g.*, exposure time, contrast, vertical and lateral resolution) were differently adjusted for MWCNT and GNP-based composites to successfully acquire the resulting surface topography.

4.3.4. Mechanical tests

The mechanical performance of the composite materials developed in this work was in detail characterized through tensile, compression and impact tests.

4.3.4.1. Tensile tests

The mechanical properties, namely the elastic modulus, tensile strength, tensile stress at yield (0.2% offset), tensile stress at break, tensile strain at yield and tensile strain at break (ISO 527-1), were evaluated through tensile tests carried out in an Instron 5969 Universal Testing System. Five test specimens, type 1BA (ISO 527-2) (Figure 3.3), were tested at 1 mm/min at room temperature with a load-cell of 50 kN (ISO, 1996).

4.3.4.2. Compression tests

The compression tests were carried out in an Instron 5969 Universal Testing System with a load-cell of 50 kN at room temperature in order to determine the compressive modulus and compressive strength of the test specimens. Five test specimens with the geometry illustrated in Figure 4.5 were tested at 1.3 mm/min, according to ASTM D695 (ASTM, 2002). Corrections for slack, alignment and seating effects were applied to the stress-strain curves.

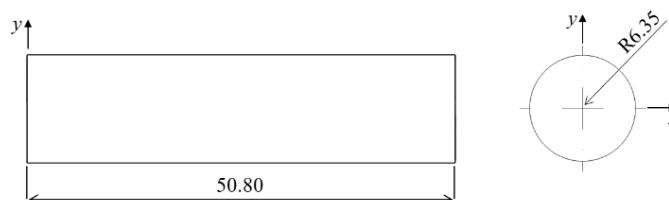


Figure 4.5 Test specimen for compression tests (dimensions in mm).

4.3.4.3. Izod impact tests

The Izod impact tests were performed in a CEAST Impact Testing Machine at room temperature according to Test Method A described in ASTM D256 (ASTM, 2004). The test specimens shown in Figure

Chapter 4. Development and characterization of SLS composite materials

4.6 were prepared with a v-notch in a CEAST notching machine operating with a linear cutting technique. The tests were conducted in five test specimens using a pendulum with 4 J of capacity (*i.e.*, lightest standard pendulum available for the analysis). The resulting impact resistance was determined in kJ/m^2 , considering the width and depth of the test specimens under the notch. Corrections for windage and friction were applied.

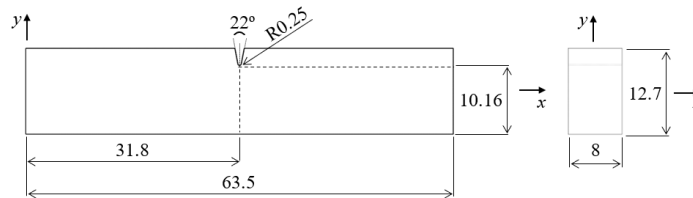


Figure 4.6. Test specimen for Izod impact tests (dimensions in mm).

4.3.5. Electrical tests

A Keithley Model 8009 Resistivity Test Fixture operating at 10 V was used to determine the electrical resistance and resistivity of the composite materials in a minimum of three test specimens per condition through an average of 100 readings, based on the standard test norm ASTM D257. As an inverse of the determined resistivity, the electrical conductivity was also quantified. The test norm IEC 61340-5 (IEC, 1998) was used to categorize the appropriateness of each composite material for ESD protection applications, depending on the insulative, dissipative or conductive range. For the analysis, test specimens with the nominal dimensions 100 x 100 x 1.5 mm were produced, in accordance with the electrode configuration (Figure 4.7).

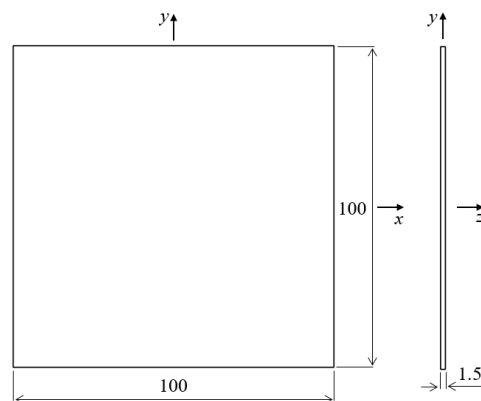


Figure 4.7 Test specimen for electrical tests (dimensions in mm).

4.3.6. Thermal tests

4.3.6.1. Differential Scanning Calorimetry (DSC)

Differential Scanning Calorimetry (DSC) measurements were performed to evaluate the melting and crystallization temperatures of the composite materials prepared through mechanical mixing in order to

identify their thermal processing window. The analyses were carried out in a Netzsch DSC 200 F3 Maia with a small portion of sample (*i.e.*, 2 – 40 mg, according to ISO 11357 (ISO, 2016)) using the following scanning program: i) isothermal of 1 min at 30 °C, ii) first heating at 10 °C/min from 30°C to 230 °C, iii) isothermal of 1 min at 230 °C, iv) cooling at 10 °C/min from 230 °C to 30 °C, v) isothermal of 1 min at 30 °C and vi) second heating at 10 °C/min to 230 °C, under a nitrogen atmosphere.

A small portion of the test specimens was also evaluated through DSC in order to determine the specific heat capacity of the materials, since this is an important property that directly influences the amount of energy that the sintering process should provide (Tan *et al.*, 2020). The measurements were conducted from 20 °C to 200 °C at 10 °C/min and the specific heat capacity of the samples ($C_{p,sample}$) was determined according to ASTM E1269 based on Eq. (4.1) (ASTM, 2011):

$$C_{p,sample} = \frac{m_{sapphire}}{m_{sample}} \times \frac{\varphi_{sample}(T) - \varphi_0(T)}{\varphi_{sapphire}(T) - \varphi_0(T)} \times C_{p,sapphire} \quad (4.1)$$

which depends on the DSC signal of the baseline (φ_0), mass and DSC signal of the sample (m_{sample} , φ_{sample} , respectively) and mass, DSC signal and specific heat capacity of a synthetic sapphire⁶ ($m_{sapphire}$, $\varphi_{sapphire}$, $C_{p,sapphire}$, respectively).

4.3.6.2. Thermogravimetric analysis (TGA)

A TA Q500 was used to perform a Thermogravimetric Analysis (TGA) in order to evaluate the thermal stability of the composite materials during a heating program at 10 °C/min, from 40 °C to 700 °C, under a nitrogen atmosphere, according to the standard test method ASTM E1131 (ASTM, 2008).

4.3.7. Morphological assessment

Scanning Electron Microscopy (SEM) analyses were carried out to characterize the cross-section of test specimens produced with the developed composite materials with regard to the dispersion and distribution of the carbon-based reinforcements and resulting content of porosity. The micrographs were taken in a Nano SEM FEI Nova 200 equipment operating with an acceleration voltage of 10 kV. Before the analyses, the samples were cryogenically cut and prepared with 15 nm of gold coating.

4.3.8. Process characterization

Figure 4.8 shows the position and orientation of the test specimens at 0° in relation to the powder bed in the central region of the EOS P 396 building platform, in reference to the x, y and z axes. This building

⁶ Reference material with known specific heat capacity (ASTM E1269).

Chapter 4. Development and characterization of SLS composite materials

configuration was selected to guarantee a reduced number of test specimens per layer and their central positioning on the platform, without a significant increase in the height of construction along the z-axis.

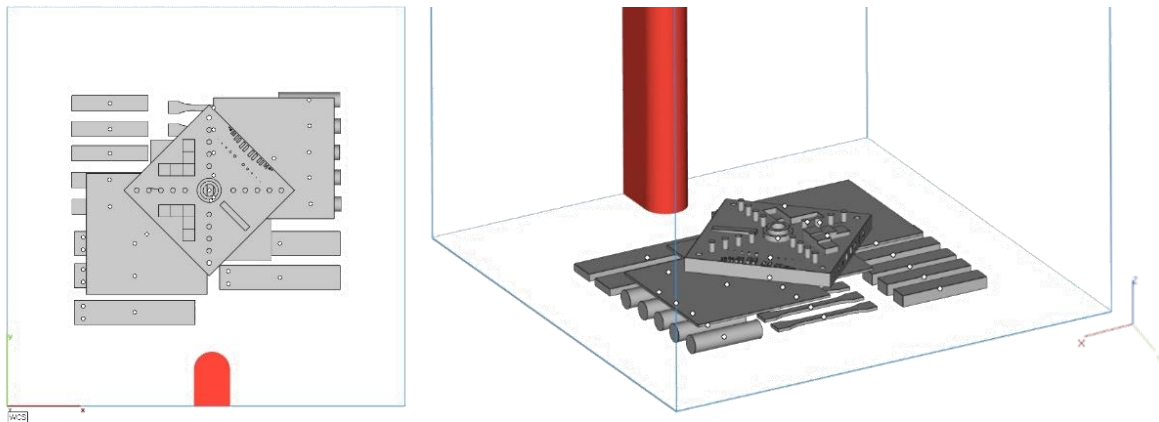


Figure 4.8 Position and orientation of the test specimens in the EOS P 396 building platform.

In addition to the assessment of properties of test specimens, qualitative properties of the SLS process were recorded by monitoring the sintering chamber during the period of building. This practice allowed to control problems of unsmooth spread of powder particles, atypical thermal mechanisms, surface heterogeneities, smoke release, etc, which could negatively affect the laser-sintering equipment.

4.4. Results and discussion

The main results obtained from the characterization tests regarding the development of multi-functional composite materials integrating conductive reinforcements are presented in this section. All quantitative results collected for discussion were prior validated with a statistical treatment to ensure a normal distribution of the data. Thus, a Normality Test (Anderson-Darling test type) combined with an Outlier Test with a significance level of 0.05 were applied using the Basic Statistics Tools of the MINITAB software.

4.4.1. PA12-MWCNT composites

4.4.1.1. Description of observations

The experiments conducted to evaluate the properties of the composite materials produced with MWCNT provided useful insights regarding their preparation and processing. About the preparation, the analysis revealed that obtaining a homogeneous mixture for SLS becomes more difficult as the amount of MWCNT increases, considering same periods of mixing. This was verified through the higher amount of unmixed particles of reinforcement migrated to the top and outer edges of the powder mixture. That effect was minimized through manual mixing conducted before and after the automatic method.

From the sintering point of view, the analysis demonstrated that the laser-sintering machine operating with a roller (*i.e.*, sPro 60 SLS Center) is preferred to process the developed composite materials than the laser-sintering machine operating with a blade (*e.g.*, EOS P 396). In the first configuration, the powder is spread from lower feed containers that rise to a height corresponding to the layer thickness, while in the second one the powder has to flow from upper feed containers, which becomes more complex due to compaction effects. In that situation, powder vibrating devices coupled to the feed containers are recommended.

In terms of processing conditions, it was verified that as the amount of MWCNT increases, the EDv value needed for a successful sintering process gradually decreases. High values of energy supplied to polymeric materials integrating a large amount of carbon-based reinforcement intensifies the thermal gradients inside the building chamber. In the context of this research, 0.238 J/mm^3 was found as the maximum allowable value to process PA12 material incorporating 0.50 wt% to 3.00 wt% of MWCNT for the number of test specimens defined per layer. Using the highest possible EDv value, within the suitable range identified in *Chapter 3*, ensures that the properties of the composites are maximized with respect to those that are controllable through the processing conditions.

Once the challenges were overcome and the process optimized, the sintering processes corresponding to experiments P1 to P3 (Table 4.1) proceeded normally. The first observations evidenced differences in colour between the test specimens produced with different composite materials. As expected, the test specimens become darker with the increasing amount of MWCNT (Figure 4.9).



Figure 4.9 Test artefacts produced by SLS with PA12 incorporating 0.50 wt%, 1.75 wt% and 3.00 wt% of MWCNT.

Different surface finishing was also observed between the test specimens produced (Figure 4.10). In this regard, a tactile perception suggested higher surface roughness in test specimens produced with greater amounts of MWCNT that may be influenced by the higher number of carbon-based particles

Chapter 4. Development and characterization of SLS composite materials

migrated and sintered close to the outer surfaces. This effect was responsible for a more difficult cleaning of the parts after the sintering process.



Figure 4.10 Top surface of test specimens produced by SLS with PA12 incorporating 0.50 wt% (left), 1.75 wt% (middle) and 3.00 wt% (right) of MWCNT.

Even with prior process optimization, the test specimens presented some warpage characteristics as a consequence of the thermal gradients intensified by the carbon-based reinforcements, including the test specimens incorporating 0.50 wt% of MWCNT (*i.e.*, the smallest amount of incorporation considered in the analysis). However, for same EDv values, these effects were more pronounced in test specimens produced with higher amounts of MWCNT, in particular in test specimens with high length/thickness ratio (Figure 4.11).



Figure 4.11 Warpage in test specimens produced by SLS with PA12 incorporating 3.00 wt% of MWCNT.

The quality of features reproduced in the top surface of the test artefacts also depended on the amount of MWCNT embedded into the polymeric matrix, as shown in Figure 4.12. Compared with the test artefact produced with neat-PA12 with 0.238 J/mm^3 where fine pins until 0.25 mm and fine holes until 1.50 mm were manufactured (even with some dimensional nonconformities), an initial qualitative evaluation revealed that the incorporation of MWCNT is disadvantageous to reproduce fine features in surfaces at 0° directed to the top. In fact, the test artefacts produced with such carbon-based composites did not reproduce any quality hole with a nominal diameter of less than 2.00 mm, even the material with the smallest incorporation of MWCNT (*i.e.*, 0.50 wt%) which, in turn, exhibited fine pins until 0.25 mm of nominal diameter. In comparison with the condition of reference, fine pins showed a more brittle

behaviour with the increasing incorporation of MWCNT. In consequence, some finer pins were broken during the challenging cleaning process, particularly in the test artefact incorporating 3.00 wt% of MWCNT.

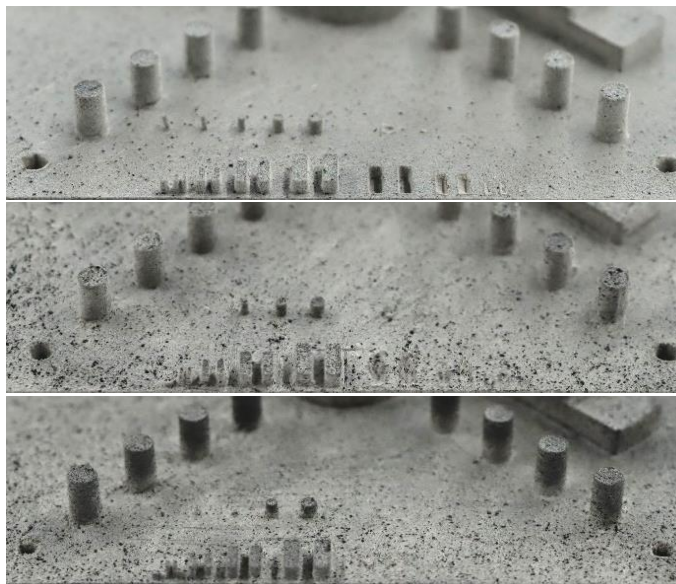


Figure 4.12 Fine features of test artefacts produced by SLS with PA12 incorporating 0.50 wt% (top), 1.75 wt% (middle) and 3.00 wt% (bottom) of MWCNT.

4.4.1.2. Mass and general dimensions

The dimensional characterization of test specimens produced with PA12 incorporating MWCNT are shown in Figure 4.13 and Figure 4.14. The results indicated that the length, width and thickness of the test specimens were not significantly modified with the inclusion of MWCNT until 3.00 wt%. In this research, the test specimens produced with composite materials ensured great dimensional accuracy with dimensions close to the nominal 100 mm in length, 20 mm in width and 5 mm in thickness. Slight variations observed may be caused by differences in the thermal gradients of processing, compared to the reference condition. In turn, the mass of test specimens produced with composite materials gradually decreased with the increasing amount of MWCNT from 0.50 wt% to 3.00 wt% (Figure 4.13 (left)). The maximum variation was verified in test specimens produced with 3.00 wt% of MWCNT that recorded a mass of 8.675 ± 0.015 g, significantly lower than the mass of test specimens produced with neat-PA12 (*i.e.*, 9.470 ± 0.040 g). This highest difference of 8.4% can be explained by the low bulk density of MWCNT (*i.e.*, 0.070 - 0.075 g/cm³ (according to NANOCYL)), in comparison to the bulk density of the neat-PA12 used in this work (*i.e.*, 0.45 g/cm³). This means that higher incorporations of MWCNT results in low density SLS parts, suggesting the suitability of such composite materials for lightweight applications.

Chapter 4. Development and characterization of SLS composite materials

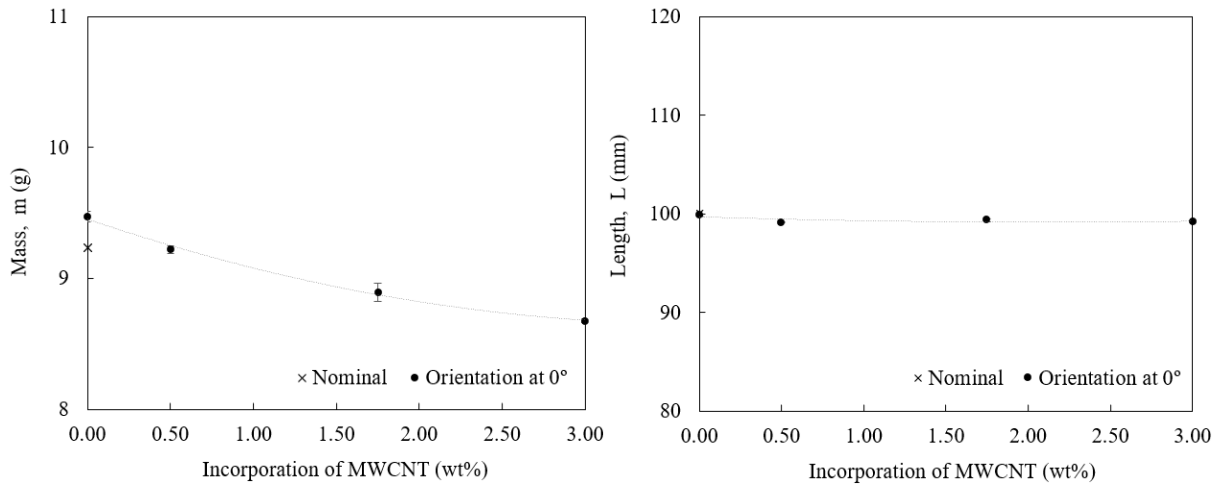


Figure 4.13 Mass (left) and length (right) of test specimens produced by SLS depending on the amount of MWCNT (in wt%).

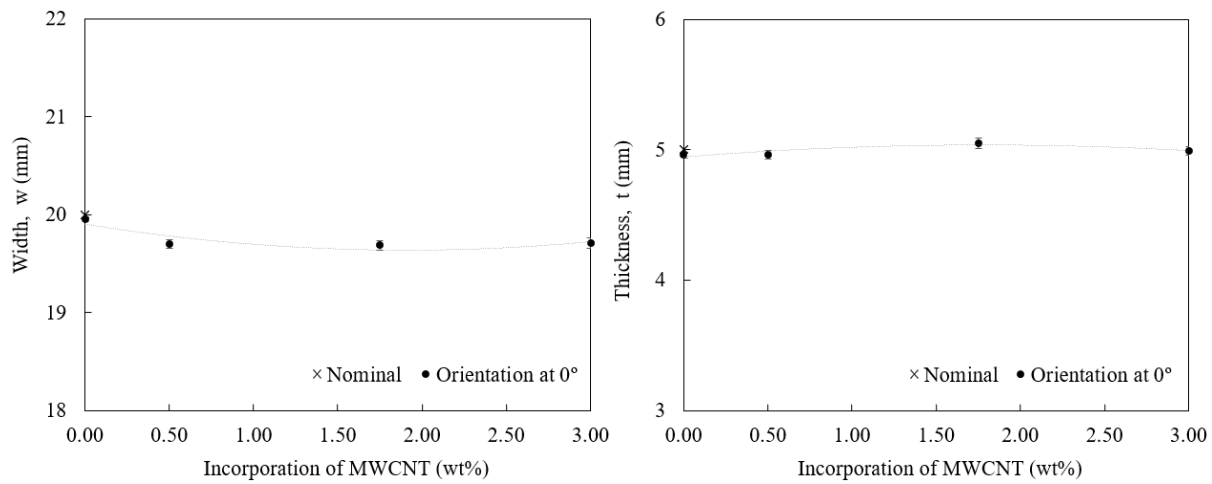


Figure 4.14 Width (left) and thickness (right) of test specimens produced by SLS depending on the amount of MWCNT (in wt%).

4.4.1.3. Dimensional and geometric accuracy

In agreement with Figure 4.12, the CT images of test artefacts produced with PA12-MWCNT composite materials revealed critical differences in terms of surface roughness and reproducibility of fine pins and holes, depending on the weight percentage of incorporation (Figure 4.15). The results proved that higher amounts of MWCNT were not advantageous to reproduce fine features with nominal diameters between 2.00 - 0.25 mm nor to ensure lower surface roughness. The magnification allowable by CT revealed fine holes until a minimum diameter of 1.50 mm in the top surface of the test artefacts produced with composite materials, contradicting the macro-scale finding shown in Figure 4.12. As revealed before, this analysis proved that the production of fine holes was negatively affected by the incorporation of MWCNT.

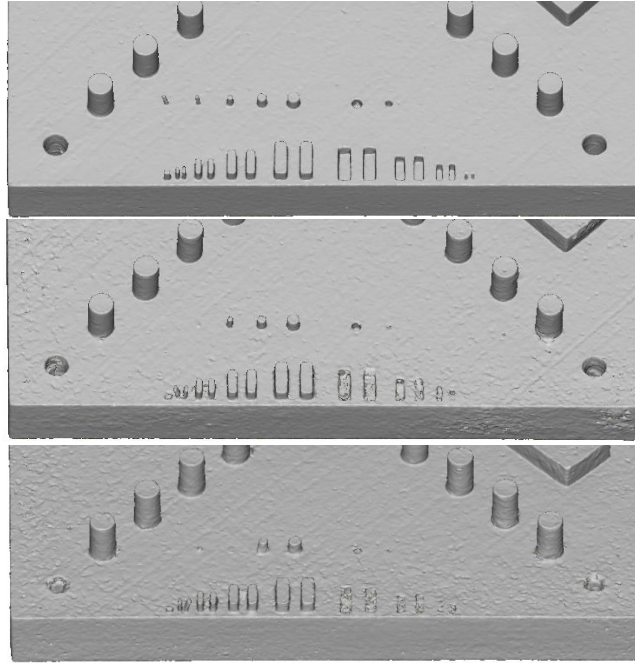


Figure 4.15 Geometric characteristics of test artefacts produced by SLS with PA12 incorporating 0.50 wt% (top), 1.75 wt% (middle) and 3.00 wt% (bottom) of MWCNT.

Moreover, the surface roughness of the horizontal top surface increased with the incorporation of MWCNT, comprising the quality of features and edges. The worst overall quality was detected in the test artefact produced with 3.00 wt% of MWCNT, which may anticipate the inappropriateness of parts produced with this material to meet design requirements and tolerances (Figure 4.16).

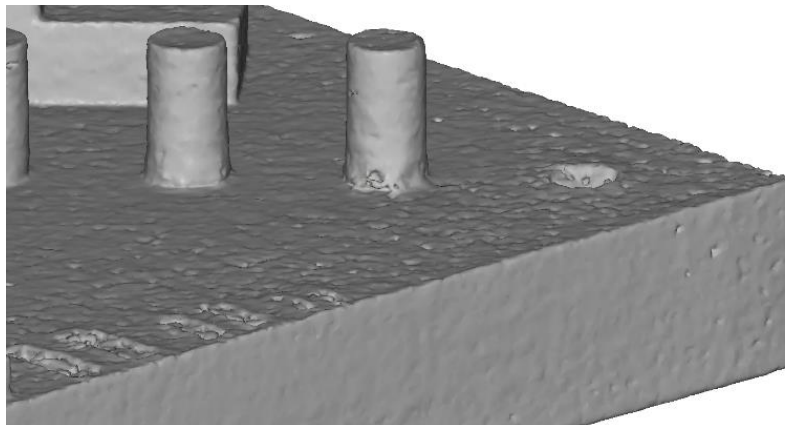


Figure 4.16 Geometric details of a test artefact produced by SLS with PA12 incorporating 3.00 wt% of MWCNT.

These primary observations had direct effects on the quantitative results. The flatness of the horizontal top plane of the test artefacts revealed that the incorporation of MWCNT was not advantageous for the manufacturing of flat surfaces (Figure 4.17). The flatness gradually increased from 0.17 ± 0.02 mm in the test artefact produced with neat-PA12 to a maximum of 0.52 ± 0.01 mm in the test artefact produced with 3.00 wt% of MWCNT, recording an average increase above 200%.

Chapter 4. Development and characterization of SLS composite materials

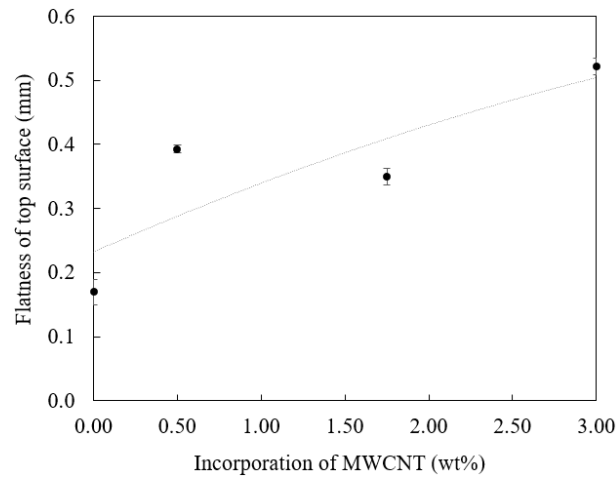


Figure 4.17 Flatness of the top surface of test artefacts produced by SLS depending on the amount of MWCNT (in wt%).

Regardless of the amount of MWCNT, the roundness of central holes was 0.10 mm higher (on average) than the roundness of the lateral ones (Figure 4.18). The roundness of central holes increased more than three times from 0.08 ± 0.01 mm in the test artefact produced with neat-PA12 to 0.24 ± 0.01 mm in the test artefact produced with 3.00 wt% of MWCNT. In turn, the roundness of lateral holes increased until a maximum value above 0.30 mm in the test artefact produced with 1.75 wt% of MWCNT but decreased until 0.20 in the condition of highest amount of incorporation.

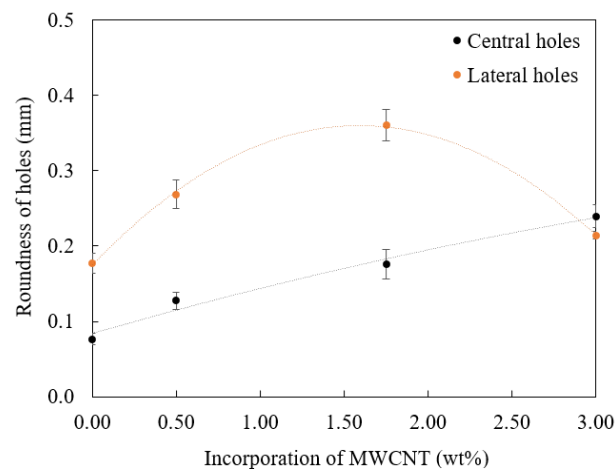


Figure 4.18 Roundness of central and lateral holes of test artefacts produced by SLS depending on the amount of MWCNT (in wt%).

The straightness of primary surfaces is presented in Figure 4.19. This element of form also revealed a rising trend with the increasing amount of MWCNT, reaching a variation of 150%. Composite materials integrating 3.00 wt% of MWCNT recorded the highest value of 0.40 ± 0.02 mm, which may be a result of the poor surface quality observed in the corresponding test artefact (Figure 4.16).

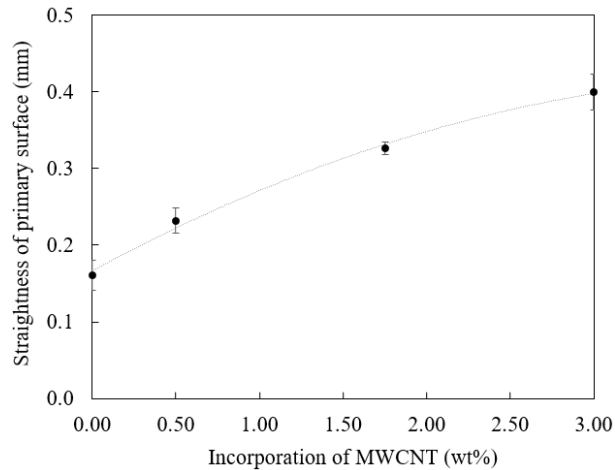


Figure 4.19 Straightness of the primary surface of test artefacts produced by SLS depending on the amount of MWCNT (in wt%).

In general, the parallelism of opposite surfaces was higher in test artefacts produced with composite materials, reaching values close to 0.40 mm in the conditions of 1.75 wt% and 3.00 wt% of MWCNT (Figure 4.20). These values exceeded the reference condition by 0.10 mm, on average.

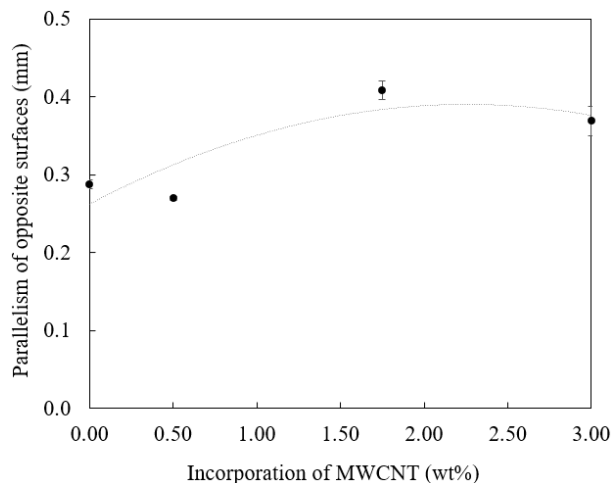


Figure 4.20 Parallelism of opposite surfaces of test artefacts produced by SLS depending on the amount of MWCNT (in wt%).

The tolerancing of location is evaluated in Figure 4.21, Figure 4.22 and Figure 4.24 with respect to the x, y and z axes, respectively. The primary results revealed that the linear displacement deviation tends to be higher when the distance between the centre of the feature and the centre of the part increases. In addition, it was verified that those deviations are mostly directed toward the centre of the part. Therefore, the positive direction of the deviations as represented in Figure 3.39 was adopted for representation.

Regarding negative and positive x-positions, the results showed that the linear displacement deviation is more influenced by the position of the features spaced 30.00 mm apart than the weight percentage of MWCNT (Figure 4.21). For example, in the test artefact produced with 3.00 wt% of MWCNT, the linear

Chapter 4. Development and characterization of SLS composite materials

displacement deviation of positive x-positions successively increased 0.10 mm between each feature positioned at 20.00 mm, 30.00 mm, 40.00 mm and 50.00 mm, reaching differences in deviation above 0.30 mm. In turn, for the feature positioned at 50.00 mm, the linear displacement deviation was 0.03 mm in the test artefact produced with neat-PA12 and 0.50 mm in the test artefact produced with composite materials, without significant variation between conditions. Regardless of the composite material, the average deviations of positive x-positions were higher than the deviations of negative x-positions, surpassing the satisfactory tolerance of ± 0.10 mm. These results proved that the incorporation of MWCNT increases the linear displacement deviation of x-positions, enhancing its dependence on the original position beyond what is acceptable.

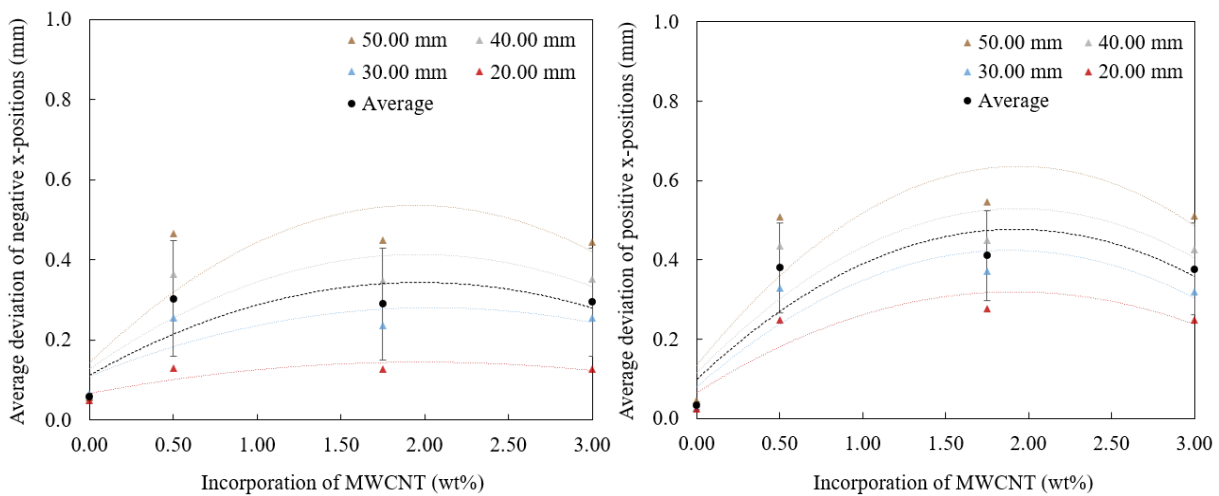


Figure 4.21 Average deviations of negative (left) and positive (right) x-positions of pins in test artefacts produced by SLS depending on the amount of MWCNT (in wt%).

The results for the y-axis were similar (Figure 4.22). Regardless of the weight percentages of MWCNT, the linear displacement deviations were significantly higher in test artefacts produced with composite materials, compared to the test artefact produced with neat-PA12. The base nature of the material (*i.e.*, reinforced or unreinforced), as well as the positioning of each feature in relation to the centre of the part, were the most influential factors on dimensional and geometric tolerancing, as opposed to the effect of different amounts of reinforcement. In this situation, the average deviations reached 1% of the nominal feature position, which means that it increases with the distance of the feature from the centre of the part up to values close to 0.50 mm in geometric elements positioned at -50.00 mm and 50.00 mm. As verified for the x-axis, no test artefact produced with composite material ensured an acceptable tolerance below 0.10 mm.

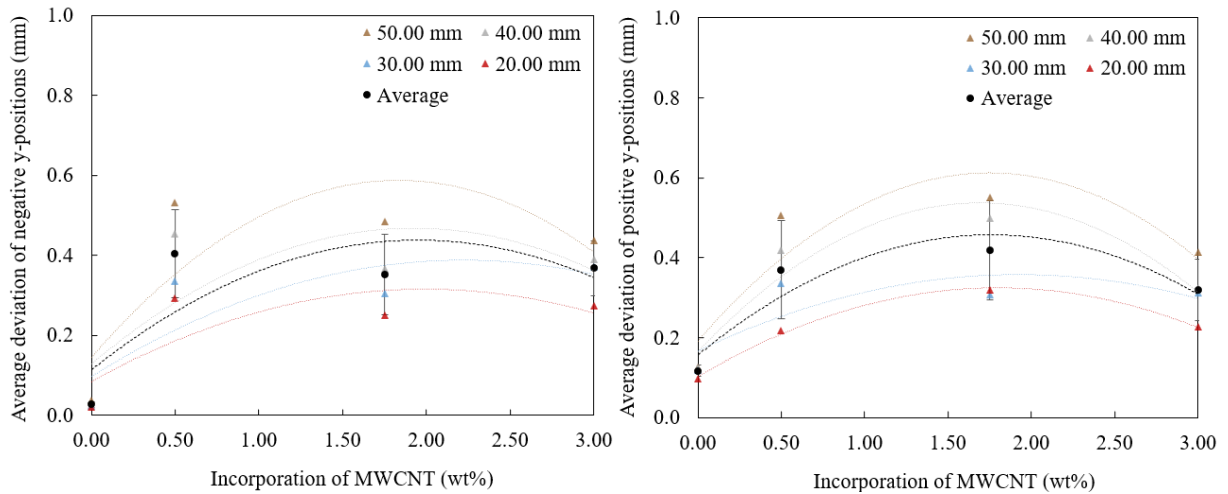


Figure 4.22 Average deviations of negative (left) and positive (right) y-positions of pins in test artefacts produced by SLS depending on the amount of MWCNT (in wt%).

These results allowed to calculate the percentage of deviation of pins placed along the x and y axes in parts produced by SLS with PA12 incorporating MWCNT, regardless of their nominal position (Figure 4.23). This is a useful output to anticipate the average deviations in positioning of pins that were not experimentally analysed in the scope of the research.

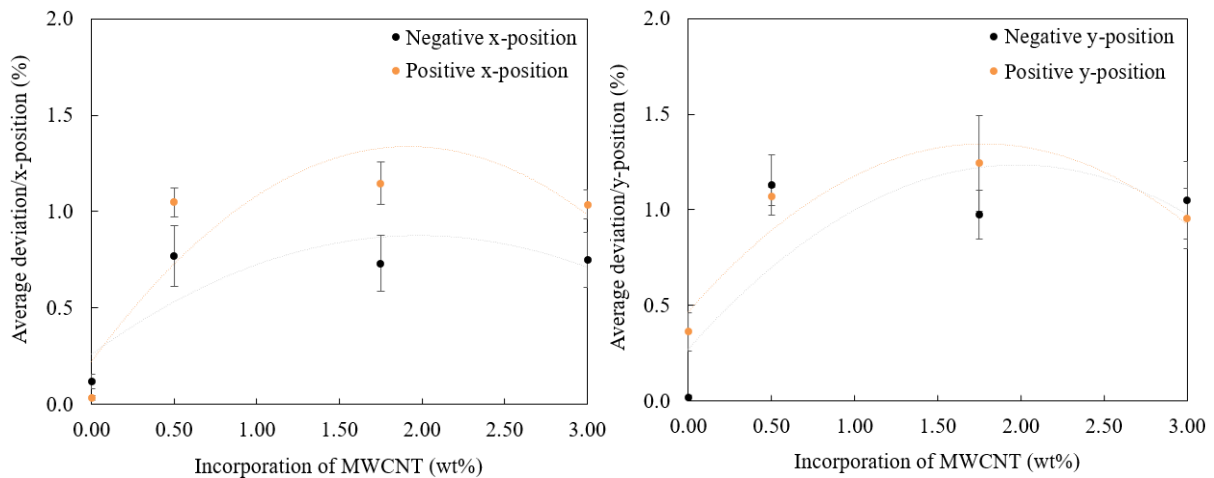


Figure 4.23 Factor of deviation (in %) for x (left) and y (right) positions of pins in test artefacts produced by SLS depending on the amount of MWCNT (in wt%).

The average deviations of negative and positive z-positions revealed dependence on the nominal height in relation to the mid-plane (Figure 4.24). In negative staircases, the linear displacement deviation was lower in planes positioned at lower depths (until 4.00 mm). The difference in the deviation depending on the positioning plane increased in test artefacts produced with composite materials incorporating higher amounts of MWCNT. While in test artefacts produced with neat-PA12 the difference in deviation of negative z-positions reached 0.10 mm, the test artefacts produced with 3.00 wt% of MWCNT attained 0.20 mm of difference in deviation in staircases positioned from -3.00 mm to -7.00 mm. These variations

Chapter 4. Development and characterization of SLS composite materials

promoted the production of staircases with lower depth, compared to the nominal. In turn, the positive staircases were tendency produced with higher height, with rising trend with the amount of incorporation of MWCNT. The highest variations were verified in the plane at 7.00 mm which reached average deviations of 0.26 mm above the nominal in the test artefact produced with PA12 incorporating 3.00 wt% of MWCNT. This may be a result of the high thermal gradients generated in the processing of these materials. In this way, the test artefact produced with 0.50 wt% of MWCNT ensured satisfactory dimensional accuracy.

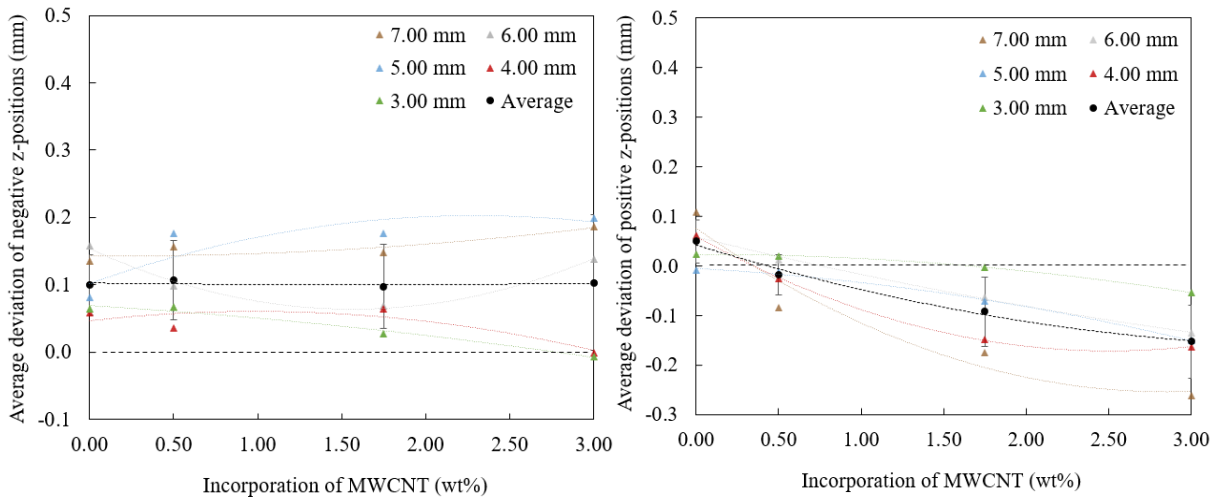


Figure 4.24 Average deviations of negative (left) and positive (right) z-positions of staircases in test artefacts produced by SLS depending on the amount of MWCNT (in wt%).

Figure 4.25 reports the average diameter of pins and holes with nominal values between 2.00 mm and 0.25 mm of test artefacts produced by SLS with different weight percentages of MWCNT. The results demonstrated that the inclusion of MWCNT was not advantageous for the manufacturing of fine features. Pins with nominal diameter equal to or less than 0.50 mm were not sintered in test artefacts produced with 1.75 wt% of MWCNT. The condition with highest amount of MWCNT (*i.e.*, 3.00 wt%) was not able to produce pins with nominal diameter equal to or less than 1.00 mm. Incorporation of 0.50 wt% of MWCNT ensured results similar to the neat-PA12 with the production of all fine pins. However, under these conditions, the pin with 0.25 mm of nominal diameter exceeded an acceptable deviation of 0.10 mm (this defines the minimum pin size achievable by the system). All other fine pins produced with composite materials met nominal specifications. In these experiments, fine holes up to a minimum diameter of 1.50 mm were observed in test artefacts produced with neat-PA12 and PA12 with 0.50 wt% of MWCNT, while the test artefacts produced with 1.75 wt% and 3.00 wt% of MWCNT only exhibited holes up to a minimum of 2.00 mm of nominal diameter. However, regardless of the condition, all produced holes exhibited deviations greater than 0.40 mm below de nominal.

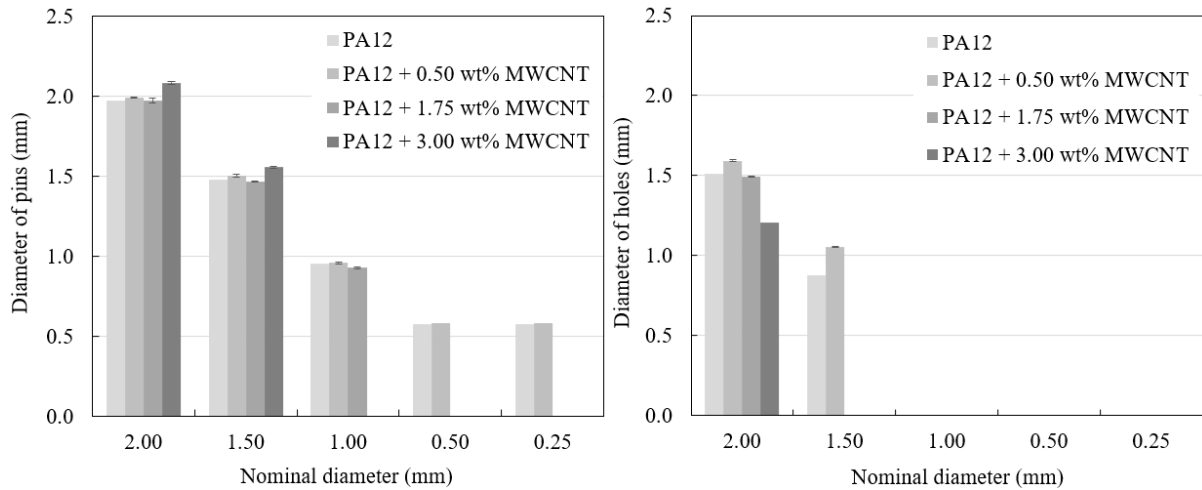


Figure 4.25 Diameter of pins (left) and holes (right) of test artefacts produced by SLS depending on the amount of MWCNT (in wt%).

The surface comparison of the test artefacts produced with PA12 and PA12 incorporating 3.00 wt% of MWCNT is shown in Figure 4.26. The analysis revealed that the incorporation of MWCNT led to higher deviations in the positioning of features towards the centre of the test artefact, supporting the aforementioned findings (see Figure 4.21 and Figure 4.22). Considerable shrinkage effects denoted by bluish regions were also clearly evidenced on the lateral surface of the test artefact produced with the highest weight percentage of MWCNT. Furthermore, critical deviation values were also observed in fine features, with more pronounced effects in holes.

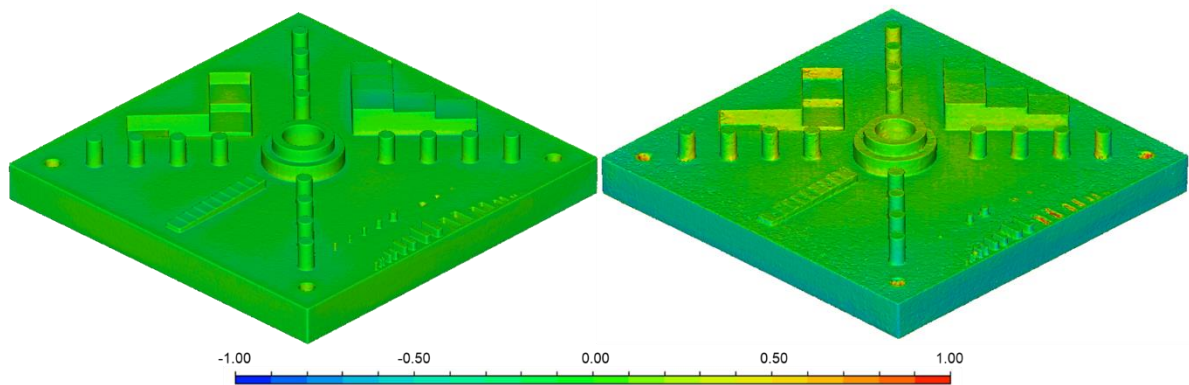


Figure 4.26 Surface comparison of test artefacts produced by SLS with PA12 (left) and PA12 incorporating 3.00 wt% of MWCNT (right) with the CAD model.

4.4.1.4. Surface roughness

Figure 4.27 shows the topography of the top surface of test specimens produced by SLS with the developed composite materials. In a first observation, it is possible to detect an increase in the range of height between peaks and valleys in relation to the midplane of the test specimens with the incorporation

Chapter 4. Development and characterization of SLS composite materials

of MWCNT (denoted by the colouring gradient), which directly influences the surface roughness parameters (Table 4.2). For an elected area of the upward-facing surface, the test specimens produced with PA12 incorporating 0.50 wt%, 1.75 wt% and 3.00 wt% of MWCNT respectively presented values of arithmetic mean height (S_a) of 13.5 μm , 15.5 μm and 16.1 μm in a rising trend. Optical measurements of the surface roughness of a similar PA12 material showed S_a values between 14-18 μm (Launhardt *et al.*, 2016). This demonstrates that the test specimens produced with the PA12-MWCNT composite materials developed in this work exhibited values of surface roughness in the order of magnitude expected for laser-sintered parts but with tendency to increase with the increasing weight percentage of MWCNT until 20% from 0.50 wt% to 3.00 wt%.

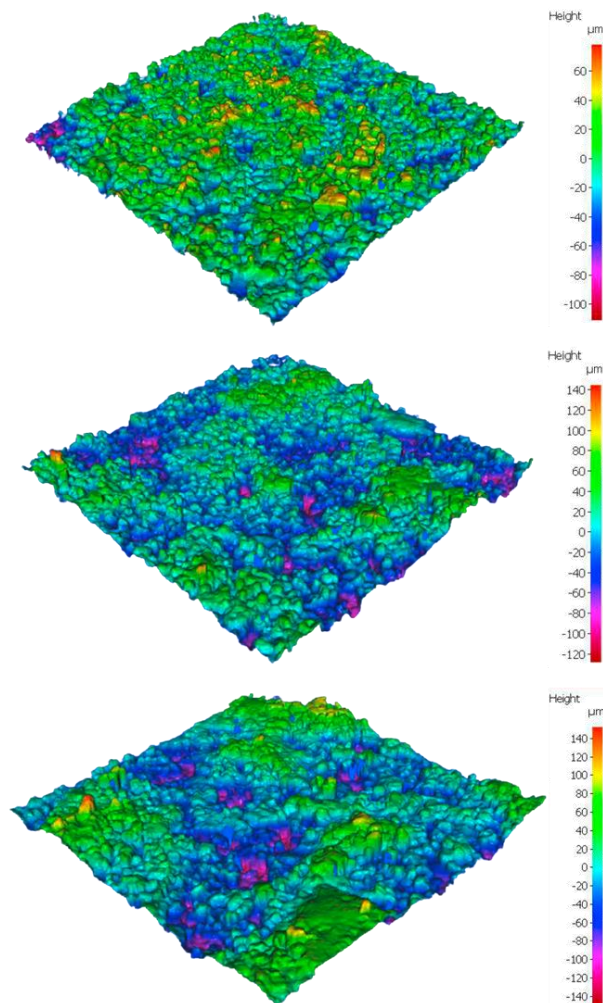


Figure 4.27 Top surface topography of test specimens produced by SLS with PA12 incorporating 0.50 wt% (top), 1.75 wt% (middle) and 3.00 wt% (bottom) of MWCNT.

Table 4.2 Surface roughness parameters of PA12-MWCNT composites processed by SLS.

MATERIALS	Arithmetic mean height Sa (μm)	Root-Mean-Square height Sq (μm)	Maximum peak height Sp (μm)	Maximum valley depth Sv (μm)	Maximum height Sz (μm)
PA12 + 0.50 wt% MWCNT	13.49	16.87	65.35	71.65	136.99
PA12 + 1.75 wt% MWCNT	15.45	19.85	110.21	96.63	206.83
PA12 + 3.00 wt% MWCNT	16.06	20.92	117.07	107.66	224.73

4.4.1.5. Mechanical properties

Tensile properties

Figure 4.28 illustrates representative engineering stress-strain curves obtained from tensile tests performed in test specimens produced with neat-PA12 and PA12 incorporating 0.50 wt%, 1.75 wt% and 3.00 wt% of MWCNT.

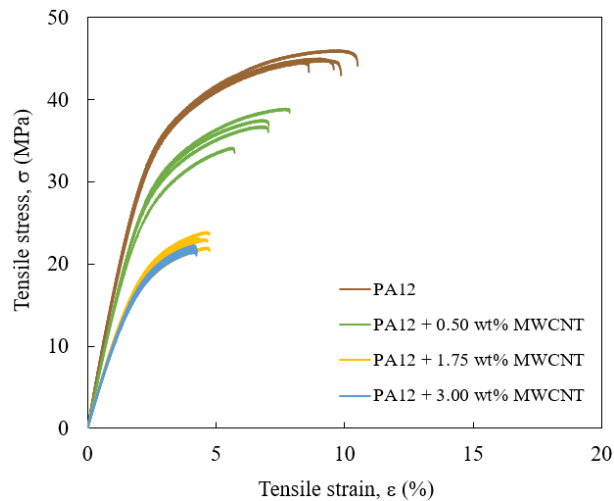


Figure 4.28 Engineering stress-strain curves of test specimens produced by SLS depending on the amount of MWCNT (in wt%).

The results revealed that the mechanical properties resulting from uniaxial tensile loads decreased with the increasing amount of MWCNT incorporated in the polymeric matrix. Compared to the neat-PA12, the reduction was lower in test specimens produced with 0.50 wt% of MWCNT and higher for the weight percentages of 1.75 wt% and 3.00 wt% which exhibited similar mechanical performance between each other. In this respect, the elastic modulus showed a maximum decrease of 37% from 1723.6 ± 48.2 MPa in test specimens produced with neat-PA12 to 1088.0 ± 19.6 MPa in test specimens produced with 3.00 wt% of MWCNT (Figure 4.29).

Chapter 4. Development and characterization of SLS composite materials

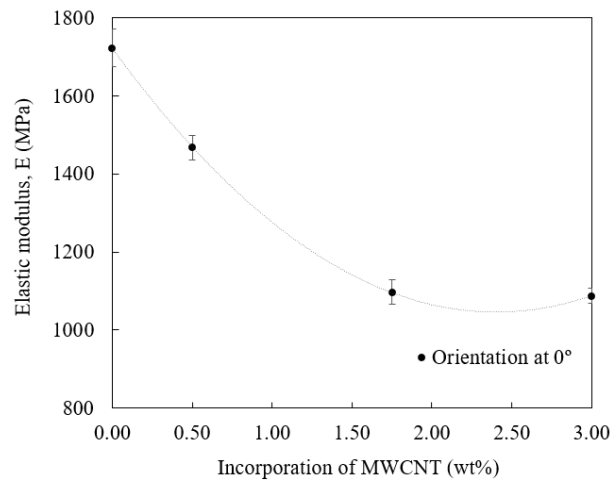


Figure 4.29 Elastic modulus of test specimens produced by SLS depending on the amount of MWCNT (in wt%).

The tensile stress at yield also decreased with the amount of MWCNT until 48% in test specimens incorporating the highest amount of MWCNT, reaching a minimum of 14.1 ± 0.6 MPa (Figure 4.30 (left)). The maximum decrease was verified from test specimens produced with 0.50 wt% MWCNT to test specimens produced with 1.75 wt% of MWCNT. Between 1.75 wt% and 3.00 wt% of MWCNT the tensile stress at yield was similar. The corresponding tensile strain at yield did not show a significant variation, but also revealed a gradual reduction from 1.9 ± 0.1 % in test specimens produced with neat-PA12 to 1.5 ± 0.1 % in test specimens produced with 3.00 wt% of MWCNT (Figure 4.30 (right)).

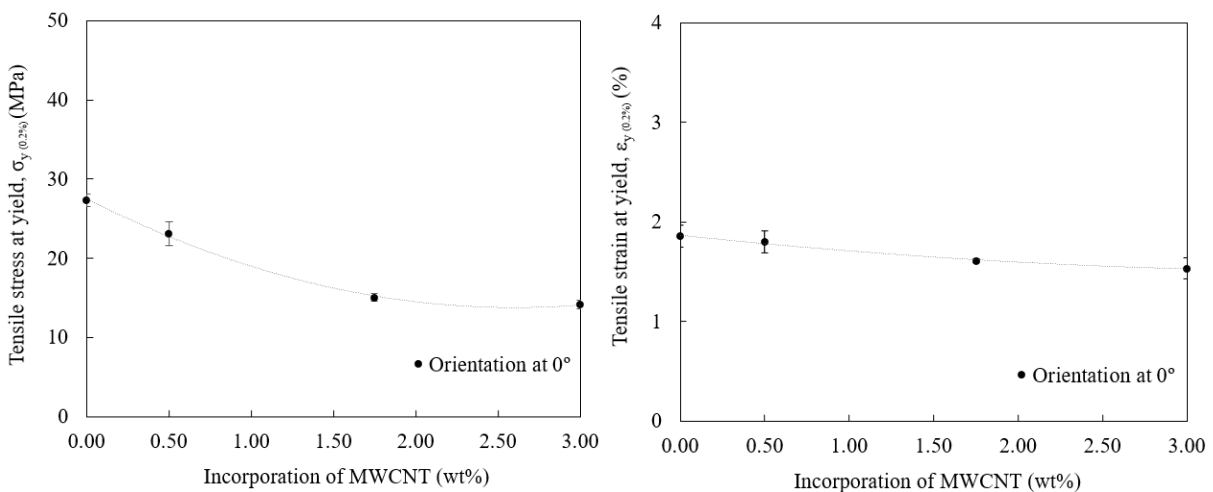


Figure 4.30 Tensile stress at yield (left) and tensile strain at yield (right) of test specimens produced by SLS depending on the amount of MWCNT (in wt%).

The tensile stress at break and tensile strain at break showed a coherent behavior. Compared to the reference condition, the decrease in tensile stress at break exceeded 50% in test specimens produced with 3.00 wt% of MWCNT, recording the minimum value of 21.5 ± 0.4 MPa (Figure 4.31 (left)). In turn, the variation in tensile strain at break was greater than that verified at the yield point (Figure 4.31 (right)). The tensile strain at break decreased a maximum of 57% in test specimens produced with composite

materials until 4.2 ± 0.1 % compared to test specimens produced with neat-PA12 which exhibited a tensile strain at break of 9.6 ± 0.8 %.

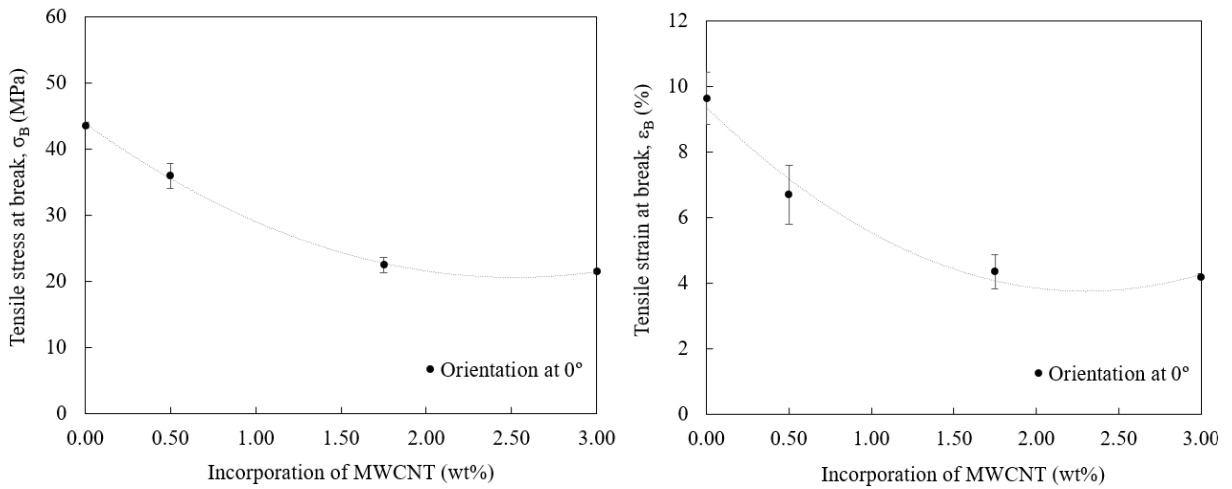


Figure 4.31 Tensile stress at break (left) and tensile strain at break (right) of test specimens produced by SLS depending on the amount of MWCNT (in wt%).

The results of tensile strength agreed with the findings that the mechanical properties decrease up to 50% with the increasing amount of MWCNT until 3.00 wt% (Figure 4.32). In this regard, the maximum tensile load supported by the materials reached 45.0 ± 0.6 MPa for neat-PA12, 36.5 ± 1.8 MPa for PA12 with 0.50 wt% of MWCNT, 22.7 ± 1.2 MPa for PA12 with 1.75 wt% of MWCNT and 21.9 ± 0.3 MPa for PA12 with 3.00 wt% of MWCNT.

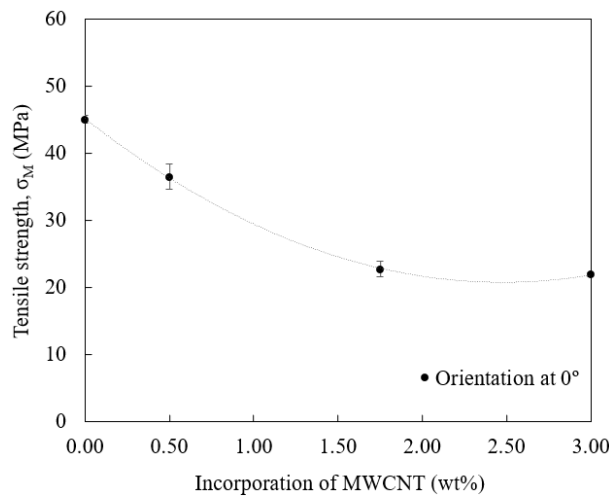


Figure 4.32 Tensile strength of test specimens produced by SLS depending on the amount of MWCNT (in wt%).

Compression properties

The compression tests also demonstrated the influence of the MWCNT on the mechanical properties of the composite materials in relation to the neat polymeric matrix. Representative engineering stress-strain curves obtained from compression tests are shown in Figure 4.33.

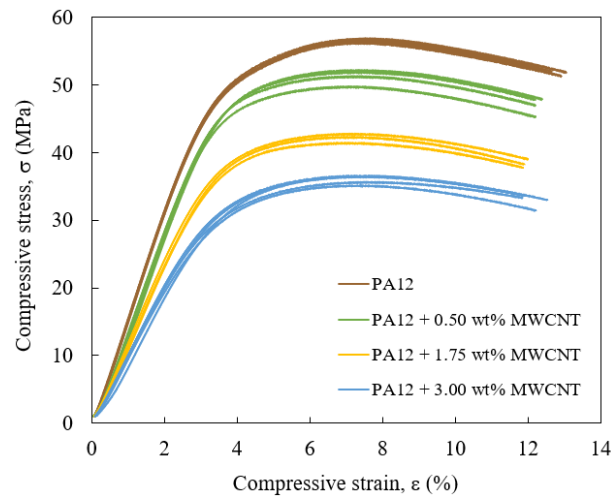


Figure 4.33 Engineering compressive stress-strain curves of test specimens produced by SLS depending on the amount of MWCNT (in wt%).

As previously stated for tensile testing, the compressive properties also gradually decreased with the incorporation of MWCNT. The elastic modulus exhibited a maximum decrease of 34%, from 1511.1 ± 22.1 MPa in test specimens produced with neat-PA12 to 1003.0 ± 51.1 in test specimens incorporating 3.00 wt% of MWCNT (Figure 4.34 (left)). In accordance, the compressive strength was reduced 36% under the same conditions, from 56.5 ± 0.3 MPa to 36.0 ± 0.7 MPa (Figure 4.34 (right)). The lowest reduction was verified in test specimens produced with 0.50 wt% of MWCNT, recording an elastic modulus of 1299.3 ± 39.5 MPa and compressive strength of 51.2 ± 1.0 MPa.

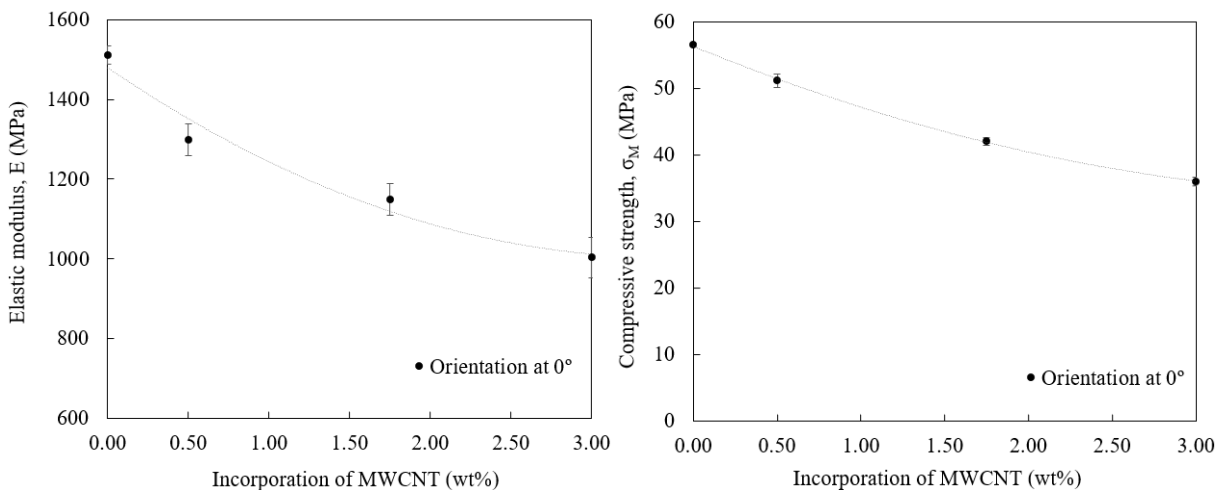


Figure 4.34 Compressive elastic modulus (left) and compressive strength (right) of test specimens produced by SLS depending on the amount of MWCNT (in wt%).

Izod impact properties

In the Izod impact tests, all test specimens exhibited a complete break in the section of v-notch using a pendulum with 4 J of capacity. In this regard, the test specimens produced with neat-PA12 showed an impact resistance of 5.1 ± 0.3 kJ/m², while the test specimens produced with composite materials

reached values between 4.1 - 4.6 kJ/m² (Figure 4.35). Compared to other mechanical characterization tests, it is possible to argue that the incorporation of MWCNT does not significantly influence the impact resistance of parts produced by SLS.

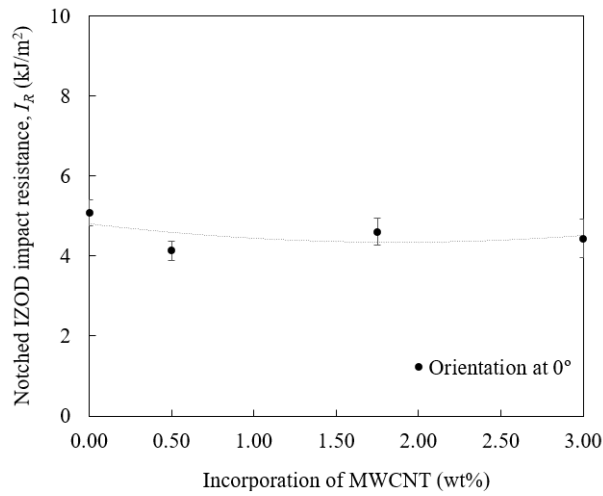


Figure 4.35 Notched Izod impact resistance of test specimens produced by SLS depending on the amount of MWCNT (in wt%).

In sum, Table 4.3 presents the mechanical properties of the developed PA12-MWCNT composites.

Table 4.3 Summary of mechanical properties of PA12-MWCNT composites.

	PA12	PA12 + 0.50 wt% MWCNT	PA12 + 1.75 wt% MWCNT	PA12 + 3.00 wt% MWCNT
TENSILE PROPERTIES				
E (MPa)	1723.60 ± 48.20	1467.85 ± 32.26	1097.06 ± 31.80	1088.04 ± 19.57
σ_{Ced} (MPa)	27.29 ± 0.80	23.13 ± 1.50	15.02 ± 0.47	14.14 ± 0.58
ϵ_{Ced} (%)	1.85 ± 0.11	1.80 ± 0.11	1.61 ± 0.02	1.53 ± 0.11
σ_{Rut} (MPa)	43.60 ± 0.40	35.95 ± 1.86	22.45 ± 1.16	21.48 ± 0.39
ϵ_{Rut} (%)	9.64 ± 0.79	6.70 ± 0.91	4.34 ± 0.52	4.19 ± 0.09
σ_{Max} (MPa)	45.04 ± 0.62	36.49 ± 1.82	22.71 ± 1.17	21.85 ± 0.32
COMPRESSIVE PROPERTIES				
E (MPa)	1511.11 ± 22.12	1299.32 ± 39.53	1148.79 ± 40.37	1002.99 ± 51.06
σ_{Max} (MPa)	56.51 ± 0.26	51.15 ± 0.96	42.05 ± 0.57	36.02 ± 0.64
IMPACT PROPERTIES				
I_K (kJ/m ²)	5.08 ± 0.32	4.13 ± 0.24	4.61 ± 0.34	4.43 ± 0.48

4.4.1.6. Electrical properties

The results of electrical resistance, resistivity and conductivity of the neat-PA12 and developed PA2-MWCNT composite materials obtained from surface and volume measurements are presented in Table 4.4. To more clearly illustrate the electrical behaviour and resulting ESD category, the results obtained from surface measurements are shown in Figure 4.36 through logarithmic scale.

Table 4.4 Electrical properties of PA12-MWCNT composites obtained through surface and volume measurements.

	MATERIALS	Electrical resistance (Ω)	Electrical resistivity ($\Omega.cm$)	Electrical conductivity (S/cm)
SURFACE (FLAT PLATES)	PA12	$4.29 \times 10^{10} \pm 3.83 \times 10^9$	$2.29 \times 10^{12} \pm 2.03 \times 10^{11}$	$4.39 \times 10^{-13} \pm 3.75 \times 10^{-14}$
	PA12 + 0.50 wt% MWCNT	$1.52 \times 10^{10} \pm 1.24 \times 10^{10}$	$8.11 \times 10^{11} \pm 6.62 \times 10^{11}$	$2.19 \times 10^{-12} \pm 1.98 \times 10^{-12}$
	PA12 + 1.75 wt% MWCNT	$4.45 \times 10^4 \pm 1.02 \times 10^4$	$2.37 \times 10^6 \pm 5.41 \times 10^5$	$4.36 \times 10^{-7} \pm 1.00 \times 10^{-7}$
	PA12 + 3.00 wt% MWCNT	$2.92 \times 10^3 \pm 2.63 \times 10^2$	$1.56 \times 10^5 \pm 1.42 \times 10^4$	$6.42 \times 10^{-6} \pm 5.87 \times 10^{-7}$
VOLUME (FLAT PLATES)	PA12	$3.16 \times 10^9 \pm 2.68 \times 10^8$	$4.82 \times 10^{11} \pm 4.08 \times 10^{10}$	$2.08 \times 10^{-12} \pm 1.83 \times 10^{-13}$
	PA12 + 0.50 wt% MWCNT	$4.08 \times 10^9 \pm 1.15 \times 10^9$	$6.24 \times 10^{11} \pm 1.76 \times 10^{11}$	$1.71 \times 10^{-12} \pm 5.56 \times 10^{-13}$
	PA12 + 1.75 wt% MWCNT	$4.29 \times 10^4 \pm 8.83 \times 10^3$	$6.54 \times 10^6 \pm 1.35 \times 10^6$	$1.57 \times 10^{-7} \pm 3.15 \times 10^{-8}$
	PA12 + 3.00 wt% MWCNT	$2.93 \times 10^3 \pm 2.31 \times 10^2$	$4.47 \times 10^5 \pm 3.56 \times 10^4$	$2.25 \times 10^{-6} \pm 1.80 \times 10^{-7}$

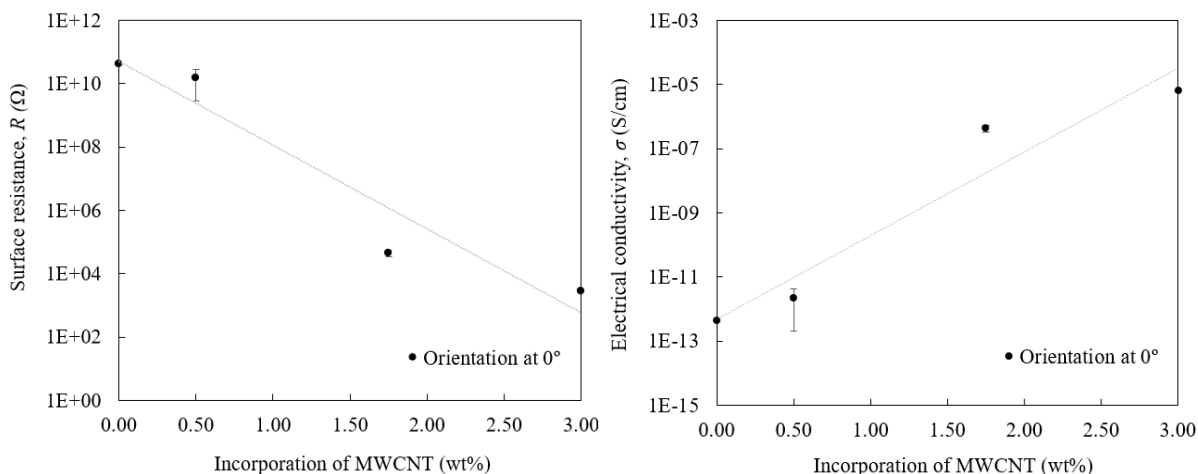


Figure 4.36 Surface resistance (left) and electrical conductivity (right) of flat plates produced by SLS depending on the amount of MWCNT (in wt%) (logarithmic scale).

This characterization test revealed that with the increasing amount of MWCNT, the electrical resistance and resistivity of the measured flat plates decreased, while the electrical conductivity increased. The surface resistance of flat plates produced with neat-PA12 and PA12 incorporating 0.50 wt% of MWCNT exhibited similar orders of magnitude in the insulative range (*i.e.*, $10^{10} \Omega$). In turn, flat plates produced with 1.75 wt% and 3.00 wt% of MWCNT revealed significant reductions of surface resistance until $10^4 \Omega$ and $10^3 \Omega$, respectively. The surface resistivity showed a coherent behaviour, with a maximum variation

from $10^{12} \Omega/\text{cm}$ in flat plates produced with neat-PA12 to $10^5 \Omega\cdot\text{cm}$ in flat plates produced with 3.00 wt% of MWCNT. The electrical conductivity increased several orders of magnitude from 10^{-13} S/cm in flat plates produced with neat-PA12 to 10^{-7} S/cm and 10^{-6} S/cm in flat plates produced with 1.75 wt% and 3.00 wt% of MWCNT, respectively. According to IEC 61340-5-1 and based on the resulting surface resistance, the flat plates produced with 1.75 wt% and 3.00 wt% of MWCNT attained the electrostatic conductive range (*i.e.*, $10^5 > \text{surface resistance} \geq 10^2$) (IEC, 1998). This indicates that, under the conditions of this study, incorporation of 1.75 wt% of MWCNT or higher can create an effective conductive path between the particles of reinforcement, allowing to significantly enhance the electrical conductivity of the polymeric base material. The electrical results obtained from volume measurements agreed with the surface measurements. This suggests that the carbon-based particles are also creating a conductive path for electrical conductivity along the cross-section of the flat plates allowing to attain values of electrical conductivity close to 10^{-7} S/cm and 10^{-6} S/cm with composite materials incorporating 1.75 wt% and 3.00 wt% of MWCNT, respectively.

4.4.1.7. Thermal properties

Differential Scanning Calorimetry (DSC)

The melting and crystallization temperatures (respectively denoted by T_m and T_c) of PA12-MWCNT composite materials determined through DSC are shown in Figure 4.37.

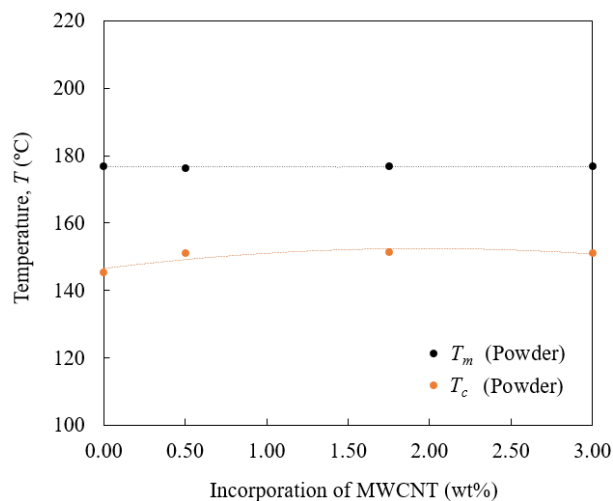


Figure 4.37 Melting and crystallization temperatures of SLS composite powders depending on the amount of MWCNT (in wt%).

This thermal characterization revealed that T_m is not significantly affected by the incorporation of MWCNT, recording values close to 177 °C in all materials. In turn, T_c increased from 145 °C in neat-PA12 to 151.1 ± 0.2 °C in composite materials produced with 0.50 wt%, 1.75 wt% and 3.00 wt% of MWCNT,

denoting that MWCNT acted as a nucleating agent influencing the crystallization behaviour of the base polymeric matrix (Xiong *et al.*, 2022). This difference of crystallinity reduced the interval between T_m and T_g and, consequently, the SLS processing window in 6 °C. This means that while the conventional PA12 material can be processed within an interval of 32 °C, the composite materials developed in this research can only be processed in a range of 26 °C. The processing temperature was fixed at 173 °C in all experiments, accomplishing the thermal specifications of the developed materials.

The specific heat capacity of the carbon-based materials did not demonstrate significant differences compared to the neat-PA12 (Figure 4.38). Within the operating thermal range between 40 - 160 °C, the specific heat capacity increased from 1.5 J/g·°C to 2.5 J/g·°C in all materials. This means that when the temperature increases, the materials need to absorb more energy to increase 1 °C, as a consequence of their enhanced vibrational energy.

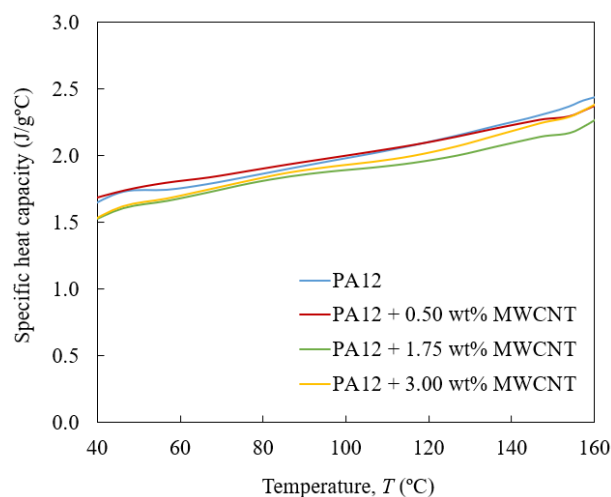


Figure 4.38 Specific heat capacity of test specimens produced by SLS depending on the amount of MWCNT (in wt%) with temperature.

Thermogravimetric analysis (TGA)

The onset temperature obtained by TGA analysis, which is a measure of the thermal stability of the materials in the initial stage of degradation, did not reveal substantial differences between the developed materials (Figure 4.39 (left)). This single-step deflection point reached values close to 400 °C in all TGA thermograms. Below that temperature, the materials demonstrated high thermal stability, without significant mass changes. With TGA analysis, the remaining combustible material at the end of heating was also determined and compared with the theoretical content of reinforcement, using a random portion of test specimen (Figure 4.39 (right)). By subtracting the neat-PA12 residue at 700 °C, it was possible to detect that for the weight percentages of 0.50 wt% and 1.75 wt% of MWCNT, the real reinforcement content was slightly higher than the theoretical, while for 3.00 wt% of MWCNT it was slightly lower. This

demonstrates the presence of carbon-based particles throughout the volume of the test specimens without significant differences from the planned portions.

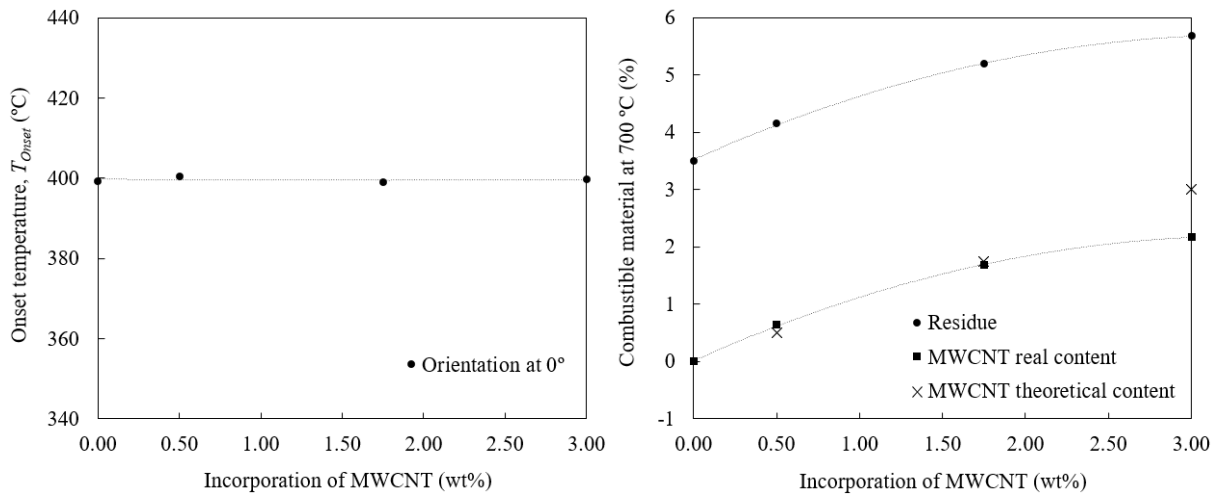


Figure 4.39 Onset temperature (left) and percentage of combustible material at 700 °C (right) of test specimens produced by SLS depending on the amount of MWCNT (in wt%).

4.4.1.8. Morphological properties

Figure 4.40 shows SEM micrographs of the cross-section of test specimens produced by SLS with neat-PA12 and PA12 incorporating 0.50 wt%, 1.75 wt% and 3.00 wt% of MWCNT. In a first observation at high magnification, the micrographs revealed that the content of porosity of test specimens produced with composite materials is higher than the content of porosity of test specimens produced with neat-PA12, with tendency to increase with the amount of MWCNT. This result suggests that the SLS process was not able to ensure a strong interparticle adhesion between the reinforcement and polymeric matrix, which could cause the disaggregation of unsintered particles during the post-production operations (*e.g.*, cleaning with compressed air), resulting in voids and gaps throughout the cross-section.

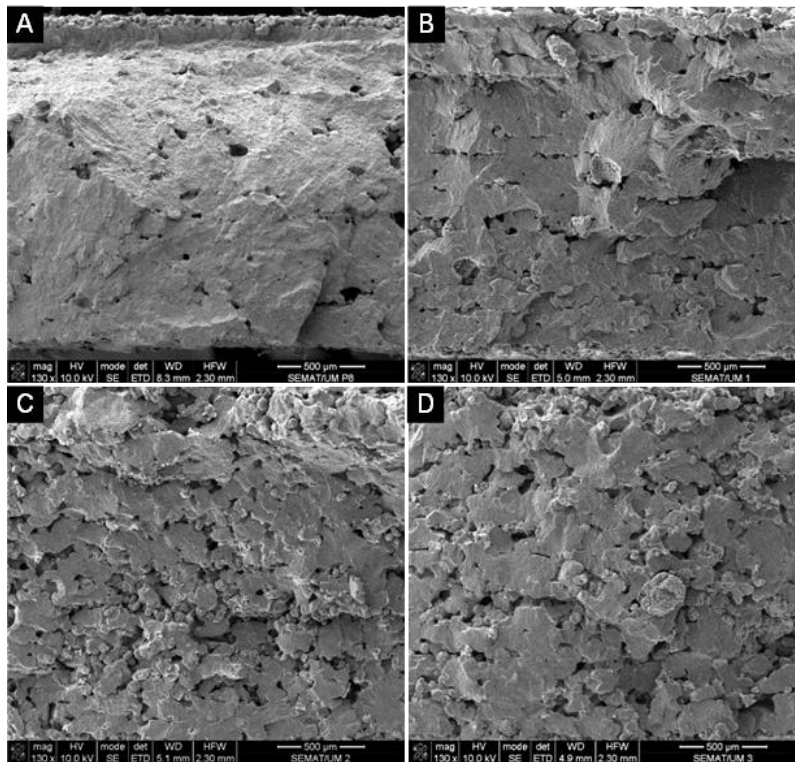


Figure 4.40 Cross-section of test specimens produced by SLS with A) PA12, B) PA12 + 0.50 wt% MWCNT, C) PA12 + 1.75 wt% MWCNT and D) PA12 + 3.00 wt% MWCNT.

In turn, the SEM micrographs obtained at lower magnification allowed to in detail observe agglomerates of MWCNT that were not well dispersed through mechanical mixing (Figure 4.41). These agglomerates combined with the high content of porosity may have induced a non-uniform stress distribution that was responsible for the reduction of mechanical properties as reported in *section 4.4.1.4*. However, it was also found that these agglomerates are present all over the cross-section of the test specimens, which may explain the reduction in the electrical surface resistance through the conductive path established between the particles of reinforcement.

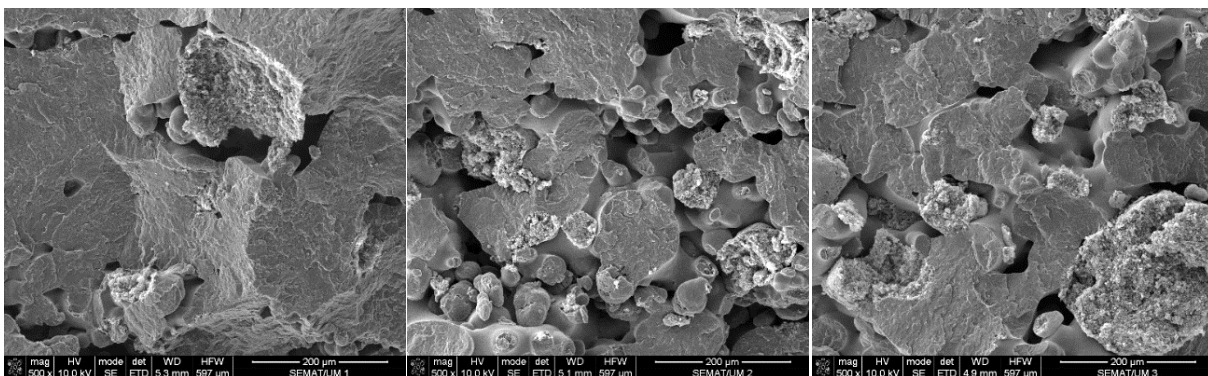


Figure 4.41 Cross-section of test specimens produced by SLS with PA12 + 0.50 wt% MWCNT (left), PA12 + 1.75 wt% MWCNT (middle) and PA12 + 3.00 wt% MWCNT (right).

4.4.2. PA12-GNP composites

4.4.2.1. Description of observations

The experiments carried out with PA12 incorporating GNP revealed some differences in terms of preparation and processing compared to the experiments conducted with MWCNT. Considering same methods and experimental conditions, particles of GNP promoted greater dispersions with fewer agglomerates than MWCNT, resulting in more homogeneous powder mixtures. However, the processing of PA12-GNP composites was challenging for the weight percentages of 0.50 wt%, 1.75 wt% and 3.00 wt% due to the high compaction of the materials. This phenomenon hindered the flow of powder to the recoater even using vibrating devices coupled to the feed containers and, consequently, the spread of powder over the powder bed, compromising the sintering of test specimens (Figure 4.42). In order to minimize these constraints, the fluidization flow rate of the equipment was increased from 10 L/min⁷ to 15 L/min, in a pulsed mode, trying to significantly enhance the powder vibration. However, the production of the test specimens needed for characterization demanded the implementation of artificial powder dosing strategies through the periodic interruption of the process in closed chamber. These limitations revealed that the incorporation of high amounts of GNP fostered the complexity of the SLS process and the manufacturing of quality parts within the scope of this study. Therefore, the weight percentage of 0.10 wt% was also evaluated aiming to define the maximum amount of GNP capable to ensure efficient SLS processing.



Figure 4.42 Sintering process of PA12-GNP composites evidencing difficulties in powder spread.

Despite the compaction problems, it was verified that the EDv value of 0.238 J/mm³ was appropriate to process PA12-GNP composites by SLS in a stable sintering process without critical thermal gradients and warpage effects, as observed in Figure 4.11 for PA12-MWCNT composites. Compared both carbon-based composites, the first observations allowed evidence that test specimens produced with GNP

⁷ Fluidization flow rate used to produce PA12-MWCNT composites (see *section 4.4.1*).

Chapter 4. Development and characterization of SLS composite materials

presented smoother finishing with reduced surface roughness, as a result of the base typology of each reinforcement (Figure 4.43).

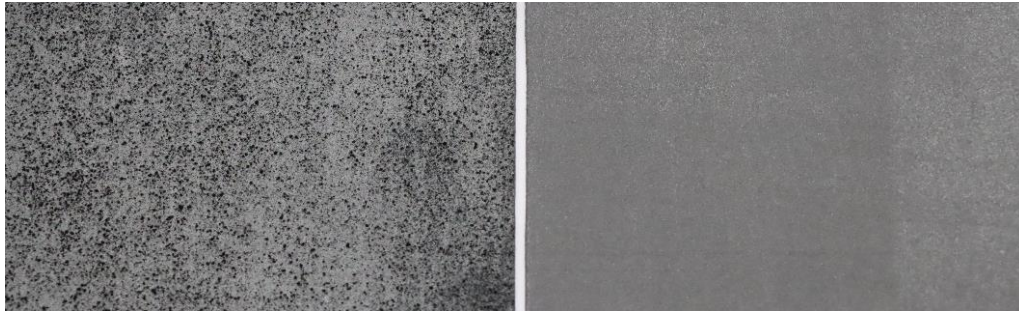


Figure 4.43 Surface finishing of test specimens produced by SLS with PA12 incorporating 3.00 wt% of MWCNT (left) and 3.00 wt% of GNP (right).

At macroscopical observation, the surface finishing of the test specimens was not significantly modified with the increasing amount of GNP, despite colour differences. As previously verified for MWCNT-based composites, the test specimens become darker with the increasing amount of GNP (Figure 4.44).



Figure 4.44 Surface finishing of test specimens produced by SLS with PA12 incorporating 0.50 wt% (left), 1.75 wt% (middle) and 3.00 wt% (right) of GNP.

Regarding the test artefacts, the initial qualitative evaluation demonstrated that incorporation of 0.10 wt% of GNP did not critically influence the reproducibility of features in surfaces at 0° directed to the top when compared with the test artefact produced with neat-PA12 (Figure 4.45). In this regard, the results suggested greater ability to produce fine pins than holes, since pins until 0.25 mm of nominal diameter were produced as opposed to the holes.

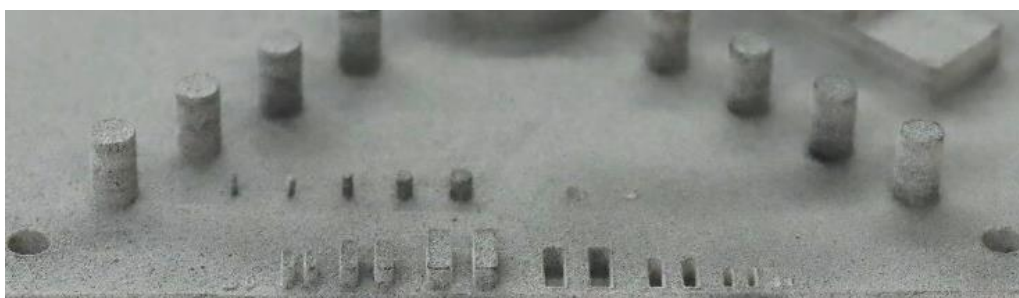


Figure 4.45 Fine features of test artefacts produced by SLS with PA12 incorporating 0.10 wt% of GNP.

Despite the challenging processing, test artefacts incorporating 0.50 wt% and 1.75 wt% of GNP were also produced for evaluation. In turn, the highest weight percentage of 3.00 wt% of GNP critically influenced the SLS process, restricting the manufacturing of the test artefact for dimensional and geometric analysis.

4.4.2.2. Mass and general dimensions

The results of mass, length, width and thickness of test specimens produced with PA12 incorporating GNP are shown in Figure 4.46 and Figure 4.47. Of all parameters, the mass showed the highest decrease of 15.6% from test specimens produced with 0.10 wt% of GNP to test specimens produced with 3.00 wt% of GNP, until the minimum value of 0.75 ± 0.01 g. As previously verified for composite materials integrating MWCNT, this is a consequence of the low bulk density of GNP in comparison to the bulk density of neat-PA12. Compared to the reference condition, the length decreased until 1-1.5% in test specimens produced with composite materials, regardless of the amount of GNP embedded in the matrix. In turn, the width presented a variation above 10%, from 5.19 ± 0.03 mm in test specimens produced with neat-PA12 to 4.66 ± 0.10 mm in test specimens produced with 3.00 wt% of GNP. The thickness did not exhibit a significant variation with the inclusion of GNP, reproducing with accuracy the nominal dimension of 2.00 mm. In addition to the effect of GNP itself, these dimensional variations may also be a result of the challenging sintering process that may have hindered the production of test specimens with dimensional and geometric conformity.

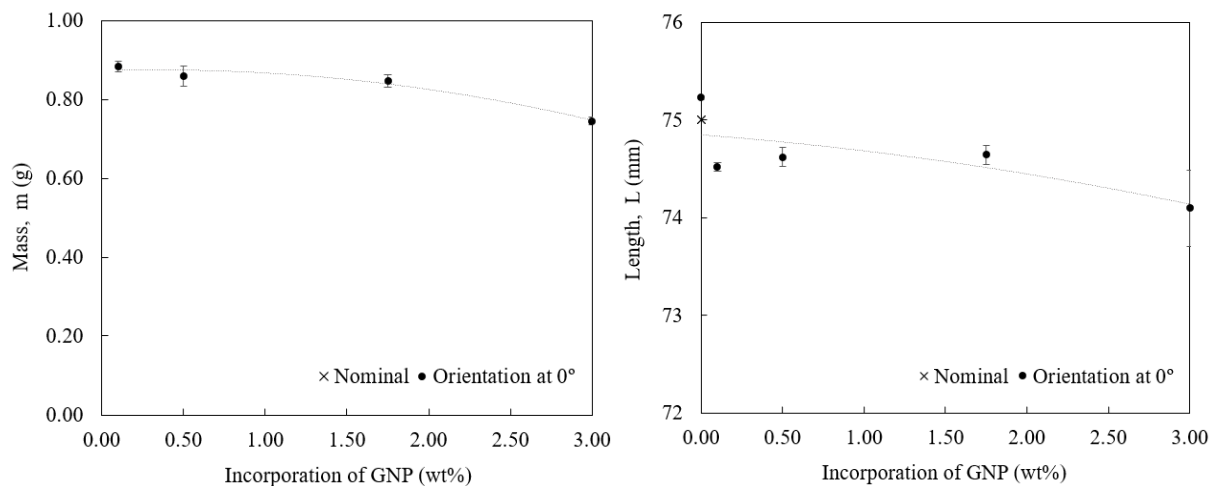


Figure 4.46 Mass (left) and length (right) of test specimens produced by SLS depending on the amount of GNP (in wt%).

Chapter 4. Development and characterization of SLS composite materials

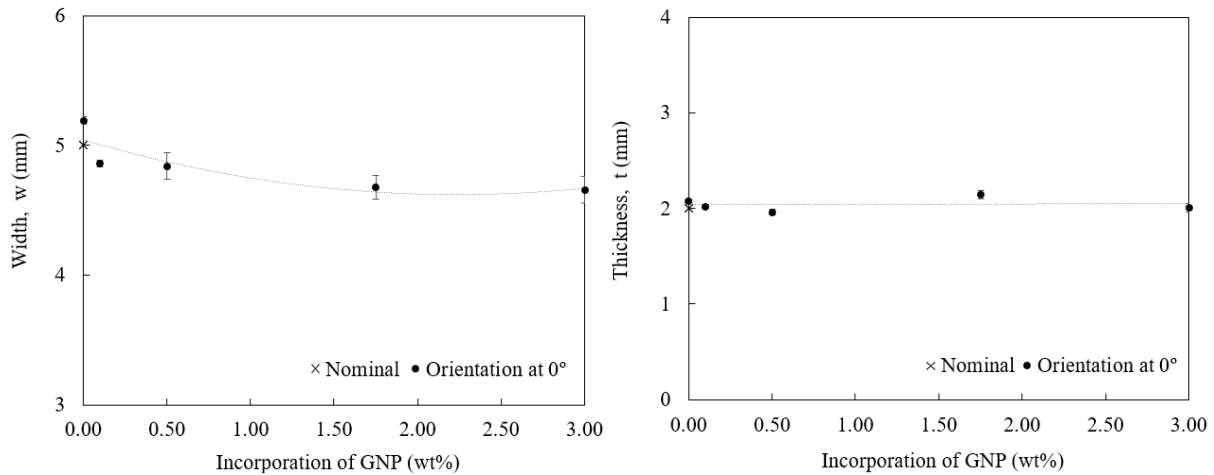


Figure 4.47 Width (left) and thickness (right) of test specimens produced by SLS depending on the amount of GNP (in wt%).

4.4.2.3. Dimensional and geometric accuracy

The surface comparison of the test artefacts produced with PA12 and PA12 incorporating 1.75 wt% of GNP is shown in Figure 4.48. In a first observation, the results evidenced significant effects of shrinkage on the lateral surface of the test artefact produced with GNP-based composites (bluish regions). This phenomenon was also verified in MWCNT-based composites but with lower dimensional deviation (see Figure 4.26). Despite that, the test artefact produced with 1.75 wt% of GNP revealed a top surface with great dimensional and geometric conformity (evidenced by the green colouring), similar to the CAD model. With regard to the quality of surfaces, this primary analysis suggests better results in test artefacts produced with GNP than with MWCNT-based materials.

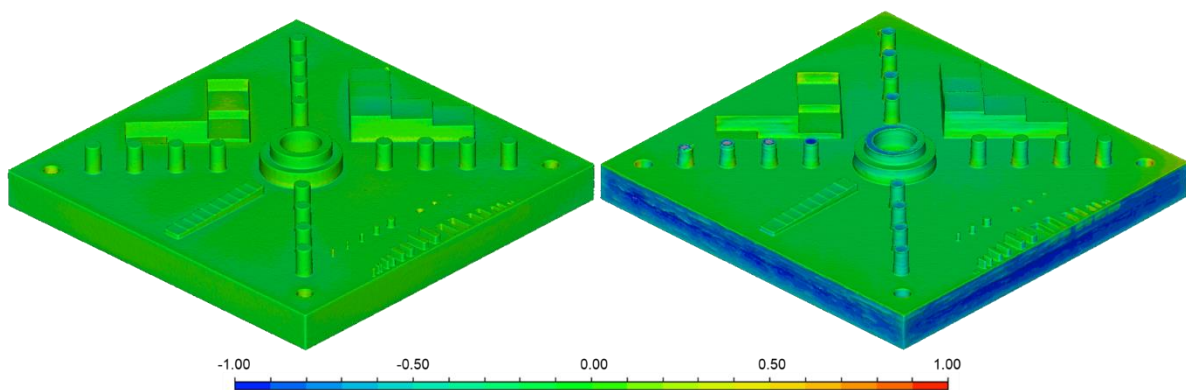


Figure 4.48 Surface comparison of test artefacts produced by SLS with PA12 (left) and PA12 incorporating 1.75 wt% of GNP (right) with the CAD model.

However, the GD&T measurements taken in this study were affected by superficial defects developed in the test artefacts during the complex processing of these high-compaction materials. This was verified in the flatness which, unexpectedly, presented a higher value in the test artefact produced with 0.50 wt% than with 1.75 wt% of GNP (Figure 4.49). Despite the increasing of the flatness with the incorporation of

GNP, the artefact produced with 1.75 wt% of GNP recorded a value of 0.43 ± 0.02 mm, 2.5 times higher than the flatness of the test artefact produced with neat-PA12 but similar to those obtained with PA12-MWCNT composites.

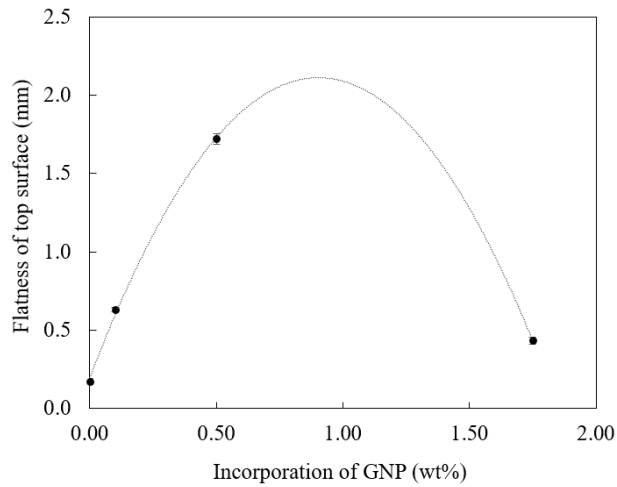


Figure 4.49 Flatness of the top surface of test artefacts produced by SLS depending on the amount of GNP (in wt%).

As verified in previous analyses, the roundness of lateral holes is tendency higher than the roundness of central holes, in an average difference of 0.10 mm, regardless of the SLS material. With regard to this tolerancing of form, it was demonstrated that the roundness was higher in test artefacts produced with GNP-composites than with neat-PA12, recording values above 0.10 mm in holes of the top surface and above 0.20 mm in holes of the lateral surfaces which in Figure 4.48 revealed weak dimensional and geometric conformity (Figure 4.50).

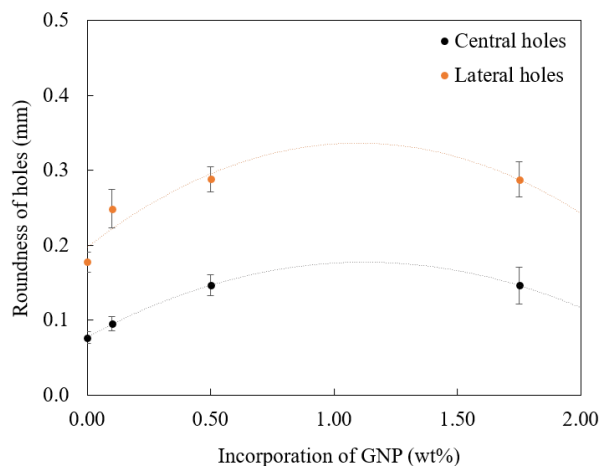


Figure 4.50 Roundness of central and lateral holes of test artefacts produced by SLS depending on the amount of GNP (in wt%).

The parallelism of surfaces exhibited a coherent behaviour (Figure 4.51). This parameter highly increased with the incorporation of GNP, with more expressive variation from 0.10 wt% to 0.50 wt%. The test artefacts produced with 0.50 wt% and 1.75 wt% of GNP respectively presented values of 0.48 ± 0.01

Chapter 4. Development and characterization of SLS composite materials

and 0.45 ± 0.01 mm, exceeding the values obtained in all test artefacts produced with MWCNT-based materials. This may also be a result of the effects of shrinkage observed in lateral surfaces of the test artefacts produced with PA12 incorporating GNP.

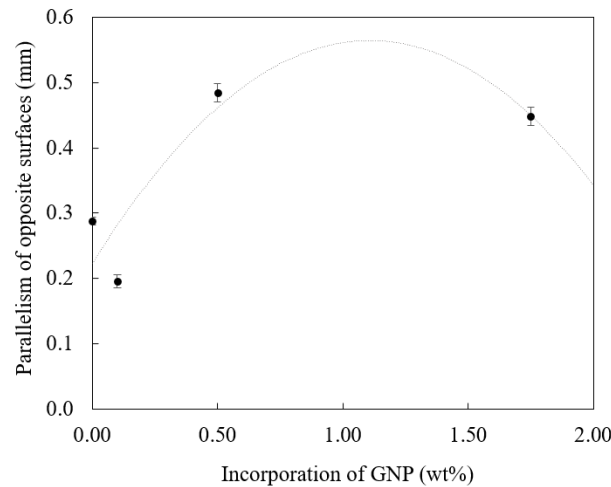


Figure 4.51 Parallelism of opposite surfaces of test artefacts produced by SLS depending on the amount of GNP (in wt%).

The analysis of the dimensional and geometric accuracy of fine features is shown in Figure 4.52 as a function of the amount of GNP incorporated in the matrix.

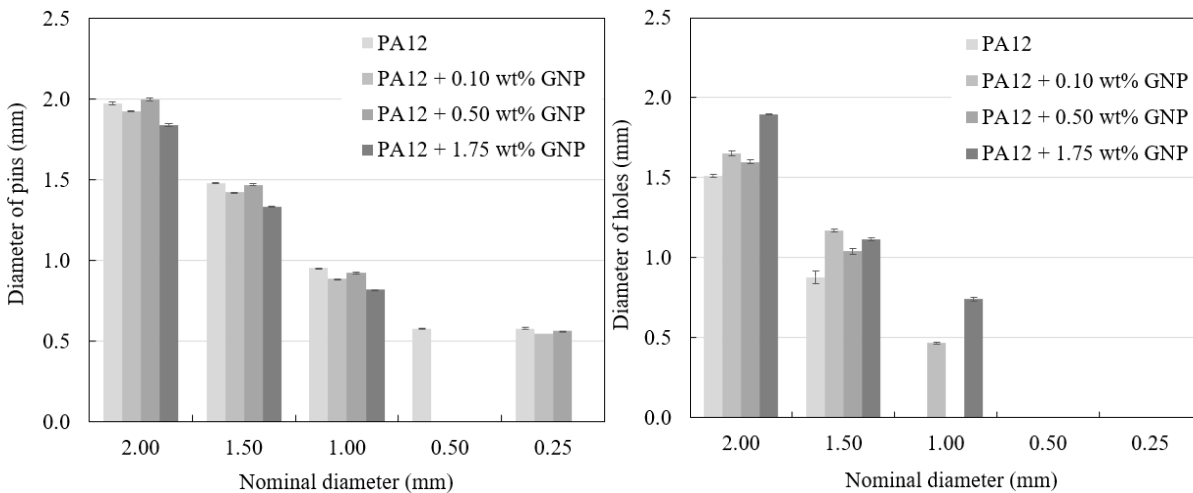


Figure 4.52 Diameter of pins (left) and holes (right) of test artefacts produced by SLS depending on the amount of GNP (in wt%).

In general, the results revealed that the inclusion of GNP decreases the dimensional and geometric accuracy of the features, compared with the neat-PA12 material. With regard to pins, it was verified that incorporations of 0.10 wt% and 0.50 wt% of GNP were able to produce nominal diameters equal to or higher than 1.00 mm with deviations below ± 0.10 mm. In turn, the test artefact produced with 1.75 wt% of GNP did not exhibit any pin with nominal diameter equal to or below 2.00 mm with acceptable dimensional tolerance. In this regard, all deviations exceeded -0.15 mm. Concerning holes, the results showed dimensional deviations above 0.30 mm in all nominal diameters for all materials under study,

except for PA12 incorporating 1.75 wt% of GNP which was able to produce the hole with 2.00 mm of nominal diameter meeting the dimensional tolerance of ± 0.10 mm.

4.4.2.4. Surface roughness

Figure 4.53 shows the topography of the top surface of test specimens produced by SLS with the developed PA12-GNP composite materials, evidencing some irregularities as previously verified in the MWCNT-based solutions. Critical local deviations were evidenced with the increasing weight percentage of incorporation of GNP with more pronounced effects on the depth of valleys, suggesting some level of porosity in the superficial layers of the laser-sintered test specimens.

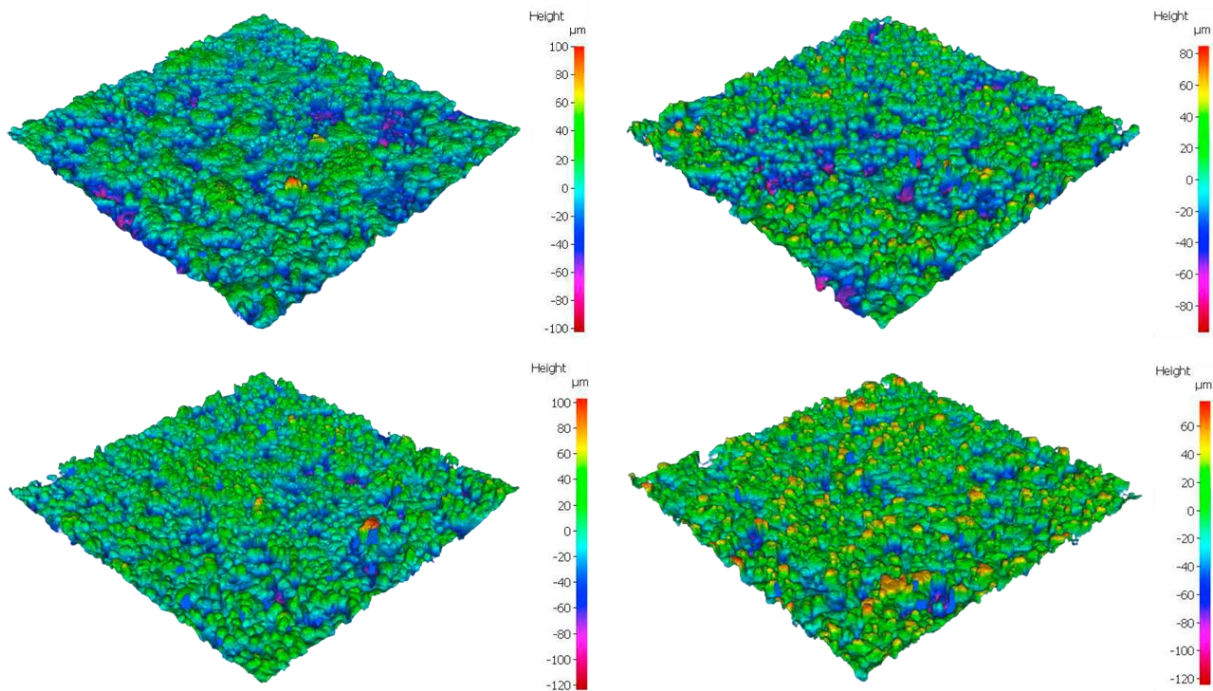


Figure 4.53 Top surface topography of test specimens produced by SLS with PA12 incorporating 0.10 wt% (top-left), 0.50 wt% (top-right), 1.75 wt% (bottom-left) and 3.00 wt% (bottom-right) of GNP.

In accordance with these findings, the quantitative analysis revealed that the average surface roughness of upward-facing surfaces increases with the increasing amount of GNP (Table 4.5). This was shown by the increase of the Sa value from 13.5 μm in test specimens produced with PA12 incorporating 0.10 wt% of GNP to 17.7 μm in test specimens produced with PA12 incorporating 3.00 wt% of GNP. The test specimens produced with 1.75 wt% of GNP exhibited the highest maximum peak height and highest maximum valley depth of 91.9 μm and 111.9 μm , respectively.

Table 4.5 Surface roughness parameters of PA12-GNP composites processed by SLS.

MATERIALS	Arithmetic mean height Sa (μm)	Root-Mean-Square height Sq (μm)	Maximum peak height Sp (μm)	Maximum valley depth Sv (μm)	Maximum height Sz (μm)
PA12 + 0.10 wt% GNP	13.49	16.56	86.93	72.53	159.46
PA12 + 0.50 wt% GNP	16.32	20.15	82.48	79.65	162.13
PA12 + 1.75 wt% GNP	16.94	21.38	91.91	111.94	203.85
PA12 + 3.00 wt% GNP	17.71	22.52	85.48	106.10	191.58

4.4.2.5. Mechanical properties

Tensile properties

Representative engineering stress-strain curves of test specimens produced with neat-PA12 and PA12 incorporating 0.10 wt%, 0.50 wt%, 1.75 wt% and 3.00 wt% of GNP are shown in Figure 4.54. Compared to PA12-MWCNT composites (Figure 4.28), these primary results revealed that test specimens produced with PA12 incorporating GNP allow values of elastic modulus similar to test specimens produced with neat-PA12 but lower tensile strain at break, evidencing the higher mechanical stiffness of such composites. Despite these assumptions, an overall decrease in the mechanical properties with the increasing amount of GNP was verified.

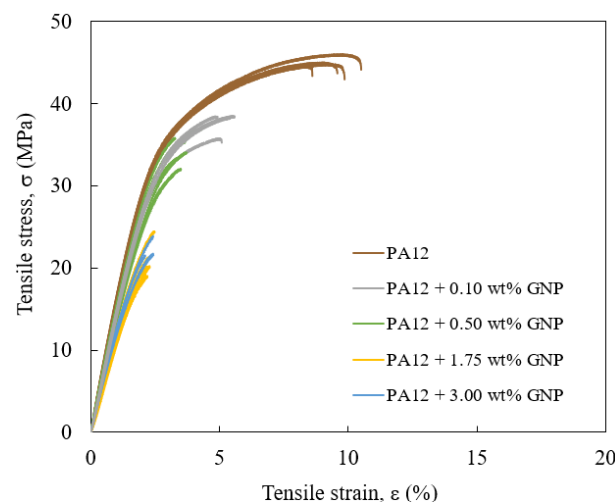


Figure 4.54 Engineering stress-strain curves of test specimens produced by SLS depending on the amount of GNP (in wt%).

The elastic modulus decreased from 1723.6 ± 48.2 MPa in test specimens produced with neat-PA12 to values close to 1200 MPa in test specimens produced with 1.75 wt% and 3.00 wt% of GNP, recording differences between 25-30% (Figure 4.55). Similar conditions with MWCNT presented variations of 37% with higher stiffness losses. On the other hand, composite materials with 0.10 wt% and 0.50 wt% of GNP ensured higher values of elastic modulus, with a maximum decrease of less than 20% in relation to test specimens produced with neat-PA12 material.

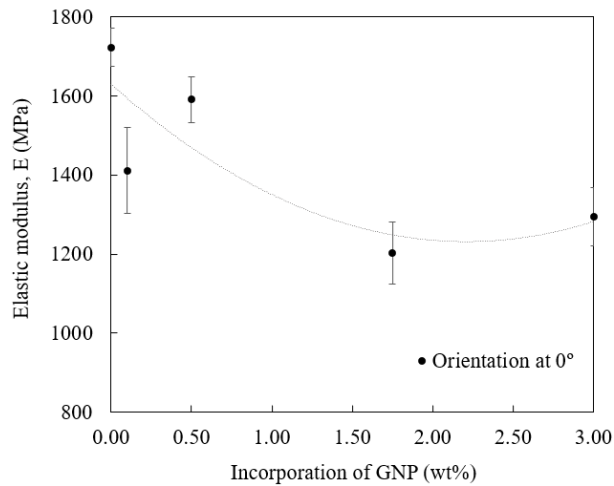


Figure 4.55 Elastic modulus of test specimens produced by SLS depending on the amount of GNP (in wt%).

The tensile stress at yield gradually decreased with the incorporation of GNP (Figure 4.56 (left)). Test specimens produced with the highest amount of GNP reached a tensile stress at yield of 18.12 ± 1.62 MPa, 34% lower than the values attained by test specimens produced with neat-PA12. In turn, the weight amount of 0.10 wt% of GNP ensured a reduction below 1%, proving the appropriateness of this powder material to guarantee adequate values of tensile stress at yield. Compared with the reference value, test specimens produced with 0.10 wt% and 0.50 wt% of GNP presented 8-12% higher tensile strain at yield, while test specimens produced with 1.75 wt% and 3.00 wt% exhibited 8-12% lower values (Figure 4.56 (right)).

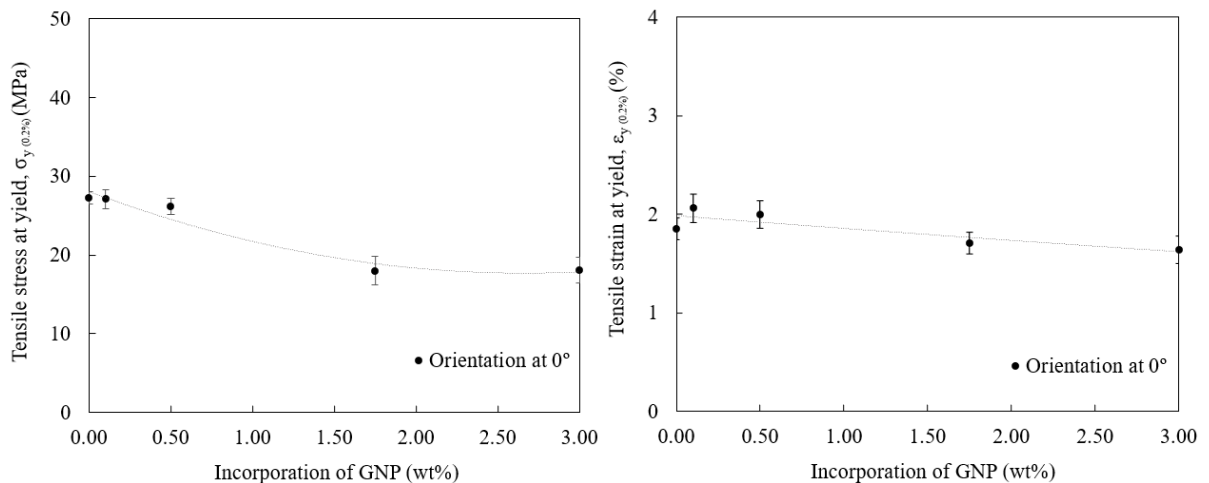


Figure 4.56 Tensile stress at yield (left) and tensile strain at yield (right) of test specimens produced by SLS depending on the amount of GNP (in wt%).

The tensile stress at break and tensile strain at break of all materials are shown in Figure 4.57. The tensile stress at break decreased 50% (on average) in test specimens produced with 1.75 wt% and 3.00 wt% of GNP, until minimum values between 20 - 23 MPa. A small decrease was verified in test specimens

Chapter 4. Development and characterization of SLS composite materials

produced with 0.10 wt% and 0.50 wt% which recorded 37.8 ± 1.5 MPa and 33.9 ± 1.9 MPa of tensile stress at break, respectively. The corresponding tensile strain at break significantly decreased in the composite materials, achieving a maximum reduction of 75% in test specimens produced with 3.00 wt% of GNP.

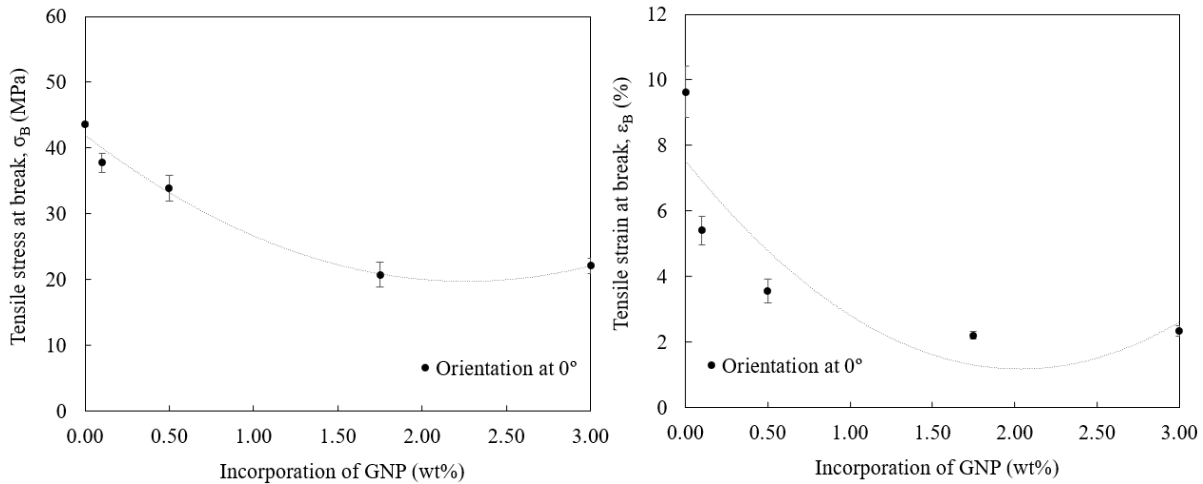


Figure 4.57 Tensile stress at break (left) and tensile strain at break (right) of test specimens produced by SLS depending on the amount of GNP (in wt%).

Finally, the tensile strength agreed with the results of tensile stress at break (Figure 4.58). The analysis demonstrated that test specimens produced with 1.75 wt% and 3.00 wt% of GNP withstood one-half of the tensile strength reached by test specimens produced with neat-PA12. The minimum amount of GNP considered (*i.e.*, 0.10 wt%) presented a reduction of 16% until 38.0 ± 1.4 MPa.

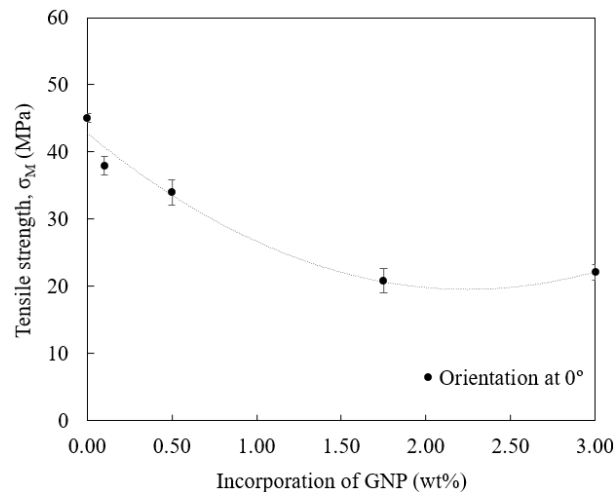


Figure 4.58 Tensile strength of test specimens produced by SLS depending on the amount of GNP (in wt%).

Compression properties

The engineering stress-strain curves obtained from compression tests also demonstrated the influence of GNP on the mechanical behaviour of carbon-based composites (Figure 4.59). The results revealed a

significant reduction of the compressive properties in test specimens produced with 1.75 wt% and 3.00 wt% of GNP, compared to the reference condition. In addition to the material-dependent characteristics, the divergence of results may also be a consequence of the periodic interruption of the process that was most often promoted during the sintering of these test specimens due to their higher building height.

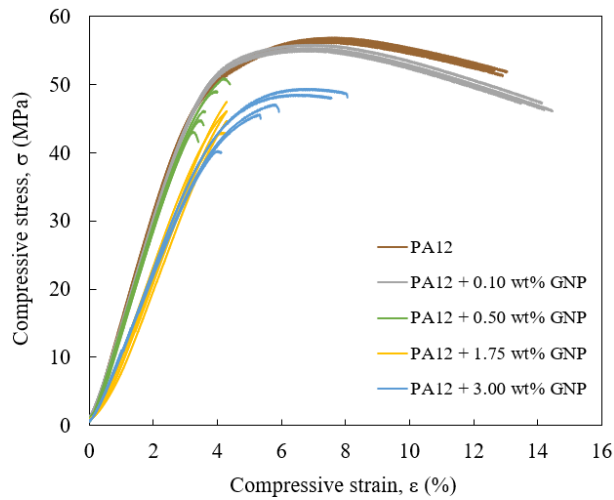


Figure 4.59 Engineering compressive stress-strain curves of test specimens produced by SLS depending on the amount of GNP (in wt%).

Based on the stress-strain curves, it was verified that the compressive elastic modulus remained close to 1450 MPa in test specimens produced with 0.10 wt% and 0.50 wt% of GNP, recording a reduction below 5% of the neat-PA12 (Figure 4.60 (left)). In turn, test specimens produced with 1.75 wt% and 3.00 wt% exhibited a decrease of 26% until 1120 MPa of elastic modulus (on average). Compared to the 56.5 MPa of compressive strength obtained in test specimens produced with neat-PA12, the test specimens produced with 0.10 wt% of GNP reached a reduction below 3% while the other composite formulations exhibited reductions between 9 - 19% until a minimum value of 46.1 MPa (Figure 4.60 (right)).

Chapter 4. Development and characterization of SLS composite materials

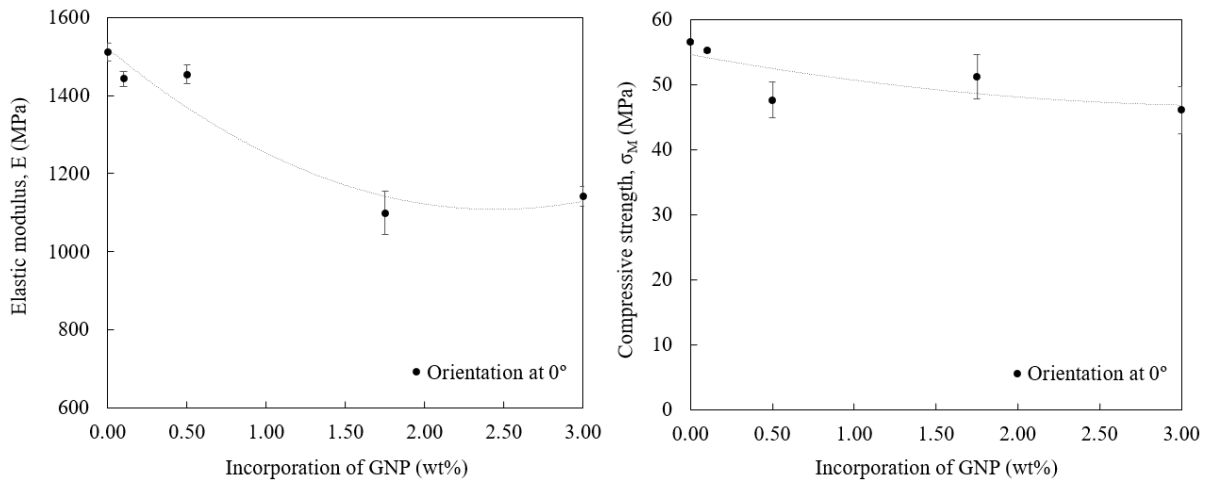


Figure 4.60 Compressive elastic modulus (left) and compressive strength (right) of test specimens produced by SLS depending on the amount of GNP (in wt%).

These results suggested that GNP-based composites allow to ensure greater mechanical performance under compressive loads, as higher values of compressive modulus and strength were achieved compared to MWCNT-based composites which recorded minimum values of 1003.0 MPa and 36.0 MPa, respectively, under similar conditions of preparation and processing.

Izod impact properties

The Izod impact resistance of test specimens produced with PA12 and PA12 incorporating 0.10 wt%, 0.50 wt%, 1.75 wt% and 3.00 wt% of GNP is shown in Figure 4.61.

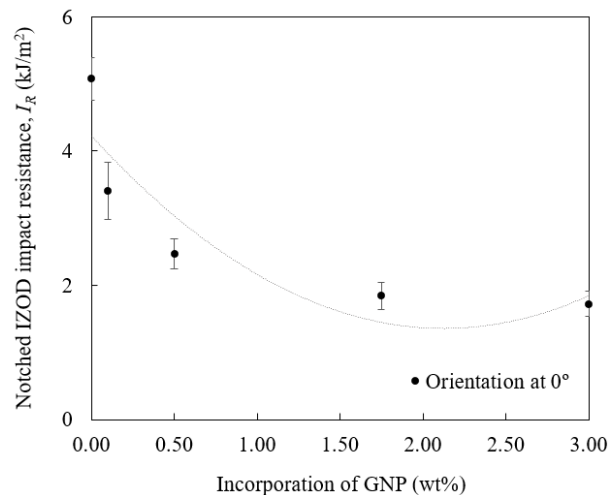


Figure 4.61 Notched Izod impact resistance of test specimens produced by SLS depending on the amount of GNP (in wt%).

As opposed to MWCNT, the inclusion of GNP significantly influenced the impact resistance of the base material. Compared to the reference condition (*i.e.*, 5.1 kJ/m²), test specimens produced with 0.10 wt% of GNP presented 18.4% lower impact resistance, while test specimens produced with weight percentages above 0.50 wt% presented a reduction above 50% until a minimum value of 1.7 kJ/m² with 3.00 wt% of

GNP. This proves that test specimens produced with GNP-based composites are less resistant to a mechanical impact directed to notched cantilever beam configurations than test specimens produced with MWCNT-based composites.

In sum, Table 4.6 presents the mechanical properties of the developed PA12-GNP composites.

Table 4.6 Summary of mechanical properties of PA12-GNP composites.

	PA12	PA12 + 0.10 wt% GNP	PA12 + 0.50 wt% GNP	PA12 + 1.75 wt% GNP	PA12 + 3.00 wt% GNP
TENSILE PROPERTIES					
E (MPa)	1723.60 ± 48.20	1411.64 ± 109.57	1591.40 ± 58.48	1203.25 ± 78.91	1295.09 ± 74.15
σ_{Ced} (MPa)	27.29 ± 0.80	27.12 ± 1.24	26.14 ± 1.04	18.02 ± 1.83	18.12 ± 1.62
ϵ_{Ced} (%)	1.85 ± 0.11	2.06 ± 0.15	2.00 ± 0.14	1.71 ± 0.11	1.64 ± 0.14
σ_{Rut} (MPa)	43.60 ± 0.40	37.77 ± 1.45	33.94 ± 1.94	20.76 ± 1.82	22.11 ± 1.15
ϵ_{Rut} (%)	9.64 ± 0.79	5.41 ± 0.44	3.56 ± 0.36	2.21 ± 0.12	2.34 ± 0.16
σ_{Max} (MPa)	45.04 ± 0.62	38.01 ± 1.38	33.99 ± 1.93	20.79 ± 1.83	22.11 ± 1.15
COMPRESSIVE PROPERTIES					
E (MPa)	1511.11 ± 22.12	1443.07 ± 18.78	1454.29 ± 24.16	1099.28 ± 55.78	1141.23 ± 25.49
σ_{Max} (MPa)	56.51 ± 0.26	55.24 ± 0.31	47.63 ± 2.76	51.24 ± 3.39	46.08 ± 3.60
IMPACT PROPERTIES					
K (kJ/m ²)	5.08 ± 0.32	3.41 ± 0.43	2.47 ± 0.23	1.85 ± 0.20	1.73 ± 0.19

4.4.2.6. Electrical properties

The results of electrical resistance, resistivity and conductivity of the neat-PA12 and developed GNP composite materials are presented in Table 4.7. Due to the challenging sintering process of these materials, the electrical analysis was also performed in tensile specimens through volume measurements using metal alligator clips for comparison with surface and volume measurements taken in standard flat plates. To more clearly illustrate the electrical behaviour and resulting ESD category, the results obtained from surface measurements are shown in Figure 4.62 through logarithmic scale.

Table 4.7 Electrical properties of PA12-GNP composites obtained through surface and volume measurements.

	MATERIALS	Electrical resistance (Ω)	Electrical resistivity ($\Omega.cm$)	Electrical conductivity (S/cm)
VOLUME (TENSILE TEST SPECIMENS)	PA12	-	-	-
	PA12 + 0.10 wt% GNP	$5.54 \times 10^{11} \pm 3.88 \times 10^{11}$	$5.92 \times 10^{10} \pm 4.36 \times 10^{10}$	$2.43 \times 10^{-11} \pm 1.62 \times 10^{-11}$
	PA12 + 0.50 wt% GNP	$9.74 \times 10^{10} \pm 2.17 \times 10^{10}$	$1.03 \times 10^{10} \pm 2.82 \times 10^9$	$1.01 \times 10^{-10} \pm 2.40 \times 10^{-11}$
	PA12 + 1.75 wt% GNP	$2.44 \times 10^7 \pm 6.50 \times 10^6$	$3.11 \times 10^6 \pm 1.19 \times 10^6$	$3.55 \times 10^{-7} \pm 1.35 \times 10^{-7}$

Chapter 4. Development and characterization of SLS composite materials

SURFACE (FLAT PLATES)	PA12 + 3.00 wt% GNP	$1.41 \times 10^5 \pm 3.56 \times 10^5$	$5.99 \times 10^4 \pm 5.87 \times 10^3$	$1.68 \times 10^5 \pm 1.82 \times 10^6$
	PA12	$4.29 \times 10^{10} \pm 3.83 \times 10^9$	$2.29 \times 10^{12} \pm 2.03 \times 10^{11}$	$4.39 \times 10^{13} \pm 3.75 \times 10^{14}$
	PA12 + 0.10 wt% GNP	$7.90 \times 10^{10} \pm 1.42 \times 10^9$	$4.22 \times 10^{12} \pm 7.64 \times 10^{10}$	$2.37 \times 10^{13} \pm 4.04 \times 10^{15}$
	PA12 + 0.50 wt% GNP	$2.68 \times 10^9 \pm 7.05 \times 10^8$	$1.43 \times 10^{11} \pm 3.74 \times 10^{10}$	$7.35 \times 10^{12} \pm 2.13 \times 10^{12}$
	PA12 + 1.75 wt% GNP	$6.85 \times 10^5 \pm 3.91 \times 10^5$	$3.66 \times 10^7 \pm 2.08 \times 10^7$	$3.63 \times 10^8 \pm 2.17 \times 10^8$
	PA12 + 3.00 wt% GNP	$1.02 \times 10^4 \pm 3.90 \times 10^3$	$5.44 \times 10^5 \pm 2.07 \times 10^5$	$2.00 \times 10^6 \pm 6.22 \times 10^7$
VOLUME (FLAT PLATES)	PA12	$3.16 \times 10^9 \pm 2.68 \times 10^8$	$4.82 \times 10^{11} \pm 4.08 \times 10^{10}$	$2.08 \times 10^{12} \pm 1.83 \times 10^{13}$
	PA12 + 0.10 wt% GNP	$1.71 \times 10^9 \pm 1.59 \times 10^8$	$2.34 \times 10^{11} \pm 2.26 \times 10^{10}$	$4.30 \times 10^{12} \pm 4.30 \times 10^{13}$
	PA12 + 0.50 wt% GNP	$2.89 \times 10^9 \pm 8.55 \times 10^8$	$4.40 \times 10^{11} \pm 1.14 \times 10^{11}$	$2.40 \times 10^{12} \pm 7.31 \times 10^{13}$
	PA12 + 1.75 wt% GNP	$3.02 \times 10^5 \pm 3.81 \times 10^6$	$4.77 \times 10^8 \pm 6.02 \times 10^8$	$5.91 \times 10^9 \pm 5.07 \times 10^9$
	PA12 + 3.00 wt% GNP	$1.11 \times 10^4 \pm 3.72 \times 10^3$	$1.73 \times 10^6 \pm 5.64 \times 10^5$	$6.28 \times 10^7 \pm 2.06 \times 10^7$

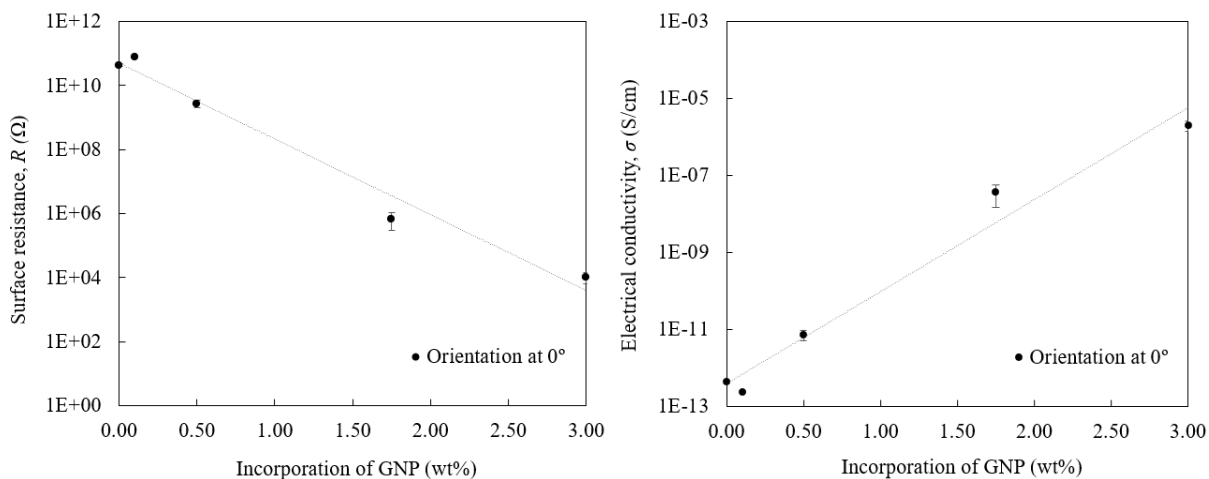


Figure 4.62 Surface resistance (left) and electrical conductivity (right) of flat plates produced by SLS depending on the amount of GNP (in wt%) (logarithmic scale).

As verified for the MWCNT-based composites, the inclusion of GNP into the insulative PA12 matrix gradually decreased its electrical resistance and resistivity, enhancing its electrical conductivity. The flat plates produced with 0.10 wt% and 0.50 wt% of GNP presented values of surface resistance of $10^{10} \Omega$ and $10^9 \Omega$, respectively. In these materials, the electrical conductivity reached a maximum of 10^{-12} S/cm . In turn, the electrical conductivity of flat plates produced with 1.75 wt% and 3.00 wt% of GNP increased several orders of magnitude until 10^{-8} S/cm and 10^{-6} S/cm , respectively, while the surface resistance decreased until $10^5 \Omega$ and $10^4 \Omega$, respectively. According to the standard norm IEC 61340-5-1, the flat plates produced with 1.75 wt% of GNP reached the electrostatic dissipative range (*i.e.*, $10^{11} >$ surface resistance $\geq 10^5$), while the flat plates produced with 3.00 wt% were electrostatic conductive (IEC, 1998). This indicates that, under the conditions of this study, incorporation of 1.75 wt% of GNP or higher can create an effective conductive path between the particles of reinforcement, allowing to significantly

enhance the electrical conductivity of the polymeric base material. The electrical results obtained from volume measurements agreed with the surface measurements. This suggests that the carbon-based particles are also creating a conductive path for electrical conductivity along the cross-section of the flat plates allowing to attain values of electrical conductivity close to 10^9 S/cm and 10^7 S/cm with composite materials incorporating 1.75 wt% and 3.00 wt% of GNP, respectively. Compared both carbon-based composites, the results showed that the drop in electrical surface resistance tended to be higher in MWCNT-based materials, which, consequently, recorded higher values of electrical conductivity.

4.4.2.7. Thermal properties

Differential Scanning Calorimetry (DSC)

Figure 4.63 shows the melting and crystallization temperatures (*i.e.*, T_m and T_c) of the developed PA12-GNP composite materials revealed by DSC analysis. The incorporation of GNP did not critically modify the T_m of the materials since it remained close to 177 °C in all of them. This evidence was also reported for PA12-MWCNT composites, proving that the inclusion of these carbon-based reinforcements does not significantly affect the thermal behaviour of the polymeric base material during its heating until 230 °C. In turn, T_c increased from 145 °C in neat-PA12 to values close to 150 °C in composite materials produced with 0.10 wt%, 0.50 wt%, 1.75 wt% and 3.00 wt% of GNP. This difference of 5 °C (on average) established the thermal processing window of 150 - 177 °C for these materials, which is narrower than the thermal processing window of the neat-PA12.

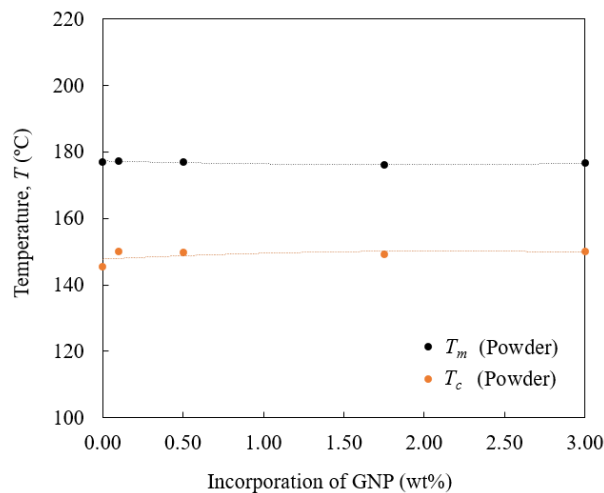


Figure 4.63 Melting and crystallization temperatures of SLS composite powders depending on the amount of GNP (in wt%).

Within the thermal range of 40 - 160 °C, the specific heat capacity of the PA12-GNP composite materials did not reveal substantial differences compared to the neat-PA12 (Figure 4.64). Under these

conditions, the specific heat capacity increased with temperature from 1.5 J/g·°C to 2.5 J/g·°C in all materials.

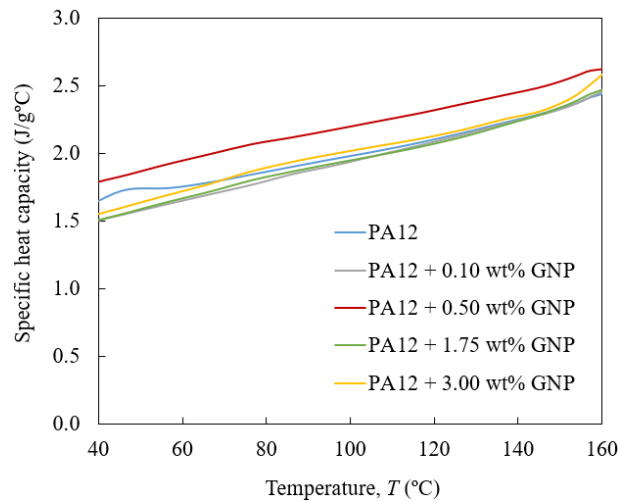


Figure 4.64 Specific heat capacity of test specimens produced by SLS depending on the amount of GNP (in wt%) with temperature.

Thermogravimetric analysis (TGA)

The onset temperature obtained from the TGA thermograms and the combustible material remaining at the end of the test are shown in Figure 4.65 for all GNP-based materials. The initial deflection point reached 400 °C in all materials, proving their great thermal stability without significant mass changes below that temperature. This result agrees with the findings aforementioned for composite materials integrating MWCNT (see Figure 4.39). Regarding the final combustible material at the end of the heating, the analysis showed real weight percentages of GNP slightly higher than the theoretical, except for the condition of 3.00 wt%, which revealed lower content of reinforcement.

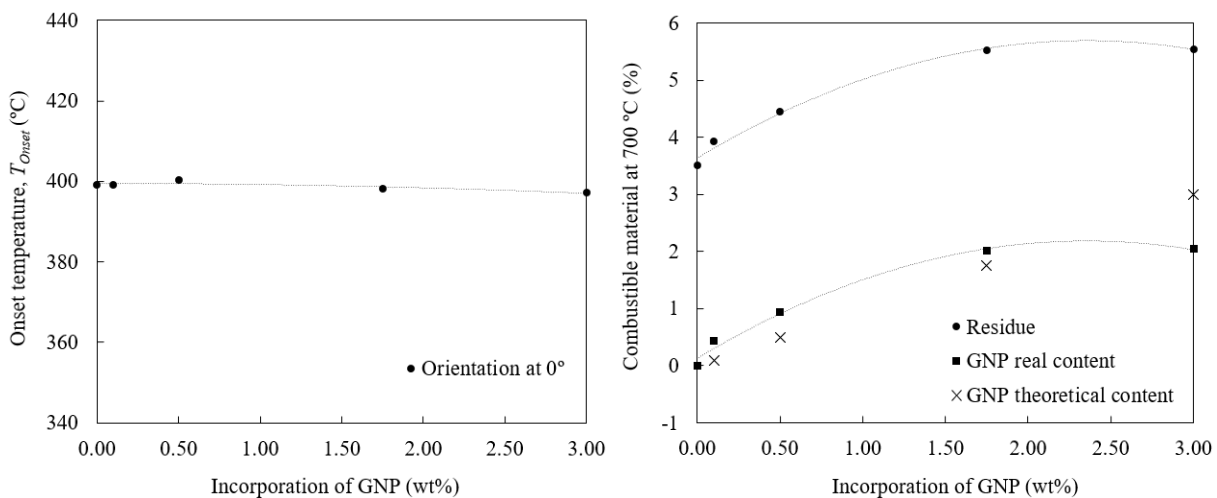


Figure 4.65 Onset temperature (left) and percentage of combustible material at 700 °C (right) of test specimens produced by SLS depending on the amount of GNP (in wt%).

4.4.2.8. Morphological properties

The cross-section of test specimens produced by SLS with neat-PA12 and PA12 incorporating 0.50 wt%, 1.75 wt% and 3.00 wt% of GNP is shown in Figure 4.66. The SEM micrographs obtained at high magnification revealed that the microstructure of the cross-section becomes less homogeneous with the increasing amount of GNP. The analysis showed that the inclusion of GNP weakens the interparticle adhesion, resulting in a cross-section where unsintered powder particles are clearly distinguished. This suggests that GNP acts as an inhibitor to the flow and consolidation of the polymeric powder particles.

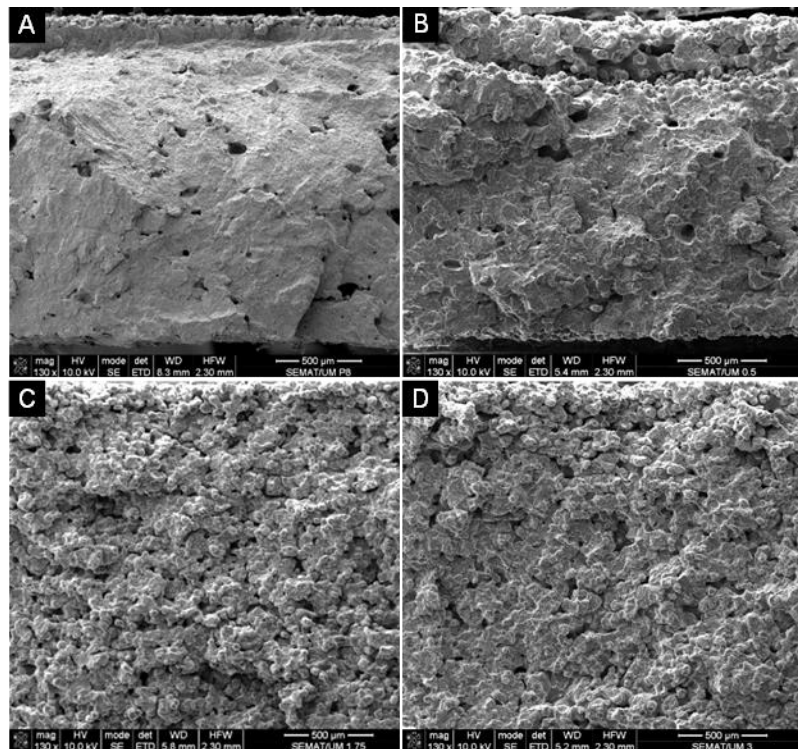


Figure 4.66 Cross-section of test specimens produced by SLS with A) PA12, B) PA12 + 0.50 wt% GNP, C) PA12 + 1.75 wt% GNP and D) PA12 + 3.00 wt% GNP.

At lower magnification, the SEM micrographs revealed the impregnation of GNP all over the PA12 powder particles (Figure 4.67). As the amount of impregnated GNP particles increases from 0.10 wt% to 3.00 wt%, the surface area of polymeric material available to establish a quality interparticle coalescence decrease. This impairs the definition of a strong, uniform and homogeneous cross-section, which results in the production of test specimens with reduced mechanical performance (see *section 4.4.2.4*).

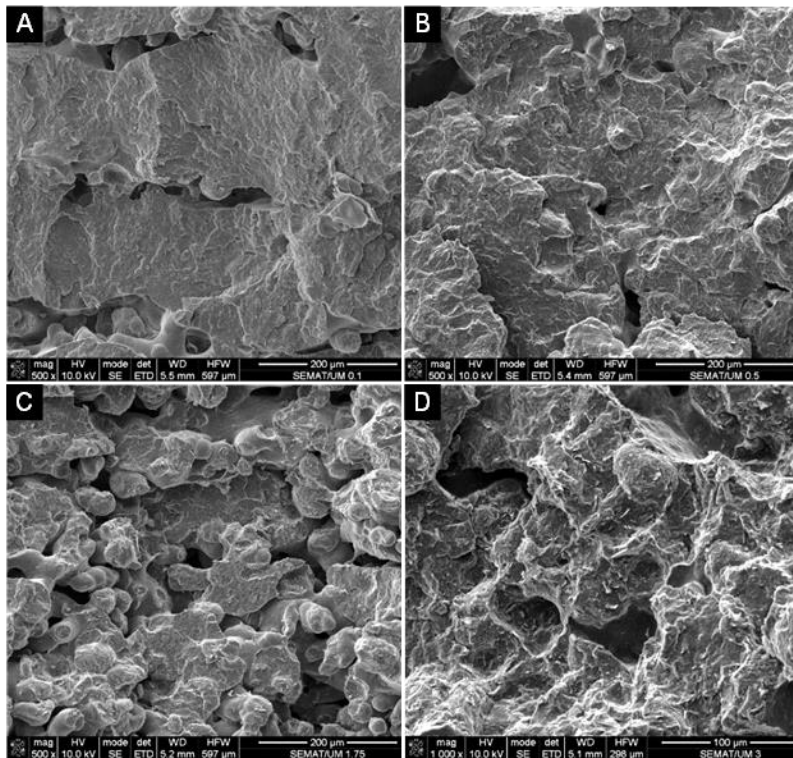


Figure 4.67 Cross-section of test specimens produced by SLS with A) PA12 + 0.10 wt% GNP, B) PA12 + 0.50 wt% GNP, C) PA12 + 1.75 wt% GNP and D) PA12 + 3.00 wt% GNP.

4.4.3. PA12-MWCNT-GNP composites

4.4.3.1. Description of observations

The experiments presented in this chapter were performed to evaluate the synergistic effect of weight percentages of MWCNT and GNP that did not exhibit desired mechanical and electrical functionality on their own. As lower amounts of reinforcement ensured greater mechanical properties (see *sections 4.4.1* and *4.4.2*), the combination of 0.50 wt% of MWCNT with 0.10 wt% of GNP was tested in order to assess its potential to reduce the electrical surface resistance up to the ESD range ensuring higher tensile and compressive strength with lower development costs. As shown in previous sections, above 0.50 wt% of MWCNT and 0.10 wt% of GNP the electrical surface resistance and resistivity significantly decrease while the complexity of processing and overall costs increase, which makes the assessment of a combined effect less relevant. The composite solution considered for analysis in this section was compared with the following materials: i) PA12 with 0.50 wt% of MWCNT, ii) PA12 with 0.10 wt% of GNP, iii) PA12 with 1.75 wt% of MWCNT and iv) PA12 with 1.75 wt% of GNP, in order to identify the improvement of properties in relation to the corresponding individual formulations (*i.e.*, i) and ii)) and to ESD materials developed in this research up to this stage (*i.e.*, iii) and iv)).

Through macro-scale observation, the analysis revealed that a homogeneous powder mixture of PA12 incorporating 0.50 wt% of MWCNT with 0.10 wt% of GNP was prepared through mechanical mixing. This

allowed the smooth spread of powder particles during the SLS process, contradicting the complexity of processing observed with the incorporation of higher amounts of these carbon-based reinforcements (Figure 4.68).

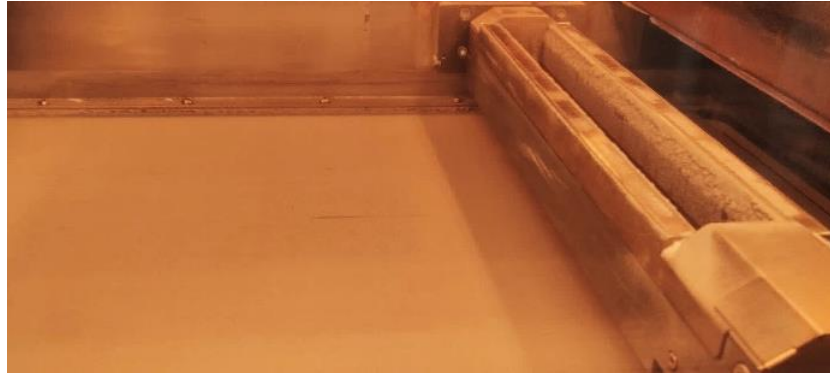


Figure 4.68 Sintering process of PA12-MWCNT-GNP composites evidencing the powder bed.

Based on the results obtained from the individual analysis, it was verified that the surface finishing of the test specimens produced with composite materials combining MWCNT and GNP showed greater similarity with test specimens produced with MWCNT than with GNP (Figure 4.69). Besides the different weight percentages of incorporation, this may be a consequence of the base typology of the carbon allotropes which to a different extent influences the outer surfaces of SLS parts (see Figure 4.43).

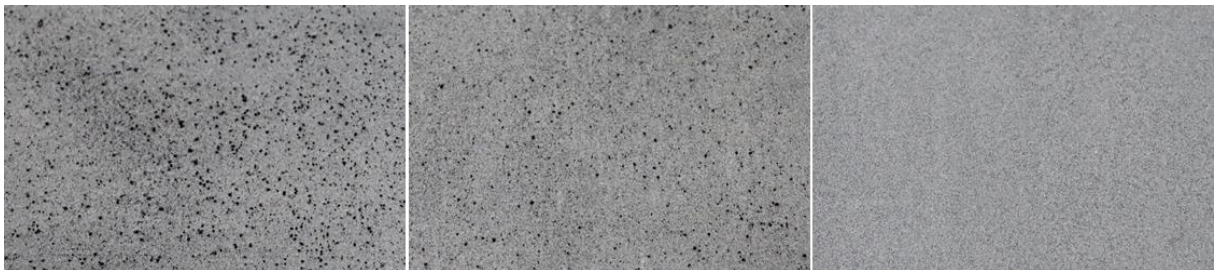


Figure 4.69 Details of the top surface of test specimens produced by SLS with PA12 incorporating 0.50 wt% of MWCNT (left), 0.50 wt% of MWCNT and 0.10 wt% of GNP (middle) and 0.10 wt% of GNP (right).

The test artefact produced with a combination of MWCNT and GNP showed fine pins until 0.25 mm and no hole of less than 2.00 mm of nominal diameter in its surface directed to the top (Figure 4.70). This agrees with the dimensional and geometric results obtained in the test artefacts produced with PA12 integrating 0.50 wt% of MWCNT and PA12 integrating 0.10 wt% of GNP.

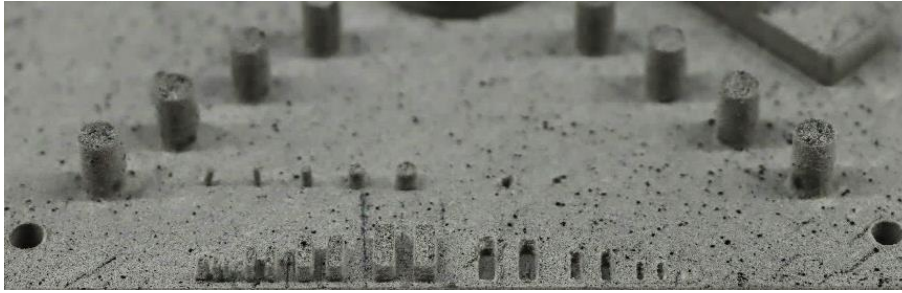


Figure 4.70 Fine features of test artefacts produced by SLS with PA12 incorporating 0.50 wt% of MWCNT and 0.10 wt% of GNP.

4.4.3.2. Mass and general dimensions

The results of mass, length, width and thickness of test specimens produced with PA12-MWCNT-GNP composite material are shown in Table 4.8. In relation to the nominal, there was a decrease of 0.47 mm in length and 0.18 mm in width. This may be mostly justified by the inclusion of GNP, since in the individual analysis it was demonstrated that such reinforcement causes a more prominent decrease in these dimensional parameters than MWCNT-based materials (see *section 4.4.2.2*). In turn, it was verified a slight increase in the thickness of the test specimens produced with the combined solution until 2.09 ± 0.02 mm, surpassing the nominal value. As expected, the mass decreased in relation to the individual formulations due to the combined effects of both low-density reinforcements, recording a minimum value of 0.871 ± 0.003 g.

Table 4.8 Dimensional properties of PA12-MWCNT-GNP composites.

	Length (mm)	Width (mm)	Thickness (mm)	Mass (g)
Nominal dimensions	75.00	5.00	2.00	-
PA12 + 0.10 wt% GNP + 0.50 wt% MWCNT	74.53 ± 0.03	4.82 ± 0.03	2.09 ± 0.02	0.871 ± 0.003

4.4.3.3. Dimensional and geometric accuracy

The GD&T analysis revealed that the combination of 0.50 wt% of MWCNT with 0.10 wt% of GNP allowed a reduction of flatness until 0.22 ± 0.01 mm in relation to the corresponding individual formulations, assuming values close to those obtained in the test artefact produced with neat-PA12 (Figure 4.71). The flatness of this combined solution is half of that observed in the test artefact produced with PA12 integrating 1.75 wt% of GNP, which presented electrostatic dissipative properties.

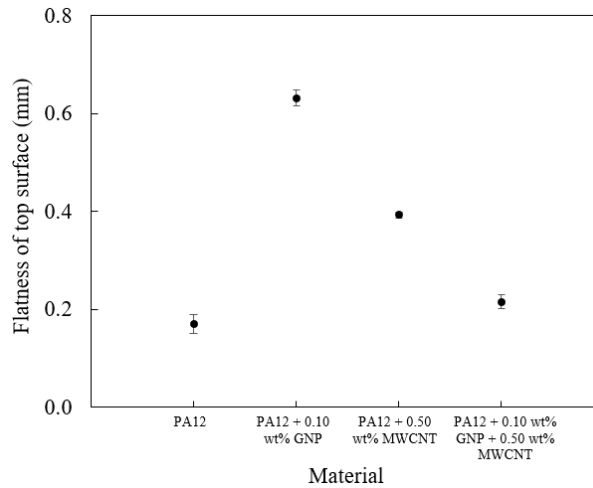


Figure 4.71 Flatness of the top surface of test artefacts produced by SLS depending on the carbon-based material.

The combination of such carbon-based reinforcements was also advantageous to reduce the roundness of central and lateral holes manufactured in the surfaces of the test artefact (Figure 4.72). The test artefact produced with PA12-MWCNT-GNP composite material reached a value of roundness of 0.09 ± 0.01 mm in central holes. This value is similar to that measured in holes produced with PA12 matrix and 36% lower (on average) than that measured in the ESD materials developed in this work.

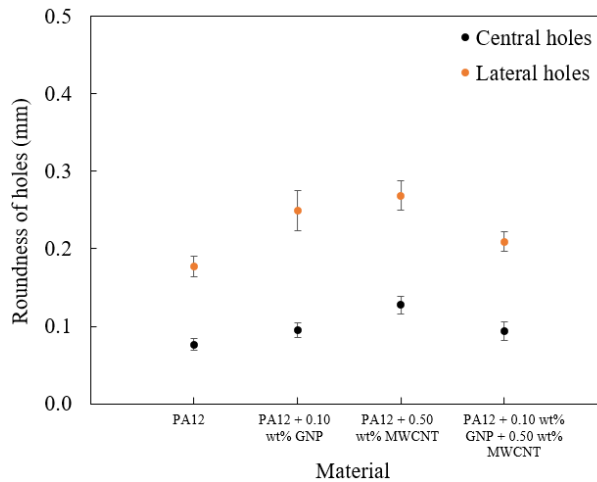


Figure 4.72 Roundness of central and lateral holes of test artefacts produced by SLS depending on the carbon-based material.

Figure 4.73 shows the straightness of the primary surface of the test artefacts produced with the different carbon-based materials. The test artefact produced with the combined solution recorded the lowest value of 0.16 ± 0.01 mm. Once again, this value was lower than those obtained in the test artefacts produced with the corresponding individual formulations and the materials with ESD characteristics.

Chapter 4. Development and characterization of SLS composite materials

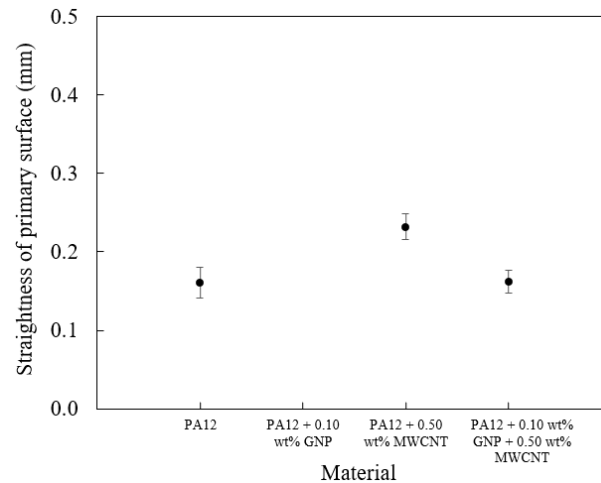


Figure 4.73 Straightness of the primary surface of test artefacts produced by SLS depending on the carbon-based material.

The test artefact produced with PA12 integrating 0.50 wt% of MWCNT and 0.10 wt% of GNP recorded a parallelism of surfaces of 0.20 ± 0.01 mm (Figure 4.74). This demonstrates the potential of the combined solution in the production of parallel surfaces within the dimensional and geometric tolerances.

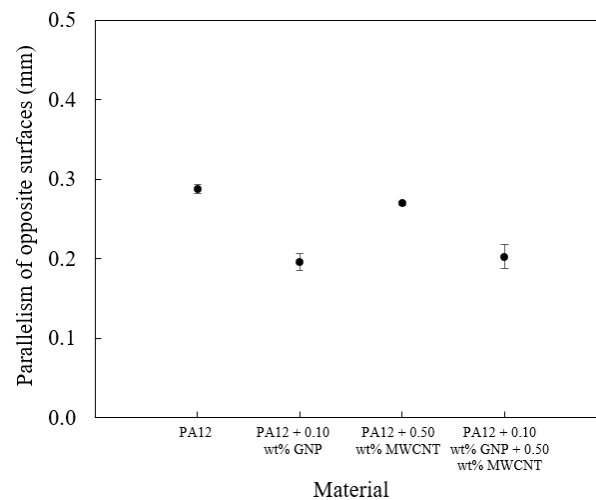


Figure 4.74 Parallelism of opposite surfaces of test artefacts produced by SLS depending on the carbon-based material.

The tolerancing of location is evaluated in Figure 4.75, Figure 4.76, Figure 4.21 and Figure 4.77 with respect to the x, y and z axes, respectively, according to the representation illustrated in Figure 3.39. Compared with the neat-PA12 matrix, the linear displacement deviation of features in the x-y plane increased with the incorporation of carbon-based reinforcements, regardless of the typology and weight percentage. In such composite materials, the deviation in the positioning increased with the increase of the distance between the centre of the feature and the centre of the test artefact. The combination of MWCNT with GNP did not allow the reduction of the linear displacement deviation along the x and y axes, revealing critical dependence on the nominal position of the features. In the combined solution, features until ± 50.00 mm from the centre of the test artefact reached maximum deviations close to 0.50 mm in

both axes, surpassing the satisfactory tolerance of ± 0.10 mm. On average, these deviations reached 1% of the nominal position of the features.

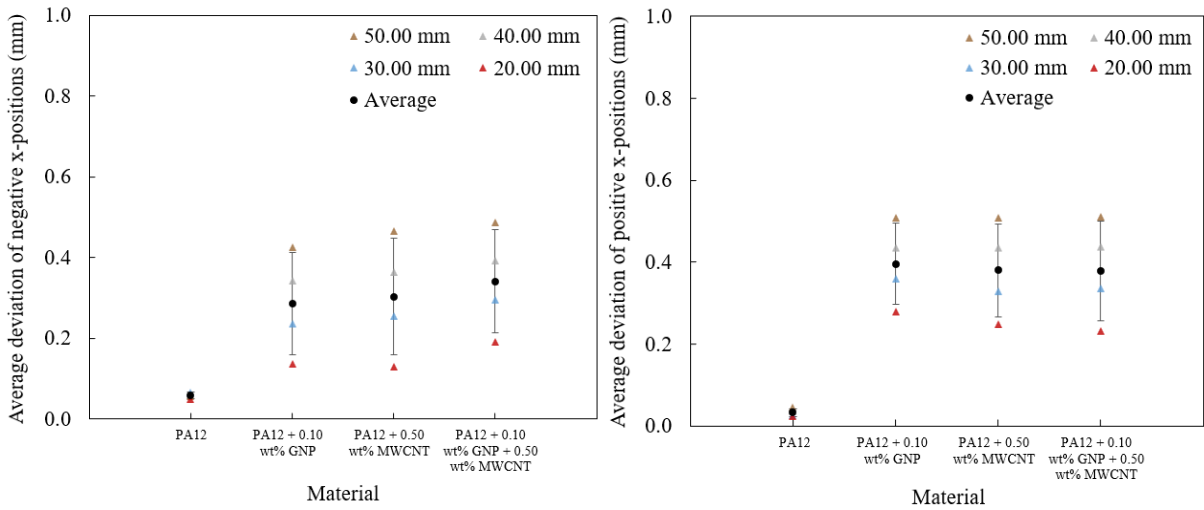


Figure 4.75 Average deviations of negative (left) and positive (right) x-positions of pins in test artefacts produced by SLS depending on the carbon-based material.

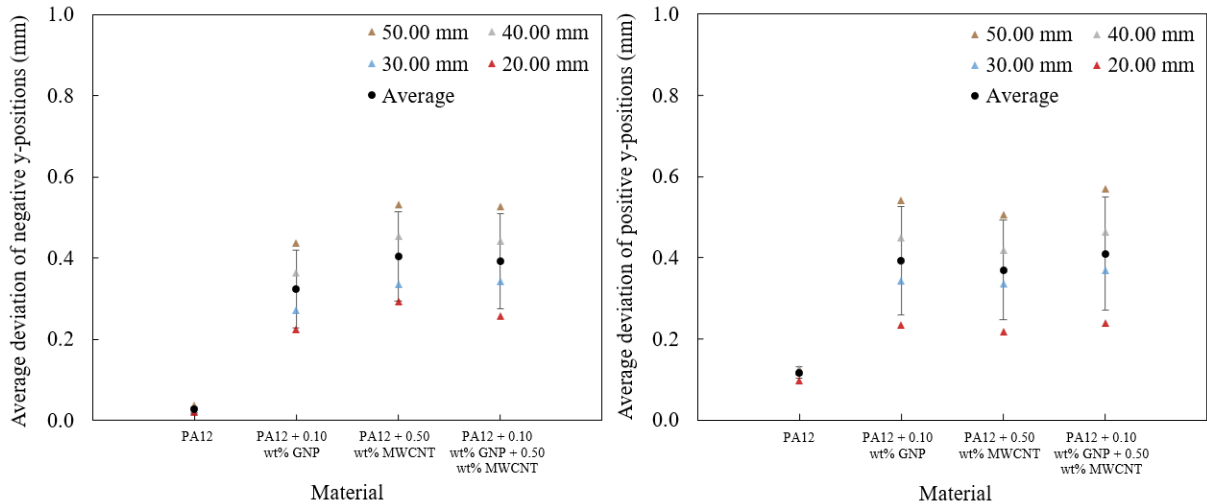


Figure 4.76 Average deviations of negative (left) and positive (right) y-positions of pins in test artefacts produced by SLS depending on the carbon-based material.

The results obtained from this analysis allowed to determine the percentage of deviation of pins positioned along the x and y axes in parts produced by SLS with PA12 and PA12 integrating carbon-based reinforcements, regardless of their nominal position (Figure 4.77).

Chapter 4. Development and characterization of SLS composite materials

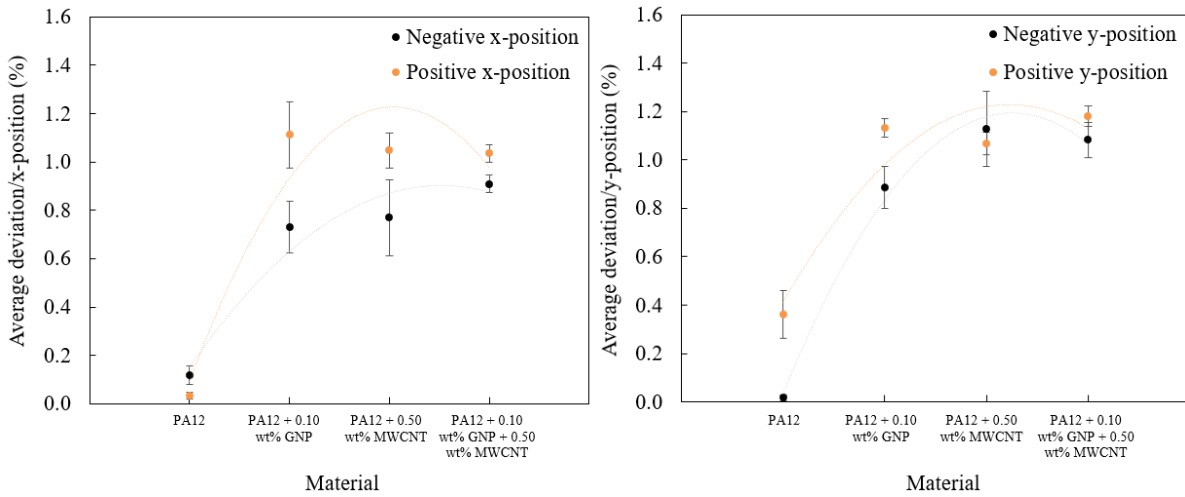


Figure 4.77 Factor of deviation (in %) for x (left) and y (right) positions of pins in test artefacts produced by SLS depending on the carbon-based material.

The average deviations of negative and positive z-positions did not reveal a clear tendency as a function of the SLS material (Figure 4.78). Positive and negative linear displacement deviations were observed in the test artefacts produced with carbon-based composites, without significant differences in relation to the matrix, except for the test artefact produced with 0.10 wt% of GNP that revealed more critical values in negative z-positions.

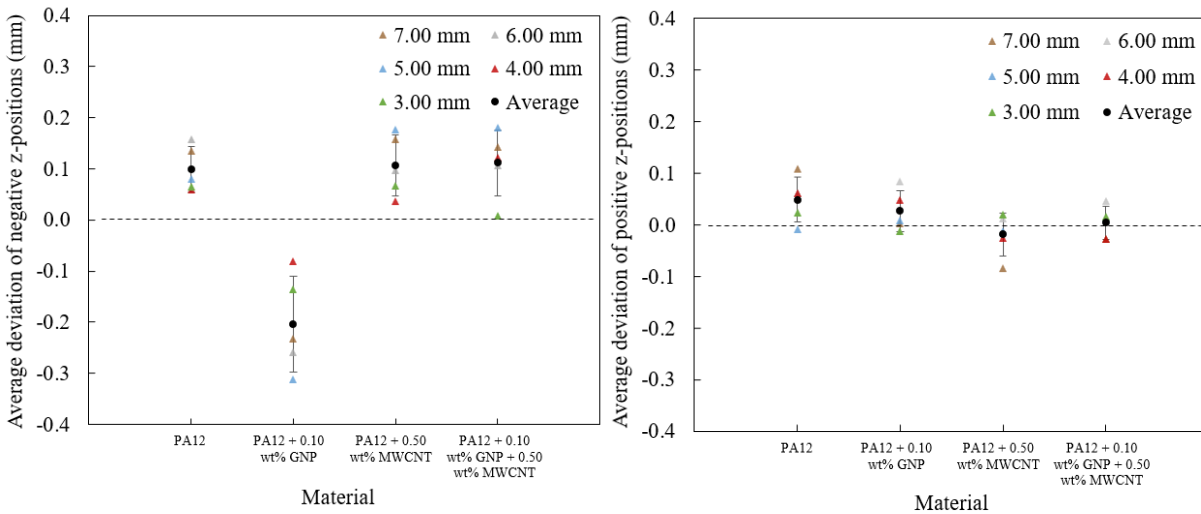


Figure 4.78 Average deviations of negative (left) and positive (right) z-positions of staircases in test artefacts produced by SLS depending on the carbon-based material.

Figure 4.79 reports the average diameter of pins and holes with nominal values between 2.00 mm and 0.25 mm of test artefacts produced by SLS with different carbon-based composite materials. The analysis showed that pins with nominal diameter of less than 0.50 mm were not sintered with satisfactory dimensional tolerance in any test artefact. In turn, all other fine pins produced with PA12-MWCNT-GNP composite material met nominal specifications, including the pin with 1.00 mm of nominal diameter that was not produced with PA12 incorporating 0.10 wt% of GNP. In this regard, the results were similar to

those obtained in the test artefact produced with neat-PA12. In terms of holes, the results demonstrated dimensional deviations above 0.30 mm in all nominal diameters for all materials under study, exceeding the common dimensional tolerance of ± 0.10 mm for SLS parts.

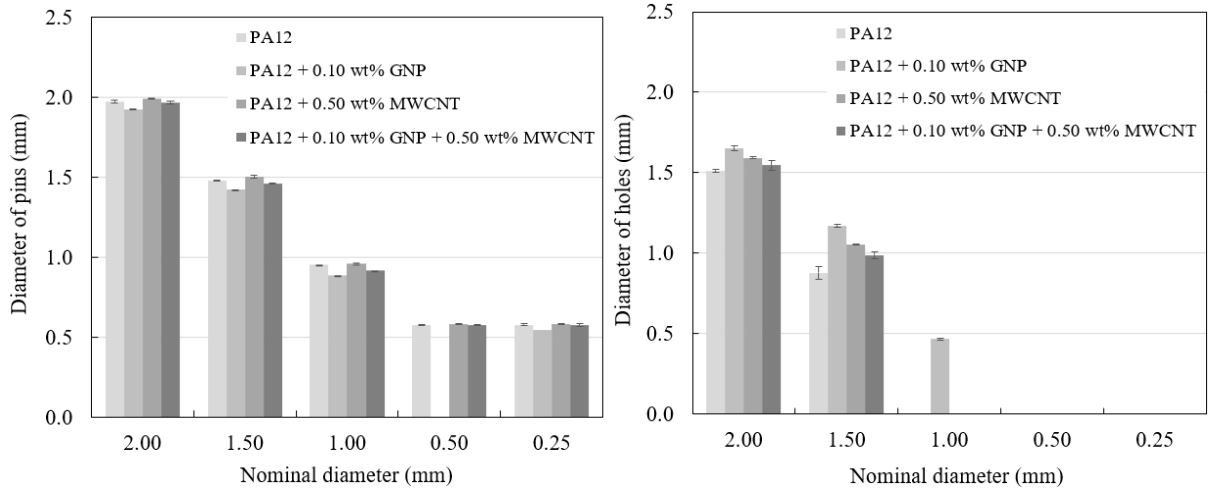


Figure 4.79 Diameter of pins (left) and holes (right) of test artefacts produced by SLS depending on the carbon-based material.

All previously discussed findings were validated through the analysis of the dimensional deviations in surfaces of the test artefacts produced with the composite materials in relation to the CAD model (Figure 4.80). Despite the non-significant differences observed between these test artefacts, the most significant effects observed in the combined solution were the shrinkage of the lateral surfaces of the test artefact and deviations in the positioning of features in relation to the nominal. The upward-facing surface revealed great conformity, which agrees with the results of flatness (see Figure 4.71).

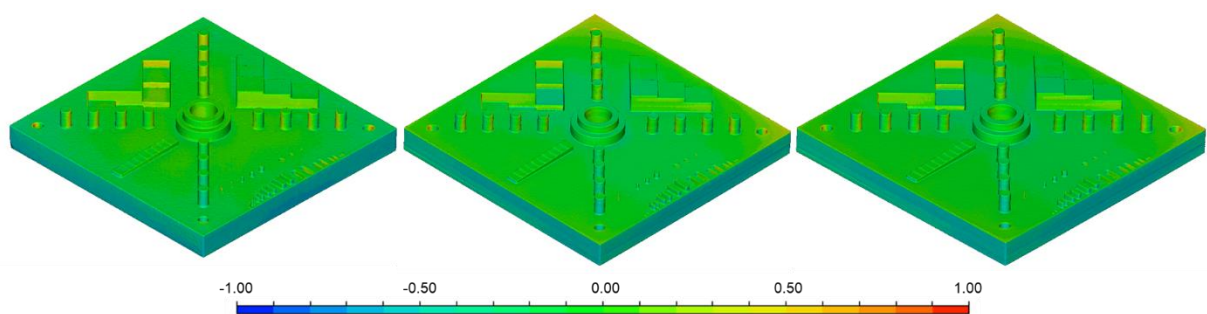


Figure 4.80 Surface comparison of test artefacts produced by SLS with PA12 incorporating 0.50 wt% of MWCNT (left), 0.10 wt% of GNP (middle) and 0.50 wt% of MWCNT with 0.10 wt% of GNP (right) with the CAD model.

4.4.3.4. Surface roughness

Figure 4.81 shows the topography of the top surface of test specimens produced by SLS with PA12-MWCNT-GNP composite materials and Table 4.9 lists the corresponding surface roughness parameters. Compared to the individual formulations, the results showed a significant increase of the Sa value in the

Chapter 4. Development and characterization of SLS composite materials

combined solution, until 17.9 μm . This represents an average increase close to 33% in relation to the individual formulations. The maximum peak height and maximum valley depth also recorded the highest values in test specimens produced with PA12 incorporating 0.50 wt% of MWCNT and 0.10 wt% of GNP, namely 93.08 μm and 206.45 μm , respectively.

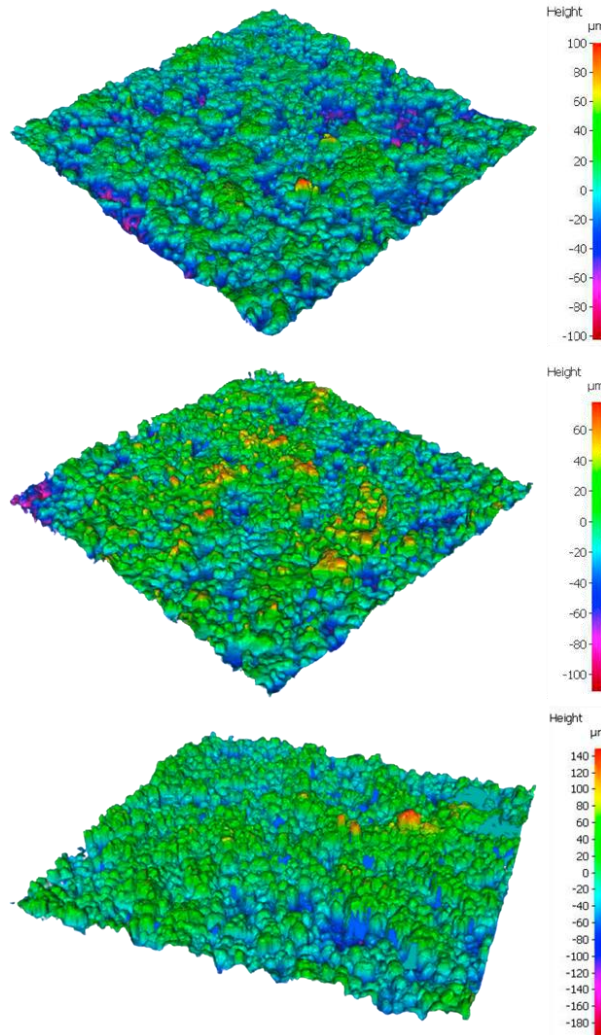


Figure 4.81 Top surface topography of test specimens produced by SLS with PA12 incorporating 0.10 wt% of GNP (top), 0.50 wt% of MWCNT (middle) and 0.50 wt% of MWCNT and 0.10 wt% of GNP (bottom).

Table 4.9 Surface roughness parameters of PA12-MWCNT-GNP composites processed by SLS.

MATERIALS	Arithmetic mean height S_a (μm)	Root-Mean-Square height S_q (μm)	Maximum peak height S_p (μm)	Maximum valley depth S_v (μm)	Maximum height S_z (μm)
PA12 + 0.10 wt% GNP	13.49	16.56	86.93	72.53	159.46
PA12 + 0.50 wt% MWCNT	13.49	16.87	65.35	71.65	136.99
PA12 + 0.10 wt% GNP + 0.50 wt% MWCNT	17.91	22.56	93.08	206.45	299.53

4.4.3.5. Mechanical properties

Tensile properties

Figure 4.82 presents engineering stress-strain curves of test specimens produced with PA12 incorporating 0.50 wt% of MWCNT and 0.10 wt% of GNP. The results indicate that a combination of both carbon-based reinforcements was not advantageous to enhance the mechanical performance of the individual formulations.

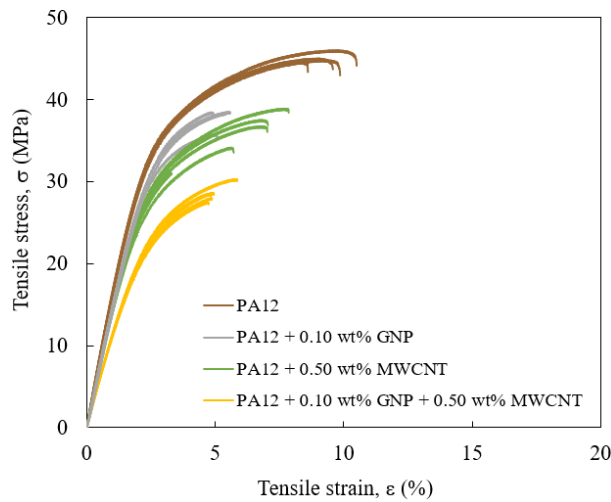


Figure 4.82 Engineering stress-strain curves of test specimens produced by SLS with combination of MWCNT and GNP.

This combined solution revealed an elastic modulus of 1194.9 ± 19.4 MPa, which represents a decrease of 18% and 13% of the individual formulations with MWCNT and GNP, respectively (Figure 4.83). In turn, this value is similar to the value obtained with PA12 incorporating 1.75 wt% of GNP and 8% higher than that obtained with PA12 incorporating 1.75 wt% of MWCNT, which revealed greater electrical potential.

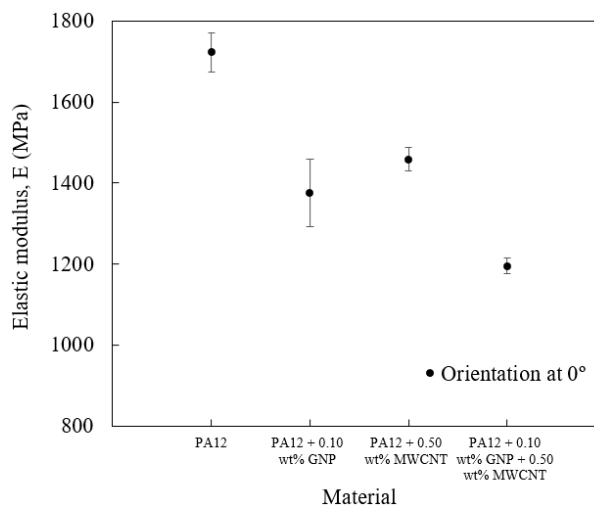


Figure 4.83 Elastic modulus of test specimens produced by SLS with combination of MWCNT and GNP.

Chapter 4. Development and characterization of SLS composite materials

The tensile stress at yield also decreased until 18.3 ± 0.7 MPa, recording a reduction of 21% and 33% in relation to the corresponding PA12-MWCNT and PA12-GNP composites (Figure 4.84 (left)). The composite materials incorporating 1.75 wt% of GNP and 1.75 wt% of MWCNT respectively revealed 1.5% and 22% lower tensile stress at yield. The tensile strain at yield did not reveal significant modifications (Figure 4.84 (right)). All conditions exhibited values of tensile strain at yield close to 2%.

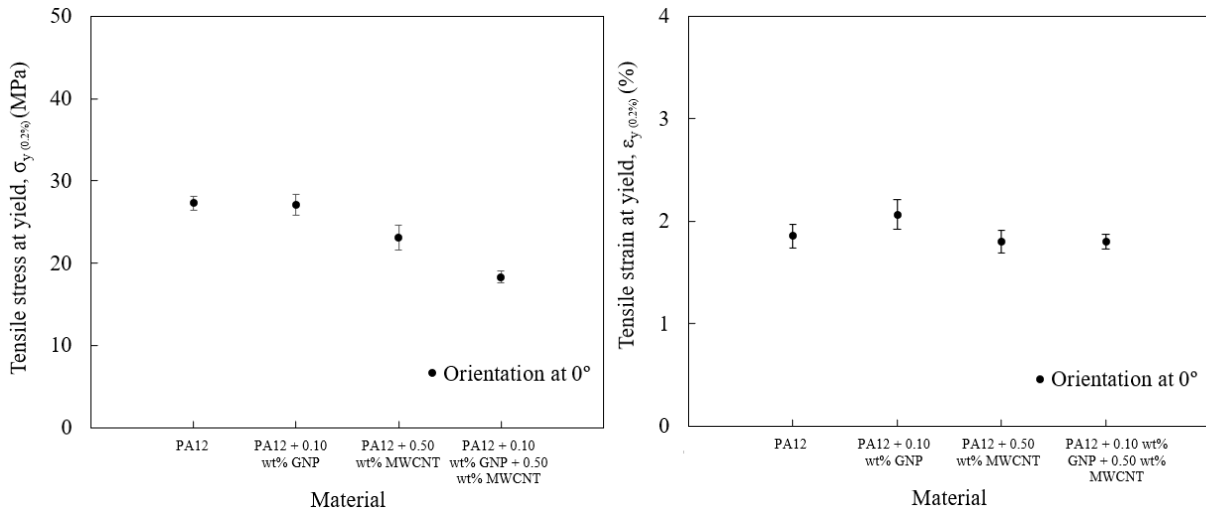


Figure 4.84 Tensile stress at yield (left) and tensile strain at yield (right) of test specimens produced by SLS with combination of MWCNT and GNP.

The results of tensile stress at break and tensile strain at break showed coherent behaviour (Figure 4.85). The combined solution recorded 28.3 ± 1.1 MPa of tensile stress at break, which is more than 20% lower than the individual formulations. In turn, this value represents an increase above 26% and 36% of the solutions with MWCNT and GNP that presented higher electrical potential, respectively. The tensile strain at break reached $5.1 \pm 0.5\%$.

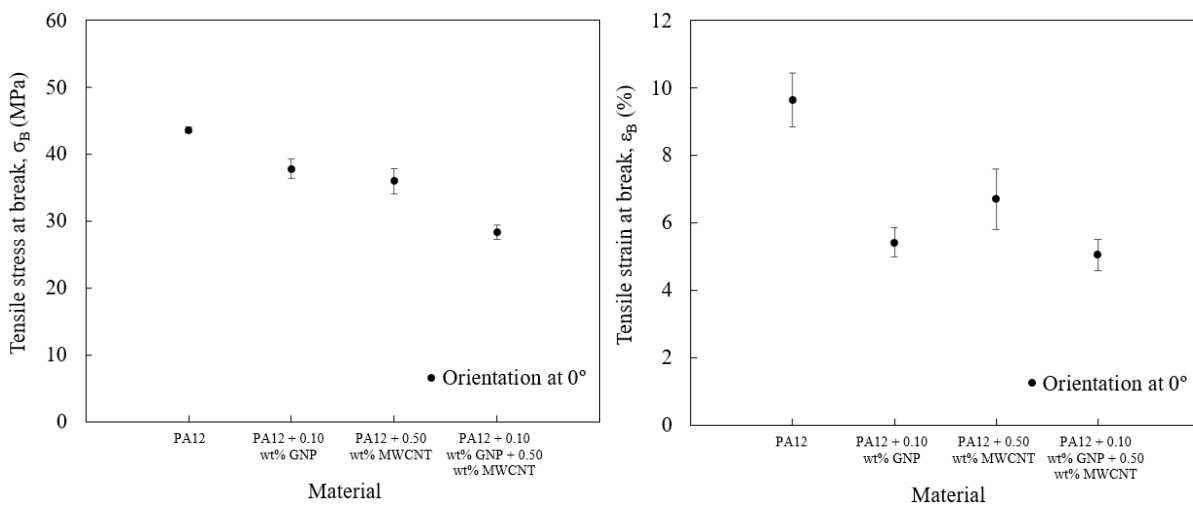


Figure 4.85 Tensile stress at break (left) and tensile strain at break (right) of test specimens produced by SLS with combination of MWCNT and GNP.

The composite materials produced with MWCNT and GNP presented 28.5 ± 1.1 MPa of tensile strength (Figure 4.86). This value decreased 22% and 25% from the corresponding conditions with MWCNT and GNP, respectively.

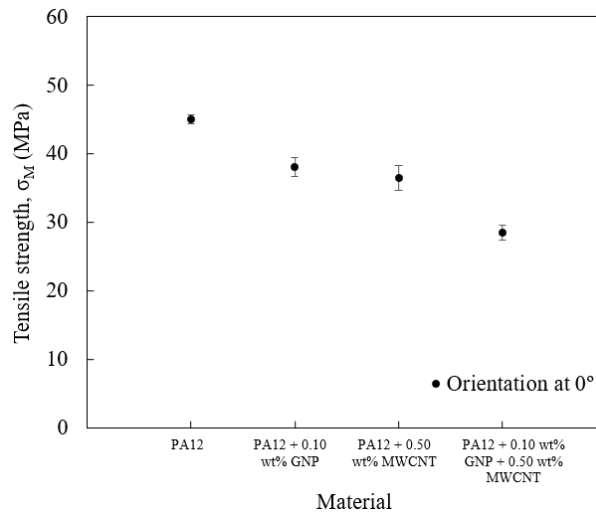


Figure 4.86 Tensile strength of test specimens produced by SLS with combination of MWCNT and GNP.

Compression properties

Figure 4.87 shows engineering stress-strain curves obtained from compression tests. The results revealed a significant reduction of compressive properties in test specimens produced with combination of GNP and MWCNT, compared to the corresponding individual solutions.

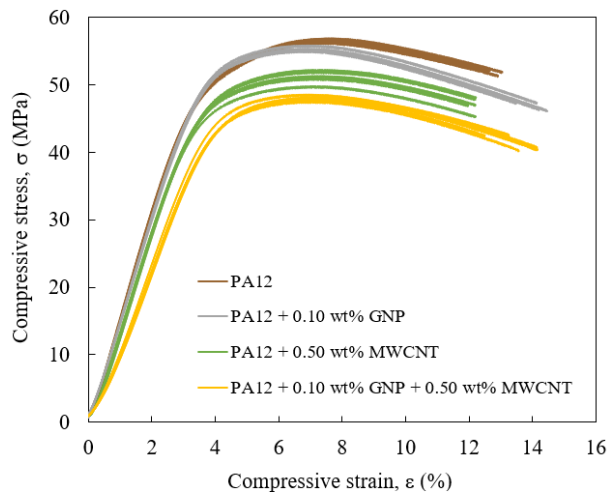


Figure 4.87 Engineering compressive stress-strain curves of test specimens produced by SLS with combination of MWCNT and GNP.

The test specimens produced with PA12-MWCNT-GNP composite material presented a compressive elastic modulus of 1196.6 ± 29.9 MPa (Figure 4.88 (left)). This value decreased 17% of that obtained in test specimens produced with PA12 incorporating 0.10 wt% of GNP and 8% of that obtained in test specimens produced with 0.50 wt% of MWCNT. In turn, this value is higher than those values obtained in

Chapter 4. Development and characterization of SLS composite materials

test specimens which revealed electrical surface range in the electrostatic conductive and dissipative range. The compressive strength presented a similar tendency (Figure 4.88 (right)). In this regard, the test specimens produced with combination of MWCNT and GNP recorded 48.0 ± 0.4 MPa of compressive strength.

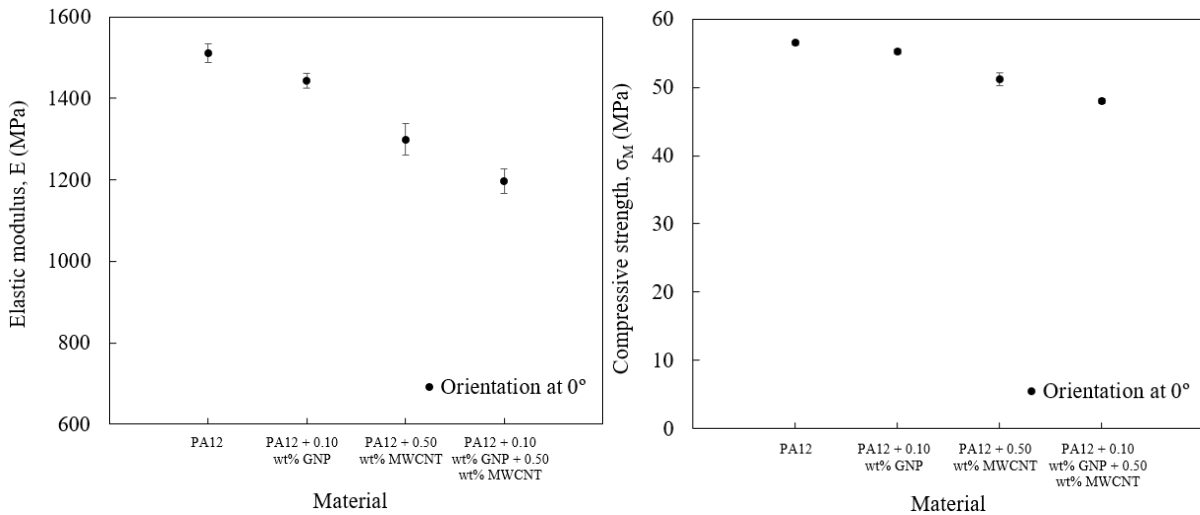


Figure 4.88 Compressive elastic modulus (left) and compressive strength (right) of test specimens produced by SLS with combination of MWCNT and GNP.

Izod impact properties

Figure 4.89 shows the Izod impact resistance of test specimens produced with PA12 incorporating 0.10 wt% of GNP, 0.50 wt% of MWCNT and 0.50 wt% of MWCNT with 0.10 wt% of GNP. The test specimens produced with PA12-MWCNT-GNP composite material revealed an intermediate value, recording a reduction of 27% of the base polymeric matrix.

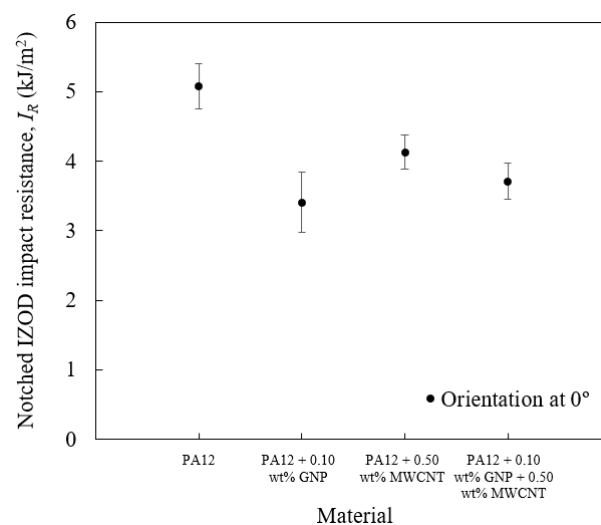


Figure 4.89 Notched Izod impact resistance of test specimens produced by SLS with combination of MWCNT and GNP.

Table 4.10 summarizes the mechanical properties of the developed PA12-MWCNT-GNP composites.

Table 4.10 Summary of mechanical properties of PA12-MWCNT-GNP composites.

	PA12	PA12 + 0.10 wt% GNP	PA12 + 0.50 wt% MWCNT	PA12 + 0.10 wt% GNP + 0.50 wt% MWCNT
TENSILE PROPERTIES				
E (MPa)	1723.60 ± 48.20	1411.64 ± 109.57	1467.85 ± 32.26	1194.91 ± 19.44
σ_{Ced} (MPa)	27.29 ± 0.80	27.12 ± 1.24	23.13 ± 1.50	18.29 ± 0.72
ϵ_{Ced} (%)	1.85 ± 0.11	2.06 ± 0.15	1.80 ± 0.11	1.80 ± 0.07
σ_{Rut} (MPa)	43.60 ± 0.40	37.77 ± 1.45	35.95 ± 1.86	28.32 ± 1.07
ϵ_{Rut} (%)	9.64 ± 0.79	5.41 ± 0.44	6.70 ± 0.91	5.05 ± 0.46
σ_{Max} (MPa)	45.04 ± 0.62	38.01 ± 1.38	36.49 ± 1.82	28.50 ± 1.06
COMPRESSIVE PROPERTIES				
E (MPa)	1511.11 ± 22.12	1443.07 ± 18.78	1299.32 ± 39.53	1196.57 ± 29.88
σ_{Max} (MPa)	56.51 ± 0.26	55.24 ± 0.31	51.15 ± 0.96	47.96 ± 0.37
IMPACT PROPERTIES				
K (kJ/m ²)	5.08 ± 0.32	3.41 ± 0.43	4.13 ± 0.24	3.71 ± 0.26

4.4.3.6. Electrical properties

Table 4.11 shows the electrical resistance, resistivity and conductivity of PA12-MWCNT-GNP composite material in comparison to the neat solution and corresponding individual formulations. To more clearly illustrate the electrical behaviour and resulting ESD category, the results obtained from surface measurements are shown in Figure 4.90 through logarithmic scale.

Table 4.11 Electrical properties of PA12-MWCNT-GNP composites obtained through surface and volume measurements.

	MATERIALS	Electrical resistance (Ω)	Electrical resistivity ($\Omega.cm$)	Electrical conductivity (S/cm)
SURFACE (FLAT PLATES)	PA12	$4.29 \times 10^{10} \pm 3.83 \times 10^9$	$2.29 \times 10^{12} \pm 2.03 \times 10^{11}$	$4.39 \times 10^{-13} \pm 3.75 \times 10^{-14}$
	PA12 + 0.10 wt% GNP	$7.90 \times 10^{10} \pm 1.42 \times 10^9$	$4.22 \times 10^{12} \pm 7.64 \times 10^{10}$	$2.37 \times 10^{-13} \pm 4.04 \times 10^{-15}$
	PA12 + 0.50 wt% MWCNT	$1.52 \times 10^{10} \pm 1.24 \times 10^{10}$	$8.11 \times 10^{11} \pm 6.62 \times 10^{11}$	$2.19 \times 10^{-12} \pm 1.98 \times 10^{-12}$
	PA12 + 0.10 wt% GNP + 0.50 wt% MWCNT	$8.11 \times 10^8 \pm 2.60 \times 10^8$	$4.29 \times 10^{10} \pm 1.35 \times 10^{10}$	$2.51 \times 10^{-11} \pm 9.64 \times 10^{-12}$
VOLUME (FLAT PLATES)	PA12	$3.16 \times 10^9 \pm 2.68 \times 10^8$	$4.82 \times 10^{11} \pm 4.08 \times 10^{10}$	$2.08 \times 10^{-12} \pm 1.83 \times 10^{-13}$
	PA12 + 0.10 wt% GNP	$1.71 \times 10^9 \pm 1.59 \times 10^8$	$2.34 \times 10^{11} \pm 2.26 \times 10^{10}$	$4.30 \times 10^{-12} \pm 4.30 \times 10^{-13}$
	PA12 + 0.50 wt% MWCNT	$4.08 \times 10^9 \pm 1.15 \times 10^9$	$6.24 \times 10^{11} \pm 1.76 \times 10^{11}$	$1.71 \times 10^{-12} \pm 5.56 \times 10^{-13}$
	PA12 + 0.10 wt% GNP + 0.50 wt% MWCNT	n/a	n/a	n/a

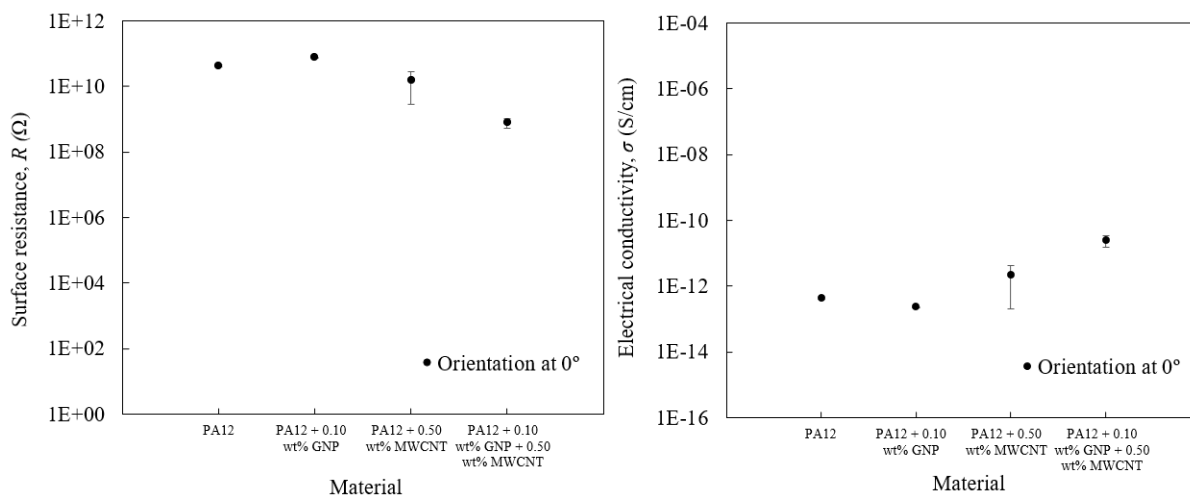


Figure 4.90 Surface resistance (left) and electrical conductivity (right) of flat plates produced by SLS with combination of MWCNT and GNP (logarithmic scale).

The combined incorporation of MWCNT and GNP into the insulative PA12 matrix gradually decreased its electrical resistance and resistivity, enhancing its electrical conductivity. While test specimens produced with 0.50 wt% of MWCNT and 0.10 wt% of GNP reached values of surface resistance of $10^{10} \Omega$, the combination of both reinforcements allowed to decrease that value until $10^8 \Omega$. This material presented electrical resistivity of $10^{10} \Omega \cdot \text{cm}$ and electrical conductivity of 10^{-11} S/cm . According to the standard norm IEC 61340-5-1, the flat plates produced with the combination of materials reached the electrostatic dissipative range (*i.e.*, $10^{11} > \text{surface resistance} \geq 10^9$) (IEC, 1998). This indicates that, under the conditions of this study, the combination of MWCNT with GNP is able to create an effective conductive path between the particles of reinforcement, allowing to significantly enhance the electrical conductivity of the polymeric base material.

4.4.3.7. Thermal properties

Differential Scanning Calorimetry (DSC)

Figure 4.91 shows the melting and crystallization temperatures (*i.e.*, T_m and T_c) of the developed PA12-MWCNT-GNP composite materials revealed by DSC analysis. As previously verified, T_m is not critically sensitive to the inclusion of carbon-based reinforcements in amounts of incorporation ranging between 0.10 wt% to 3.00 wt%. The greatest difference is in T_c which tends to decrease in relation to the polymeric matrix. For the material developed with combination of reinforcements, that difference reached 5.2°C , an intermediate value between 4.2°C obtained in PA12 incorporating 0.10 wt% of GNP and 6.2°C in PA12 incorporating 0.50 wt% of MWCNT. This established the SLS processing window in a range of 24.6°C for PA12 incorporating 0.50 wt% of MWCNT and 0.10 wt% of GNP.

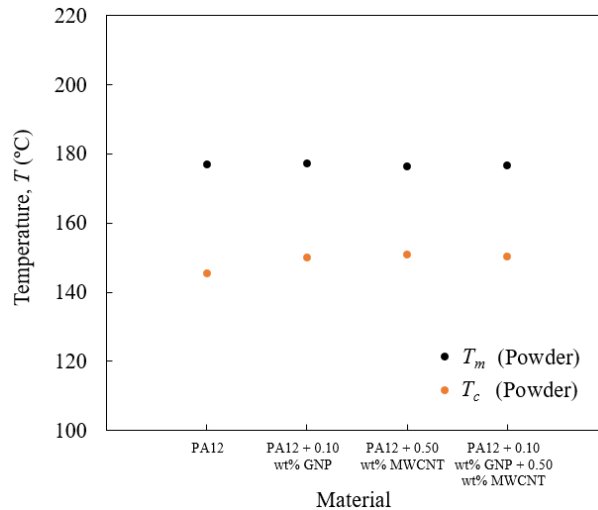


Figure 4.91 Melting and crystallization temperatures of SLS composite powders with combination of MWCNT and GNP.

Within the thermal range of 40 - 160 °C, the specific heat capacity of the PA12-MWCNT-GNP composite material did not reveal substantial differences compared to the neat-PA12 and corresponding individual formulations (Figure 4.92Figure 4.64). Under these conditions, the specific heat capacity increased with temperature from 1.5 J/g.°C to 2.5 J/g.°C in all materials.

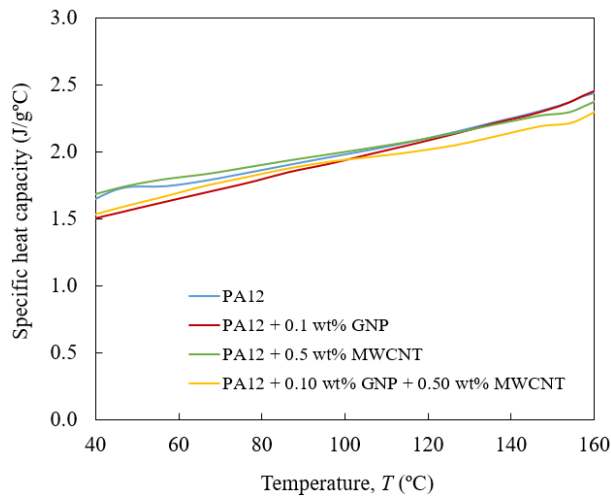


Figure 4.92 Specific heat capacity of test specimens produced by SLS with combination of MWCNT and GNP with temperature.

Thermogravimetric analysis (TGA)

The onset temperature obtained from the TGA thermograms and the combustible material remaining at the end of the test is shown in Figure 4.93 for PA12-MWCNT, PA12-GNP and PA12-MWCNT-GNP composite materials. The initial deflection point reached 400 °C for all materials, proving their great thermal stability without significant mass changes below that temperature. The real content of combustible material at the end of the heating was slightly higher than the theoretical, proving the presence of carbon-based particles throughout the volume of the test specimens.

Chapter 4. Development and characterization of SLS composite materials

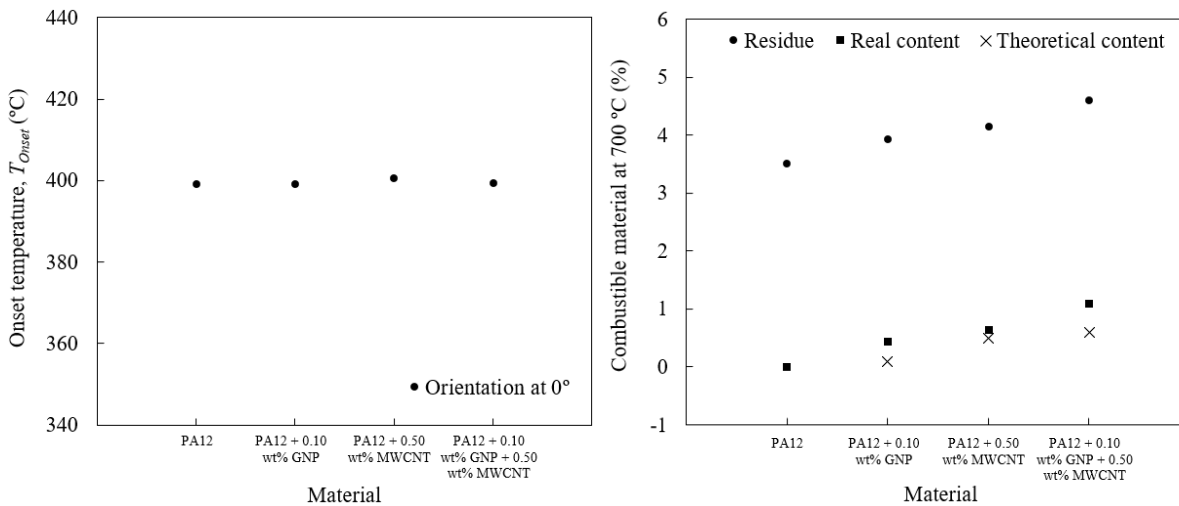


Figure 4.93 Onset temperature (left) and percentage of combustible material at 700 °C (right) of test specimens produced by SLS with combination of MWCNT and GNP.

4.4.3.8. Morphological properties

The cross-section of test specimens produced by SLS with neat-PA12 and PA12 incorporating 0.50 wt% of MWCNT and 0.10 wt% of GNP is shown in Figure 4.94. The SEM micrographs revealed that the microstructure of the cross-section of test specimens produced with the combination of reinforcements presents higher content porosity and reduced microstructural homogeneity than the cross-section of test specimens produced with neat polymeric matrix. At low magnification, it was possible to observe agglomerates of MWCNT that were not well dispersed through mechanical mixing. This suggests that the decrease in mechanical properties reported in *section 4.4.3.4* may be consequence of the weak interparticle adhesion between the matrix and reinforcements, with pronounced influence of the MWCNT agglomerates.

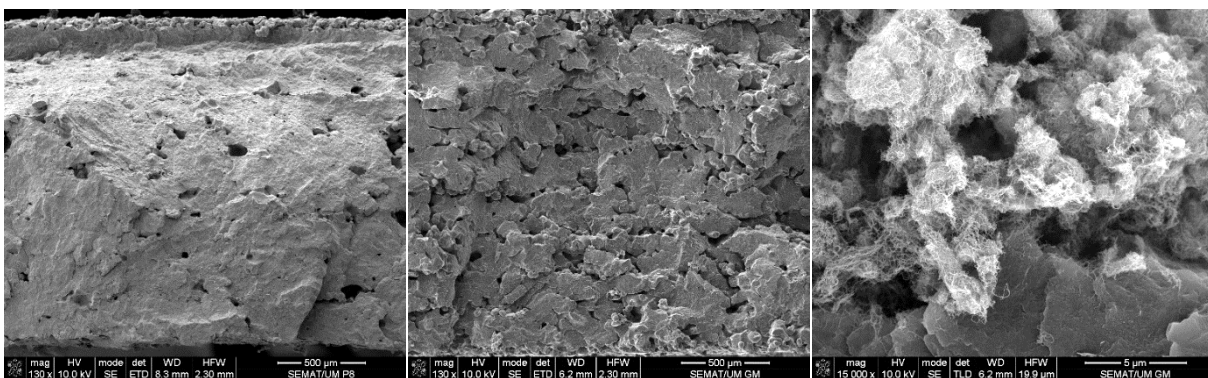


Figure 4.94 Cross-section of test specimens produced by SLS with PA12 (left), PA12 + 0.10 wt% GNP + 0.50 wt% MWCNT at high magnification (middle) and PA12 + 0.10 wt% GNP + 0.50 wt% MWCNT at low magnification (right).

In general, the analysis presented in this section demonstrated that the combination of MWCNT with GNP greatly influenced the dimensional and geometric accuracy and the mechanical properties of the test specimens produced, compared to the reference conditions. The dimensional and geometric

properties maintained or even decreased in relation to the individual formulations, including flatness and parallelism. In addition, the mechanical properties decreased in relation to the individual formulations, above 10% in elastic modulus and 20% in tensile strength. However, such tensile properties were typically higher than those verified in test specimens produced with 1.75 wt% of MWCNT and 1.75 wt% of GNP, which revealed great electrical potential. The electrical surface resistance and electrical conductivity respectively decreased until $10^8 \Omega$ and 10^{-11} S/cm in test specimens produced with a combination of MWCNT and GNP.

4.4.4. Cost analysis

In AM, materials are a significant cost factor. Thus, the industrial implementation of new materials demands the assessment of their economic viability as it directly influences the total cost per part. This becomes particularly relevant in SLS since it is a high material consumption technology that requires extra amounts of material to act as natural support during the process, in addition to the amounts needed to produce the parts themselves. According to these assumptions, this section aims to estimate the costs of the carbon-based composites integrating MWCNT and GNP developed in this research. The analysis accounted for the costs of raw matrix and reinforcements, mixing machine hour-rate (*e.g.*, amortization, energy consumption, maintenance) and human resources for the total number of productions listed in Table 4.1. Table 4.12 presents the final costs of each material per production and kg. The costs of commercial PA2200 (*i.e.*, conventional PA12 used as polymeric matrix) and HP11-30 (*i.e.*, high-performance PA11 with electrostatic-dissipative properties) supplied by EOS GmbH were considered for comparison.

Table 4.12 Summary of costs of the development of carbon-based composites.

MATERIALS	COSTS	
	Per production (€)	Per kg (€)
HP11-30	562.50	125.00
PA2200 - PA12 (50:50%)	228.75	50.83
PA12 + 0.50 wt% MWCNT	316.93	70.43
PA12 + 1.75 wt% MWCNT	319.69	71.04
PA12 + 3.00 wt% MWCNT	322.46	71.66
PA12 + 0.10 wt% GNP	316.94	70.43
PA12 + 0.50 wt% GNP	321.43	71.43
PA12 + 1.75 wt% GNP	335.44	74.54
PA12 + 3.00 wt% GNP	349.46	77.66
PA12 + 0.10 wt% GNP + 0.50 wt% MWCNT	318.05	70.68

Chapter 4. Development and characterization of SLS composite materials

Table 4.12 revealed that the carbon-based composite materials developed in this research presented an average cost of over 70€/kg, increasing the cost of the PA12 matrix by about 40%. Within this average value, GNP-based composites presented a total cost slightly higher than MWCNT-based composites for same weight percentages of incorporation, since the GNP used in this work was three times more expensive than the selected MWCNT. In turn, the developed composite materials presented 42% lower cost than HP11-30 (on average). Compared with this commercial solution, PA12 with 1.75 wt% of GNP with potential for ESD protection allows a cost savings of more than 200€ in a production with a building volume of 360 x 360 x 45 mm³. Despite the differences in mechanical properties, this analysis demonstrated the feasibility of selecting the developed composite material when electrical surface resistance in the ESD range is required, compared to similar options available in the market of SLS materials. In productions with higher building height, this difference allows significant economic savings in the total cost per part, enhancing the competitiveness of SLS in relation to conventional manufacturing technologies.

³ Building volume needed to produce the test specimens for the characterization tests described in *section 4.3*.

Final Remarks of Chapter 4

Chapter 4 presents the methodological approach used in this research to develop composite materials for SLS incorporating carbon-based reinforcements, answering the RQ2 (see *Chapter 1*). The experiments evaluated in this chapter revealed that the simplest method of mechanical mixing allows the preparation of composite materials for SLS with economic and sustainable benefits. Regardless of the preparation method, it was found that the inclusion of MWCNT and GNP in conventional SLS materials mostly requires lower values of energy density, specific fluidisation flow rates and some machine setup adjustments (*e.g.*, coupling of powder vibrating devices) for successful processability. Besides the base nature of the reinforcement, the analysis proved that the weight percentage of incorporation is the most influential factor on the dimensional, geometric, mechanical, electrical and morphological properties of the composites. The thermal properties did not exhibit significant variation for the weight percentages of 0.50 wt%, 1.75 wt% and 3.00 wt%. In turn, compared to the polymeric matrix, the overall mechanical properties and dimensional and geometric accuracy decreased with the increasing amount of these carbon-based reinforcements, as well as the electrical surface resistance until the electrostatic conductive range. In this regard, materials with $10^4 \Omega$ of electrical surface resistance and 10^6 S/cm of electrical conductivity were developed. Among both reinforcements, MWCNT stood out for its ease of processing, greater tensile strain, higher impact resistance but pronounced surface roughness. In comparison, GNP presented advantages in the production of parts with reduced surface roughness, higher elastic modulus and in-range ESD values, despite its more difficult processing and mechanical brittleness. Besides the different typology of the reinforcements, such results may be a consequence of the complexity in obtaining a strong and homogeneous interparticle adhesion without agglomerates and porosity. In fact, these were the main challenges in the development of functional materials noticeable during the experiments. Nevertheless, through the implemented framework, useful insights to develop tailored materials for SLS capable of meeting technical requirements of advanced fields of application were provided in this chapter.

Chapter 5. Case-study: Experimental and numerical analysis

Chapter 5 focuses on an action-research methodology that was implemented to expand, optimize and ensure the representativeness of the results of this research through an up-close characterization of a case-study in real context of application. Numerical analyses based on experimental data were used to comprehend and characterize the structural mechanical performance of the elected product depending on the input process variables. The composite materials developed in *Chapter 4* were then considered to manufacture the product with electrostatic dissipative properties required for application in the automotive electronics industry. In the end, the validation of the proposed solution in an industrial manufacturing process flow is demonstrated.

5.1. Introduction

With the technological progress, the industrial implementation of automated robots programmed to perform handling tasks through grippers and end-effectors, such as packaging and palletizing operations, has expanded in several sectors (*e.g.*, automotive, biomedical) with promising benefits of efficiency and productivity (Schroeffler *et al.*, 2019; Dilibal *et al.*, 2021). Compared with conventional technologies that do not allow the development of highly complex geometries, AM enables the production of personalized and task-specific robot end-effectors with fewer geometric constraints, using both soft or rigid materials, through more flexible processing methods (Sugavaneswaran *et al.*, 2018; Dilibal *et al.*, 2021; Goh *et al.*, 2022). Based on this field of application, the focus of this chapter is to develop and produce a robot end-effector by SLS for implementation in the automotive electronics industry, *viz.*, in the Bosch Car Multimedia S.A. The main goal of such activities is to make use of a case-study to exploit experimental and numerical capabilities in the development of a product suitable for practical applications where ESD interferences are a critical point. To do so, an action-research methodology was implemented to create knowledge in practical contexts through cycles of planning, action, observation and reflection. In last instance, this methodological approach aims to provide useful insights in guiding process parameters optimization and materials selection for SLS parts, depending on the technical requirements demanded by industrials. The following sections present the main sequential activities of this work, namely i) description of the case-study and its technical requirements, ii) production and characterization of prototypes by SLS with conventional and functional materials, iii) numerical analysis for process parameters optimization and materials selection and iv) validation of the developed product for application in industrial environment.

5.2. Case-study

The case-study evaluated in this chapter is a robot end-effector needed to be implemented in a pick-and-place system planned to execute palletizing operations. The automated robotic system makes use of a UR10e collaborative robot arm for the positioning of Printed Circuit Boards (PCB) in thermoformed trays using vacuum suction cups. These boards allocate electronic elements and connections, making them electrostatic discharge-sensitive devices (ESDS) susceptible to mechanical efforts during transportation, storage and operation (Silva *et al.*, 2020). Therefore, the robot end-effector to be developed must comply with a series of technical requirements with regard to physical, thermal, electrical and mechanical properties to guarantee its functionality under real conditions of implementation (Table 5.1).

Table 5.1 Technical requirements and specifications of the case-study.

CATEGORY	TECHNICAL REQUIREMENTS & SPECIFICATIONS
Material	Polymer-based material
Manufacturing technology	Powder bed fusion
Physical	Airtight internal channels, low density
Thermal	Service temperature: 23 °C (Room temperature)
Electrical	Surface resistance: $10^4 - 10^9 \Omega$ (N51M M24) ⁹
Mechanical	10 N (PCB and components weight)
Economics	Minimum possible costs

In terms of materials and processing technologies, main targets of development include the implementation of a polymeric solution integrating conductive reinforcements processed by powder bed fusion in the production of a lightweight, cost-efficient and customer-specific product capable to ensure safe transportation of the PCB, without significantly increasing the costs. The primary purpose of using AM technologies is to be able to obtain complex geometries without resorting to multiple conventional machine tools. Other significant requirements are the integration of airtight internal channels to ensure vacuum generation and transmission, ESD protection due to the contact with electronic components and mechanical resistance for a 10 N load that accounts for the weight of the PCB and other components. Regions of screwing must also be taken into consideration due to the successive operations of assembly-disassembly. The system also has to comply with two main dimensional and geometric constraints, namely with regard to i) regions of screwing with the collaborative robotic arm, vacuum tube connector and vacuum suction cups and ii) points of contact with the PCB that are dependent on the height and position of their connectors.

Figure 5.1 shows the PCB, with maximum dimensions of 173 x 139 x 27 mm, and four points where contact with the robot end-effector is possible. As can be seen, conditioned by the available connectors-free area, there is expected the use of three vacuum suction cups with a circular cross-section and one vacuum suction cup with an oval cross-section. The dimensional and geometric characteristics of the vacuum suction cups, namely the differences in height between each typology, is a fundamental issue to take into consideration during the conceptual design of the robot end-effector (Figure 5.2).

⁹ N51M M24 – Bosch delivery instructions for ESD

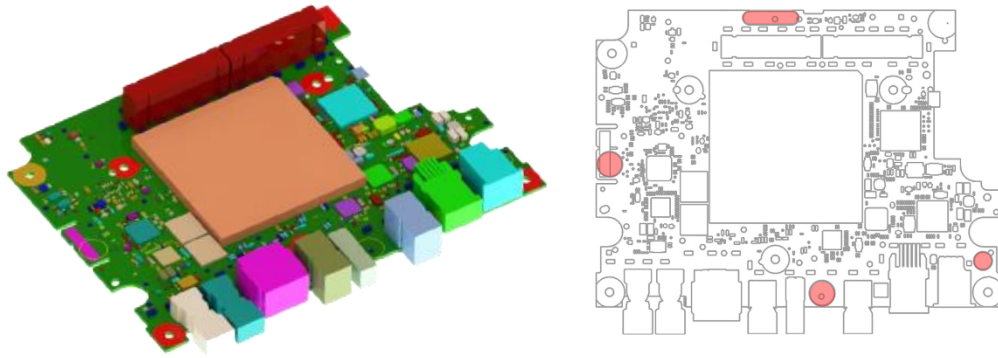


Figure 5.1 Representation of the PCB detailing four possible points of contact with the robot end-effector (red marks).

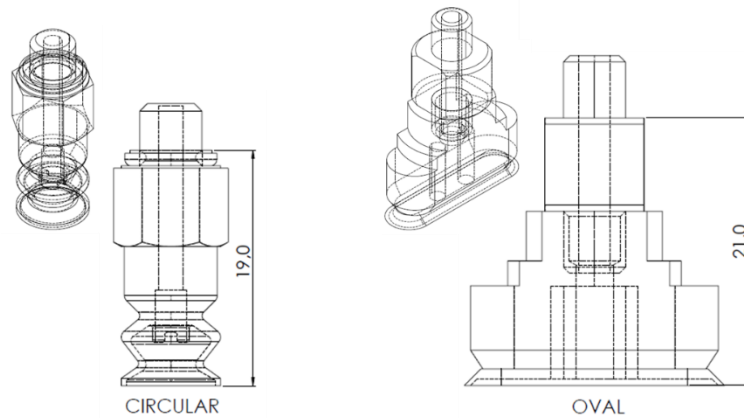


Figure 5.2 Types of vacuum suction cups used in the system (dimensions in mm).

Based on the imposed technical specifications, a number of different geometric models of the robot end-effector were designed employing basic design criteria for AM. Figure 5.3 shows the elected version which presents an organic shape composed of a main structure that directly connects to the collaborative robotic arm through four screws. An additional hole was included to accommodate a metallic dowl pin for an accurate alignment with the UR10e collaborative robot arm. From that main structure, four arms branch off to couple the vacuum suction cups in the positions defined in Figure 5.1. In addition, the part includes a lateral hole needed to connect the vacuum tube.



Figure 5.3 Proposed robot end-effector.

The proposed robot end-effector integrates a continuous internal conformal vacuum channel, running along the entire perimeter of the central region and branching to each arm where the vacuum suction cups must be coupled (Figure 5.4). The internal channel was designed with 6.0 mm of nominal diameter allowing the connection with the vacuum suction cups that were selected for the system and an easy powder removal after the sintering process. This configuration was designed in a way to allow uniform vacuum transmission without sudden changes in the flow direction from the region of connection of the vacuum tube until each vacuum suction cup.

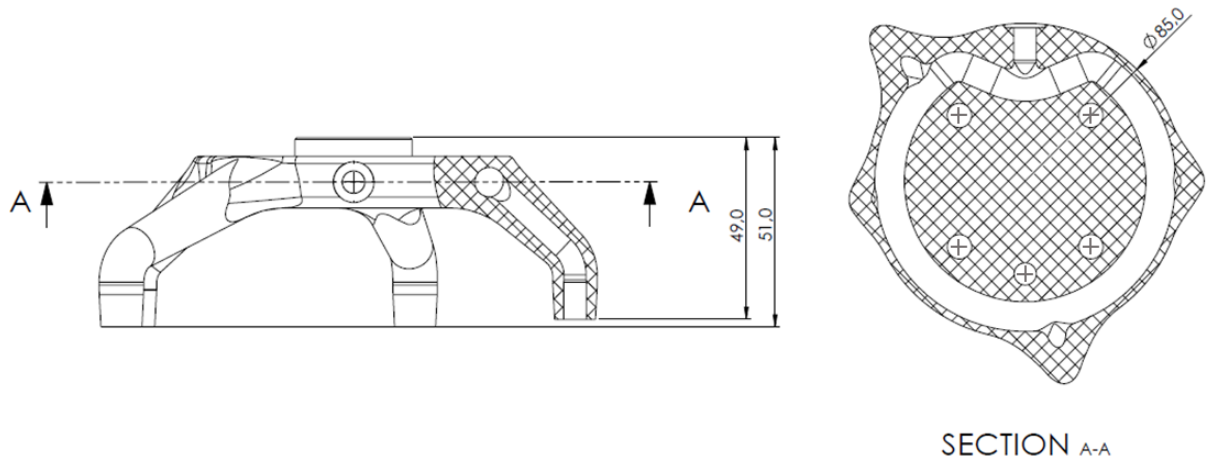


Figure 5.4 Details of the internal conformal vacuum channel of the robot end-effector (dimensions in mm).

This version was considered for analysis in the following activities of the work as in the course of the development stages there was verified that it accomplishes all dimensional and geometric requirements imposed for the robotic system. Figure 5.5 presents a 3D CAD rendering of the final version of the robot end-effector in mounted condition. The corresponding 2D CAD drawing can be found in *Appendix C*.

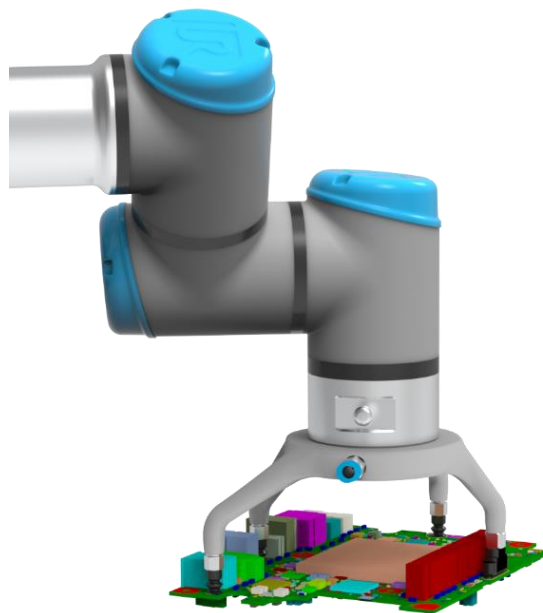


Figure 5.5 3D representation of the robot end-effector in mounted condition.

5.3. Production of prototypes

After conceptualization and 3D modelling, prototypes of the proposed robot end-effector were produced in an EOS P 396 laser-sintering machine with PA12 incorporating 1.75 wt% of GNP, considering the parameterization set previously optimized for this carbon-based composite (Figure 5.6) (see *section 4.4.2*). This material was used to comply with the technical instructions of Bosch Car Multimedia S.A. for ESD products, as in previous activities there was demonstrated that it presents an electrical surface resistance of $10^5 \Omega$, and also because it ensures better surface finishing than MWCNT-based solutions.



Figure 5.6 Prototype produced by SLS with PA12-GNP.

Prototypes of PA12 material were also produced for reference (Figure 5.7).



Figure 5.7 Prototype produced by SLS with PA12.

The prototypes were produced in the YXZ orientation, due to the greater ability of SLS in producing round holes in surfaces directed to the top (see Figure 3.35, *section 3.4.1.3*). In fact, producing conform holes was considered an essential condition to guarantee an accurate screwing of the robot end-effector with the robotic system, and, consequently, a pick-and-place with minimum deviations in positioning. Furthermore, this orientation ensures the lowest height along the z-axis, which is beneficial in terms of material consumption with effects in costs and sustainability. Figure 5.8 shows the manufacturing of a PA12-GNP prototype, evidencing the sintering of holes and the internal conformal vacuum channel.



Figure 5.8 Production of a PA12-GNP prototype by SLS.

In post-production operations, metallic inserts were welded to the final prototypes to further screw the vacuum tube connector and vacuum suction cups in an attempt to increase the stability and durability of the robot end-effector in successive operations of assembly-disassembly when implemented in industrial environment (Figure 5.9). In order to replicate real conditions of use, the characterization tests were performed with prototypes incorporating metallic inserts.



Figure 5.9 Prototype produced with PA12-GNP evidencing metallic inserts.

5.4. Characterization of prototypes

After production, cooling and cleaning, some characterization tests were performed. First, the mass of the prototypes produced with both materials was determined with a KERN Precision balance. The main purpose was to understand the advantages of the inclusion of the carbon-based reinforcement in reducing the mass of the product. Then, the electrical surface resistance of upward and downward-facing surfaces was measured point-to-point with a METRISO 3000 operating with a Miniprobe Set 840. The objective was to ensure that the ESD range imposed by the company was achieved. Finally, the mechanical properties were evaluated through tensile and compression tests performed in three prototypes of each material, in order to understand its overall performance. In one test of each, four biaxial strain gauges were coupled to the top surface of each arm of the prototypes for local strain monitoring. To install the

Chapter 5. Case-study: Experimental and numerical analysis

strain gauges in each prototype, the following procedure was performed (Figure 5.10): i) clean and prepare the surfaces where the gauges were applied with abrasive paper and appropriate solvent in repetitive actions until obtaining a flat, uniform and contamination-free area; ii) hold and align the strain gauges in its specific position using specific transparent tape; iii) slightly and manually compress the bonding area to remove air bubbles and heat the bonding; iv) carefully remove the transparent tape; and v) weld the measurement cables to the strain gauges. After these steps, the prototypes were ready for mechanical characterization.



Figure 5.10 Installation of the strain gauges in a PA12 prototype.

The mechanical tests were carried out in a Shimadzu Universal Testing System at 0.5 mm/min at room temperature with a load-cell of 50 kN, resorting to aluminium parts needed to support and fix the prototypes during the experiments (Figure 5.11). To do so, there were machined four parts, namely:

- Part A - needed to lock the prototype to the machine-cross head using a metallic dowel pin;
- Part B - used to simulate the robotic arm and, therefore, define the area for load application;
- Part C - needed to fix the prototype during the experiments through screwing;
- Part D - needed to lock the components to the base of the machine using a metallic dowel pin;

The experimental setup was properly adjusted to each mechanical test. In tensile tests the prototypes were loaded through the part A. In turn, in compression tests the compression plate directly contacted the part B to load the prototypes.

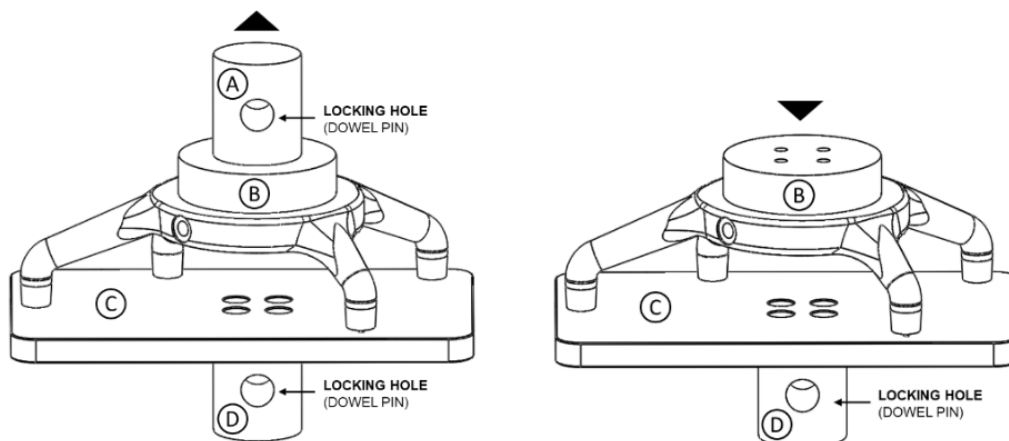


Figure 5.11 Experimental setup used to perform tensile (left) and compression (right) tests.

Figure 5.12 and Figure 5.13 respectively show the experimental setup of the tensile and compression tests performed on prototypes produced with PA12 and PA12-GNP materials.

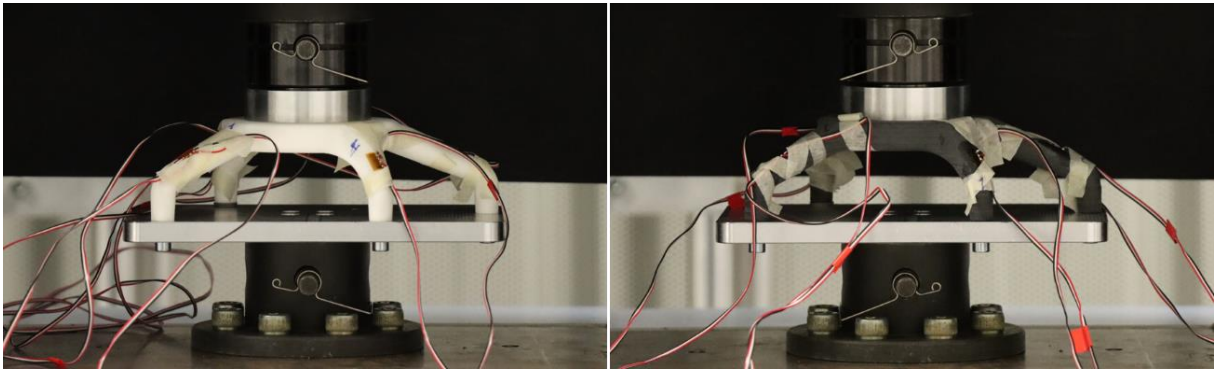


Figure 5.12 Experimental setup of the tensile test on PA12 (left) and PA12-GNP (right) prototypes.

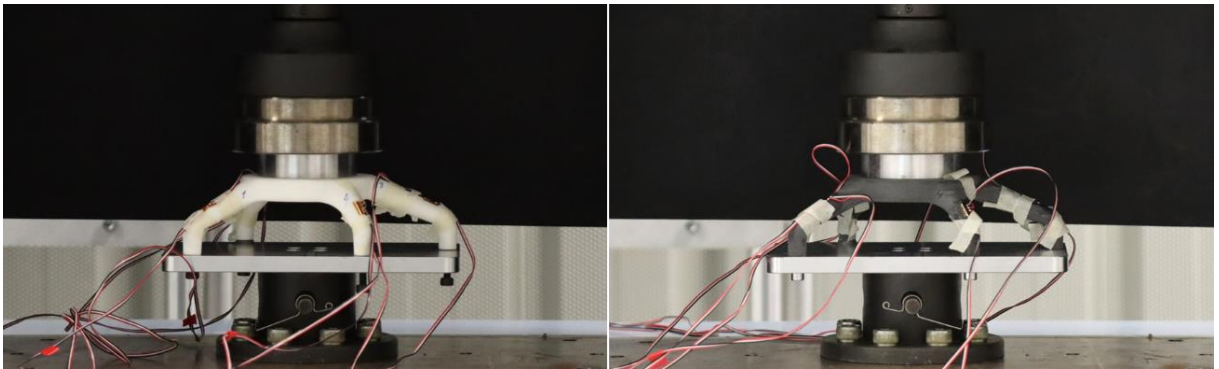


Figure 5.13 Experimental setup of the compression test on PA12 (left) and PA12-GNP (right) prototypes.

5.4.1. Results and discussion

The results obtained from the characterization tests are presented in Table 5.2.

Table 5.2 Physical, electrical and mechanical characterization of the robot end-effector.

		CASE-STUDY		
		PA12	PA12 + 1.75 wt% GNP	
MASS (kg)		0.09	0.08	
ELECTRICAL SURFACE RESISTANCE (Ω)	Upward-facing surface	$> 10^{10}$	$9.88 \times 10^5 \pm 1.22 \times 10^4$	
	Downward-facing surface		$5.89 \times 10^5 \pm 2.12 \times 10^4$	
Range		Insulative	ESD	
MECHANICAL PROPERTIES	TENSILE	Maximum load (N)	3487.40 ± 160.37	506.22 ± 90.67
		Maximum displacement (mm)	2.46 ± 0.32	0.35 ± 0.06
	COMPRESSION	Maximum load (N)	6295.94 ± 554.21	2252.63 ± 1100.99
		Maximum displacement (mm)	5.93 ± 0.11	1.88 ± 0.95

Chapter 5. Case-study: Experimental and numerical analysis

The results demonstrated that prototypes produced with composite material presented a mass slightly lower than prototypes produced with neat PA12, which is in agreement with the data shown in *section 4.4.2.2*. Despite that and regardless of the material, the proposed robot end-effector presented a mass below 0.1 kg, displaying valuable lightweight characteristics.

In terms of electrical characterization, there was verified that the prototypes produced with PA12 incorporating 1.75 wt% of GNP exhibited values of surface resistance between $10^5 - 10^6 \Omega$ depending on the surface, accomplishing the Bosch internal norm N51M M24 that specifies values of surface resistance between $10^4 - 10^9 \Omega$ for components in direct contact with ESDS.

With regard to mechanical characterization, it was proven that the robot end-effector is able to comply with the imposed requirements. Only data obtained until a first failure on the prototype, partial or total, were considered for such analysis, as exemplarily illustrated in Figure 5.14.

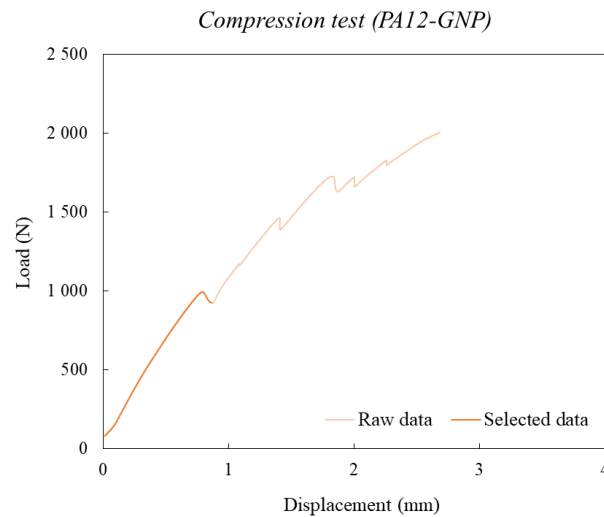


Figure 5.14 Compression load-displacement curve obtained for a prototype produced with PA12-GNP: raw and selected data.

Based on this assumption, experimental load-displacement curves are shown in Figure 5.15.

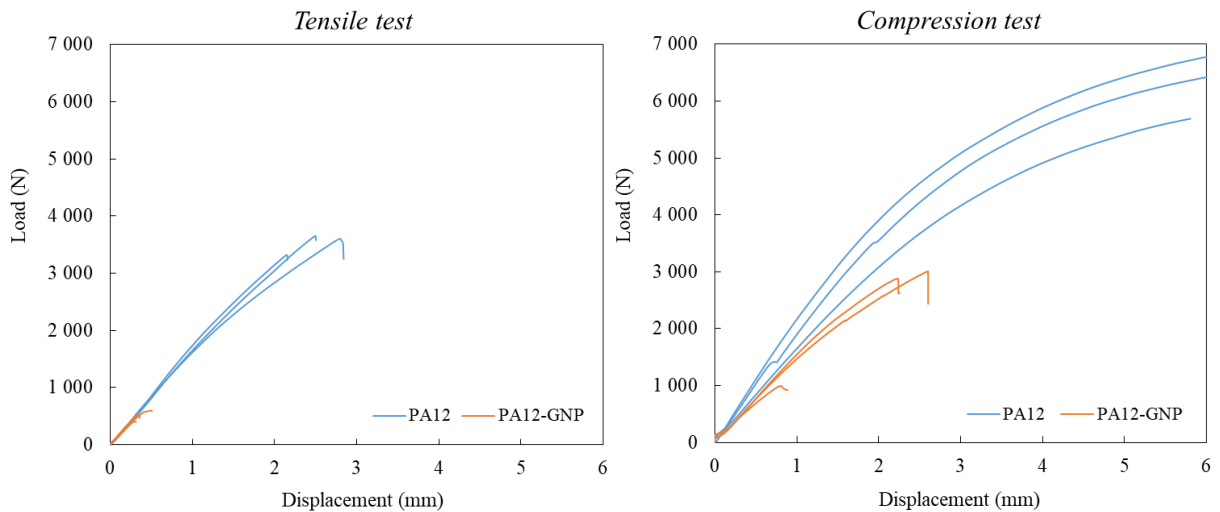


Figure 5.15 Load-displacement curves obtained for prototypes produced with PA12 and PA12-GNP in tensile (left) and compression (right) tests.

In a first observation, the results revealed that the performance of the prototypes produced with PA12 was higher than the prototypes produced with PA12-GNP material. Regardless of the material, the prototypes exhibited greater mechanical properties under compressive than tensile loads. In compression tests, prototypes of PA12-GNP showed a maximum displacement close to 2 mm and a maximum load of 2253 N until failure. Under similar loading conditions, prototypes of PA12 withstood 6 mm of displacement and 6296 N without failure. In tensile tests, prototypes of PA12 presented a half of the displacement recorded in compression tests, demonstrating great mechanical performance until 3487 N and 2.5 mm, on average. The worst mechanical performance was verified with PA12-GNP prototypes in tensile tests with a first failure verified after the maximum load of 506 N at 0.4 mm of displacement. This worst mechanical behaviour was expected as in tensile tests the load acts in the normal direction of the layers. Of all part orientations, this is the most prone condition for failure, particularly when a strong interlayer adhesion is not ensured. This may explain the reduced tensile load recorded by prototypes produced with composite material that mainly failed in the interlayers region close to the curvature of the arms, evidencing lower interparticle strength than prototypes produced with PA12 (Figure 5.16).

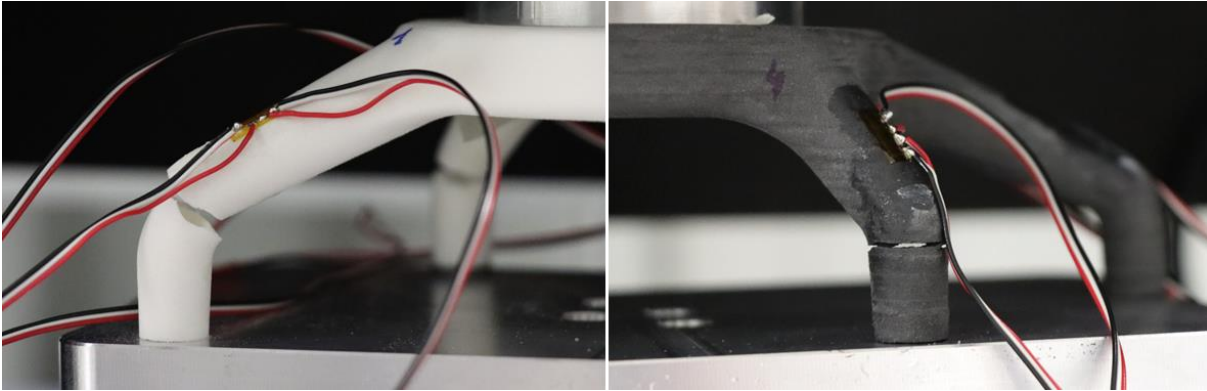


Figure 5.16 Rupture of prototypes produced with PA12 (left) and PA12-GNP (right) prototypes (tensile test).

5.5. Numerical analysis

In this research, computational tools were used for two main purposes, mainly i) to control and predict the mechanical performance of the robot end-effector under real conditions of implementation and ii) to establish a numerical methodology capable to guide the selection of process parameters and materials for SLS parts, making use of the case-study analysed in this chapter. To do so, the experimental results reported in *Chapters 3* and *4*, respectively obtained for different process parameters and materials, were used as input process variables in a commercial engineering simulation software to simulate the tensile and compression tests experimentally performed, under the same boundary conditions. The reliability of the numerical results was verified through the definition of a numerical-experimental agreement, allowing to propose a methodology capable of predicting the mechanical properties of SLS parts for different materials and processing conditions depending on the input variables.

5.5.1. ANSYS simulation

The numerical analysis was performed in the ANSYS software, through the static structural menu. For the analyses, the geometry shown in Figure 5.3 was first loaded into the software. The aluminum part B (see Figure 5.11) and four main bolts (modeled without threads) were also loaded and included in the analysis to easily replicate the experimental setup and boundary conditions. All these components were meshed by applying a body sizing of 1.0 mm defining a total of 801297 tetrahedral elements (Figure 5.17).

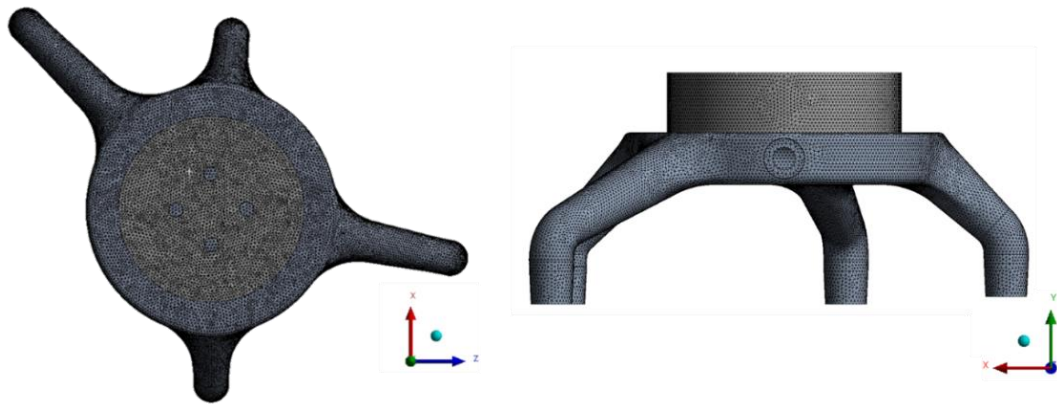


Figure 5.17 Mesh of components used in the numerical analysis.

Experimental true stress-strain curves obtained from the tensile and compression tests were used to define multilinear isotropic hardening models for PA12 and PA12-GNP materials that were further assigned to the respective bodies. In the analysis settings, there was defined a manual stepping with a minimum of 50 steps and activated the option of large deflection. Then, the boundary conditions were imposed in such a way as to replicate the experimental setup. In terms of contacts and connections between bodies, there was considered that in surfaces directly interacting with the bolts no separation in normal and tangential directions is allowed. Between the aluminum part and the robot end-effector it was considered that no sliding is allowed but the components can separate out in the normal direction.

Two steps were defined to simulate the system. As it comprises bolted connections, a bolt pretension was applied in the first step, considering local coordinate systems (Figure 5.18).

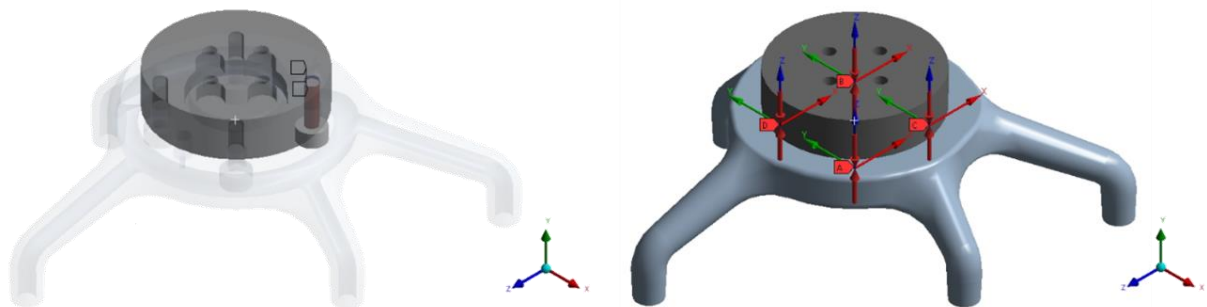


Figure 5.18 Modelling of the pretension in the bolts.

In the second step, the loads in the bolts were locked while a positive or negative displacement in the top surface of the aluminum part was applied to respectively simulate tensile and compression tests. Figure 5.19 shows the surface considered to apply the displacement and the regions of the prototypes that were screwed to the aluminum platform that were defined as fixed support. The resulting load, displacement and von Mises stress were selected as output data.

Chapter 5. Case-study: Experimental and numerical analysis

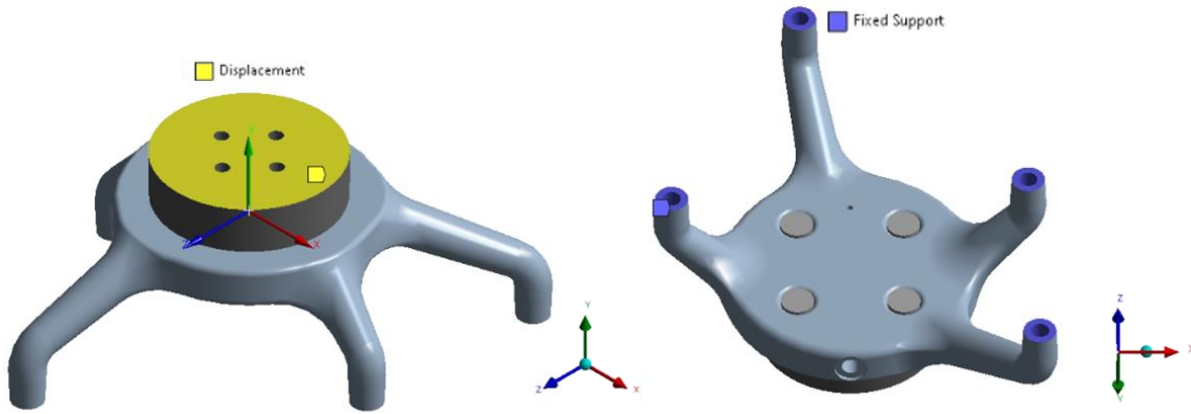


Figure 5.19 Boundary conditions imposed for numerical analysis.

Figure 5.20 summarizes the procedure that was adopted in ANSYS to perform the numerical analyses.

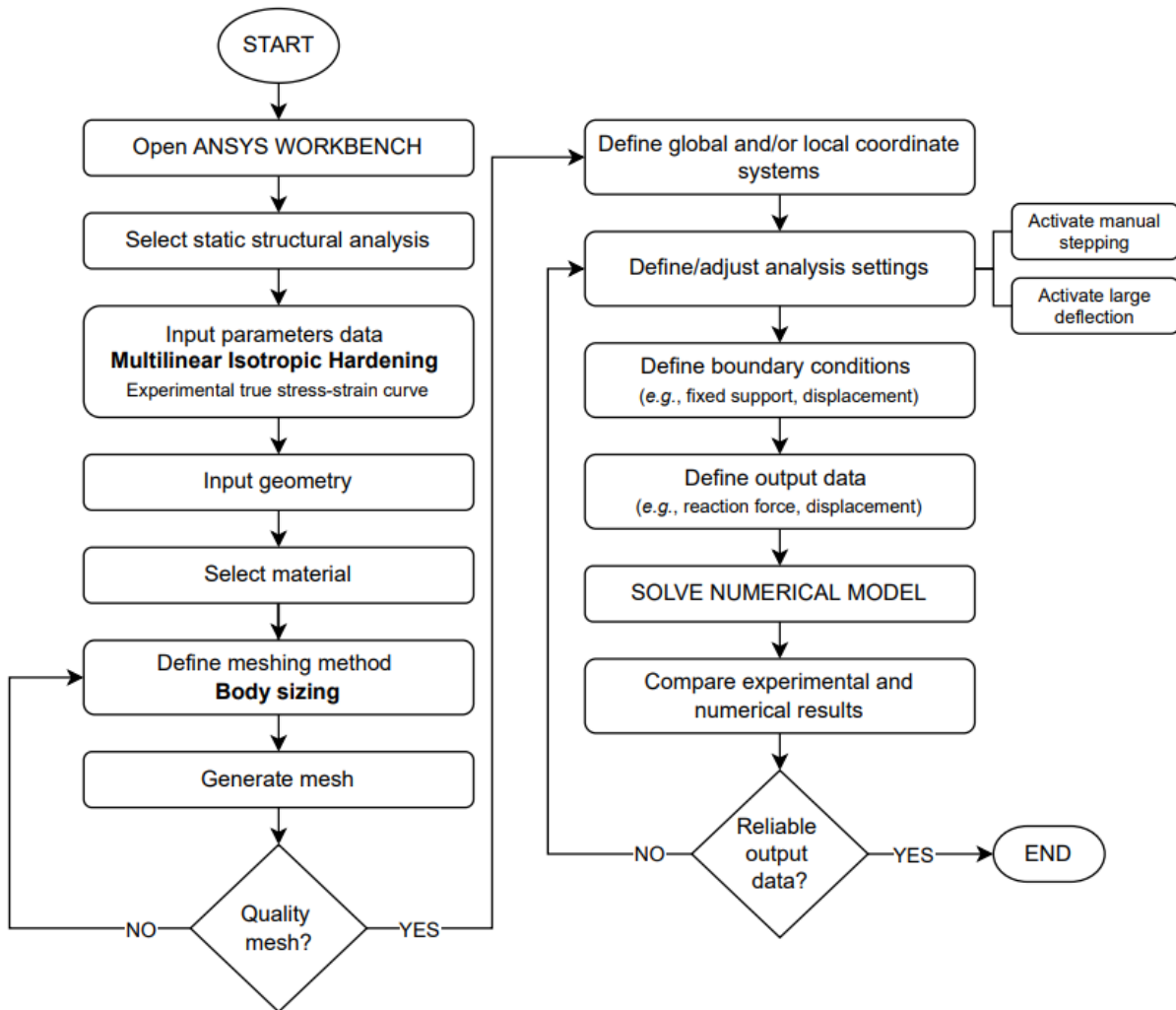


Figure 5.20 Flowchart of the numerical analysis in ANSYS.

5.5.2. Global numerical-experimental agreement

Employing the computational methodology shown in Figure 5.20, numerical load-displacement curves were obtained. Figure 5.21 and Figure 5.22 show the comparison between experimental and numerical results obtained for tensile and compression tests performed under the same boundary conditions.

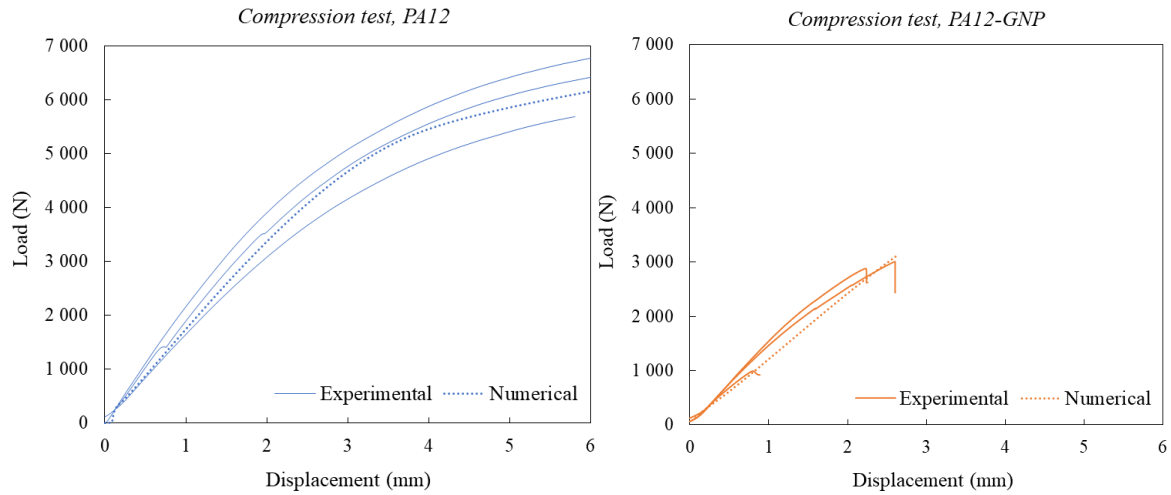


Figure 5.21 Load-displacement curves obtained for prototypes produced with PA12 (left) and PA12-GNP (right) in tensile tests. Dotted-lines refers to numerical data.

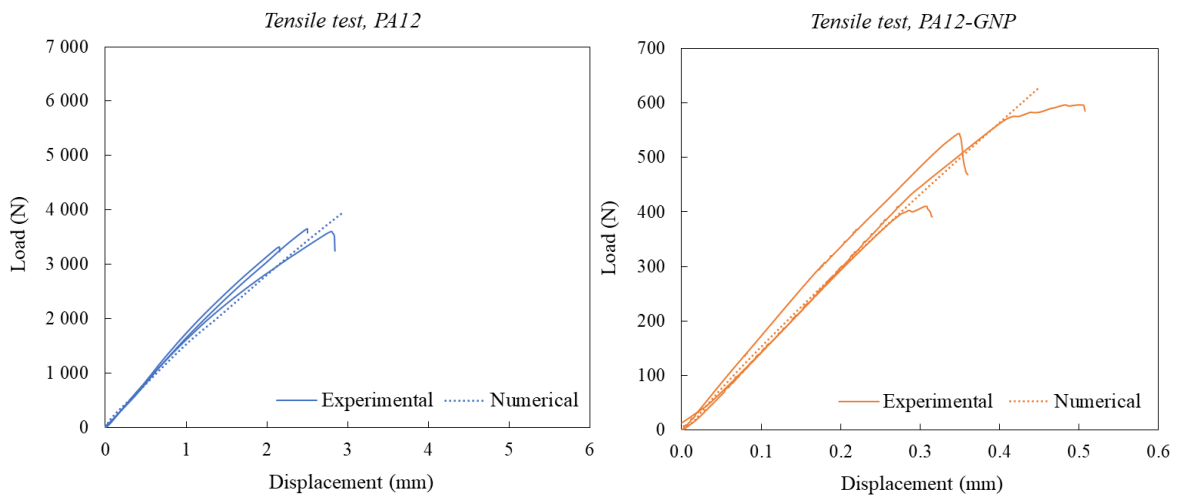


Figure 5.22 Load-displacement curves obtained for prototypes produced with PA12 (left) and PA12-GNP (right) in compression tests. Dotted-lines refers to numerical data.

In a first observation, the results showed that the numerical load-displacement curve obtained for each mechanical test and material is in good agreement with the corresponding experimental data, suggesting that the applied numerical methodology is suitable to characterize the mechanical performance of the robot end-effector. Table 5.3 presents the experimental load-displacement values at which the prototypes exhibited partial or total failure during the tensile and compression tests and the numerical load obtained for those values of displacement.

Table 5.3 Variation between experimental and numerical load for same displacement.

CASE-STUDY	MECHANICAL TEST	Experimental displacement (mm)	Experimental load (N)	Numerical load (N)	Variation (%)
PA12	Tensile	2.46 ± 0.32	3487.40 ± 160.37	3373.60	3.3
	Compression	5.93 ± 0.11	6295.94 ± 554.21	6125.40	2.7
PA12 + 1.75 wt% GNP	Tensile	0.35 ± 0.06	506.22 ± 90.67	497.17	1.8
	Compression	1.88 ± 0.95	2252.63 ± 1100.99	2263.70	0.5

The results showed that the variation between experimental and numerical loads at the end of tensile and compression tests reached a maximum below 4% for PA12 and PA12-GNP materials. This good global numerical-experimental agreement obtained for both mechanical tests and materials demonstrates that when the system is properly defined, the properties of the base material are completely characterized and experimental true stress-strain curves are well-known, it is possible to define multilinear isotropic hardening models in commercial engineering simulation software able to reliably mimic the mechanical performance of the parts under analysis. Such numerical approach can be employed in the simulation of neat or composite materials since the effect of porosity and other heterogeneities commonly observed in laser-sintered parts is to some extent accounted for by introducing the experimental results as input parameters for the numerical analysis. Although most commercial engineering simulation software assumes homogeneous structures, this work showed that the variation between experimental and numerical results tends to be smaller when there is a critical knowledge base on the properties of the materials and a large number of experiments needed to define an average behaviour with minimum deviation between mechanical stress-strain curves. This highlights the relevance of creating a wide experimental database covering the response of the materials to different input process variables with the aim of predicting the performance of parts under different environments and boundary conditions.

5.5.3. Local numerical-experimental agreement

After obtaining a global numerical-experimental agreement, the local strain was numerically evaluated in order to validate the experimental results acquired with the strain gauges in the tensile and compression tests. In order to obtain the local strain values, there was selected a set of elements in the regions where the strain gauges were bonded and defined a local coordinate system to be able to analyse the resulting strain in both longitudinal and transversal directions (Figure 5.23).

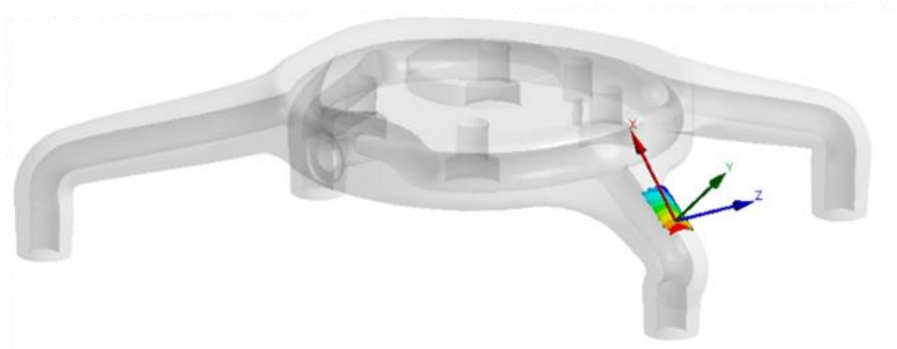


Figure 5.23 Representation of the set of elements selected for numerical local strain monitoring.

For the analysis, it was only considered the longitudinal strain in each arm of the robot end-effector as it presented higher variation with the tensile and compressive loads than the transversal strain. The numbering shown in Figure 5.24, from 1 to 4, was adopted to represent the data obtained in each arm.

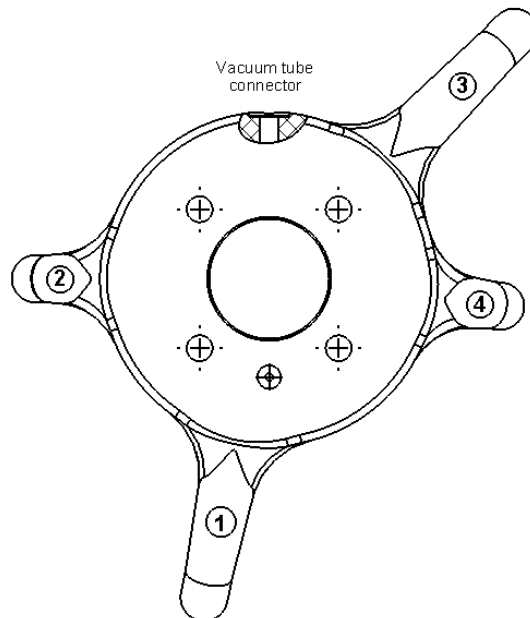


Figure 5.24 Numbering of the arms considered for local strain monitoring.

Figure 5.25 shows the absolute values of local longitudinal strain obtained with prototypes produced with PA12 and PA12-GNP as a function of tensile loads, with numerical data represented by dotted-lines.

Chapter 5. Case-study: Experimental and numerical analysis

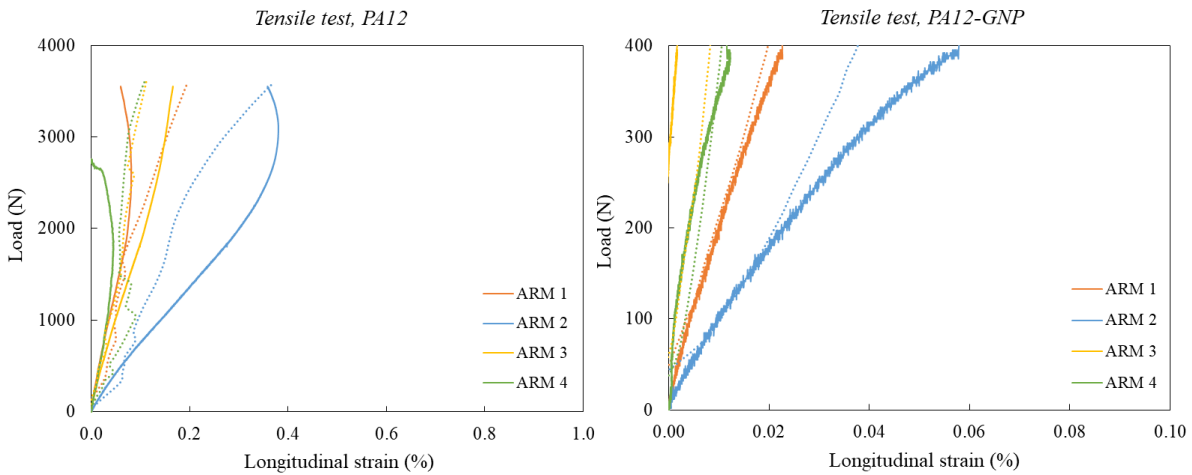


Figure 5.25 Local longitudinal strain of prototypes produced with PA12 (left) and PA12-GNP (right) in function of the tensile load. Dotted-lines refers to numerical data.

In agreement with the global mechanical behaviour, the local analysis demonstrated that under similar conditions of testing, prototypes produced with PA12 withstand higher values of longitudinal strain than prototypes produced with composite material that reveals higher brittleness. Under tensile loads, maximum longitudinal strain values reached 0.4 % in prototypes produced with PA12 and 0.06 % in prototypes produced with PA12-GNP, both recorded in the surfaces of the arm number 2 (see Figure 5.24). In the numerical analysis, the highest values of longitudinal strain were also verified in that arm with same orders of magnitude. This agrees with the highest value of von-Mises stress recorded in such arm of the robot end-effector for both materials (*i.e.*, 50 MPa for PA12 and 15 MPa for PA12-GNP), suggesting that it is the most prone to failure under tensile loads (Figure 5.26 and Figure 5.27).

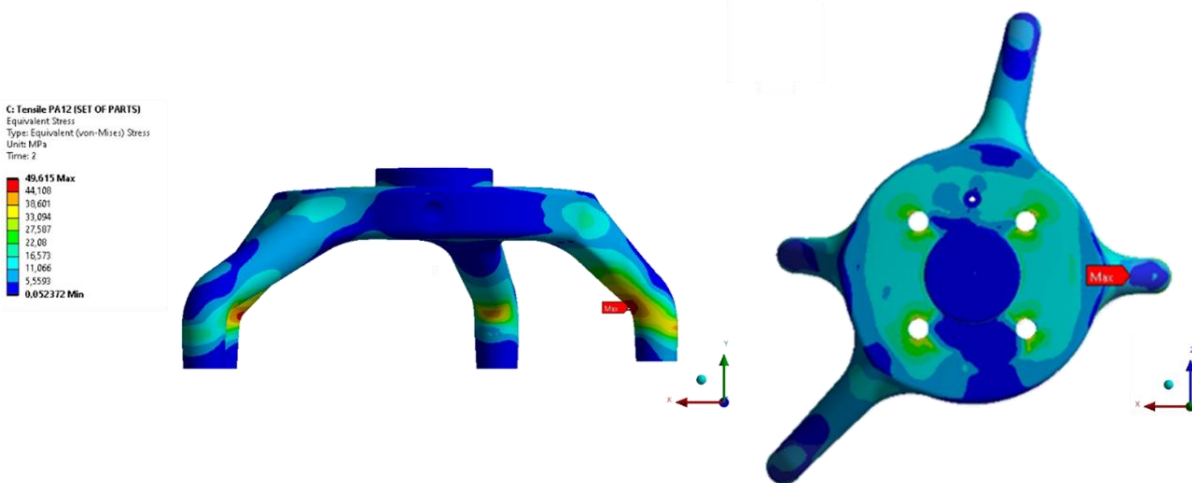


Figure 5.26 von-Mises stress of a prototype produced with PA12 under tensile loads.

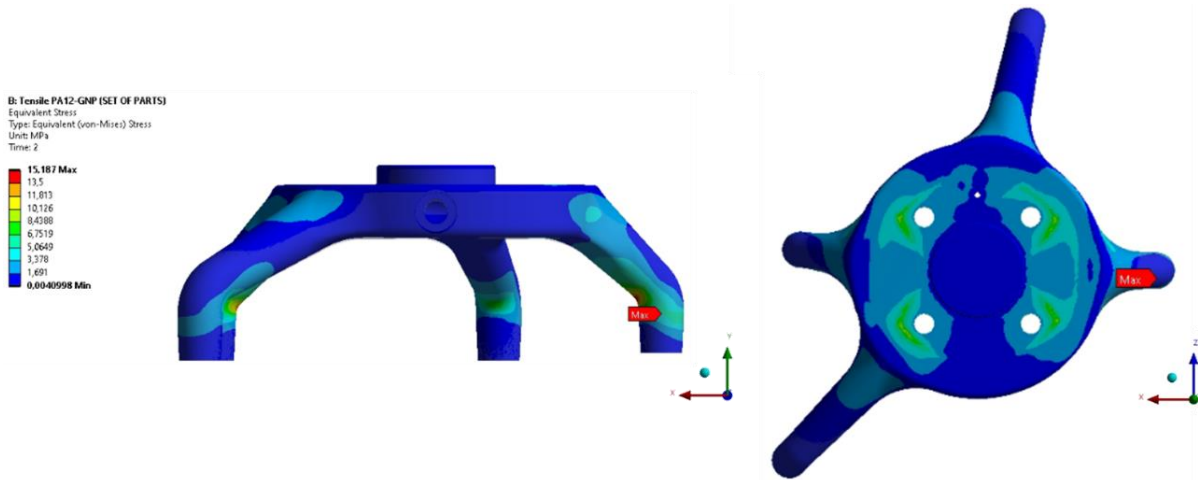


Figure 5.27 von-Mises stress of a prototype produced with PA12-GNP under tensile loads.

Moreover, Figure 5.28 shows the absolute values of local longitudinal strain obtained with prototypes produced with PA12 and PA12-GNP as a function of compressive loads, with numerical data represented by dotted-lines.

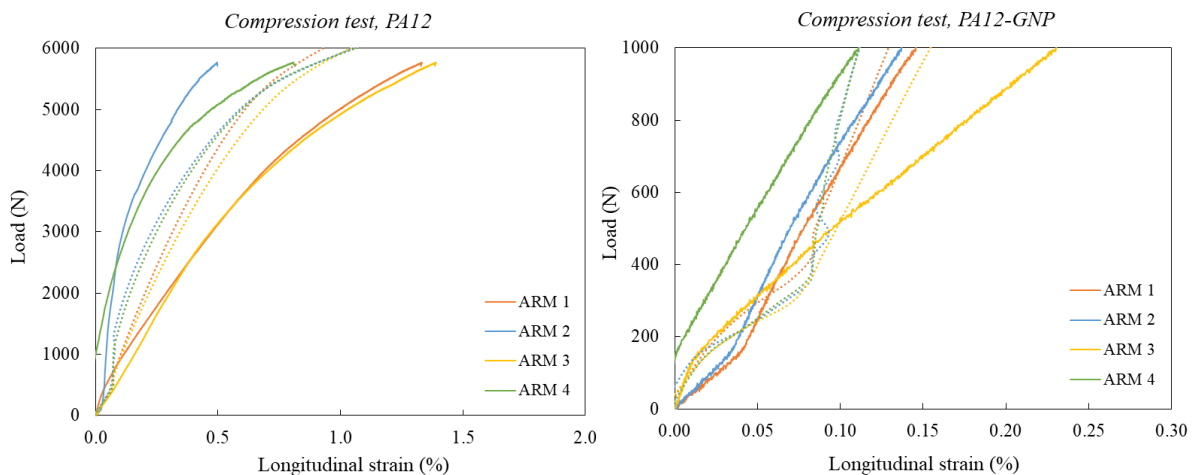


Figure 5.28 Local longitudinal strain of prototypes produced with PA12 (left) and PA12-GNP (right) in function of the compressive load. Dotted-lines refers to numerical data.

For both materials, the compressive longitudinal strain was higher than the tensile longitudinal strain, recording a maximum value of 1.5 % in prototypes produced with PA12 and 0.25 % in prototypes produced with PA12-GNP. In compression tests, the longest arms, *i.e.*, arms number 1 and 3, recorded the highest variation of longitudinal strain with the increasing mechanical load. In the numerical analysis, the highest values of longitudinal strain were also verified in those arms. In turn, the arm 2 exhibited the highest value of von-Mises stress in the robot end-effector assigned with PA12 and PA12-GNP materials (*i.e.*, 57 MPa and 49 MPa, respectively) (Figure 5.29 and Figure 5.30). This may be caused by the lower height of such arm needed to screw the vacuum suction cup with an oval typology (see Figure 5.2). This suggests

Chapter 5. Case-study: Experimental and numerical analysis

that such geometric difference may be responsible for a premature mechanical failure in the robot end-effector when subjected to tensile and/or compressive loads.

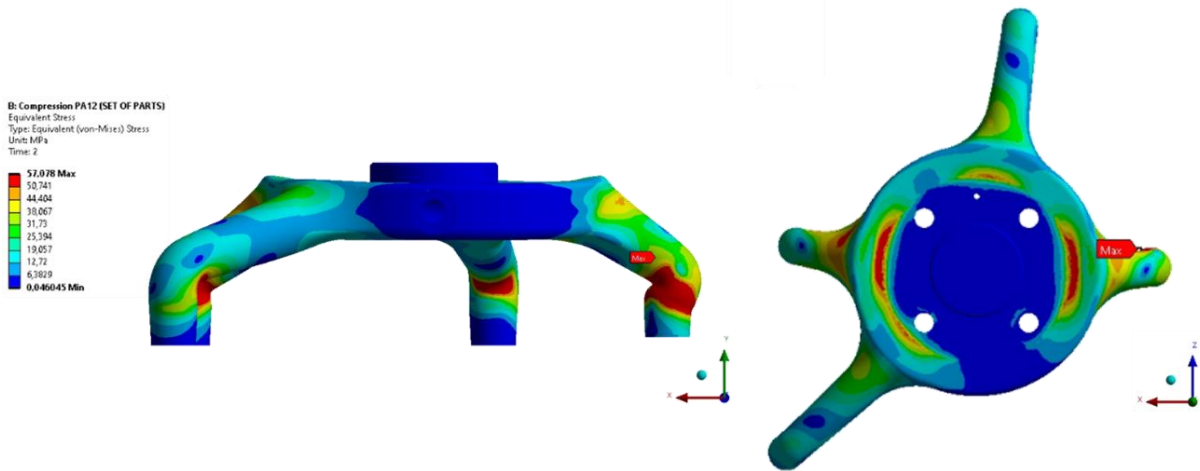


Figure 5.29 von-Mises stress of a prototype produced with PA12 under compressive loads.

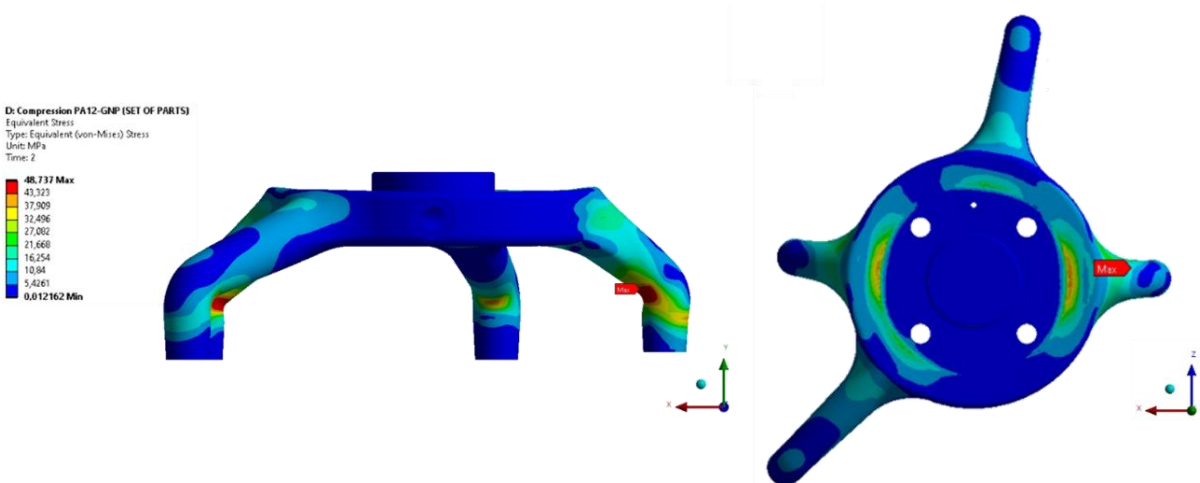


Figure 5.30 von-Mises stress of a prototype produced with PA12-GNP under compressive loads.

5.6. Validation of the product for industrial implementation

Until the implementation of the developed robot end-effector in the manufacturing process flow of Bosch Car Multimedia S.A., several validation tests were performed in the company during the development process. These activities included the assembling of the system in order to evaluate functional and geometric aspects, such as the airtightness of the internal channel, regions of screwing with the collaborative robot arm and vacuum connectors and points of contact with the PCB. In these initial tests, there was also evaluated the robotic pathway and the pick-and-place task (Figure 5.31). This allowed to verify that the proposed robot end-effector is capable to be used in the pick-and-place system operating through vacuum as the airtightness requirements were accomplished by both materials, even

with the microstructural heterogeneities commonly developed in SLS parts during the processing, especially in composite solutions (see Figure 4.67, Chapter 4)

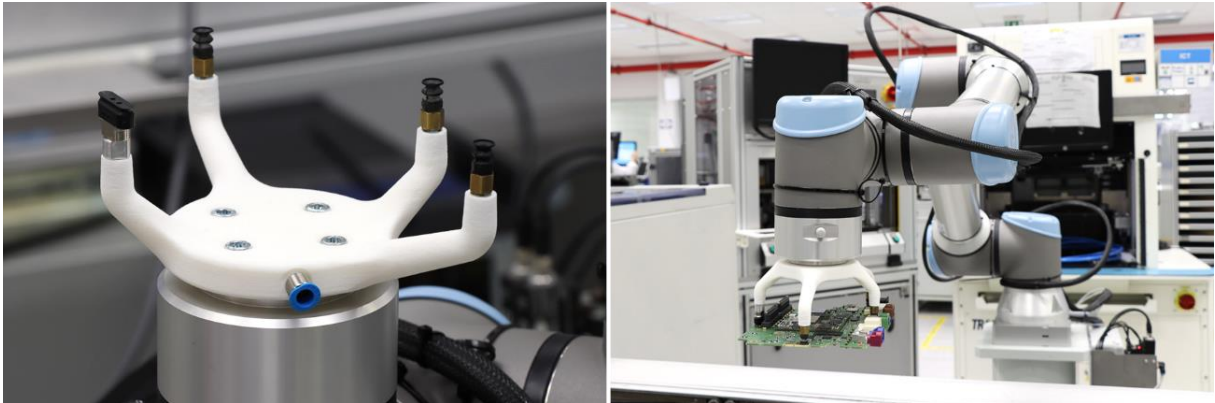


Figure 5.31 Validation of the robot end-effector produced with PA12 at Bosch Car Multimedia S.A.

The ability of the robot end-effector in executing precise pick-and-place movements while ensuring no damage to the solder joints and most fragile components of the PCB was also evaluated. To this aim, robot end-effectors produced with PA12 and PA12-GNP materials were coupled to a UR10e collaborative robot arm and programmed to execute successive operational cycles with a PCB previously prepared with strain gauges for local strain monitoring. The company identified the components most sensitive to strain and prepared the PCB and all instrumentation accordingly. Several strain gauges were coupled to the top and bottom sides of the PCB, namely i) general-purpose foil strain gauges used to evaluate the strain in glass and ceramic chips along the entire perimeter of the board (*i.e.*, strain gauges labelled from 1 to 8) and ii) rosette strain gauges used to evaluate strain in the four corners of the ball grid array (BGA) (*i.e.*, strain gauges labelled from R1 to R4) (Figure 5.32). These tests were carried out individually by changing the measuring cables.

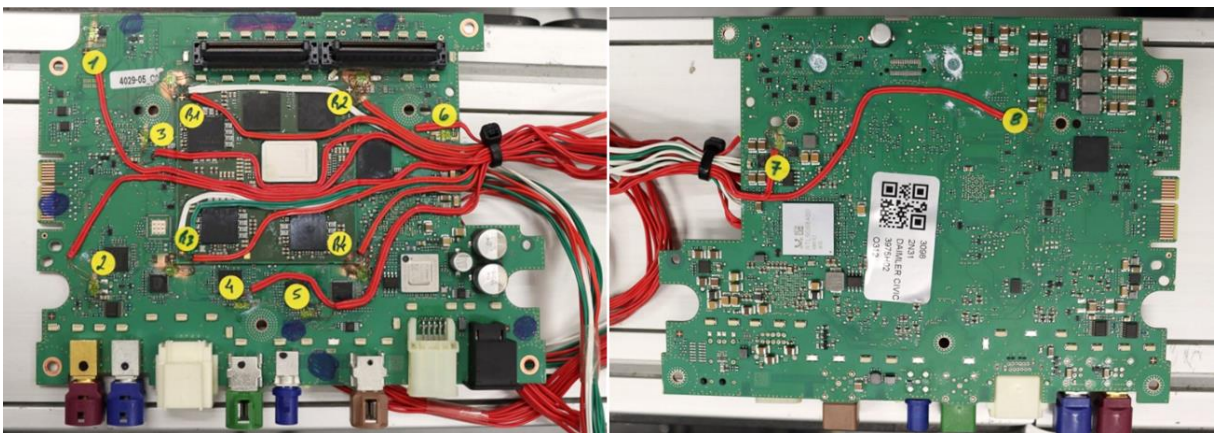


Figure 5.32 Instrumented PCB for local strain monitoring.

Chapter 5. Case-study: Experimental and numerical analysis

The tests were performed according to internal Bosch norms, defined based on the standards IEC 60068-2-21, IPC/JEDEC-9702, IPC/JEDEC-9704 and IPC TM-650. The experimental setup comprised a poka-yoke tool that was fabricated to accommodate the PCB in successive pick-and-place operations (Figure 5.33). The measurements of the PCB strain were dynamic and in real-time. For the company, the target value of PCB strain that secures a valid system is $500 \mu\text{m}/\text{m}$, up to which no critical corrective actions need to be implemented in the production line. This test ultimately allows the company to validate or reprove a product regarding PCB strain before its implementation.

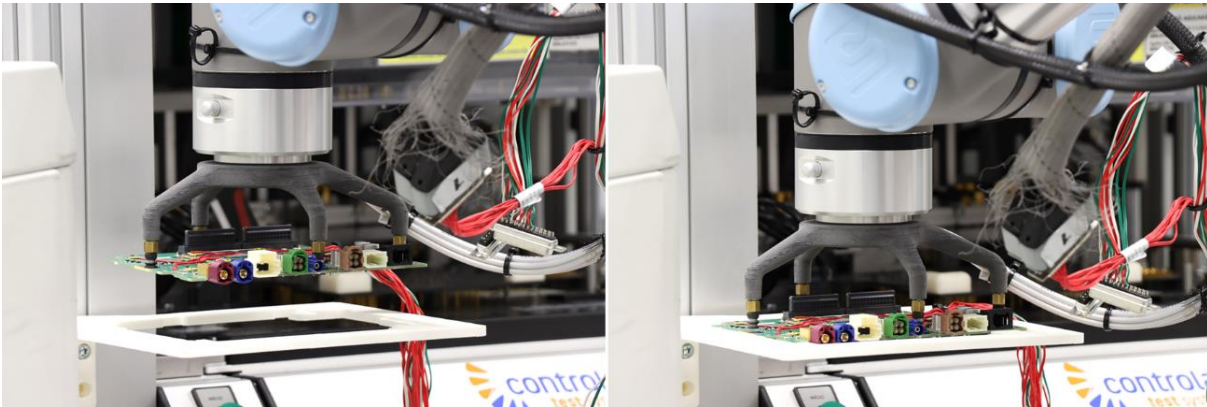


Figure 5.33 Experimental setup used in PCB strain measurements.

Figure 5.34 and Figure 5.35 respectively show the strain measurements recorded on the ceramic connectors and BGA during the pick-and-place of the PCB with a robot end-effector produced with PA12. In turn, Figure 5.36 and Figure 5.37 present the strain measurements obtained with the robot-end effector produced with PA12-GNP material throughout the time, using the same testing conditions.

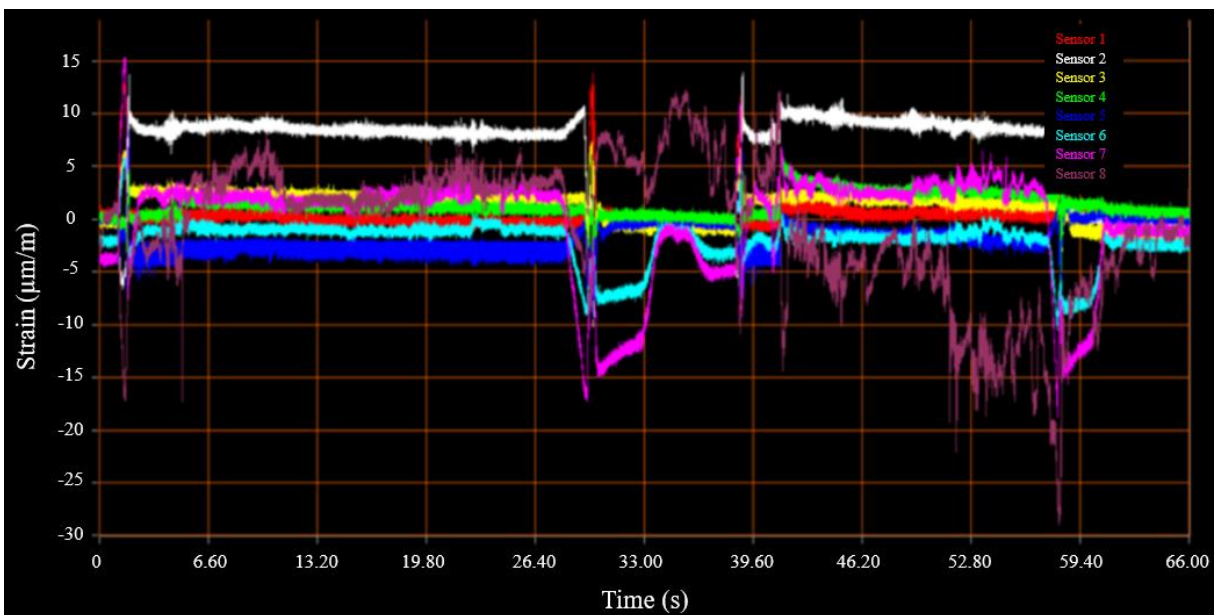


Figure 5.34 PCB strain measured with the robot end-effector produced with PA12 (general-purpose foil strain gauges).

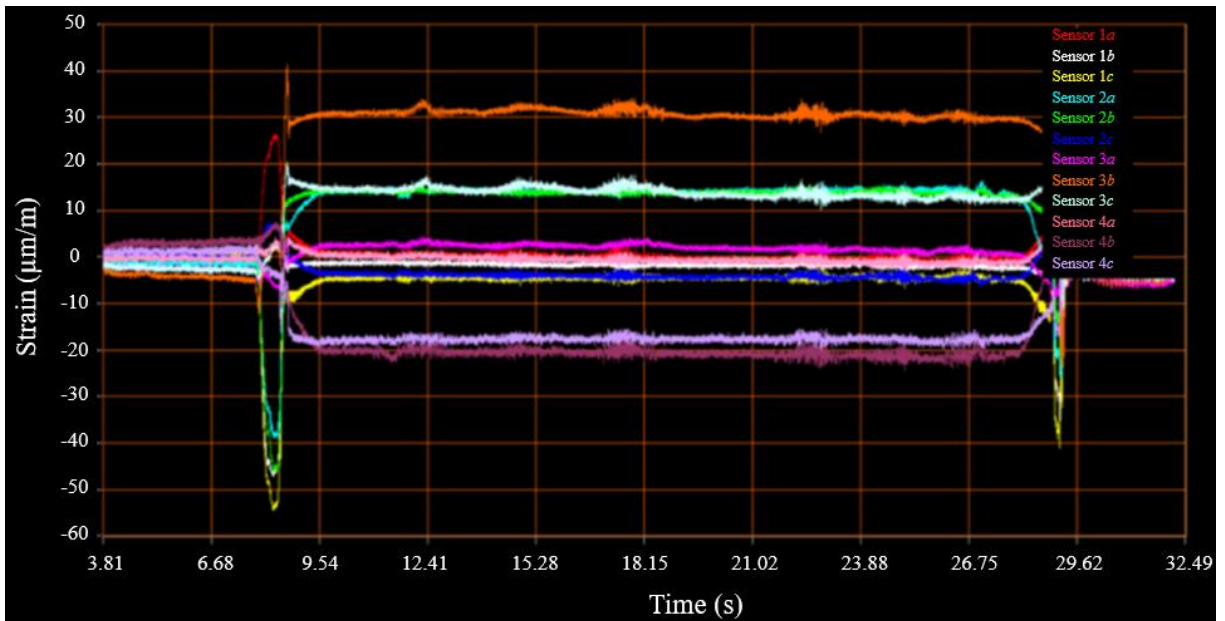


Figure 5.35 PCB strain measured with the robot end-effector produced with PA12 (rosette strain gauges).

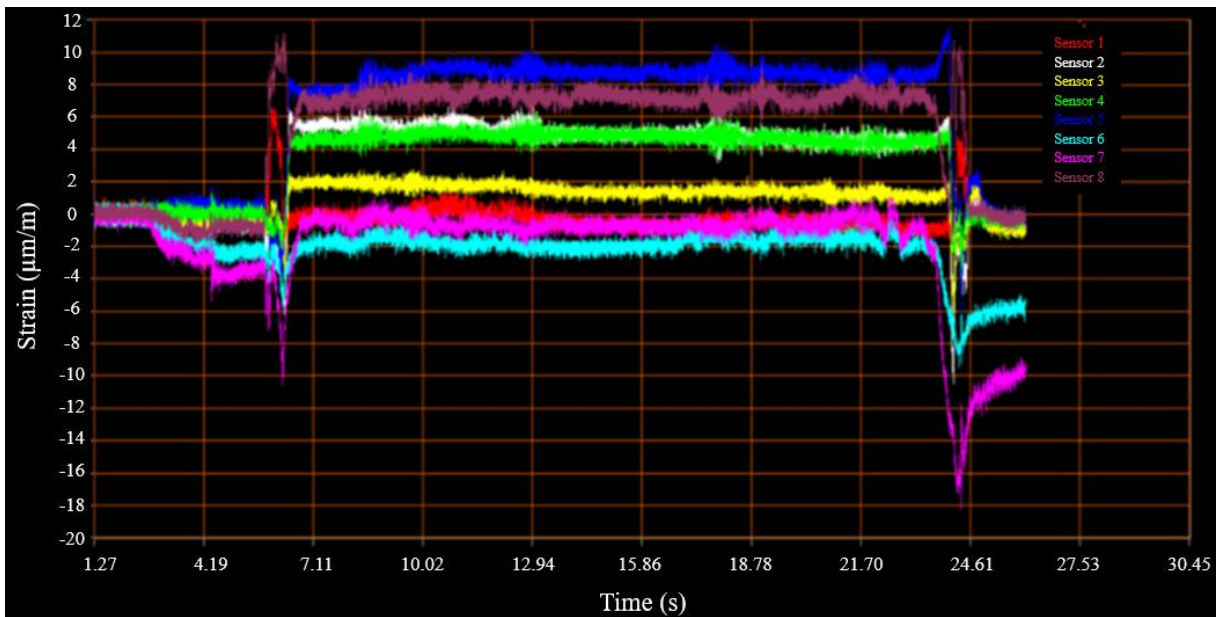


Figure 5.36 PCB strain measured with the robot end-effector produced with PA12-GNP (general-purpose foil strain gauges).

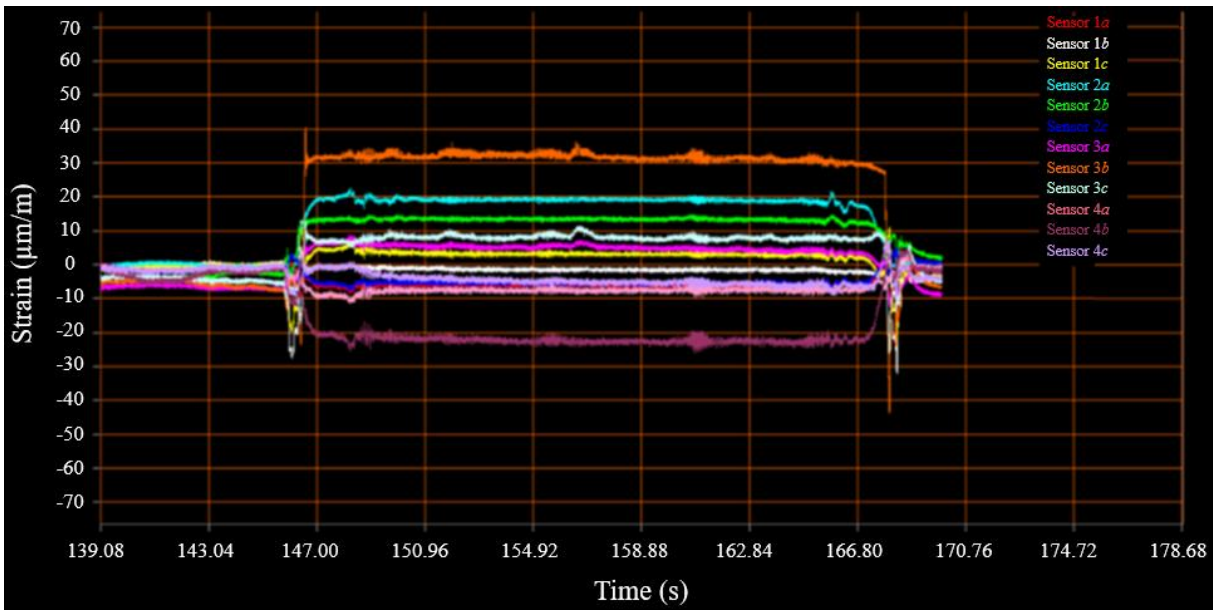


Figure 5.37 PCB strain measured with the robot end-effector produced with PA12-GNP (rosette strain gauges).

Table 5.4 reports the maximum absolute values obtained in the PCB strain measurements.

Table 5.4 Maximum absolute values obtained in the PCB strain measurements.

		CASE-STUDY	
		PA12	PA12 + 1.75 wt% GNP
PCB strain ($\mu\text{m}/\text{m}$)	General-purpose foil strain gauges	27	18
	Rosette strain gauges	54	44

Regardless of the material, the data showed that the maximum strain values obtained in the tests were recorded at the moment at which the robot end-effector contacts the PCB at the beginning and end of the pick-and-place cycle. The rosette strain gauges measured the highest values, meaning that in this system the BGA component is more sensitive to strain than the glass and ceramic chips. However, the maximum absolute values of $54 \mu\text{m}/\text{m}$ and $44 \mu\text{m}/\text{m}$ respectively obtained with the robot end-effector produced with PA12 and PA12-GNP were below the specified target strain recommended by the company for this type of applications. This proved that the proposed robotic concept is able of ensuring safe pick-and-place of the PCB, without damaging the sensitive components of the board (Figure 5.38).



Figure 5.38 Robot end-effector produced with PA12-GNP (final version).

Besides the mechanical and electrical characterization, this test validates that the product is functional and accomplishes all technical specifications defined for its application purpose. Ultimately, the development of this product demonstrates that engineering parts can be designed and successfully produced by SLS with customer-specific composite materials, enabling it to effectively respond to the rapidly changing market trends demanded by the industry.

Final Remarks of Chapter 5

Chapter 5 presents the conceptualization, development, production and characterization of a robot end-effector to be implemented in the automotive electronics industry. Experimental and numerical methods were considered to evaluate the mechanical performance of the case-study under real conditions of implementation depending on its geometry, material and input parameters, answering the RQ3 (see *Chapter 1*). The robot-end effector was designed according to the dimensional and geometric constraints imposed for the system and produced with carbon-based composite materials aiming to obtain the electrostatic-dissipative properties needed to protect the electronic components with which it comes into contact. The design flexibility allowed by SLS enabled the production of a robot end-effector with an organic shape and an internal conformal channel that is essential for uniform vacuum transmission. The experimental data obtained from the characterization tests was then used to define numerical models in a commercial engineering software to analyse and predict the structural mechanical performance of the robot end-effector. The numerical-experimental agreement obtained proved the reliability of using the methodology formulated in this work to produce functional parts by SLS for other engineering sectors, when the properties of the base material depending on the input processing variables are properly defined, *viz.*, true stress-strain curves. Through experimental and numerical characterization, there was verified that the developed robot end-effector successfully accomplished the technical specifications imposed for the system. This ultimately demonstrates the promising contribution of AM to produce customer-specific robotic equipment for industrial application.

Chapter 6. Conclusions and future developments

Chapter 6 summarizes the main conclusions of the research with respect to the activities discussed in each chapter. In the end, suggestions for future developments are also proposed.

6.1. Conclusions

This thesis pursued to in-depth understand the Selective Laser Sintering (SLS) technology in relation to the process parameters and better-performing materials, through experiments and numerical analysis. Scientific research in the field revealed that the definition of operating parameters suited to each SLS process is essential to improve the properties of parts and to allow the successful processing of innovative materials. In turn, it was also demonstrated that even with critical control of the process, the implementation of functional composite materials is still a complex assignment owing to its dependence on a variety of factors related to the constituents, preparation methods, pre- and post-treatments, etc. With such literature review, the importance of a comprehensive understanding of the process-structure-property relationships for different laser-sintering systems and materials, either by experimental or numerical approaches, was highlighted at first. This allowed to demonstrate that scientific research in the field is still necessary to enable the successful applicability of functional SLS parts in novel applications.

Regarding the process parameters, there was demonstrated, in Chapter 3, that the thermal energy supplied by the laser beam to the powder particles during the processing, quantified by the laser power, scan speed, hatch distance and layer thickness, critically influences the dimensional, geometric, mechanical and morphological properties of parts horizontally produced (RQ1). The experiments revealed that medium-low EDv values defining the hatching layers are advantageous for dimensional and geometric properties, while medium-high EDv values are beneficial for the mass and mechanical properties, within the range of values allowable for the laser-sintering system. Thus, there was demonstrated that for conventional PA12, a maximum variation of 10% in thickness, 15% in mass, 73% in flatness of the top surface, 30% in elastic modulus, 22% in tensile strength and 295% in mode I critical energy release rate can be obtained with EDv values ranging between 0.158 J/mm³ and 0.398 J/mm³. About the strategy of the laser beam, there was verified that it should preferably be operating in the xy-direction-alternating or y-direction, rather than the xy-direction-simultaneous or x-direction, to ensure an efficient processing and the production of parts with quality outputs. For instance, test specimens produced with the Y strategy recorded the highest value of tensile strength, 9.8% higher than that obtained with the conventional XY-A strategy. Despite the non-significant effect of the contour parameters themselves, a promising balance between non-compatible properties can be achieved by proper definition of a multiple exposure type combining hatching and contour settings with different energy levels. The results of this research proved that such advanced parameterization mode may be considered in the production of laser-sintered parts with valuable strength-accuracy trade-off.

In terms of SLS materials, this research demonstrated the suitability of the mechanical mixing in the development of novel composite solutions with economic and sustainable benefits. Despite its well-known advantages, in this method there is not a chemical interaction between the matrix and the reinforcements, which makes uniform dispersions and distributions challenging to obtain, especially for carbon-based particles that exhibit high tendency for agglomeration. Regardless of these constraints, useful insights to incorporate MWCNT and GNP into a conventional PA12 matrix were provided in *Chapter 4*. The methodological approach showed that the processing of PA12 incorporating MWCNT and GNP requires lower values of energy density (*i.e.*, 0.238 J/mm³), specific fluidisation flow rates (*i.e.*, 10L/min for MWCNT-based solutions and 15L/min for GNP-based solutions) and the coupling of powder vibrating devices to minimize the compaction effects of the materials. With such modifications, composite materials incorporating carbon-based reinforcements can be successfully processed by SLS (RQ2). The analysis also proved that the typology of the reinforcement and percentage of incorporation are the most influential factors on the dimensional, geometric, mechanical, electrical and morphological properties of the composites, with less prominent effects on the thermal properties. In consequence of problems of agglomeration, weak interparticle adhesion and porosity, there was observed a decrease in dimensional accuracy and mechanical properties of the composites developed in this research, compared to the neat matrix. In turn, promising values of electrical surface resistance in the electrostatic-dissipative range, *i.e.*, 10⁴ Ω, were obtained in materials incorporating 1.75 wt% of GNP. Moreover, values of electrical conductivity of 10⁶ S/cm were obtained with PA12 incorporating 3.0 wt% of MWCNT and PA12 incorporating 3.0 wt% of GNP. Despite the functional solutions available on the market, the study of limitations and capabilities in the processing of non-conventional materials in this work allowed to acquire fundamental knowledge for the development and production of other custom-specific composites by SLS.

Finally, the comprehension on processing parameters and materials was corroborated with the development and production of a robot end-effector by SLS for industrial implementation in the automotive industry, taking advantage of this technology in addressing rapidly changing market trends in a targeted manner. After a detailed analysis of all technical requirements, there was proposed a robot end-effector with an organic shape not possible to produce with conventional processing technologies. Through the evaluation of this case-study in *Chapter 5*, there was demonstrated that the mechanical structural behavior of SLS parts can be successfully analysed through computational methods, as demonstrated in this work by using the ANSYS software. There was proved that a wide experimental database covering the response of the materials to different input process variables is essential to define multilinear isotropic hardening models capable to reliably characterize the performance of SLS parts, making it unnecessary

the programming of complex problem-specific scripts. By introducing experimental values as input parameters for numerical analyses, the porosity and other defects developed during the processing that have direct influence on the performance of the parts are accounted. Such comprehension becomes particularly relevant in composite materials as the presence of the reinforcements often creates regions more susceptible to stress concentrations that also needs to be taken into consideration. Hence, the proposed methodology allows to comprehend the properties of SLS parts depending on the geometry, material and process parameters, by proper definition of the input variables and boundary conditions (RQ3).

In brief, through hundreds of experimental tests, this thesis provides an in-depth knowledge base on three fundamental SLS areas, namely on i) the influence of the most relevant SLS process parameters in a wide range of properties of the parts produced, ii) the development of functional SLS composite materials with potential for ESD shielding applications and iii) the numerical characterization of SLS parts, through a computational methodology allowing to guide process parameters optimization and materials selection depending on the input process variables. A critical understanding of these three interrelated topics is crucial for the successful manufacturing of functional SLS parts for industrial implementation, supporting the growth and competitiveness of this AM technology in advanced areas of application.

6.2. Future developments

This section presents research topics that can be considered in further investigations to complement the findings of this thesis. With regard to the process parameters, future developments should consider the characterization of laser-sintered parts produced with other building orientations, exposure types and/or processing variables (*e.g.*, field of temperatures). Rheological properties may also be included as it directly influences the flowability of the powder particles over the building platform. The assessment of the energy consumption of the system for different processing settings could also be interesting from a sustainable point of view. This will allow to acquire a wider knowledge base of the influence of fundamental SLS process parameters quantified by EDv on the process itself and on the parts produced. Concerning the development of composite materials, smaller intervals of weight percentages of incorporation between 0.50 wt% and 1.75 wt% of MWCNT and GNP should be considered aiming to obtain a valuable compromise between mechanical and electrical properties within the ESD range. Besides the value of energy density that was focus of analysis in this research, the SLS process may also be optimized with other operating parameters (*e.g.*, field of temperatures) for the most promising materials in order to ensure a quality printability and maximum outputs. Pre-treatments and/or complementary mixing methods may also be considered in future work trying to improve the adhesion of the carbon-based

reinforcements with the matrix, enhancing its dispersion and distribution throughout the cross-section of the parts with the minimum possible cost. Disregarding economic concerns, multi-step methods may also be considered in the development of composite parts meeting technical requirements of advanced fields, such as melt-compounding combined with micronization procedures. These advanced methods were not considered in this research since the minimum quantity order required by most companies far exceeded the amount needed for the productions, and even for small quantities these processes are extremely expensive due to the high consumption of nitrogen required for the micronization of materials. The micro-scale characterization of the powder materials after the mechanical mixing could also provide useful insights to more clearly understand the macro-scale findings reported in this thesis. Finally, the reprocessing of the composite materials through successive building cycles should be evaluated. With regard to the case-study, fatigue properties may be characterized in order to guarantee the maximum performance of the robot end-effector during its expected life-time.

References

- Aldahash, S. A. (2018) 'Optimum manufacturing parameters in selective laser sintering of PA12 with white cement additives', *The International Journal of Advanced Manufacturing Technology*, Vol. 96 No. 1–4, pp. 257–270.
- Aldahash, S. A., Salman, S. A. and Gadelmoula, A. M. (2020) 'Towards selective laser sintering of objects with customized mechanical properties based on ANFIS predictions', *Journal of Mechanical Science and Technology*, Vol. 34 No. 12, pp. 5075–5084.
- Amado-Becker, A., Ramos-Grez, J., José Yañez, M., Vargas, Y. and Gaete, L. (2008) 'Elastic tensor stiffness coefficients for SLS Nylon 12 under different degrees of densification as measured by ultrasonic technique', *Rapid Prototyping Journal*, Vol. 14 No. 5, pp. 260–270.
- Asadi, A. and Kalaitzidou, K. (2018) 'Process-Structure-Property Relationship in Polymer Nanocomposites', in Marotti de Sciarra, F. and Russo, P. (eds) *Experimental Characterization, Predictive Mechanical and Thermal Modeling of Nanostructures and Their Polymer Composites*, pp. 25–100.
- ASTM (2002) 'ASTM D695 - Standard Test Method for Compressive Properties of Rigid Plastics'.
- ASTM (2004) 'ASTM D256 - Standard Test Methods for Determining the Izod Pendulum Impact Resistance of Plastics'.
- ASTM (2008) 'ASTM E1131 08 - Standard Test Method for Compositional Analysis by Thermogravimetry'.
- ASTM (2011) 'ASTM E1269 - Standard Test Method for Determining Specific Heat Capacity by Differential Scanning Calorimetry'.
- ASTM (2012) 'ASTM F2792 12a - Standard Terminology for Additive Manufacturing Technologies'.
- Athreya, S. R., Kalaitzidou, K. and Das, S. (2010) 'Processing and characterization of a carbon black-filled electrically conductive Nylon-12 nanocomposite produced by selective laser sintering', *Materials Science and Engineering A*, Vol. 527 No. 10–11, pp. 2637–2642.
- Athreya, S. R., Kalaitzidou, K. and Das, S. (2012) 'Microstructure, Thermomechanical Properties, and Electrical Conductivity of Carbon Black-Filled Nylon-12 Nanocomposites Prepared by Selective Laser Sintering', *Polymer Engineering and Science*, Vol. 52 No. 1, pp. 12–20.
- Bacchewar, P. B., Singhal, S. K. and Pandey, P. M. (2007) 'Statistical Modelling and Optimization of Surface Roughness in the Selective Laser Sintering Process', *Proceedings of the Institution of Mechanical Engineers, Part B: Journal of Engineering Manufacture*, Vol. 221 No. 1, pp. 35–52.
- Badini, C., Padovano, E., De Camillis, R., Lambertini, V. G. and Pietroluongo, M. (2020) 'Preferred orientation of chopped fibers in polymer-based composites processed by selective laser sintering and fused deposition modeling: Effects on mechanical properties', *Journal of Applied Polymer Science*.
- Bai, J., Goodridge, R. D., Hague, R. J. M. and Song, M. (2013) 'Improving the Mechanical Properties of Laser-Sintered Polyamide 12 Through Incorporation of Carbon Nanotubes', *Polymer Engineering and Science*, Vol. 53 No. 9, pp. 1937–1946.
- Bai, J., Goodridge, R. D., Hague, R. J. M., Song, M. and Okamoto, M. (2014) 'Influence of carbon nanotubes on the rheology and dynamic mechanical properties of polyamide-12 for laser sintering', *Polymer Testing*, Vol. 36, pp. 95–100.
- Bai, J., Goodridge, R. D., Yuan, S., Zhou, K., Chua, C. K. and Wei, J. (2015) 'Thermal Influence of CNT on the Polyamide 12 Nanocomposite for Selective Laser Sintering', *Molecules*, Vol. 20 No. 10, pp. 19041–19050.
- Bai, J., Yuan, S., Shen, F., Zhang, B., Chua, C. K., Zhou, K. and Wei, J. (2017) 'Toughening of polyamide 11 with carbon nanotubes for additive manufacturing', *Virtual and Physical Prototyping*, Vol. 12 No. 3, pp. 235–240.
- Bai, L., Gong, C., Chen, X., Sun, Y., Xin, L., Pu, H., Peng, Y. and Luo, J. (2020) 'Mechanical properties and energy absorption capabilities of functionally graded lattice structures: Experiments and simulations', *International Journal of Mechanical Sciences*, Vol. 182.
- Balemans, C., Jaensson, N. O., Hulsen, M. A. and Anderson, P. D. (2018) 'Temperature-dependent sintering of two viscous particles', *Additive Manufacturing*, Vol. 24, pp. 528–542.
- Balemans, C., Looijmans, S. F. S. P., Grosso, G., Hulsen, M. A. and Anderson, P. D. (2020) 'Numerical analysis of the crystallization kinetics in SLS', *Additive Manufacturing*, Vol. 33, p. 101126.
- Balzereit, S., Proes, F., Altstädt, V. and Emmelmann, C. (2018) 'Properties of copper modified polyamide 12-powders and their potential for the use as laser direct structurable electronic circuit carriers', *Additive Manufacturing*, Vol. 23, pp. 347–354.
- Baturynska, I. (2019) 'Application of machine learning techniques to predict the mechanical properties of polyamide 2200 (PA12) in additive manufacturing', *Applied Sciences*, Vol. 9 No. 6.
- Beal, V. E., Paggi, R. A., Salmoria, G. V. and Lago, A. (2009) 'Statistical Evaluation of Laser Energy Density Effect on Mechanical

- Properties of Polyamide Parts Manufactured by Selective Laser Sintering', *Journal of Applied Polymer Science*, Vol. 113 No. 5, pp. 2910–2919.
- Beard, M. A., Ghita, O. R. and Evans, K. E. (2011a) 'Monitoring the Effects of Selective Laser Sintering (SLS) Build Parameters on Polyamide Using Near Infrared Spectroscopy', *Journal of Applied Polymer Science*, Vol. 121, pp. 3153–3158.
- Beard, M. A., Ghita, O. R. and Evans, K. E. (2011b) 'Using Raman spectroscopy to monitor surface finish and roughness of components manufactured by selective laser sintering', *Journal of Raman Spectroscopy*, Vol. 42 No. 4, pp. 744–748.
- Becker, A. (2016) *Characterization and prediction of SLS processability of polymer powders with respect to powder flow and part warpage*, *ETH Zurich Research Collection*. Pontifical Catholic University of Chile.
- Beitz, S., Uerlich, R., Bokelmann, T., Diener, A., Vietor, T. and Kwade, A. (2019) 'Influence of Powder Deposition on Powder Bed and Specimen Properties', *Materials*, Vol. 12 No. 2.
- Bierwisch, C., Mohseni-Mofidi, S., Diemann, B., Grünwald, M., Rudloff, J. and Lang, M. (2021) 'Universal process diagrams for laser sintering of polymers', *Materials and Design*, Vol. 199.
- Blattmeier, M., Witt, G., Wortberg, J., Eggert, J. and Toepker, J. (2012) 'Influence of surface characteristics on fatigue behaviour of laser sintered plastics', *Rapid Prototyping Journal*, Vol. 18 No. 2, pp. 161–171.
- Bourell, D. L., Watt, T. J., Leigh, D. K. and Fulcher, B. (2014) 'Performance Limitations in Polymer Laser Sintering', *Physics Procedia*, Vol. 56, pp. 147–156.
- Brugo, T., Palazzetti, R., Ciric-Kostic, S., Yan, X. T., Minak, G. and Zucchelli, A. (2016) 'Fracture mechanics of laser sintered cracked polyamide for a new method to induce cracks by additive manufacturing', *Polymer Testing*, Vol. 50, pp. 301–308.
- Bugeda, G., Cervera, M. and Lombera, G. (1999) 'Numerical prediction of temperature and density distributions in selective laser sintering processes', *Rapid Prototyping Journal*, Vol. 5 No. 1, pp. 21–26.
- Cahill, S., Lohfeld, S. and McHugh, P. E. (2009) 'Finite element predictions compared to experimental results for the effective modulus of bone tissue engineering scaffolds fabricated by selective laser sintering', *Journal of Materials Science: Materials in Medicine*, Vol. 20 No. 6, pp. 1255–1262.
- Castoro, M. (2013) 'Impact of Laser Power and Build Orientation on the Mechanical Properties of Selectively Laser Sintered Parts', *Proceedings of The National Conference On Undergraduate Research*.
- Caulfield, B., McHugh, P. E. and Lohfeld, S. (2007) 'Dependence of mechanical properties of polyamide components on build parameters in the SLS process', *Journal of Materials Processing Technology*, Vol. 182 No. 1–3, pp. 477–488.
- Cerardi, A., Caneri, M., Meneghello, R., Concheri, G. and Ricotta, M. (2013) 'Mechanical characterization of polyamide cellular structures fabricated using selective laser sintering technologies', *Materials and Design*, Vol. 46, pp. 910–915.
- Chatham, C. A., Bortner, M. J., Johnson, B. N., Long, T. E. and Williams, C. B. (2021) 'Predicting mechanical property plateau in laser polymer powder bed fusion additive manufacturing via the critical coalescence ratio', *Materials and Design*, Vol. 201, p. 109474.
- Chatham, C. A., Long, T. E. and Williams, C. B. (2019) 'A review of the process physics and material screening methods for polymer powder bed fusion additive manufacturing', *Progress in Polymer Science*, Vol. 93, pp. 68–95.
- Chen, P., Wu, H., Zhu, W., Yang, L., Li, Z., Yan, C., Wen, S. and Shi, Y. (2018) 'Investigation into the processability, recyclability and crystalline structure of selective laser sintered Polyamide 6 in comparison with Polyamide 12', *Polymer Testing*, Vol. 69, pp. 366–374.
- Chuang, K. C., Gornet, T. J., Schneidau, K. and Koerner, H. (2019) 'Laser sintering of thermoset polyimide composites', *CAMX 2019 - Composites and Advanced Materials Expo*.
- Chunze, Y., Yusheng, S., Jinsong, Y. and Jinhui, L. (2009) 'A nanosilica/nylon-12 composite powder for selective laser sintering', *Journal of Reinforced Plastics and Composites*, Vol. 28 No. 23, pp. 2889–2902.
- Crookston, J. J., Long, A. C., Bingham, G. A. and Hague, R. J. M. (2008) 'Finite-element modelling of mechanical behaviour of rapid manufactured textiles', *Proceedings of the Institution of Mechanical Engineers, Part L: Journal of Materials: Design and Applications*, Vol. 222 No. 1, pp. 29–36.
- Czelusniak, T. and Amorim, F. L. (2020) 'Influence of energy density on selective laser sintering of carbon fiber-reinforced PA12', *International Journal of Advanced Manufacturing Technology*, Vol. 111, pp. 2361–2376.
- Dadbakhsh, S., Verbelen, L., Verkinderen, O., Strobbe, D., Van Puyvelde, P. and Kruth, J. P. (2017) 'Effect of PA12 powder reuse on coalescence behaviour and microstructure of SLS parts', *European Polymer Journal*, Vol. 92, pp. 250–262.
- Dastjerdi, A. A., Movahhedy, M. R. and Akbari, J. (2017) 'Optimization of process parameters for reducing warpage in selected laser sintering of polymer parts', *Additive Manufacturing*, Vol. 18, pp. 285–294.
- Delfs, P., Tows, M. and Schmid, H. J. (2016) 'Optimized Build Orientation of Additive Manufactured Parts for Improved Surface Quality and Build Time', *Additive Manufacturing*, Vol. 12, pp. 314–320.
- Dencheva, N., Denchev, Z., Jovita Oliveira, M., Nunes, T. G. and Funari, S. S. (2008) 'Relationship Between the Crystalline Structure and Mechanical Behavior in Isotropic and Oriented Polyamide 12', *Journal of Applied Polymer Science*, Vol. 109

- No. 1, pp. 288–302.
- Dewulf, W., Pavan, M., Craeghs, T. and Kruth, J.-P. (2016) 'Using X-ray computed tomography to improve the porosity level of polyamide-12 laser sintered parts', *CIRP Annals - Manufacturing Technology*, CIRP, Vol. 65 No. 1, pp. 205–208.
- Dilibal, S., Sahin, H., Danquah, J. O., Emon, M. O. F. and Choi, J.-W. (2021) 'Additively Manufactured Custom Soft Gripper with Embedded Soft Force Sensors for an Industrial Robot', *International Journal of Precision Engineering and Manufacturing*, Vol. 22 No. 4, pp. 709–718.
- Dong, L., Makradi, A., Ahzi, S. and Remond, Y. (2009) 'Three-dimensional transient finite element analysis of the selective laser sintering process', *Journal of Materials Processing Technology*, Vol. 209 No. 2, pp. 700–706.
- Dong, L., Makradi, A., Ahzi, S., Remond, Y. and Sun, X. (2008) 'Simulation of the densification of semicrystalline polymer powders during the selective laser sintering process: Application to Nylon 12', *Polymer Science Series A*, Vol. 50 No. 6, pp. 704–709.
- Doyle, H., Lohfeld, S., McDonnell, P. and McHugh, P. (2015) 'Evaluation of a Multiscale Modelling Methodology to Predict the Mechanical Properties of PCL/ β -TCP Sintered Scaffold Materials', *Annals of Biomedical Engineering*, Vol. 43 No. 8, pp. 1989–1998.
- Drummer, D., Rietzel, D. and Kühnlein, F. (2010) 'Development of a characterization approach for the sintering behavior of new thermoplastics for selective laser sintering', *Physics Procedia*, Vol. 5, pp. 533–542.
- Duan, B. and Wang, M. (2011) 'Selective laser sintering and its application in biomedical engineering', *MRS Bulletin*, Vol. 36 No. 12, pp. 998–1005.
- Dupin, S., Lame, O., Barrès, C. and Charmeau, J. Y. (2012) 'Microstructural origin of physical and mechanical properties of polyamide 12 processed by laser sintering', *European Polymer Journal*, Vol. 48 No. 9, pp. 1611–1621.
- EOS GmbH (2018) 'PA2200 Balance 1.0 Technical Data Sheet'. Available at: www.eos.info.
- Eshraghi, S., Karevan, M., Kalaitzidou, K. and Das, S. (2013) 'Processing and properties of electrically conductive nanocomposites based on polyamide-12 filled with exfoliated graphite nanoplatelets prepared by selective laser sintering', *International Journal of Precision Engineering and Manufacturing*, Vol. 14 No. 11, pp. 1947–1951.
- Espera, A. H., Valino, A. D., Palaganas, J. O., Souza, L., Chen, Q. and Advincula, R. C. (2019) '3D Printing of a Robust Polyamide-12-Carbon Black Composite via Selective Laser Sintering: Thermal and Electrical Conductivity', *Macromolecular Materials and Engineering*, Vol. 304 No. 4, pp. 1–8.
- Ferreira, T. (2013) *Microinjection moulding of polymeric composites with functionalized carbon nanotubes*. University of Minho.
- Flodberg, G., Pettersson, H. and Yang, L. (2018) 'Pore analysis and mechanical performance of selective laser sintered objects', *Additive Manufacturing*, Vol. 24, pp. 307–315.
- Fountas, N. A. and Vaxevanidis, N. M. (2021) 'Multi-objective optimization of engineering properties for laser-sintered durable thermoplastic/polyamide specimens by applying a virus-evolutionary genetic algorithm', *Computers in Industry*, Vol. 128, p. 103430.
- Francis, V. and Jain, P. K. (2015) 'Advances in nanocomposite materials for additive manufacturing', *International Journal of Rapid Manufacturing*, Vol. 5, pp. 215–233.
- Franco, A., Lanzetta, M. and Romoli, L. (2010) 'Experimental analysis of selective laser sintering of polyamide powders: An energy perspective', *Journal of Cleaner Production*, Vol. 18 No. 16–17, pp. 1722–1730.
- Franco, A. and Romoli, L. (2012) 'Characterization of laser energy consumption in sintering of polymer based powders', *Journal of Materials Processing Technology*, Vol. 212 No. 4, pp. 917–926.
- Gaikwad, S., Tate, J. S., Theodoropoulou, N. and Koo, J. H. (2013) 'Electrical and mechanical properties of PA11 blended with nanographene platelets using industrial twin-screw extruder for selective laser sintering', *Journal of Composite Materials*, Vol. 47 No. 23, pp. 2973–2986.
- Ganci, M., Zhu, W., Buffa, G., Fratini, L., Bo, S. and Yan, C. (2017) 'A macroscale FEM-based approach for selective laser sintering of thermoplastics', *International Journal of Advanced Manufacturing Technology*, Vol. 91 No. 9–12, pp. 3169–3180.
- Ganeriwala, R. and Zohdi, T. I. (2016) 'A coupled discrete element-finite difference model of selective laser sintering', *Granular Matter*, Vol. 18 No. 2, pp. 1–15.
- Gibson, I., Rosen, D. and Stucker, B. (2010) 'Powder Bed Fusion Processes', in *Additive Manufacturing Technologies - Rapid Prototyping to Direct Digital Manufacturing*. Springer International Publishing, pp. 103–142.
- Goh, G. L., Yeong, W. Y., Altherr, J., Tan, J. and Campolo, D. (2022) '3D printing of soft sensors for soft gripper applications', *Materials Today: Proceedings*.
- Goodridge, R. D., Shofner, M. L., Hague, R. J. M., McClelland, M., Schlea, M. R., Johnson, R. B. and Tuck, C. J. (2011) 'Processing of a Polyamide-12/carbon nanofibre composite by laser sintering', *Polymer Testing*, Vol. 30 No. 1, pp. 94–100.

- Goodridge, R. D., Tuck, C. J. and Hague, R. J. M. (2012) 'Laser sintering of polyamides and other polymers', *Progress in Materials Science*, Vol. 57 No. 2, pp. 229–267.
- Graphenest (2017) 'Graphenest Patented Technology Process'. Available at: www.graphenest.com.
- Greiner, S., Wudy, K., Lanzl, L. and Drummer, D. (2017) 'Selective laser sintering of polymer blends : Bulk properties and process behavior', *Polymer Testing*, Vol. 64, pp. 136–144.
- Gusarov, A. V., Laoui, T., Froyen, L. and Titov, V. I. (2003) 'Contact thermal conductivity of a powder bed in selective laser sintering', *International Journal of Heat and Mass Transfer*, Vol. 46 No. 6, pp. 1103–1109.
- Ha, S., Park, E. and Kim, N. (2020) 'Analysis of Shape Deformation from Densification of Additive Manufacturing Parts in Selective Laser Sintering', *International Journal of Precision Engineering and Manufacturing*, Vol. 21 No. 8, pp. 1571–1580.
- Ha, S., Ransikarbum, K., Han, H., Kwon, D., Kim, H. and Kim, N. (2018) 'A dimensional compensation algorithm for vertical bending deformation of 3D printed parts in selective laser sintering', *Rapid Prototyping Journal*, Vol. 24 No. 6, pp. 955–963.
- Ho, H. C. H., Cheung, W. L. and Gibson, I. (2002) 'Effects of graphite powder on the laser sintering behaviour of polycarbonate', *Rapid Prototyping Journal*, Vol. 8 No. 4, pp. 233–242.
- Ho, H. C. H., Gibson, I. and Cheung, W. L. (1999) 'Effects of energy density on morphology and properties of selective laser sintered polycarbonate', *Journal of Materials Processing Technology*, Vol. 89–90, pp. 204–210.
- Hofland, E. C., Baran, I. and Wismeijer, D. A. (2017) 'Correlation of Process Parameters with Mechanical Properties of Laser Sintered PA12 Parts', *Advances in Materials Science and Engineering*.
- Hong, R., Zhao, Z., Leng, J., Wu, J. and Zhang, J. (2019) 'Two-step approach based on selective laser sintering for high performance carbon black/ polyamide 12 composite with 3D segregated conductive network', *Composites Part B: Engineering*, Vol. 176.
- Hur, S.-M., Choi, K.-H., Lee, S.-H. and Chang, P.-K. (2001) 'Determination of fabricating orientation and packing in SLS process', *Journal of Materials Processing Technology*, Vol. 112 No. 2–3, pp. 236–243.
- IEC (1998) 'IEC 61340-5 Electrostatics –Protection of electronic devices from electrostatic phenomena – General requirements'.
- ISO (1996) 'ISO 527 Plastics – Determination of Tensile Properties'.
- ISO (2016) 'ISO 11357 Plastics – Differential Scanning Calorimetry (DSC)'.
- Jain, P. K., Pandey, P. M. and Rao, P. V. M. (2008) 'Experimental investigations for improving part strength in selective laser sintering', *Virtual and Physical Prototyping*, Vol. 3 No. 3, pp. 177–188.
- Jain, P. K., Pandey, P. M. and Rao, P. V. M. (2009) 'Effect of delay time on part strength in selective laser sintering', *International Journal of Advanced Manufacturing Technology*, Vol. 43 No. 1–2, pp. 117–126.
- Jiang, J., Yang, S., Li, L. and Bai, S. (2020) 'High thermal conductivity polylactic acid composite for 3D printing: Synergistic effect of graphene and alumina', *Polymers for Advanced Technologies*, pp. 1–9.
- Jin, X., Li, G. X. and Zhang, M. (2018) 'Optimal design of three-dimensional non-uniform nylon lattice structures for selective laser sintering manufacturing', *Advances in Mechanical Engineering*, Vol. 10 No. 7, pp. 1–19.
- Jing, W., Hui, C., Qiong, W., Hongbo, L. and Zhanjun, L. (2017) 'Surface modification of carbon fibers and the selective laser sintering of modified carbon fiber/nylon 12 composite powder', *Materials and Design*, Vol. 116, pp. 253–260.
- Joseph, N., Janardhanan, C. and Sebastian, M. T. (2014) 'Electromagnetic interference shielding properties of butyl rubber-single walled carbon nanotube composites', *Composites Science and Technology*, Vol. 101, pp. 139–144.
- Josupeit, S., Ordia, L. and Schmid, H. J. (2016) 'Modelling of temperatures and heat flow within laser sintered part cakes', *Additive Manufacturing*, Vol. 12, pp. 189–196.
- Kalaitzidou, K., Athreya, S., Chun, C. and Das, S. (2009) 'Laser Sintering vs Melting Compounding: A new approach for functionally graded polymer nanocomposites', *ICCM International Conference on Composite Materials*.
- Kallio, K. J. and Hedenqvist, M. S. (2008) 'Ageing properties of polyamide-12 pipes exposed to fuels with and without ethanol', *Polymer Degradation and Stability*, Vol. 93 No. 10, pp. 1846–1854.
- Karevan, M., Eshraghi, S., Gerhardt, R., Das, S. and Kalaitzidou, K. (2013) 'Effect of processing method on the properties of multifunctional exfoliated graphite nanoplatelets/polyamide 12 composites', *Carbon*, Vol. 64, pp. 122–131.
- Karthick Raja, B., Pravin Raja, R. J., Jaran, K., Soundararajan, R. and Ashokavarthanan, P. (2019) 'Parameter Optimization for Polyamide in Selective Laser Sintering Based on Mechanical Behavior', *3D Printing and Additive Manufacturing Technologies*, pp. 217–231.
- Kharisov, B. I. and Kharisova, O. V. (2019) *Carbon Allotropes: Metal-Complex Chemistry, Properties and Applications*. 1st edn. Springer International Publishing.
- Kiani, A., Khazaei, S., Badrossamay, M., Forozmehr, E. and Karevan, M. (2020) 'An Investigation into Thermal History and Its Correlation with Mechanical Properties of PA12 Parts Produced by Selective Laser Sintering Process', *Journal of Materials*

- Engineering and Performance*. Springer US, Vol. 29 No. 2, pp. 832–840.
- Kim, H. C., Hahn, H. T. and Yang, Y. S. (2013) 'Synthesis of PA12/functionalized GNP nanocomposite powders for the selective laser sintering process', *Journal of Composite Materials*, Vol. 47 No. 4, pp. 501–509.
- Koo, J. H., Ortiz, R., Ong, B. and Wu, H. (2017) 'Polymer nanocomposites for laser additive manufacturing', in Brandt, M. (ed.) *Laser Additive Manufacturing - Materials, Design, Technologies, and Applications*, pp. 205–235.
- Kruth, J., Levy, G., Schindel, R., Craeghs, T. and Yasa, E. (2008) 'Consolidation of Polymer Powders by Selective Laser Sintering', *Proceedings of the 3rd International Conference on Polymers and Moulds Innovations*, pp. 15–30.
- Kruth, J. P., Levy, G., Klocke, F. and Childs, T. H. C. (2007) 'Consolidation phenomena in laser and powder-bed based layered manufacturing', *CIRP Annals - Manufacturing Technology*, Vol. 56 No. 2, pp. 730–759.
- Kumar, N., Kumar, H. and Khurmi, J. S. (2016) 'Experimental Investigation of Process Parameters for Rapid Prototyping Technique (Selective Laser Sintering) to Enhance the Part Quality of Prototype by Taguchi Method', *Procedia Technology*, Vol. 23, pp. 352–360.
- Kumar, S. (2003) 'Selective Laser Sintering: A Qualitative and Objective Approach', *Journal of the Minerals, Metals and Materials Society*, Vol. 55 No. 10, pp. 43–47.
- Kumar, S. and Kruth, J. (2010) 'Composites by rapid prototyping technology', *Materials and Design*, Vol. 31 No. 2, pp. 850–856.
- Kummert, C. and Schmid, H. J. (2018) 'The Influence of Contour Scanning Parameters and Strategy on Selective Laser Sintering PA613 Build Part Properties', *Proceedings of the 29th Annual International Solid Freeform Fabrication Symposium*, pp. 1582–1591.
- Lahtinen, E., Kukkonen, E., Jokivartio, J., Parkkonen, J., Virkajärvi, J., Kivijärvi, L., Ahlskog, M. and Haukka, M. (2019) 'Preparation of Highly Porous Carbonous Electrodes by Selective Laser Sintering', *ACS Applied Energy Materials*, Vol. 2 No. 2, pp. 1314–1318.
- Launhardt, M., Wörz, A., Loderer, A., Laumer, T., Drummer, D., Hausotte, T. and Schmidt, M. (2016) 'Detecting surface roughness on SLS parts with various measuring techniques', *Polymer Testing*, Vol. 53, pp. 217–226.
- Leon, A. C. De, Chen, Q., Palaganas, N. B., Palaganas, J. O., Manapat, J. and Advincula, R. C. (2016) 'High performance polymer nanocomposites for additive manufacturing applications', *REACT*, Vol. 103, pp. 141–155.
- De Leon, A. C., Rodier, B. J., Bajamundi, C., Espera, A., Wei, P., Kwon, J. G., Williams, J., Ilijasic, F., Advincula, R. C. and Pentzer, E. (2018) 'Plastic Metal-Free Electric Motor by 3D Printing of Graphene-Polyamide Powder', *ACS Applied Energy Materials*, Vol. 1 No. 4, pp. 1726–1733.
- Lexow, M. M., Drexler, M. and Drummer, D. (2017) 'Fundamental investigation of part properties at accelerated beam speeds in the selective laser sintering process', *Rapid Prototyping Journal*, Vol. 23 No. 6, pp. 1099–1106.
- Li, J., Yang, Y., Zhao, Z. and Yan, R. (2021) 'Numerical modeling and experimental verification of the composite material of PA12/HA with parameterized random distribution in selective laser sintering', *Rapid Prototyping Journal*.
- Li, M., Han, Y., Zhou, M., Chen, P., Gao, H., Zhang, Y. and Zhou, H. (2020) 'Experimental investigating and numerical simulations of the thermal behavior and process optimization for selective laser sintering of PA6', *Journal of Manufacturing Processes*, Vol. 56, pp. 271–279.
- Li, X., Van Hooreweder, B., Lauwers, W., Follon, B., Witvrouw, A., Geebelen, K. and Kruth, J.-P. (2018) 'Thermal simulation of the cooling down of selective laser sintered parts in PA12', *Rapid Prototyping Journal*, Vol. 24 No. 7, pp. 1117–1123.
- Lindberg, A., Alfthan, J., Pettersson, H., Flodberg, G. and Yang, L. (2018) 'Mechanical performance of polymer powder bed fused objects – FEM simulation and verification', *Additive Manufacturing*, Vol. 24, pp. 577–586.
- Ling, Z., Wu, J., Wang, X., Li, X. and Zheng, J. (2018) 'Experimental study on the variance of mechanical properties of polyamide 6 during multi-layer sintering process in selective laser sintering', *The International Journal of Advanced Manufacturing Technology*, Vol. 6, pp. 1–8.
- Liu, J., Gao, C., Feng, P., Xiao, T., Shuai, C. and Peng, S. (2015) 'A bioactive glass nanocomposite scaffold toughened by multi-wall carbon nanotubes for tissue engineering', *Journal of the Ceramic Society of Japan*, Vol. 123 No. 6, pp. 485–491.
- Liu, Y., Zhu, L., Zhou, L. and Li, Y. (2019) 'Microstructure and mechanical properties of reinforced polyamide 12 composites prepared by laser additive manufacturing', *Rapid Prototyping Journal*, Vol. 25 No. 6, pp. 1127–1134.
- Ma-Hock, L., Strauss, V., Treumann, S., Küttler, K., Wohlleben, W., Hofmann, T., Gröters, S., Wiench, K., van Ravenzwaay, B. and Landsiedel, R. (2013) 'Comparative inhalation toxicity of multi-wall carbon nanotubes, graphene, graphite nanoplatelets and low surface carbon black', *Particle and Fibre Toxicology*, Vol. 10 No. 1.
- Ma, F., Zhang, H., Hon, K. K. B. and Gong, Q. (2018) 'An optimization approach of selective laser sintering considering energy consumption and material cost', *Journal of Cleaner Production*, Vol. 199, pp. 529–537.
- Maeshima, T., Kim, Y. and Zohdi, T. I. (2021) 'Particle-scale numerical modeling of thermo-mechanical phenomena for additive

- manufacturing using the material point method', *Computational Particle Mechanics*, Vol. 8 No. 3, pp. 613–623.
- Majewski, C., Zarringhalam, H. and Hopkinson, N. (2008) 'Effect of the degree of particle melt on mechanical properties in selective laser-sintered Nylon-12 parts', *Proceedings of the Institution of Mechanical Engineers, Part B: Journal of Engineering Manufacture*, Vol. 222 No. 9, pp. 1055–1064.
- Makuch, A., Trzaska, M., Skalski, K. and Bajkowski, M. (2015) 'PA-G composite powder for innovative additive techniques', *Composites Theory and Practice*, Vol. 15 No. 3, pp. 152–157.
- Malekipour, E. and El-Mounayri, H. (2018) 'Common defects and contributing parameters in powder bed fusion AM process and their classification for online monitoring and control: a review', *International Journal of Advanced Manufacturing Technology*, Vol. 95 No. 1–4, pp. 527–550.
- Mark, J. E. (1999) *Polymer Data Handbook*. Oxford University Press.
- MarketsandMarkets (2018) *Selective Laser Sintering Equipment Market by Material, Application, Industry, Laser Type, and Geography - Global Forecast to 2023*. Available at: <https://www.marketsandmarkets.com/Market-Reports/selective-laser-sintering-equipment-market-27853684.html> (Accessed: 28 January 2021).
- Marrey, M., Malekipour, E., El-Mounayri, H. and Faierson J., E. (2019) 'A Framework for Optimizing Process Parameters in Powder Bed Fusion (PBF) Process Using Process Artificial Neural Network (ANN)', *Procedia Manufacturing*, Vol. 34, pp. 505–515.
- Mavoori, N. K., Vekatesh, S. and Manzoor Hussain, M. (2019) 'Investigation on surface roughness of sintered PA2200 prototypes using Taguchi method', *Rapid Prototyping Journal*, Vol. 25 No. 3, pp. 454–461.
- Minetola, P., Calignano, F. and Galati, M. (2020) 'Compared geometric tolerance capabilities of additive manufacturing systems for polymers', *Additive Manufacturing*, Vol. 32, p. 101103.
- Mokrane, A., Boutaous, M. and Xin, S. (2018) 'Process of selective laser sintering of polymer powders: Modeling, simulation, and validation', *Comptes Rendus - Mecanique*, Vol. 346 No. 11, pp. 1087–1103.
- de Moura, M. F. S. F., Morais, J. J. L. and Durado, N. (2008) 'A new data reduction scheme for mode I wood fracture characterization using the double cantilever beam test', *Engineering Fracture Mechanics*, Vol. 75, pp. 3852–3865.
- Mousa, A. A. (2014) 'The effects of content and surface modification of filler on the mechanical properties of selective laser sintered polyamide12 composites', *Jordan Journal of Mechanical and Industrial Engineering*, Vol. 8 No. 5, pp. 265–274.
- Mousa, A. A. (2016) 'Experimental investigations of curling phenomenon in selective laser sintering process', *Rapid Prototyping Journal*, Vol. 22 No. 2, pp. 405–415.
- Moylan, S., Slotwinski, J., Cooke, A., Jurens, K. and Donmez, M. A. (2014) 'An Additive Manufacturing Test Artefact', *Journal of Research of the National Institute of Standards and Technology*, Vol. 119, pp. 429–459.
- Munguia, J., Ciurana, J. and Riba, C. (2009) 'Neural-network-based model for build-time estimation in selective laser sintering', *Proceedings of the Institution of Mechanical Engineers, Part B: Journal of Engineering Manufacture*, Vol. 223 No. 8, pp. 995–1003.
- NANOCYL (2016) 'NC7000 Technical Data Sheet V08'. Available at: www.nanocyl.com.
- Narkis, M., Lidor, G., Vaxman, A. and Zuri, L. (1999) 'New injection moldable electrostatic dissipative (ESD) composites based on very low carbon black', *Journal of Electrostatics*, Vol. 47, pp. 201–214.
- Nazir, A., Yu, H., Wang, L., Fahad, S., Naveed, K. ur R., Khan, A., Amin, B. U., Lin, T., Usman, M., Elshaarani, T. and Haq, F. (2019) 'Electrical conductivity and electromagnetic interference shielding properties of polymer/carbon composites', *Journal of Materials Science: Materials in Electronics*, Vol. 30 No. 17, pp. 16636–16650.
- Nazir, A., Yu, H., Wang, L., Haroon, M., Ullah, R. S., Fahad, S., Naveed, K.-R., Elshaarani, T., Khan, A. and Usman, M. (2018) 'Recent progress in the modification of carbon materials and their application in composites for electromagnetic interference shielding', *Journal of Materials Science*, Vol. 53 No. 12, pp. 8699–8719.
- Negi, S. and Sharma, R. K. (2016) 'Study on shrinkage behaviour of laser sintered PA 3200GF specimens using RSM and ANN', *Rapid Prototyping Journal*, Vol. 22 No. 4, pp. 645–659.
- Nofal, M., Al-Hallaj, S. and Pan, Y. (2019) 'Experimental investigation of phase change materials fabricated using selective laser sintering additive manufacturing', *Journal of Manufacturing Processes*, Vol. 44, pp. 91–101.
- O'Connor, H. J., Dickson, A. N. and Dowling, D. P. (2018) 'Evaluation of the mechanical performance of polymer parts fabricated using a production scale multi jet fusion printing process', *Additive Manufacturing*, Vol. 22, pp. 381–387.
- Odian, G. (2004) 'Ring-Opening Polymerization', in *Principles of Polymerization*. Wiley - John Wiley & Sons, pp. 544–618.
- Paggi, R. A., Beal, V. E. and Salmoria, G. V. (2013) 'Process optimization for PA12/MWCNT nanocomposite manufacturing by selective laser sintering', *International Journal of Advanced Manufacturing Technology*, Vol. 66 No. 9–12, pp. 1977–1985.
- Papazoglou, E. L., Karkalos, N. E., Karmiris-Obratański, P. and Markopoulos, A. P. (2021) 'On the Modeling and Simulation of SLM and SLS for Metal and Polymer Powders: A Review', *Archives of Computational Methods in Engineering*. Springer

Netherlands.

- Parandoush, P. and Lin, D. (2017) 'A review on additive manufacturing of polymer-fiber composites', *Composite Structures*, Vol. 182, pp. 36–53.
- Pavan, M., Faes, M., Strobbe, D., Hooreweder, B. Van, Craeghs, T., Moens, D. and Dewulf, W. (2017) 'On the influence of inter-layer time and energy density on selected critical-to-quality properties of PA12 parts produced via laser sintering', *Polymer Testing*, Vol. 61, pp. 386–395.
- Paz, R., Monzón, M. D., Benítez, A. N. and González, B. (2016) 'New lightweight optimisation method applied in parts made by selective laser sintering and Polyjet technologies', *International Journal of Computer Integrated Manufacturing*, Vol. 29 No. 4, pp. 462–472.
- Pereira, F. A. M., de Moura, M. F. S. F., Dourado, N., Morais, J. J. L., Xavier, J. and Dias, M. I. R. (2017) 'Direct and inverse methods applied to the determination of mode I cohesive law of bovine cortical bone using the DCB test', *International Journal of Solids and Structures*, Vol. 128, pp. 210–220.
- Pham, D. T., Dotchev, K. D. and Yusoff, W. A. Y. (2008) 'Deterioration of polyamide powder properties in the laser sintering process', *Proceedings of the Institution of Mechanical Engineers, Part C: Journal of Mechanical Engineering Science*, Vol. 222 No. 11, pp. 2163–2176.
- Picard, M., Mohanty, A. K. and Misra, M. (2020) 'Recent advances in additive manufacturing of engineering thermoplastics: challenges and opportunities', *RSC Advances*, Vol. 10 No. 59, pp. 36058–36089.
- Pilipović, A., Bogdan, V., Brajljić, T., Haramina, T., Balic, J., Kodvanj, J., Sercer, M. and Drstvenšek, I. (2010) 'Influence of Laser Sintering Parameters on Mechanical Properties of Polymer Products', *The 3rd International Conference on Additive Technologies*.
- Pilipović, A., Brajljić, T. and Drstvenšek, I. (2018) 'Influence of processing parameters on tensile properties of SLS polymer product', *Polymers*, Vol. 10 No. 11.
- Pilipović, A., Drstvenšek, I., Šerčer, M., Pilipovic, A., Drstvensek, I. and Sercer, M. (2014) 'Mathematical Model for the Selection of Processing Parameters in Selective Laser Sintering of Polymer Products', *Advances in Mechanical Engineering*, Vol. 6 No. 1.
- Puncochar, D. E. (1997) *Interpretation of Geometric Dimensioning and Tolerancing*. 3th edn. Edited by K. Evans. Industrial Press, Inc.
- Qi, X., Chen, G., Li, Y., Cheng, X. and Li, C. (2019) 'Applying Neural-Network-Based Machine Learning to Additive Manufacturing: Current Applications, Challenges, and Future Perspectives', *Engineering*, Vol. 5 No. 4, pp. 721–729.
- Razeghi, M. (2019) 'The carbon atom', in *The Mystery of Carbon - An introduction to carbon materials*. Institute of Physics Publishing, pp. 1–12.
- Riedlbauer, D., Drexler, M., Drummer, D., Steinmann, P. and Mergheim, J. (2014) 'Modelling, simulation and experimental validation of heat transfer in selective laser melting of the polymeric material PA12', *Computational Materials Science*, Vol. 93, pp. 239–248.
- Rong-Ji, W., Xin-Hua, L., Qing-Ding, W. and Lingling, W. (2009) 'Optimizing process parameters for selective laser sintering based on neural network and genetic algorithm', *International Journal of Advanced Manufacturing Technology*, Vol. 42 No. 11–12, pp. 1035–1042.
- Ross, S., Korostynska, O., Cordova-Lopez, L. E. and Mason, A. (2022) 'A review of unilateral grippers for meat industry automation', *Trends in Food Science and Technology*, Vol. 119, pp. 309–319.
- Salazar, A., Rico, A., Rodríguez, J., Segurado Escudero, J., Seltzer, R. and Martin De La Escalera Cutillas, F. (2014) 'Fatigue crack growth of SLS polyamide 12: Effect of reinforcement and temperature', *Composites Part B: Engineering*, Vol. 59, pp. 285–292.
- Salmoria, G. V., Leite, J. L. and Paggi, R. A. (2009) 'The microstructural characterization of PA6/PA12 blend specimens fabricated by selective laser sintering', *Polymer Testing*, Vol. 28 No. 7, pp. 746–751.
- Salmoria, G. V., Paggi, R. A. and Beal, V. E. (2017) 'Graded Composites of Polyamide/Carbon Nanotubes Prepared by Laser Sintering', *Lasers in Manufacturing and Materials Processing*, Vol. 4 No. 1, pp. 36–44.
- Salmoria, G. V., Paggi, R. A., Lago, A. and Beal, V. E. (2011) 'Microstructural and mechanical characterization of PA12/MWCNTs nanocomposite manufactured by selective laser sintering', *Polymer Testing*, Vol. 30 No. 6, pp. 611–615.
- Savio, G., Curtarello, A., Rosso, S., Meneghello, R. and Concheri, G. (2019) 'Homogenization driven design of lightweight structures for additive manufacturing', *International Journal on Interactive Design and Manufacturing*, Vol. 13 No. 1, pp. 263–276.
- Schmid, M., Amado, A. and Wegener, K. (2014) 'Materials perspective of polymers for additive manufacturing with selective laser sintering', *Journal of Materials Research*, Vol. 29 No. 17, pp. 1824–1832.

- Schmid, M. and Wegener, K. (2016) 'Additive Manufacturing: Polymers applicable for Laser Sintering (LS)', *Procedia Engineering*, Vol. 149, pp. 457–464.
- Schneider, J. and Kumar, S. (2020) 'Multiscale characterization and constitutive parameters identification of polyamide (PA12) processed via selective laser sintering', *Polymer Testing*, Vol. 86 No. 106357.
- Schneider, S. (2011) 'Basic Training EOSINT P 395', pp. 1–98.
- Schroeffler, A., Rehekampff, C. and Lueth, T. C. (2019) 'An automated design approach for task-specific two finger grippers for industrial applications', *International Conference on Robotics and Biomimetics*, pp. 184–189.
- Setti, G., Oliveira, M., Maia, I., Silva, J., Savu, R. and Joanni, E. (2014) 'Correlation between mechanical and surface properties of SLS parts', *Rapid Prototyping Journal*, Vol. 20 No. 4, pp. 285–290.
- Sharma, V. S., Singh, S., Sachdeva, A. and Kumar, P. (2015) 'Influence of sintering parameters on dynamic mechanical properties of selective laser sintered parts', *International Journal of Material Forming*, Vol. 8 No. 1, pp. 157–166.
- Shaw, B. and Dirven, S. (2016) 'Investigation of Porosity and Mechanical Properties of Nylon SLS Structures', *23rd International Conference on Mechatronics and Machine Vision in Practice*.
- Shen, F., Yuan, S., Chua, C. K. and Zhou, K. (2018) 'Development of process efficiency maps for selective laser sintering of polymeric composite powders: Modeling and experimental testing', *Journal of Materials Processing Technology*, Vol. 254, pp. 52–59.
- Shen, X., Yao, J., Wang, Y. and Yang, J. (2004) 'Density prediction of Selective Laser Sintering parts based on Artificial Neural Network', *International Symposium on Neural Networks*, pp. 832–840.
- Shi, D. and Gibson, I. (1997) 'Material properties and fabrication parameters in selective laser sintering process', *Rapid Prototyping Journal*, Vol. 3 No. 4, pp. 129–136.
- Shuai, C., Liu, T., Gao, C., Feng, P., Xiao, T., Yu, K. and Peng, S. (2016) 'Mechanical and structural characterization of diopside scaffolds reinforced with graphene', *Journal of Alloys and Compounds*, Vol. 655, pp. 86–92.
- Shuai, C., Zeng, Z., Yang, Y., Qi, F., Peng, S., Yang, W., He, C., Wang, G. and Qian, G. (2020) 'Graphene oxide assists polyvinylidene fluoride scaffold to reconstruct electrical microenvironment of bone tissue', *Materials and Design*, Vol. 190.
- Silva, C. S., Lima, A., Rodrigues, S. J. F., Gonçalves, L. F. F., Sampaio, Á. M., Oliveira, L., Fernandes, A. and Pontes, A. J. (2020) 'Development of functionalised foam for electrostatic discharge applications', *Plastics, Rubber and Composites*, Vol. 49 No. 10, pp. 470–478.
- Silva, F. G. A., de Moura, M. F. S. F., Dourado, N., Xavier, J., Pereira, F. A. M., Morais, J. J. L., Dias, M. I. R., Lourenço, P. J. and Judas, F. M. (2016) 'Fracture characterization of human cortical bone under mode II loading using the end-notched flexure test', *Journal of the International Federation for Medical and Biological Engineering*, pp. 1249–1260.
- Sindinger, S.-L., Kralovec, C., Tasch, D. and Schagerl, M. (2020) 'Thickness dependent anisotropy of mechanical properties and inhomogeneous porosity characteristics in laser-sintered polyamide 12 specimens', *Additive Manufacturing*, Vol. 33, p. 101141.
- Singh, A. K. and Prakash, R. S. (2010) 'Response surface-based simulation modeling for selective laser sintering process', *Rapid Prototyping Journal*, Vol. 16 No. 6, pp. 441–449.
- Singh, S., Sachdeva, A. and Sharma, V. S. (2017) 'Optimization of selective laser sintering process parameters to achieve the maximum density and hardness in polyamide parts', *Progress in Additive Manufacturing*, Vol. 2 No. 1–2, pp. 19–30.
- Singh, S., Sharma, V. S. and Sachdeva, A. (2012) 'Optimization and analysis of shrinkage in selective laser sintered polyamide parts', *Materials and Manufacturing Processes*, Vol. 27 No. 6, pp. 707–714.
- Singhal, S. K., Jain, P. K., Pandey, P. M. and Nagpal, A. K. (2009) 'Optimum part deposition orientation for multiple objectives in SL and SLS prototyping', *International Journal of Production Research*, Vol. 47 No. 22, pp. 6375–6396.
- SmarTech Markets (2017) *Markets for Automated 3D Printing 2016 to 2027: An Opportunity Analysis and Ten-Year Forecast*.
- Soe, S. P. (2012) 'Quantitative analysis on SLS part curling using EOS P700 machine', *Journal of Materials Processing Technology*, Vol. 212 No. 11, pp. 2433–2442.
- Soe, S. P., Evers, D. R. and Setchi, R. (2013) 'Assessment of non-uniform shrinkage in the laser sintering of polymer materials', *International Journal of Advanced Manufacturing Technology*, Vol. 68 No. 1–4, pp. 111–125.
- Sohrabpoor, H., Negi, S., Shaiesteh, H., Ahad, I. U. and Brabazon, D. (2018) 'Optimizing selective laser sintering process by grey relational analysis and soft computing techniques', *Optik*, Vol. 174, pp. 185–194.
- Soldner, D., Greiner, S., Burkhardt, C., Drummer, D., Steinmann, P. and Mergheim, J. (2021) 'Numerical and experimental investigation of the isothermal assumption in selective laser sintering of PA12', *Additive Manufacturing*, Vol. 37, p. 101676.
- Song, C., Huang, A., Yang, Y., Xiao, Z. and Yu, J. K. (2017) 'Effect of energy input on the UHMWPE fabricating process by selective laser sintering', *Rapid Prototyping Journal*, Vol. 23 No. 6, pp. 1069–1078.
- de Souza Vieira, L., dos Anjos, E. G. R., Verginio, G. E. A., Oyama, I. C., Braga, N. F., da Silva, T. F., Montagna, L. S., Rezende, M. C. and Passador, F. R. (2021) 'Carbon-based materials as antistatic agents for the production of antistatic packaging: a

- review', *Journal of Materials Science: Materials in Electronics*, Vol. 32 No. 4, pp. 3929–3947.
- Starr, T. L., Gornet, T. J. and Usher, J. S. (2011) 'The effect of process conditions on mechanical properties of laser-sintered nylon', *Rapid Prototyping Journal*, Vol. 17 No. 6, pp. 418–423.
- Stichel, T., Frick, T., Laumer, T., Tenner, F., Hausotte, T., Merklein, M. and Schmidt, M. (2018) 'A Round Robin study for selective laser sintering of polymers: Back tracing of the pore morphology to the process parameters', *Journal of Materials Processing Technology*, Vol. 252, pp. 537–545.
- Sugavaneswaran, M., Rajesh, N. and Sathishkumar, N. (2018) 'Design of Robot Gripper with Topology Optimization and Its Fabrication Using Additive Manufacturing', in Shunmugam, M. S. and Kanthababu, M. (eds) *Advances in Additive Manufacturing and Joining*. Spring.
- Tan, L. J., Zhu, W. and Zhou, K. (2020) 'Recent Progress on Polymer Materials for Additive Manufacturing', *Advanced Functional Materials*, Vol. 30 No. 43.
- Tang, H., Chen, H., Sun, Q., Chen, Z. and Yan, W. (2021) 'Experimental and computational analysis of structure-property relationship in carbon fiber reinforced polymer composites fabricated by selective laser sintering', *Composites Part B: Engineering*, Vol. 204, p. 108499.
- Telenko, C. and Seepersad, C. C. (2012) 'A comparison of the energy efficiency of selective laser sintering and injection molding of nylon parts', *Rapid Prototyping Journal*, Vol. 18 No. 6, pp. 472–481.
- Tian, X., Peng, G., Yan, M., He, S. and Yao, R. (2018) 'Process prediction of selective laser sintering based on heat transfer analysis for polyamide composite powders', *International Journal of Heat and Mass Transfer*, Vol. 120, pp. 379–386.
- Tiwari, S. K., Pande, S., Bobade, S. M. and Kumar, S. (2018) 'A Targeted Functional Value Based Nanoclay/PA12 Composite Material Development for Selective Laser Sintering Process', *Procedia Manufacturing*, Vol. 21, pp. 630–637.
- Tong, Q., Xue, K., Wang, T. and Yao, S. (2020) 'Laser sintering and invalidating composite scan for improving tensile strength and accuracy of SLS parts', *Journal of Manufacturing Processes*, Vol. 56, pp. 1–11.
- Türk, D., Brenni, F., Zogg, M. and Meboldt, M. (2017) 'Mechanical characterization of 3D printed polymers for fiber reinforced polymers processing', *Materials & Design*, Vol. 118, pp. 256–265.
- Vasquez, G. M., Majewski, C. E., Haworth, B. and Hopkinson, N. (2014) 'A targeted material selection process for polymers in laser sintering', *Additive Manufacturing*, Vol. 1, pp. 127–138.
- Vasquez, M., Haworth, B. and Hopkinson, N. (2011) 'Optimum sintering region for laser sintered Nylon-12', *Proceedings of the Institution of Mechanical Engineers, Part B: Journal of Engineering Manufacture*, Vol. 225 No. 12, pp. 2240–2248.
- Velu, R. and Singamneni, S. (2015) 'Evaluation of the influences of process parameters while selective laser sintering PMMA powders', *Proceedings of the Institution of Mechanical Engineers, Part C: Journal of Mechanical Engineering Science*, Vol. 229 No. 4, pp. 603–613.
- Verbelen, L., Dadbakhsh, S., Van Den Eynde, M., Kruth, J. P., Goderis, B. and Van Puyvelde, P. (2016) 'Characterization of polyamide powders for determination of laser sintering processability', *European Polymer Journal*, Vol. 75, pp. 163–174.
- Verma, A. and Rai, R. (2017) 'Sustainability-induced dual-level optimization of additive manufacturing process', *International Journal of Advanced Manufacturing Technology*, Vol. 88 No. 5–8, pp. 1945–1959.
- Vijayaraghavan, V., Garg, A., Wong, C. H., Tai, K., Regalla, S. P. and Tsai, M. C. (2016) 'Density characteristics of laser-sintered three-dimensional printing parts investigated by using an integrated finite element analysis-based evolutionary algorithm approach', *Proceedings of the Institution of Mechanical Engineers, Part B: Journal of Engineering Manufacture*, Vol. 230 No. 1, pp. 100–110.
- Wakeman, M. D. and Manson, J.-A. E. (2005) 'Composites manufacturing-thermoplastics', in *Design and Manufacture of Textile Composites*, pp. 197–241.
- Wang, C. Y., Dong, Q. and Shen, X. X. (2010) 'Research on Warpage of Polystyrene in Selective Laser Sintering', *Applied Mechanics and Materials*, Vol. 43, pp. 578–582.
- Wang, G., Qi, F., Yang, W., Yang, Y., He, C., Peng, S. and Shuai, C. (2019) 'Crystallinity and Reinforcement in Poly-L-Lactic Acid Scaffold Induced by Carbon Nanotubes', *Advances in Polymer Technology*, pp. 1–10.
- Wang, R.-J., Li, J., Wang, F., Li, X. and Wu, Q. (2009) 'ANN model for the prediction of density in Selective Laser Sintering', *Int. J. Manufacturing Research*, Vol. 4 No. 3, pp. 362–373.
- Wang, R.-J., Wang, L., Zhao, L. and Liu, Z. (2007) 'Influence of process parameters on part shrinkage in SLS', *International Journal of Advanced Manufacturing Technology*, Vol. 33 No. 5–6, pp. 498–504.
- Wang, X., Jiang, M., Zhou, Z., Gou, J. and Hui, D. (2017) '3D printing of polymer matrix composites : A review and prospective', *Composites Part B*, Vol. 110, pp. 442–458.
- Wang, Y., DiNapoli, C. M., Tofig, G. A., Cunningham, R. W. and Pearson, R. A. (2017) 'Selective Laser Sintering Processing Behavior of Polyamide Powders', *ANTEC 2017 - The Plastics Technology Conference*, pp. 112–116.

- Wegner, A., Harder, R., Witt, G. and Drummer, D. (2015) 'Determination of Optimal Processing Conditions for the Production of Polyamide 11 Parts using the Laser Sintering Process', *IJEP*, Vol. 3 No. 1, pp. 5–12.
- Wegner, A. and Witt, G. (2012) 'Correlation of Process Parameters and Part Properties in Laser Sintering using Response Surface Modeling', *Physics Procedia*, Vol. 39, pp. 480–490.
- Westphal, E. and Seitz, H. (2021) 'A machine learning method for defect detection and visualization in selective laser sintering based on convolutional neural networks', *Additive Manufacturing*, Vol. 41, p. 101965.
- Wikipedia (2019) *Nylon 12*.
- Wörz, A., Wudy, K., Drummer, D., Wegner, A. and Witt, G. (2018) 'Comparison of long-term properties of laser sintered and injection molded polyamide 12 parts', *Journal of Polymer Engineering*, Vol. 38 No. 6, pp. 573–582.
- Wu, H., Fahy, W. P., Kim, S., Kim, H., Zhao, N., Pilato, L., Kafi, A., Bateman, S. and Koo, J. H. (2020) 'Recent developments in polymers/polymer nanocomposites for additive manufacturing', *Progress in Materials Science*, Vol. 111.
- Wu, J., Xu, X., Zhao, Z., Wang, M. and Zhang, J. (2018) 'Study in performance and morphology of polyamide 12 produced by selective laser sintering technology', *Rapid Prototyping Journal*, Vol. 24 No. 5, pp. 813–820.
- Xi, S., Zhang, P., Huang, Y., Kong, M., Yang, Q. and Li, G. (2020) 'Laser sintering of cryogenically ground polymer powders into high-performance parts: The role of dry particle coating with a conductive flow agent', *Polymer*, Vol. 186.
- Xiao, L., Lu, M. and Huang, H. (2020) 'Detection of powder bed defects in selective laser sintering using convolutional neural network', *International Journal of Advanced Manufacturing Technology*, Vol. 107 No. 5–6, pp. 2485–2496.
- Xin, L., Boutaous, M., Xin, S. and Siginer, D. A. (2017) 'Numerical modeling of the heating phase of the selective laser sintering process', *International Journal of Thermal Sciences*, Vol. 120, pp. 50–62.
- Xiong, Y., Pei, H., Lv, Q. and Chen, Y. (2022) 'A Facile Fabrication of PA12/CNTs Nanocomposites with Enhanced Three-Dimensional Segregated Conductive Networks and Electromagnetic Interference Shielding Property through Selective Laser Sintering', *ACS Omega*, Vol. 7 No. 5, pp. 4293–4304.
- Xu, Z., Liang, P., Yang, W., Li, S. and Cai, C. (2014) 'Effects of laser energy density on forming accuracy and tensile strength of selective laser sintering resin coated sands', *China Foundry*, Vol. 11 No. 3, pp. 151–156.
- Yan, Chunze, Hao, L., Xu, L. and Shi, Y. (2011) 'Preparation, characterisation and processing of carbon fibre/polyamide-12 composites for selective laser sintering', *Composites Science and Technology*, Vol. 71 No. 16, pp. 1834–1841.
- Yan, C., Shi, Y. and Hao, L. (2011) 'Investigation into the Differences in the Selective Laser Sintering between Amorphous and Semi-crystalline Polymers', *International Polymer Processing*, Vol. 26 No. 4, pp. 416–423.
- Yan, C. Z., Shi, Y. S., Yang, J. S. and Liu, J. H. (2009) 'Preparation and selective laser sintering of nylon-coated metal powders for the indirect SLS process', *Rapid Prototyping Journal*, Vol. 15 No. 5, pp. 355–360.
- Yan, M., Tian, X., Peng, G., Li, D. and Zhang, X. (2018) 'High temperature rheological behavior and sintering kinetics of CF/PEEK composites during selective laser sintering', *Composites Science and Technology*, Vol. 165, pp. 140–147.
- Yao, B., Li, Z. and Zhu, F. (2020) 'Effect of powder recycling on anisotropic tensile properties of selective laser sintered PA2200 polyamide', *European Polymer Journal*, Vol. 141.
- Yeganeh, A. M., Movahhedy, M. R. and Khodaygan, S. (2019) 'An efficient scanning algorithm for improving accuracy based on minimising part warping in selected laser sintering process', *Virtual and Physical Prototyping*, Vol. 14 No. 1, pp. 59–78.
- Yu, Y., Guo, Y., Jiang, T., Li, J., Jiang, K., Zhang, H. and Zhuang, Y. (2018) 'Study on the characteristics of Walnut Shell/Co-PES/Co-PA powder produced by selective laser sintering', *Materials*, Vol. 11 No. 5.
- Yuan, S., Bai, J., Chua, C. K., Wei, J. and Zhou, K. (2016) 'Material Evaluation and Process Optimization of CNT-Coated Polymer Powders for Selective Laser Sintering', *Polymers*, Vol. 8 No. 10.
- Yuan, S., Chua, C. K., Zhou, K., Bai, J. and Wei, J. (2016) 'Dynamic Mechanical Behaviours of Laser Sintered Polyurethane Incorporated with MWCNTs', *Proceedings of the 2nd International Conference on Progress in Additive Manufacturing*, pp. 3–8.
- Yuan, S., Li, J., Yao, X., Zhu, J., Gu, X., Gao, T., Xu, Y. and Zhang, W. (2020) 'Intelligent optimization system for powder bed fusion of processable thermoplastics', *Additive Manufacturing*, Vol. 34, p. 101182.
- Yuan, S., Shen, F., Chua, C. K. and Zhou, K. (2019) 'Polymeric composites for powder-based additive manufacturing: Materials and applications', *Progress in Polymer Science*, Vol. 91, pp. 141–168.
- Yuan, S., Zheng, Y., Chua, C. K., Yan, Q. and Zhou, K. (2018) 'Electrical and thermal conductivities of MWCNT/polymer composites fabricated by selective laser sintering', *Composites Part A: Applied Science and Manufacturing*, Vol. 105, pp. 203–213.
- Zarringhalam, H., Hopkinson, N., Kamperman, N. F. and Vlieger, J. J. (2006) 'Effects of Processing on Microstructure and Properties of SLS Nylon 12', *Materials Science and Engineering A*, Vol. 435, pp. 172–180.
- Zhang, Y., Fang, J., Li, J., Guo, Y. and Wang, Q. (2017) 'The effect of carbon nanotubes on the mechanical properties of wood plastic composites by selective laser sintering', *Polymers*, Vol. 9 No. 12.

Zhu, W., Yan, C., Shi, Yunsong, Wen, S., Liu, J., Wei, Q. and Shi, Yusheng (2016) 'A novel method based on selective laser sintering for preparing high-performance carbon fibres/polyamide12/epoxy ternary composites', *Scientific Reports*, Vol. 6, pp. 1–10.

Appendices

Appendix A. List of scientific publications focused on SLS computational modelling

The data presented in this section is based on a comprehensive search made by analysing publications related with the addressed topic in four scientific databases (*i.e.*, B-ON, Scopus, Web of Science and Science Direct), considering the following list of keywords: Selective Laser Sintering, prediction, simulation, computational modelling, numerical analysis.

Table A.1 Scientific publications focused on computational modelling of SLS (I - SLS process).

SLS PROCESS					
AREA OF APPLICATION	NUMERICAL METHODOLOGY	NUMERICAL TOOL	EXPERIMENTAL VALIDATION	POLYMERIC MATERIAL	REFERENCE
Temperature and density distribution	Finite Element Analysis (FEA)	ABAQUS	✓ (Literature results)	Polyamide 12 (PA12)	(Dong <i>et al.</i> , 2008)
Temperature and density distribution	FEA	ABAQUS	✓ (Literature results)	Polycarbonate (PC)	(Dong <i>et al.</i> , 2009)
Cooling down stage	FEA	COMSOL Multiphysics	✓ (Own experiments)	PA12	(Li <i>et al.</i> , 2018)
Temperature and melting pool	n/a	n/a	✓ (Own experiments)	PA12 composite	(Shen <i>et al.</i> , 2018)
Temperature and melting pool	FEA	ABAQUS	✓ (Own experiments)	Polyamide 6 (PA6)	(Li <i>et al.</i> , 2020)
Temperature fields and parts distortion	FEA	DEFORM 3D™	✓ (Own experiments)	Polypropylene (PP)	(Ganci <i>et al.</i> , 2017)
Temperature distribution and parts density	FEA	ANSYS	✓ (Literature results)	PC	(Singh and Prakash, 2010)
Temperature and density distribution	FEA	n/a	×	PC	(Bugada <i>et al.</i> , 1999)
Temperature and density distribution	FEA	ABAQUS	✓ (Literature results)	PC	(Dong <i>et al.</i> , 2009)
Temperature and melting pool	FEA	n/a	✓ (Own experiments)	Polyurethane (PU)	(Yuan <i>et al.</i> , 2020)
Heating phase and temperature history	FEA and Discrete Element Model (DEM)	COMSOL and MATLAB	×	n/a	(Xin <i>et al.</i> , 2017)
Temperature history-dependent defects	FEA	ABAQUS	✓ (Own experiments)	PA12	(Josupeit <i>et al.</i> , 2016)
Temperature and melting pool	FEA	n/a	✓ (Own experiments)	PA12	(Riedlbauer <i>et al.</i> , 2014)
Temperature distribution and melting depth	FEA	ANSYS	✓ (Own experiments)	PA12 composite	(Tian <i>et al.</i> , 2018)
Flow, temperature and crystallization kinetics	FEA	n/a	×	PA12	(Balemans <i>et al.</i> , 2020)
Temperature and crystallization fields	FEA	n/a	✓ (Own experiments)	PA12	(Soldner <i>et al.</i> , 2021)
Temperature, melting pools and stress changes	FEA	ABAQUS	✓ (Own experiments & literature results)	PA12 composite	(Li <i>et al.</i> , 2021)
Thermal history (EFFECTS ON SHRINKAGE)	DEM	n/a	✓ (Literature results)	PA12	(Mokrane <i>et al.</i> , 2018)

Flow and temperature fields/distribution	FEA	n/a	×	PA12	(Baemans <i>et al.</i> , 2018)
Depth and temperature of the melting pools	Smoothed Particle Hydrodynamics	SimPARTIX	✓ (Literature results)	PA12 and PEEK	(Bierwisch <i>et al.</i> , 2021)
Temperature profiles and coalescence	'Mathematical models'	n/a	✓ (Own experiments)	PA12	(Chatham <i>et al.</i> , 2021)

Table A.2 Scientific publications focused on computational modelling of SLS (II - Process-part relationship).

PROCESS & PART RELATIONSHIP					
AREA OF APPLICATION	NUMERICAL METHODOLOGY	NUMERICAL TOOL	EXPERIMENTAL VALIDATION	POLYMERIC MATERIAL	REFERENCE
Building time	Artificial Neural Network (ANN)	MATLAB	n/a	PA	(Munguia <i>et al.</i> , 2009)
Energy consumption and material cost (SUSTAINABILITY)	Non-dominated sorting genetic algorithm II	MATLAB	✓ (Case-study)	Polystyrene (PS)	(Ma <i>et al.</i> , 2018)
Energy consumption and material wastage (SUSTAINABILITY)	Mathematical models (<i>e.g.</i> , ED _v), GA and others	MATLAB	✓ (Comparison with similar literature approaches)	PC	(Verma and Rai, 2017)

Table A.3 Scientific publications focused on computational modelling of SLS (III - Part properties).

PART PROPERTIES					
AREA OF APPLICATION	NUMERICAL METHODOLOGY	NUMERICAL TOOL	EXPERIMENTAL VALIDATION	POLYMERIC MATERIAL	REFERENCE
Part density	ANN	n/a	✓ (Own experiments)	PS composite	(Wang <i>et al.</i> , 2009)
Part density	FEA and evolutionary algorithm	ANSYS	✓ (Literature results)	PC	(Vijayaraghavan <i>et al.</i> , 2016)
Part density	ANN	n/a	✓ (Own experiments)	PA12	(Shen <i>et al.</i> , 2004)
Lightweight parts (REDUCE DESIGN TIME AND COSTS)	Genetic algorithm (GA) and FEA	n/a	✓ (Case-study)	PA12 composite	(Paz <i>et al.</i> , 2016)
Part shrinkage	ANN	n/a	✓ (Own experiments)	PS composite	(Rong-Ji <i>et al.</i> , 2009)
Part shrinkage	ANN	n/a	✓ (Own experiments)	PS	(Wang <i>et al.</i> , 2007)
Part shrinkage	Response Surface Methodology and ANN	n/a	✓ (Own experiments)	PA12 composite	(Negi and Sharma, 2016)
Part warpage	Back-propagation Neural Network and GA	ABAQUS	✓ (Own experiments)	PA12	(Dastjerdi <i>et al.</i> , 2017)
Curling and bending deformation	Regression models	MATLAB	✓ (Case-study)	PA12	(Ha <i>et al.</i> , 2018)
Part defects	Convolutional Neural Networks (CNN)	n/a	✓ (Own experiments)	PA12 and PA12 composite	(Xiao <i>et al.</i> , 2020)
Part defects	CNN	n/a (Python script)	✓ (Own experiments)	PA12	(Westphal and Seitz, 2021)
Part position and orientation	GA	Open Inventor	✓ (Case-study)	n/a	(Hur <i>et al.</i> , 2001)

Part orientation	Conventional optimisation algorithm	MATLAB	✓ (Case-study)	n/a	(Singhal <i>et al.</i> , 2009)
MECHANICAL PROPERTIES					
Mechanical properties (SCAFFOLDS - BONE TISSUE ENGINEERING)	FEA	ABAQUS	✓ (Own experiments)	Polyamide and polycaprolactone (PCL)	(Cahill <i>et al.</i> , 2009; Doyle <i>et al.</i> , 2015)
Mechanical properties	FEA	ANSYS	✓ (Own experiments)	PA12	(Lindberg <i>et al.</i> , 2018)
Mechanical properties (LATTICE STRUCTURES)	FEA	ABAQUS	✓ (Own experiments)	PA12	(Bai <i>et al.</i> , 2020)
Mechanical properties (LATTICE STRUCTURES)	FEA	ANSYS	✓ (Own experiments)	PA12	(Savio <i>et al.</i> , 2019)
Mechanical properties (LATTICE STRUCTURES)	FEA	ANSYS	✓ (Own experiments)	PA12	(Jin <i>et al.</i> , 2018)
Mechanical properties	Adaptive Network-based Fuzzy Inference System (ANFIS)	MATLAB	✓ (Own experiments)	PA12 composite	(Aldahash <i>et al.</i> , 2020)
Mechanical properties	Representative Volume Element Model and FEA	ABAQUS	✓ (Own experiments)	PA12 composite	(Tang <i>et al.</i> , 2021)
Mechanical properties (DEFORMABLE TEXTILES)	FEA	ABAQUS	✓ (Own experiments)	PA12	(Crookston <i>et al.</i> , 2008)
Mechanical properties	ANFIS vs Grey Relational Analysis	n/a	✓ (Own experiments)	PA12 composite	(Sohrabpoor <i>et al.</i> , 2018)
Mechanical properties	FEA	ABAQUS and PolyUMod	✓ (Own experiments)	PA12	(Schneider and Kumar, 2020)
Porosity and strength (LATTICE STRUCTURES)	FEA	ANSYS (Python script)	✓ (Own experiments)	PA12	(Cerardi <i>et al.</i> , 2013)
Density, hardness, tensile strength	Multi-objective GA	n/a	✓ (Own experiments)	PA12	(Fountas and Vaxevanidis, 2021)
Thermo-mechanical behaviour	Material Point Method	n/a	×	PA12	(Maeshima <i>et al.</i> , 2021)
Mechanical properties	'Machine Learning'	n/a (Python script)	✓ (Own experiments)	PA12	(Baturynska, 2019)

Appendix B. Summary of properties and experimental regressions depending on fundamental SLS process parameters

Herein the experimental regressions fitting the mechanical and geometric properties of parts produced by SLS with different hatching and contour parameters are presented. These equations and corresponding coefficient of regression allow to comprehend the experimental process-structure-property relationships that are useful to monitor the sintering process by estimating the properties of laser-sintered parts as a function of the most relevant process parameters.

Table B.1 Summary of properties and experimental regressions depending on fundamental SLS process parameters.

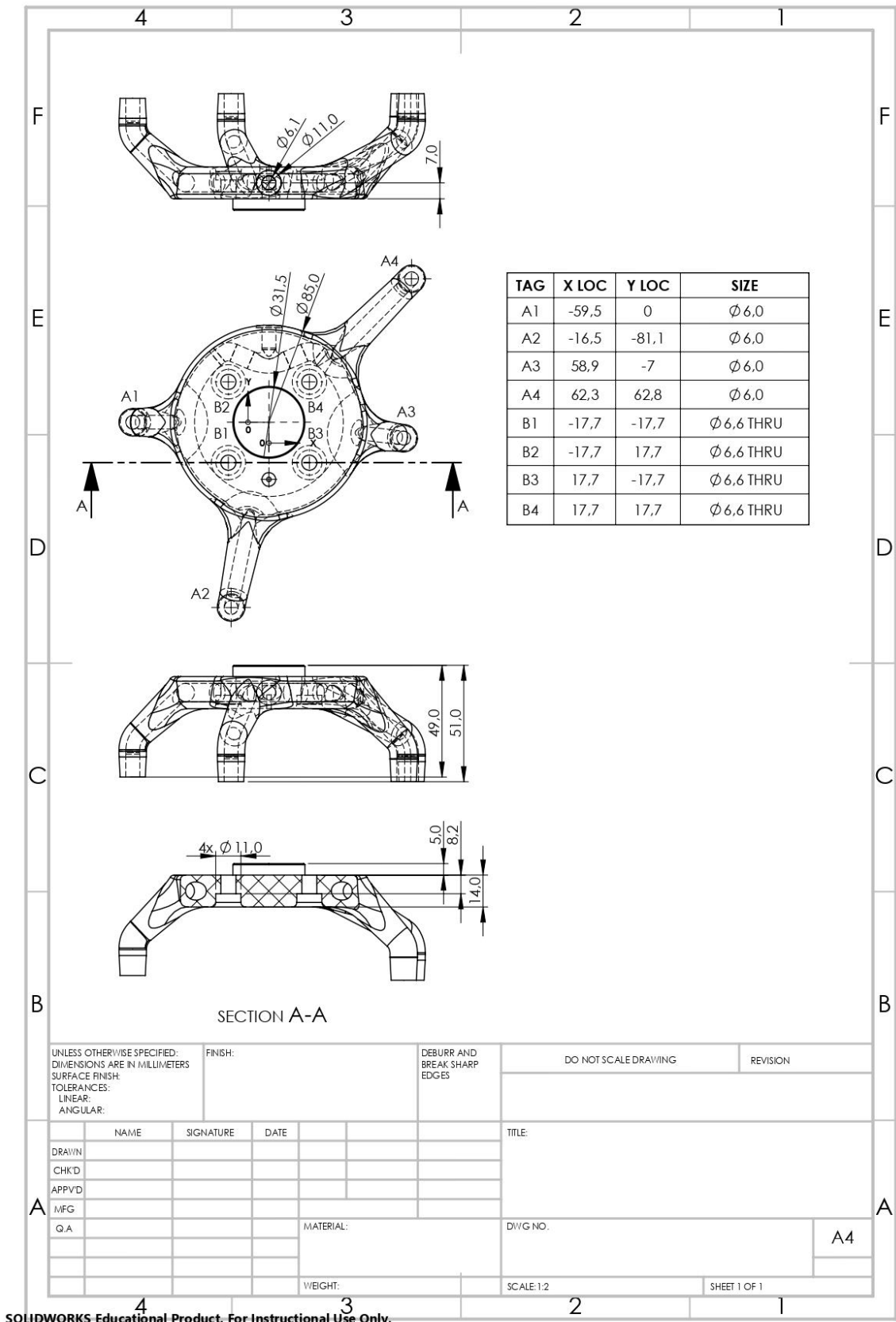
PART PROPERTIES		HATCHING PARAMETERS						EXPERIMENTAL FITTING REGRESSION		
		ED _v (J/mm ³)						Equation	R ²	
		0.158	0.198	0.238	0.278	0.318	0.358	0.398		
MECHANICAL	Elastic modulus, <i>E</i> (MPa)	1197.0 0 ± 74.20	1483.9 2 ± 69.09	1535.1 5 ± 54.12	1553.5 5 ± 93.25	1573.8 8 ± 41.47	1474.6 0 ± 56.57	1192.6 5 ± 100.83	$E = -$ $2.67 \times 10^4 \times ED_v$ $+ 2$ $1.49 \times 10^4 \times ED_v$ $- 4.67 \times 10^2$	0.9 5
	Tensile stress at yield, σ_{Ced} (MPa)	22.06 ± 1.20	25.32 ± 1.13	26.98 ± 0.28	24.87 ± 0.95	26.76 ± 1.50	29.84 ± 0.35	30.52 ± 1.29	$\sigma_{Ced} =$ $16.37 \times ED_v^2 +$ $21.44 \times ED_v +$ 19.29	0.8 2
	Tensile strain at yield, ϵ_{Ced} (%)	2.00 ± 0.24	1.93 ± 0.14	1.94 ± 0.11	1.82 ± 0.15	1.89 ± 0.11	2.22 ± 0.05	2.68 ± 0.32	$\epsilon_{Ced} =$ $34.45 \times ED_v^2 -$ $16.86 \times ED_v +$ 3.87	0.9 3
	Tensile stress at break, σ_{Rut} (MPa)	35.36 ± 0.27	39.28 ± 0.62	41.75 ± 0.56	40.90 ± 0.68	36.84 ± 0.63	37.35 ± 1.52	40.16 ± 2.10	$\sigma_{Rut} = -$ $161.98 \times ED_v^2$ $+ 95.09 \times ED_v$ $+ 25.93$	0.2 1
	Tensile strain at break, ϵ_{Rut} (%)	12.70 ± 1.40	13.17 ± 2.11	16.93 ± 2.47	21.43 ± 4.54	31.43 ± 1.27	29.06 ± 8.96	26.69 ± 7.63	$\epsilon_{Rut} =$ $78.80 \times ED_v -$ 0.28	0.7 9
	Tensile strength, σ_{Max} (MPa)	36.24 ± 0.90	39.95 ± 0.48	42.91 ± 0.55	43.08 ± 0.35	44.12 ± 0.98	44.37 ± 0.74	43.81 ± 0.59	$\sigma_{Max} = -$ $246.73 \times ED_v^2$ $+ 166.43 \times ED_v$ $+ 16.45$	0.9 8
	Critical energy release rate, G_{lc} (N/mm)	8.06 ± 0.06	11.68 ± 1.05	22.23 ± 0.34	29.19 ± 0.48	31.99 ± 1.14	26.87 ± 0.81	(1)	$G_{lc} = -$ $833.71 \times ED_v^2$ $+ 545.86 \times ED_v$ $- 59.78$	0.9 3
	Energy release rate at maximum load, G_{lu} (N/mm)	7.90 ± 0.15	11.47 ± 0.86	20.62 ± 1.62	28.91 ± 0.85	31.84 ± 1.10	25.72 ± 0.81	(1)	$G_{lu} = -$ $818.42 \times ED_v^2$ $+ 535.52 \times ED_v$ $- 58.79$	0.9 1
GEOMETRIC	Flatness of surfaces, <i>F_s</i> (mm)	0.19 ± 0.01	0.12 ± 0.02	0.17 ± 0.02	0.27 ± 0.02	0.33 ± 0.00	(1)	(1)	$F_s =$ $14.32 \times ED_v^2 -$ $5.74 \times ED_v +$ 0.73	0.9 1
	Roundness of central holes, <i>R_{CH}</i> (mm)	0.11 ± 0.02	0.08 ± 0.01	0.08 ± 0.01	0.09 ± 0.01	0.08 ± 0.01	(1)	(1)	$R_{CH} =$ $1.80 \times ED_v^2 -$ $0.97 \times ED_v +$ 0.21	0.4 7

Roundness of lateral holes, R_{LH} (mm)	0.19 ± 0.01	0.15 ± 0.02	0.18 ± 0.01	0.19 ± 0.01	0.22 ± 0.02	(1)	(1)	$R_{LH} =$ $5.48 \times ED_V^2 - 2.34 \times ED_V + 0.41$	0.8 5	
Parallelism of surfaces, P_s (mm)	0.10 ± 0.01	0.17 ± 0.01	0.29 ± 0.01	0.28 ± 0.01	0.43 ± 0.01	(1)	(1)	$P_s =$ $1.30 \times ED_V^2 + 1.31 \times ED_V - 0.14$	0.9 4	
Straightness of surfaces, S_s (mm)	0.18 ± 0.01	0.17 ± 0.02	0.16 ± 0.02	0.18 ± 0.02	0.29 ± 0.02	(1)	(1)	$S_s =$ $11.78 \times ED_V^2 - 5.02 \times ED_V + 0.69$	0.9 1	
Average deviation/positive x-position, D_{+x} (%)	0.04 ± 0.05	0.05 ± 0.02	0.03 ± 0.01	0.19 ± 0.10	0.32 ± 0.18	(1)	(1)	$D_{+x} =$ $18.51 \times ED_V^2 - 7.05 \times ED_V + 0.70$	0.9 2	
Average deviation/negative x-position, D_{-x} (%)	0.01 ± 0.03	0.05 ± 0.02	0.12 ± 0.04	0.25 ± 0.04	0.54 ± 0.01	(1)	(1)	$D_{-x} =$ $24.68 \times ED_V^2 - 8.58 \times ED_V + 0.76$	0.9 9	
Average deviation/positive y-position, D_{+y} (%)	0.15 ± 0.03	0.16 ± 0.03	0.36 ± 0.10	0.34 ± 0.01	0.80 ± 0.10	(1)	(1)	$D_{+y} =$ $22.08 \times ED_V^2 - 8.81 \times ED_V + 0.93$	0.7 8	
Average deviation/negative y-position, D_{-y} (%)	0.05 ± 0.01	0.16 ± 0.04	0.02 ± 0.01	0.18 ± 0.03	0.38 ± 0.03	(1)	(1)	$D_{-y} =$ $30.34 \times ED_V^2 - 10.72 \times ED_V + 1.10$	0.9 1	
CONTOUR PARAMETERS										
PART PROPERTIES	P_{Laser}/S_{Scan} (J/mm) ($\propto ED_V$)					EXPERIMENTAL FITTING REGRESSION				
	0.007	0.009	0.011	0.013	0.015	Equation	R^2			
MECHANICAL	Elastic modulus, E (MPa)	1674.53 ± 77.71	1610.51 ± 83.77	1511.62 ± 22.58	1582.66 ± 52.95	1611.46 ± 72.46	$E =$ $5.96 \times 10^5 \times ED_V^2 - 1.43 \times 10^5 \times ED_V + 2.41 \times 10^3$	0.8 0		
	Tensile stress at yield, σ_{Ced} (MPa)	37.16 ± 2.33	34.95 ± 1.51	34.94 ± 0.30	35.34 ± 1.54	34.73 ± 1.94	$\sigma_{Ced} =$ $5.96 \times 10^4 \times ED_V^2 - 1.58 \times 10^3 \times ED_V + 45.22$	0.7 3		
	Tensile strain at yield, ϵ_{Ced} (%)	2.40 ± 0.09	2.38 ± 0.16	2.53 ± 0.03	2.46 ± 0.07	2.26 ± 0.20	$\epsilon_{Ced} =$ $9.92 \times 10^3 \times ED_V^2 + 215.14 \times ED_V + 1.32$	0.7 2		
	Tensile stress at break, σ_{Rut} (MPa)	50.46 ± 0.53	44.24 ± 0.68	43.43 ± 1.14	43.21 ± 0.25	43.79 ± 1.58	$\sigma_{Rut} =$ $2.43 \times 10^5 \times ED_V^2 - 6.24 \times 10^3 \times ED_V + 82.59$	0.9 3		
	Tensile strain at break, ϵ_{Rut} (%)	19.89 ± 1.68	18.40 ± 2.27	19.17 ± 4.07	16.36 ± 0.75	16.11 ± 1.99	$\epsilon_{Rut} =$ $475.01 \times ED_V + 23.36$	0.8 0		
	Tensile strength, σ_{Max} (MPa)	55.58 ± 0.83	49.94 ± 1.75	48.41 ± 1.04	49.08 ± 1.92	50.09 ± 1.46	$\sigma_{Max} =$ $2.63 \times 10^5 \times ED_V^2 - 6.58 \times 10^3 \times ED_V + 89.25$	0.9 5		

	Critical energy release rate, G_c (N/mm)	26.79 ± 2.85	31.16 ± 4.15	24.90 ± 4.15	29.62 ± 3.50	31.53 ± 1.14	$G_c =$ $9.80 \times 10^3 \times ED_V^2 -$ $1.83 \times 10^3 \times ED_V$ $+ 36.21$	0.2 7
	Energy release rate at maximum load, G_u (N/mm)	26.30 ± 3.29	30.39 ± 4.03	24.63 ± 4.04	25.81 ± 2.84	29.46 ± 3.35	$G_u =$ $1.10 \times 10^3 \times ED_V^2 -$ $2.40 \times 10^3 \times ED_V$ $+ 39.52$	0.1 4
GEOMETRIC	Flatness of surfaces, F_s (mm)	0.23 ± 0.01	0.34 ± 0.02	0.33 ± 0.02	0.30 ± 0.02	0.32 ± 0.01	$F_s =$ $14.32 \times ED_V^2 +$ $76.42 \times ED_V -$ 0.15	0.6 5
	Roundness of central holes, R_{CH} (mm)	0.11 ± 0.01	0.12 ± 0.01	0.12 ± 0.01	0.14 ± 0.01	0.15 ± 0.01	$R_{CH} =$ $245.11 \times ED_V^2 -$ $1.13 \times ED_V +$ 0.11	0.8 4
	Roundness of lateral holes, R_{LH} (mm)	0.20 ± 0.01	0.20 ± 0.02	0.19 ± 0.01	0.17 ± 0.01	0.16 ± 0.02	$R_{LH} = -$ $590.15 \times ED_V^2$ $+ 7.61 \times ED_V +$ 0.18	0.9 3
	Parallelism of surfaces, P_s (mm)	0.29 ± 0.01	0.34 ± 0.01	0.35 ± 0.01	0.32 ± 0.01	0.38 ± 0.01	$P_s = -$ $224.50 \times ED_V^2$ $+ 14.139 \times ED_V$ $+ 0.21$	0.6 3
	Straightness of surfaces, S_s (mm)	0.23 ± 0.02	0.28 ± 0.01	0.27 ± 0.03	0.29 ± 0.02	0.26 ± 0.02	$S_s = -$ $2.28 \times 10^3 \times ED_V^2$ $+ 55.33 \times ED_V$ $- 0.05$	0.8 0

⁽¹⁾ Manufacturing of non-conforming parts for characterization.

Appendix C. 2D CAD drawing of the robot end-effector



SOLIDWORKS Educational Product. For Instructional Use Only.

Figure C.1 CAD drawing of the robot end-effector.